



**HAL**  
open science

# Mecanisme de fragmentation des peptides en spectrométrie de masse : couplages de techniques de caractérisation structurale

Oscar Hernandez Alba

► **To cite this version:**

Oscar Hernandez Alba. Mecanisme de fragmentation des peptides en spectrométrie de masse : couplages de techniques de caractérisation structurale. Autre [cond-mat.other]. Université Paris Sud - Paris XI, 2014. Français. NNT : 2014PA112421 . tel-01135985

**HAL Id: tel-01135985**

**<https://theses.hal.science/tel-01135985>**

Submitted on 26 Mar 2015

**HAL** is a multi-disciplinary open access archive for the deposit and dissemination of scientific research documents, whether they are published or not. The documents may come from teaching and research institutions in France or abroad, or from public or private research centers.

L'archive ouverte pluridisciplinaire **HAL**, est destinée au dépôt et à la diffusion de documents scientifiques de niveau recherche, publiés ou non, émanant des établissements d'enseignement et de recherche français ou étrangers, des laboratoires publics ou privés.



UNIVERSITÉ PARIS-SUD

ÉCOLE DOCTORALE 470 :

CHIMIE DE PARIS SUD

Laboratoire de Chimie Physique (LCP)

**THÈSE DE DOCTORAT**

CHIMIE

par

**Hernandez Alba Oscar**

**Mecanisme de fragmentation des peptides en spectrométrie de  
masse: couplages de techniques de caractérisation structurale.**

Date de soutenance : 16/12/2014

Composition du jury :

Directeur de thèse :	Maître Philippe	Directeur de Recherche CNRS (LCP)
Rapporteurs :	Salpin Jean-Yves	Directeur de Recherche (Lambe)
	Afonso Carlos	Professeur à l'Université de Rouen
Examineurs :	Grégoire Gilles	Chargé de Recherche CNRS (LPL)
	Parneix Pascal	Professeur à l'Université Paris Sud (ISMO)



## Acknowledgement

En primer lugar quisiera agradecer a los miembros del jurado por haber aceptado leer mi trabajo. Agradezco a Dr. Jean Yves Salpin y Dr. Carlos Afonso por haber aceptado ser mis examinadores. Al mismo tiempo agradecer también a los Drs. Pascal Parneix y Gille Gregoire por lo fácil que han hecho la constitución de mi jurado.

Como no podría ser de otra manera, querría destacar la gran importancia e influencia que ha tenido mi director de tesis Dr. Philippe Maître, por su predisposición a ayudarme, por su cercanía, por sus ideas y al mismo tiempo por la enorme dedicación que ha aportado a este proyecto. Gracias también por decirme las cosas claras y por exigir siempre más. Como diría el escritor irlandés Samuel Beckett: *“Ever tried. Ever failed. No matter. Try again. Fail again. Fail better”*. También quisiera tener unas palabras de agradecimiento para con mi « hermano » francés Vincent Steintmetz con el cual mi relación va mucho más allá de lo estrictamente laboral. Simplemente decirle que nunca podré estar lo suficientemente agradecido por todo lo que ha aportado a mi vida (Allons enfants de la Patrie...). Agradecer a Imen Defferrard que aunque cambio de laboratorio hace medio año su presencia se sigue notando cada día. A todos mis compañeros del grupo AFMIR: Dr. Alexandre Dazzi, Dr. Arianne Deniset y futuro Dr. Rolando Rebois. Todos ellos empezaron siendo simples compañeros de laboratorio y hoy puedo presumir orgulloso de su amistad. Agradecer a los recién llegados al laboratorio Loïc y Loren que aunque a mi pesar no he podido compartir mucho tiempo con ellos, si ha bastado para fundar unos estrechos lazos de amistad también. También destacar las personas con las que he tenido el enorme placer de colaborar durante estos tres años de mi vida. Entre ellos, Pr. Bela Paizs del que destaco su proximidad y ese afán e ilusión que muestra por la ciencia como si su carrera profesional acabara de comenzar. Agradecer también al grupo de Gary L. Glish de Carolina del Norte en general y a Gary L. Glish y Samanta Isenberg en particular por su contribución en la parte de movilidad iónica. Sin vuestra aportación, nunca habiéramos sido capaces de hacer funcionar el equipo.

A todas las personas de gran calidad humana que esta experiencia me ha permitido conocer, entre ellos Fer que para mi representa la sabiduría, la humildad, la tranquilidad, esa persona que siempre encuentra las palabras adecuadas en el momento oportuno y que poco a poco se convierte en una persona

fundamental en tu vida. A Joaquin y Rocio, el matrimonio más especial y autentico que he conocido nunca. Por favor no borréis vuestras sonrisas porque son el motor que impulsa a la gente que está alrededor. A Bea, esa chica gallega con espíritu andaluz que nunca tampoco podre olvidar. Y a un sinfín de amigos: El Ale (el sempiterno vividor), a Pilar (la “encantadora” encantadora de animales), a Raquel (la alegre Salmantina-Leonesa), a Esther (la chica de la cuenca minera ;)), a Pepelu (que hizo su postdoc en Suiza)...

Me gustaría también mostrar una sentida deferencia con la gente que ha estado a mi lado durante diferentes periodos de mi vida. Al PhD chat, que aunque se hayan sentido algo defraudados por mi escasa aportación siempre me han aceptado como uno más. A esa gente que ha crecido conmigo que son mis amigos de la infancia, en especial a mis dos “Davices” (David Carrera y David Rodriguez). Gracias por vuestras respectivas visitas y sobre todo por seguir guardando esa amistad conmigo a pesar de la distancia. Siempre tengo muy presente todo lo que hemos vivido juntos. Al que un día fue mi entrenador y que ahora es un gran amigo, José Labrador Posadilla (Labra) que me enseñó a aceptar la derrota y la victoria y me mostro que con esfuerzo todo se puede superar. A mi amiga Marta, que un día me encontré por las calles de Burdeos y que hoy sigue estando a mi lado incondicionalmente. Agradecer enormemente a Asun todo lo que ha supuesto y supondrá en mi vida. Solo ella sabe que 200 paginas como estas no serían suficientes para agradecerle todo lo que ha hecho por mi. A mi gran amigo Dani, porque él es el culpable de que mi vida tomase estos derroteros. Siempre nos quedara esa amalgama de recuerdos parisinos que espero los revivamos durante muchos años con mucha alegría y una cierta dosis de nostalgia. Al tercero en discordia, Angel, no sabes cuánto te echo de menos. Gracias por ese desparpajo y ese descarro que le echas a la vida. Darle las gracias a la chica que decidió cambiar mi vida un 18 de mayo del año 2012. Esa chica que me hace ver la vida de color de rosa. Esa chica que lo es todo para mi: mi compañera, mi amiga, mi confidente, mi cómplice, mi novia. En definitiva la chica que hace latir mi corazón. Porque lo eres todo para mi quiero darte un millón de gracias Emilie.

Por ultimo me gustaría destacar y agradecer todo lo que mi familia ha hecho por mi. Expresarles lo que tantas veces me cuesta decirles como que les quiero mucho, que son mi apoyo fundamental y que no los cambiaría por nada del mundo. Simplemente gracias. A mi hermano que tanto cariño le tengo y

que tantas buenas lecciones de vida me ha mostrado. Solo yo sé lo importante que es para mí. Por todo eso, esta tesis está dedicada a vosotros.



## Remerciements

Je tiens tout d'abord à remercier les membres du jury d'avoir accepté de lire mon travail. Je remercie Dr Jean Yves Salpin et Dr Carlos Afonso d'avoir accepté d'être mes rapporteurs. Je voudrais également remercier les docteurs Pascal Parneix ainsi que Gille Gregoire d'avoir répondu sans hésitation pour faire partie de mon jury.

Comment ne pas remercier mon directeur de thèse Dr. Philippe Maître, il est la personne la plus importante et je tiens à souligner la grande importance et l'influence de mon directeur de thèse Prof. Philippe Maître,. Je tiens à souligner son soutien au quotidien, sa proximité, ses idées constantes et son dévouement continu à ce projet. Merci d'avoir su me dire les choses clairement et d'avoir toujours exigé le meilleur de moi-même. Comme Samuel Becket dit : « *Ever tried. Ever failed. No matter. Try again. Fail again. Fail better* ». Je voudrais aussi dire un mot de remerciement à mon «frère» français Vincent Steintmetz avec qui j'ai noué une relation qui dépasse largement le cadre professionnel. Je ne pourrais jamais lui être assez reconnaissant pour tout ce qu'il m'a apporté. (Allons enfants de la Patrie ...). J'en profite pour remercier Imen Defferrard, malgré son départ du laboratoire, pour son soutien et sa présence au quotidien. A tous mes collègues du groupe AFMIR : Dr Alexandre Dazzi, Dr Arianne Deniset et le futur Dr Rolando Rebois, qui étaient initialement des collègues de laboratoire et dont je suis fier aujourd'hui de pouvoir compter parmi mes amis. Je tiens à remercier les nouveaux arrivants du laboratoire ; Loren et Loïc avec qui j'espère avoir fondé des liens d'amitié malgré le peu de temps passé ensemble.

A noter également les gens avec lesquels j'ai eu un grand plaisir à travailler au cours de ces trois dernières années. Parmi eux, Pr. Bela Paizs qui a su me mettre à l'aise et qui a su partager/ me transmettre son enthousiasme et sa passion pour la science. Je remercie aussi le groupe Gary L. Glish de la Caroline du Nord et plus particulièrement Gary L. Glish et Samantha Isenberg pour leur contribution au développement de la partie de ma thèse concernant la mobilité ionique. Sans votre aide, nous n'aurions jamais pu faire fonctionner l'équipement.

A toutes les personnes de grandes qualités humaines que cette expérience m'a permis de rencontrer, et notamment Fernando qui représente pour moi la sagesse, l'humilité, la tranquillité, trouvant toujours les mots justes au bon moment. Il est devenu petit à petit l'une des personnes les plus importantes de ma vie. A Joaquin et Rocio, le couple le plus unique et authentique que je connaisse. N'effacez jamais le sourire qui illumine vos deux visages car c'est une source de motivation pour votre entourage. Bea, la fille galicienne à l'esprit andalou que je ne pourrais jamais oublier. Sans compter sur une foule d'amis tels que Ale, Pilar, Rachel, Esther et Pepelu...

Je voudrais aussi exprimer mon profond respect pour les gens qui ont été à mes côtés pendant les différentes périodes de ma vie. Mention spéciale au « PhD Chat », même si j'ai pu en décevoir certains par ma petite contribution, je vous remercie de m'avoir toujours accepté comme tel. Merci à mes deux amis d'enfance "Davices" (David Carrera et David Rodriguez) pour vos visites, je suis ravi que notre amitié ait pu résister face à l'éloignement. Je garde toujours en mémoire tous ces bons moments de vie que nous avons vécus ensemble. A Jose Labrador Posadilla (Labra) qui est mon ancien entraîneur et mon grand ami, et qui m'a appris à accepter la défaite et la victoire et m'a montré qu'avec de la persévérance tout était surmontable. A mon amie Marta, que j'ai rencontré par hasard à Bordeaux et qui maintenant reste une amie très proche. Je tiens à dire un grand merci à Asun pour tout ce qu'elle a signifié et signifie dans ma vie. Elle est la seule à savoir que 200 pages ne suffiraient pas à la remercier pour tout ce qu'elle a fait pour moi. Pour mon grand ami Dani, qui y est pour beaucoup dans le sens qu'a pris ma vie. Pour nous, « Paris restera toujours Paris », le lieu de tant de bons souvenirs, dont j'espère que nous nous souviendrons encore pour longtemps. Enfin un merci à Angel pour sa facilité à se sortir de n'importe quelle situation et sa capacité à toujours aller de l'avant, sache que tu me manques beaucoup. Je souhaiterais remercier la personne qui a décidé de changer ma vie un certain 18 mai 2012. Depuis cette personne me fait voir la vie en rose. Elle représente tout pour moi, la considérant à la fois comme mon ami, ma confidente, ma complice et ma compagne. En définitive elle fait battre mon cœur. C'est pour tout cela, Emilie, que je tiens à te remercier un million de fois.

Enfin, je tiens à souligner et à remercier tout ce que ma famille a fait pour moi. J'aimerais leur exprimer tout l'amour que j'ai pour eux, même si je ne le fais pas assez. Ils sont mon principal soutien

et je ne les échangerais pour rien au monde. Tout simplement merci. A mon frère que j'aime tant, lui qui m'a enseigné tant de choses de la vie et qui compte tellement à mes yeux. Cette thèse vous est tout simplement dédiée.



## Table of contents

Acknowledgement.....	I
Remerciements .....	V
Table of figures.....	XIII
List of tables .....	XVII
List of abreviations .....	XIX
INTRODUCTION GENERALE .....	1
1 IR SPECTROSCOPY INTEGRATED TO MASS SPECTROMETRY: INSTRUMENTS AND METHODOLOGY	9
1.1 Introduction.....	11
1.2 Two experimental set-ups.....	12
1.2.1 Quadrupole Ion Trap mass spectrometer .....	12
1.2.2 FT-ICR tandem mass spectrometer .....	16
1.3 IRMPD with two lasers. ....	19
1.3.1 IRMPD principles .....	19
1.3.2 IR-Free Electron Laser (FEL).....	22
1.3.3 Benchtop IR OPO/OPA laser system.....	24
1.4 IRMPD Spectroscopy: Practical details.....	26
1.4.1 MS <sup>3</sup> experiment using a Quadrupole Ion Trap set-up.....	27
1.4.2 MS <sup>3</sup> experiment using the FT-ICR set-up.....	28
1.4.3 Combination with an auxiliary CO <sub>2</sub> laser. ....	29
1.5 IRMPD Spectroscopy at FELIX versus CLIO .....	32
1.5.1 Irradiation set-ups. ....	33
1.5.2 Different fragmentation methods within the ICR cell.....	33
1.5.3 In-source fragmentation.....	34
1.6 Different groups developing IR Spectroscopy .....	35
1.7 Bibliography.....	38
2 REARRANGEMENT CHEMISTRY OF $a_n$ IONS.....	43
2.1 Introduction.....	45
2.2 Results and discussion .....	49
2.2.1 Rearrangement chemistry of the $a_2$ ion of GGGH <sup>+</sup> .....	49
2.2.2 Infrared Spectra of $a_2$ ion of GGG.....	51
2.3 $a_2$ Fragment of protonated YGGFL: Evidence for side-chain proton transfer catalysis. ....	53
2.3.1 IR spectra in the 1000-2000 cm <sup>-1</sup> range: Evidence for rearrangement.....	53

2.3.2	IR spectra in the 3400-3800 cm <sup>-1</sup> : IR signature of rearranged imine-amide structure.	56
2.3.3	Potential energy surface: Evidence for proton-transfer catalysis.	57
2.3.4	Quantifying the isomer populations.	59
2.3.5	Controlling the rearrangement chemistry.	62
2.4	<i>a</i> <sub>3</sub> Fragment of protonated tetraglycine : QIT versus FT-ICR.	64
2.4.1	Structure and isomerization processes.	64
2.4.2	IR spectra in the 3400-3800 cm <sup>-1</sup> .	65
2.4.3	IRMPD spectra recorded with the FT-ICR or QIT set-ups.	67
2.4.4	<i>a</i> <sub>4</sub> ion of GGGG.	69
2.4.5	Infrared Spectroscopy of the <i>a</i> <sub>4</sub> ion of GGGGG.	70
2.5	Conclusions.	73
2.6	Annexes.	74
2.7	Bibliography.	76
3	MIDDLE SIZE <i>b</i> <sub><i>n</i></sub> IONS: ION-MOLECULE REACTION AS A DIRECT EVIDENCE OF MACROCYCLE FORMATION.	79
3.1	Introduction.	81
3.2	Methods	88
3.3	Intra-peptide hydrogen bond interactions.	91
3.4	Results and discussion.	92
3.4.1	IRMPD of <i>b</i> <sub>6</sub> ion: Zundel-type H-bonding.	92
3.4.2	Formation of an ammonia adduct with a model cyclic peptide.	98
3.4.3	[cyclic-YAGFL+NH <sub>3</sub> +H <sup>+</sup> ] predicted structure and IR spectrum.	100
3.4.4	Complex formed between middle size <i>b</i> <sub><i>n</i></sub> and NH <sub>3</sub> : mass spectrometry and IR spectra. 104	
3.4.5	IRMPD spectroscopy of the <i>b</i> <sub>9</sub> +NH <sub>3</sub> <sup>+</sup> complex: Highly symmetric structure.	107
3.4.6	IRMPD spectroscopy of the <i>b</i> <sub><i>n</i></sub> -NH <sub>3</sub> <sup>+</sup> ( <i>n</i> = [6, 8]) complexes.	110
3.5	Conclusions.	114
3.6	Annexes	115
3.7	Bibliography.	119
4	PROBING MOBILITY SELECTED SACCHARIDE ISOMERS: SELECTIVE ION-MOLECULE REACTIONS AND WAVELENGTH-SPECIFIC IR ACTIVATION	123
4.1	Ion Mobility Spectrometry (IMS).	125
4.1.1	IMS: A brief overview.	125
4.1.2	Differential Ion Mobility Spectrometry (DIMS).	127
4.2	IMS applied to sugar separation.	129
4.2.1	Saccharides: isomers.	129

4.2.2	IMS applied to saccharides.....	132
4.2.3	Alternative methods to provide structural characterization: Spectroscopic Techniques. 134	
4.3	Coupling DIMS to MS/MS.....	136
4.3.1	DIMS and MS/MS: The DIMS 3G assembly. ....	136
4.3.2	Radio-frequency waveform.....	137
4.3.3	Two DIMS modes: Scanning and Static modes. ....	138
4.3.4	Methods. ....	139
4.4	Results and discussion.....	139
4.4.1	Separation of alkali saccharide complexes by DIMS. ....	139
4.4.2	Ion-Molecule Reaction (IMR) of DIMS-Selected Ions: More insights into the structural characterization.....	141
4.4.3	Infrared Spectroscopy of Li(Sac)(H <sub>2</sub> O) <sup>+</sup> .....	143
4.4.4	Structure-specific band observed for glucose anomers.....	145
4.4.5	Comparison with previous theoretical studies on metalated monosaccharides.....	148
4.5	Conclusions.....	149
4.6	Bibliography.....	152
5	PROBING THE STRUCTURE OF METAL CATIONIZED MONOSACCHARIDES: IR SPECTROSCOPY ..	157
5.1	Introduction.....	159
5.2	Conformational search: Nomenclature and method.....	159
5.2.1	Conformation of free monosaccharides: nomenclature.....	159
5.2.2	Method of calculation.....	163
5.2.3	Free monosaccharides: structure, energetic and IR spectra.....	165
5.3	Lithiated monosaccharides: Structure and energetics.....	169
5.3.1	Li(Sac) <sup>+</sup> adducts: lowest energy structures.....	169
5.3.2	Structure and energetics of Li(Sac)(H <sub>2</sub> O) <sup>+</sup> adducts.....	175
5.4	IR spectroscopy of monosaccharide complexes. ....	181
5.4.1	Experimental infrared Spectra of Li(Sac) <sup>+</sup> and Li(Sac)(H <sub>2</sub> O) <sup>+</sup> adducts.....	181
5.4.2	IR Spectra of M(β-Me-Glc)(L) <sup>+</sup> : effect of M=(Li, Na) and L=(H <sub>2</sub> O, CH <sub>3</sub> CN).....	183
5.5	IR spectra of monosaccharide complexes: Spectral and structural assignment.....	185
5.5.1	Li(α-Me-Glc) <sup>+</sup> complexes. ....	185
5.5.2	Li(α-Me-Glc)(H <sub>2</sub> O) <sup>+</sup> complexes. ....	188
5.5.3	Li(α-Me-Man) <sup>+</sup> complexes.....	191
5.5.4	Li(α-Me-Man)(H <sub>2</sub> O) <sup>+</sup> complexes.....	193
5.5.5	Li(β-Me-Glc) <sup>+</sup> complexes. ....	195
5.5.6	Li(β-Me-Glc)(H <sub>2</sub> O) <sup>+</sup> complexes.....	197

5.6	Conclusions.....	201
5.7	Annexes .....	203
5.8	Bibliography.....	209
	CONCLUSION .....	213

## Table of figures

<i>Figure 1-1: Schematic view of our Quadrupole Ion Trap mass spectrometer (Bruker Esquire 3000+).</i>	13
<i>Figure 1-2 : Detailed view of the Ring Electrode. Ions are trapped within the trap by the potential difference established between the two endcap and the ring electrodes.</i>	14
<i>Figure 1-3 : Schematic view of our FT-ICR mass spectrometer (Bruker APEX IV).</i>	17
<i>Figure 1-4 : Detection and analysis of the ions in the ICR cell.</i>	18
<i>Figure 1-5: Multiple Photon Absorption through a single IR active vibrational mode assuming that the potential is harmonic (left) or anharmonic (right).</i>	20
<i>Figure 1-6 : Schematic representation of the multiple photon absorption process.</i>	21
<i>Figure 1-7 : Magnetic cavity of the CLIO IR FEL.</i>	23
<i>Figure 1-8 : Temporal structure of the CLIO IR FEL at Orsay.</i>	24
<i>Figure 1-9: Representation of the Laservision OPO/OPA laser system used in this work.</i>	25
<i>Figure 1-10: Duty cycle associated with an MS<sup>3</sup> sequence performed with our QIT.</i>	27
<i>Figure 1-11: Duty cycle associated with an MS<sup>3</sup> sequence performed with our FT-ICR mass spectrometer.</i>	28
<i>Figure 1-12: Synchronization of the tunable infrared lasers (red) with the auxiliary cw CO<sub>2</sub> laser (yellow).</i>	29
<i>Figure 1-13 : A mirror with a hole is used in order to get the overlap of the tunable (IR FEL or IR OPO/OPA) laser and the auxiliary CO<sub>2</sub> laser with the ion cloud in the ICR cell.</i>	30
<i>Figure 1-14 : Optical paths of CLIO IR FEL (red) and IR OPO/OPA (green) lasers.</i>	30
<i>Figure 1-15 : Infrared photodissociation mass spectra of the b<sub>2</sub> ion of protonated triglycine.</i>	31
<i>Figure 1-16 : Mass spectrum of protonated phosphotyrosine after 500 ms of irradiation time at 3665 cm<sup>-1</sup> with the tabletop OPO/OPA laser.</i>	32
<i>Figure 2-1 : General formula of a tetrapeptide. Activation by multiple low energy collisions can lead to the fragmentation of the peptide bonds forming the b<sub>2</sub> (green line) and y<sub>2</sub> (red line) ions.</i>	45
<i>Figure 2-2 : Fragmentation of the backbone of a protonated tripeptide by multiple low energy collisions leading to the formation of a b<sub>2</sub> ion which is assumed to have an oxazolone structure.</i>	46
<i>Figure 2-3 : Head-to-tail cyclization mechanism of the a<sub>2</sub> ion leading to a more energetically favorable 5-membered ring structure.</i>	47
<i>Figure 2-4 : Interconversion of cyclic a<sub>2</sub> ion structure composed by Glycine residues into the rearranged imine-amide isomer.</i>	48
<i>Figure 2-5 : Various a<sub>2</sub> Ion structures derived from rearrangement reactions starting from structure A which is generated directly from the b<sub>2</sub> ion of protonated GGG.</i>	50
<i>Figure 2-6 : Experimental (top panel) and calculated (A-E) Infrared spectra of the a<sub>2</sub> ion of protonated GGG in the 3200-3700 cm<sup>-1</sup> range.</i>	51
<i>Figure 2-7 : Experimental (top panel) and calculated (A-E) Infrared spectra of the a<sub>2</sub> ion of protonated YGGFL in the 1000-2000 cm<sup>-1</sup> range.</i>	54
<i>Figure 2-8 Experimental (top panel) and calculated (A-E) Infrared spectra of the a<sub>2</sub> ion of protonated GGG in the 3200-3700 cm<sup>-1</sup> range.</i>	56
<i>Figure 2-9 Potential energy profile associated with the rearrangement reaction of the a<sub>2</sub> Ion of protonated YGGFL.</i>	58
<i>Figure 2-10 : 1-3 proton transfer transition structures for the a<sub>2</sub> ion of protonated YGGFL.</i>	59
<i>Figure 2-11: Depletion of the a<sub>2</sub> ion of protonated YGGFL induced by isomer selective photodissociation.</i>	61

Figure 2-12: Infrared spectra of the $a_2$ fragment ion of protonated YGGFL in the 3400-3600 $\text{cm}^{-1}$ spectral range using the FT-ICR.....	63
Figure 2-13 : Various $a_3$ ion structures derived from rearrangement reactions starting from structure A which is generated directly from the $b_3$ ion of protonated GGGG.....	65
Figure 2-14: Infrared spectra of the $a_3$ fragment ions of protonated tetraglycine in the 3200-3600 $\text{cm}^{-1}$ spectral range.....	66
Figure 2-15: Infrared spectra of the $a_3$ fragment ion of protonated tetraglycine in the 1000-2000 $\text{cm}^{-1}$ spectral range.....	68
Figure 2-16: Various $a_4$ ion structures derived from rearrangement reactions starting from structure A. Relative ZPE-corrected energies and Gibbs free energies at 298 K (in parentheses) are given in $\text{kcal mol}^{-1}$ .....	70
Figure 2-17: Infrared spectra of the $a_4$ fragment ions of protonated pentaglycine in the 3200-3600 $\text{cm}^{-1}$ spectral range.....	71
Figure 3-1 : General formula of a protonated tetrapeptide. Activation by multiple low energy collisions can lead to the fragmentation of the peptide bonds forming the $b_2$ (green line) and $y_2$ (red line) ions.....	81
Figure 3-2: Fragmentation of protonated tripeptide induced by multiple low energy collisions.....	82
Figure 3-3: Predicted harmonic IR spectra of two diketopiperazine and two oxazolone structures corresponding to the $b_2$ ion of protonated GGG peptide.....	83
Figure 3-4: Rearrangement mechanism derived from Harrison and coworkers[30].....	85
Figure 3-5: Hydrogen bonding motifs found for the lowest energy structures of a) Protonated N ring oxazolone Isomer and b) protonated Macrocyclic Isomer of $b_4$ fragment ion [42].....	87
Figure 3-6: Voltage settings corresponding to the electrospray APPOLO source of the FT-ICR mass spectrometer.....	90
Figure 3-7: Mass spectra of electrosprayed $A_6$ MA peptide.....	91
Figure 3-8: Different types of hydrogen bonding motifs giving rise to the formation of hydrogen bonded cycles containing 5, 7, 10 and 13 atoms, and called $C_5$ , $C_7$ , $C_{10}$ , and $C_{13}$ , respectively.....	92
Figure 3-9: Computed structures for the all-Ala $b_6$ ion.....	93
Figure 3-10: Time evolution of the $H(O(Ala_1)) \dots H$ (green)-- $O(Ala_4) \dots H$ (red) and $O(Ala_1) \dots O(Ala_4)$ (blue) interatomic distances (in $\text{\AA}$ ) during a BOMD trajectory initiated with structure given in Figure 9a plotted as a function of time i.e. the number of steps during the MD simulation.....	94
Figure 3-11: Experimental IRMPD spectrum (red) and theoretical absorption spectrum (blue) of the $b_6$ ion in the 3200-3600 $\text{cm}^{-1}$ range.....	95
Figure 3-12 Experimental IRMPD spectrum (red) and theoretical absorption spectrum (blue) of the $b_6$ ion in the 1000-2000 $\text{cm}^{-1}$ range.....	97
Figure 3-13: IR spectra of the $b_6$ ion of protonated $A_6$ MA.....	98
Figure 3-14: Mass spectrum recorded after three seconds of ion-molecule reaction between of protonated cyclic-YAGFL peptide and $\text{NH}_3$ in the ICR cell maintained at a pressure of $\sim 10^{-8}$ mbar. .	99
Figure 3-15: IR spectra of the $[c\text{-YAGFL}+\text{NH}_3+\text{H}]^+$ adduct.....	100
Figure 3-16: Three representations of the lowest energy structure of the $[c\text{-YAGFL}+\text{NH}_3]^+$ ion....	101
Figure 3-17: Experimental (red) and calculated (blue) infrared spectra of the $[c\text{-YAGFL}+\text{NH}_4^+]$ complex.....	102
Figure 3-18: Experimental (red) and calculated (blue) infrared spectra of the $c\text{-YAGFL-NH}_3^+$ ion.	104
Figure 3-19: Mass spectra of the middle size $b_n$ ( $n=6-9$ ) ions composed by alanine residues.....	105
Figure 3-20: Experimental IR spectra of the middle size $b_n\text{-NH}_3^+$ complexes recorded in the 1000-2000 spectral region (a) and in the N-H stretching region (b).....	106
Figure 3-21: Three representations of the lowest energy structure ( $C_3$ symmetry) formed between the $b_9$ fragment ion of protonated $A_9$ YA and $\text{NH}_3$ .....	107

Figure 3-22: Experimental (red) and calculated (blue sticks) infrared spectra of the $b_9+\text{NH}_3^+$ ion in the 3200-3600 $\text{cm}^{-1}$ spectral range.....	108
Figure 3-23: Experimental (red) and calculated (blue) infrared spectra of the $b_9\text{-NH}_3^+$ complex in the 1000-2000 $\text{cm}^{-1}$ spectral range.....	110
Figure 3-24: Schematic views of the lowest energy structure complex formed between the $b_6$ , $b_7$ , and $b_8$ fragment ion of Alanine residues and $\text{NH}_3$ .....	111
Figure 3-25: Experimental (red, light blue and green) and calculated (blue) infrared spectra of the $b_6\text{-NH}_3^+$ , $b_7\text{-NH}_3^+$ , and $b_8\text{-NH}_3^+$ complex in the 3200-3600 $\text{cm}^{-1}$ spectral range.....	112
Figure 3-26 Comparative pictures of the middle size $b_n\text{-NH}_3^+$ ions.....	113
Figure 4-1 : Separation of two molecular ions with different collision cross section (CCS) by Ion Mobility Spectrometry.....	126
Figure 4-2: Ion mobilities of three different molecular ions as a function of the electric Field Strength.....	127
Figure 4-3: Ion trajectory within a Differential Ion Mobility Spectrometer.....	128
Figure 4-4: Three different methylated monosaccharide isomers.....	130
Figure 4-5: Cyclization process of D-Glucose.....	131
Figure 4-6: Schematic view of the DIMS device assembly integrated to our Esquire 3000+.....	137
Figure 4-7: Asymmetric electric field applied to the DIMS electrodes.....	137
Figure 4-8 : Ion Mobility Chromatogram of two monosaccharide epimers.....	138
Figure 4-9: DIMS spectra of complexes of Saccharides and $\text{Li}^+$ (a), $\text{Na}^+$ (b), and $\text{K}^+$ (c).....	140
Figure 4-10: $\text{MS}^2$ mass spectra where DIMS- and mass-selected of $\text{Li}(\text{Sac})^+$ ions (Sac= $\alpha$ -Me-Glucose (a); $\beta$ -Me-Glucose (b), and $\alpha$ -Me-Mannose (c)) ions were allowed to react for three seconds with water seeded in the He buffer gas. ....	142
Figure 4-11: Kinetic of the hydration reaction of the three lithiated monosaccharide isomers.....	143
Figure 4-12: IR spectra of $\text{Li}(\text{Sac})(\text{H}_2\text{O})^+$ ions. a) Sac= $\alpha$ -Me-Glucose; b) Sac= $\beta$ -Me-Glucose; c) Sac= $\alpha$ -Me-Mannose.....	144
Figure 4-13: IR spectra and corresponding lowest-energy structure of $\text{Li}(\alpha\text{-Me-Glucose})(\text{H}_2\text{O})^+$ (a), $\text{Li}(\beta\text{-Me-Glucose})(\text{H}_2\text{O})^+$ (b), and $\text{Li}(\alpha\text{-Me-Mannose})(\text{H}_2\text{O})^+$ complex ions (c).....	146
Figure 4-14: A schematic view of the lowest energy structure of $\text{Li}(\alpha\text{-Me-Glc})(\text{H}_2\text{O})^+$ is provided in the left panel. ....	147
Figure 4-15: DIMS spectra for an equimolar mixture of the three saccharides in $\text{Li}^+$ solution.....	150
Figure 5-1 : Carbon and oxygen atoms numbering for Methyl hexose with a 6-membered ring structure.....	159
Figure 5-2: Representation of three different conformers of the methylated $\beta$ -glucose: two chairs ( ${}^4\text{C}_1$ or ${}^1\text{C}_4$ ) and one boat.....	160
Figure 5-3: Structure and energetics associated with the two different conformations of each individual methylated monosaccharide isomers.....	161
Figure 5-4: Maximum coordination number of the lowest energy structure of methylated monosaccharides ( $\alpha\text{-Me-Glc}$ , $\beta\text{-Me-Glc}$ , and $\alpha\text{-Me-Glc}$ ).....	163
Figure 5-5 : Tri-coordination and bi-coordination complexes of $\text{Li}(\alpha\text{-Me-Man})^+$ and $\text{Li}(\alpha\text{-Me-Glc})^+$ respectively.....	164
Figure 5-6 : Illustration of the nomenclature using the lowest energy structure of the $\text{Li}^+$ (methyl- $\alpha$ -mannose) and $\text{Li}^+$ (methyl- $\alpha$ -mannose)( $\text{H}_2\text{O}$ ) complexes.....	165
Figure 5-7: Structure and relative energies (kJ/mol) of the lowest energy structure associated with a chair ( ${}^4\text{C}_1$ or ${}^1\text{C}_4$ ) and one boat configuration for the three methylated monosaccharides.....	166

Figure 5-8: Harmonic frequencies corresponding to the NH stretching modes involved in the intra-sugar hydrogen bond interactions formed in the lowest energy structure of the free monosaccharide ${}^4C_1$ , ${}^1C_4$ , and boat conformers .....	168
Figure 5-9 : Metal cation solvated with two water molecules .....	172
Figure 5-10 : Relative free Gibbs energies of the most stable of the $\text{Li}(\text{Sac})^+$ complexes .....	173
Figure 5-11 : Relative Gibbs free energies of the most stable ${}^4C_1$ , ${}^1C_4$ and boat conformers of the $\text{Li}(\text{Sac})(\text{H}_2\text{O})^+$ complexes .....	179
Figure 5-12 : Experimental IRMPD spectra of a) $\text{Li}(\alpha\text{-Me-Glc})^+$ (green color), b) $\text{Li}(\beta\text{-Me-Glc})^+$ (red), and c) $\text{Li}(\alpha\text{-Me-Man})^+$ (black) in the 3800-3000 $\text{cm}^{-1}$ spectral range .....	182
Figure 5-13 : Experimental IRMPD spectra of a) $\text{Li}(\alpha\text{-Me-Glc})(\text{H}_2\text{O})^+$ (green), b) $\text{Li}(\beta\text{-Me-Glc})(\text{H}_2\text{O})^+$ (red), and c) $\text{Li}(\alpha\text{-Me-Man})(\text{H}_2\text{O})^+$ (black) in the 2800-3800 $\text{cm}^{-1}$ spectral range .....	183
Figure 5-14 : Experimental IRMPD spectra of a) $\text{Li}(\beta\text{-Me-Glc})^+$ (red), b) $\text{Li}(\beta\text{-Me-Glc})(\text{H}_2\text{O})^+$ (green), c) $\text{Li}(\beta\text{-Me-Glc})(\text{CH}_3\text{CN})^+$ (black), and d) $\text{Na}(\beta\text{-Me-Glc})(\text{CH}_3\text{CN})^+$ (blue) in the 3200-3800 $\text{cm}^{-1}$ spectral range .....	184
Figure 5-15 : Lowest energy structure of $\text{Li}(\alpha\text{-Glc})^+$ system .....	186
Figure 5-16 : IRMPD spectrum of the $\text{Li}(\alpha\text{-Me-Glc})^+$ complex (upper panel) .....	187
Figure 5-17 : IRMPD spectrum of the $\text{Li}(\alpha\text{-Me-Glc})(\text{H}_2\text{O})^+$ complex (upper panel) .....	189
Figure 5-18 : Displacement vectors of the normal mode predicted at 157 $\text{cm}^{-1}$ .....	191
Figure 5-19 : IRMPD spectrum of the $\text{Li}(\alpha\text{-Me-Man})^+$ complex (upper panel) .....	192
Figure 5-20 : IRMPD spectrum of the $\text{Li}(\alpha\text{-Me-Man})(\text{H}_2\text{O})^+$ complex (upper panel) .....	194
Figure 5-21 : IRMPD spectrum of the $\text{Li}(\beta\text{-Me-Glc})^+$ complex (upper panel). In the lower b-d panels the experimental IRMPD spectrum (grey) is compared to the most energetically favored structures with the $\beta$ -glucose in a ${}^4C_1$ chair (orange), ${}^1C_4$ chair (green), and boat (blue) conformation .....	196
Figure 5-22 : IRMPD spectrum of the $\text{Li}(\beta\text{-Me-Glc})(\text{H}_2\text{O})^+$ complex (upper panel) .....	198

## List of tables

<i>Table 2-1 : Band assignment for the <math>a_2</math> ion of protonated GGG.....</i>	<i>52</i>
<i>Table 2-2: Band assignment for the <math>a_2</math> ion of protonated YGGFL.....</i>	<i>57</i>
<i>Table 2-3 : Band assignment for the <math>a_3</math> ion of protonated GGGG.....</i>	<i>67</i>
<i>Table 2-4 : Band assignment for the <math>a_4</math> ion of protonated GGGGG.....</i>	<i>72</i>
<i>Tableau 3-1 : Assignment of the IR spectrum of the <math>b_6</math> ion in the NH stretching region .....</i>	<i>96</i>
<i>Tableau 3-2 : Band assignment for the <math>[c\text{-YAGFL}+\text{NH}_3+\text{H}]^+</math> complex.....</i>	<i>103</i>
<i>Table 3-3 : Band assignment for the <math>b_9\text{-NH}_4^+</math> ion. ....</i>	<i>109</i>
<i>Table 3-4 Band assignment of the <math>b_n\text{-NH}_3^+</math> complex ions .....</i>	<i>113</i>
<i>Table 5-1 : Hydrogen bond interactions observed in the free monosaccharide <math>^1C_4</math>, <math>^4C_1</math>, and boat conformers.....</i>	<i>169</i>
<i>Table 5-2 : Experimental binding energy values (<math>\text{kJ mol}^{-1}</math>) of <math>\text{H}_2\text{O}\text{-M}^+(\text{H}_2\text{O})_{n-1}</math> complexes (<math>\text{M}^+ = \text{Li}^+</math>, <math>\text{Na}^+</math>), (<math>n \leq 4</math>) reported from previous studies of Armentrout and coworkers [16,17]. ....</i>	<i>176</i>
<i>Table 5-3 : Binding energies (in <math>\text{kJ mol}^{-1}</math>) associated with the <math>\text{Li}(\text{Sac})^+</math> and <math>\text{Li}(\text{Sac})(\text{H}_2\text{O})^+</math> complexes. ....</i>	<i>177</i>
<i>Table 5-4 : Infrared band assignment of the <math>\text{Li}(\alpha\text{-Me-Glc})^+</math> complex.....</i>	<i>188</i>
<i>Table 5-5 : Infrared band assignment of the <math>\text{Li}(\alpha\text{-Me-Glc})(\text{H}_2\text{O})^+</math> complex .....</i>	<i>190</i>
<i>Table 5-6 : Infrared band assignment of the <math>\text{Li}(\alpha\text{-Me-Man})^+</math> complex .....</i>	<i>193</i>
<i>Table 5-7 : Infrared band assignment of the <math>\text{Li}(\alpha\text{-Me-Man})(\text{H}_2\text{O})^+</math> complex.....</i>	<i>195</i>
<i>Table 5-8 Infrared band assignment of the <math>\text{Li}(\beta\text{-Me-Glc})^+</math> complex.....</i>	<i>197</i>
<i>Table 5-9 Infrared band assignment of the <math>\text{Li}(\beta\text{-Me-Glc})(\text{H}_2\text{O})^+</math> complex .....</i>	<i>200</i>



## List of abbreviations

<b>A</b>	Alanyne
<b>AFM</b>	Atomic Force Microscopy
<b><math>\alpha</math>-glc</b>	alpha glucose
<b><math>\alpha</math>-man</b>	alpha mannose
<b>AMBER</b>	Assisted Model Building with Energy Refinement
<b>B3LYP</b>	Becke 3 Lee-Yang-Parr
<b><math>\beta</math>-glc</b>	beta glucose
<b>CCS</b>	Collision Cross Section
<b>CI</b>	Chemical Ionization
<b>CID</b>	Collision Induce Dissociation
<b>CLIO</b>	Centre Laser Infrared Orsay
<b>CO</b>	Carbonyl Group
<b>CV</b>	Compensation Voltage
<b>DA</b>	Donor Acceptor
<b>DC</b>	Direct Current
<b>DFM</b>	Different Frequency Mixing
<b>DFT</b>	Density Funcional Theory
<b>DIMS</b>	Differential Ion Mobility Spectrometry
<b>DTIMS</b>	Drift Tube Ion Mobility Spectrometry
<b>DV</b>	Dispersion Voltage
<b>EI</b>	Electron Impact
<b>ESI</b>	Electrospray Source Ionization
<b>eV</b>	Electron Volt
<b>F</b>	Phenylalanine
<b>FAIMS</b>	Field Asymmetric Ion Mobility Spectrometry
<b>FEL</b>	Free Electron Laser
<b>FELIX</b>	Free Electron Laser for Infrared Experiments
<b>FT</b>	Fourier Transform
<b>FTICR</b>	Fourier Transform Ion Cyclotron Resonance
<b>G</b>	Glycine
<b>GB</b>	Gas Basicity
<b>HB</b>	Hydrogen Bond
<b>IMR</b>	Ion Molecule Reaction
<b>IMS</b>	Ion Mobility Spectrometry
<b>IR</b>	Infrared
<b>IRMPD</b>	Infrared Multiple Photon Dissociation
<b>IVR</b>	Intramolecular Vibrational Redistribution
<b>KTA</b>	Potassium Titanyle Arsenate
<b>KTP</b>	Potassium Titanyle Arsenate
<b>L</b>	Lysine
<b>M</b>	Methyonine
<b>MALDI</b>	Matrix Assisted Laser Desorption Ionization
<b>MP2</b>	Møller-Plesset truncated at second-order

<b>MS</b>	Mass Spectrum
<b>Nd:YAG</b>	Neodymium-doped yttrium aluminum garnet
<b>NH</b>	Amine Group
<b>OH</b>	Hydroxyl Group
<b>OPA</b>	Optical Parametric Amplificator
<b>OPO</b>	Optical Parametric Oscillator
<b>PBD</b>	Proton Bound Dimer
<b>QIT</b>	Quadrupole Ion Trap
<b>RF</b>	Radio Frequency
<b>SHG</b>	Second Harmonic Generation
<b>SORI</b>	Sustained Off-Resonance Irradiation
<b>TCID</b>	Threshold Collision Induce Dissociation
<b>TS</b>	Transitional State
<b>TWIMS</b>	Traveling-wave Ion Mobility
<b>UV</b>	Ultra Violet
<b>Y</b>	Tyrosine
<b>ZPE</b>	Zero Point Energy

*À mes parents et mon frère*

*“Aures vocivae si sunt, animum advertite”*







## INTRODUCTION GENERALE

La spectrométrie de masse tandem est une technique analytique versatile, notamment utilisée dans le champ de la protéomique pour lequel elle a été élue « method of the year » en 2012 par le journal Nature. La spectrométrie de masse est notamment exploitée pour dériver la séquence de peptides, information dérivée de leur spectre de masse de fragmentation induite par collisions (Collision Induced Dissociation : CID). De multiples fragments sont observés, et la séquence peptidique peut être dérivée de la mesure de la masse de série d'ions analogues dits  $b_n$ ,  $a_n$ , ou  $y_n$ , par exemple, où  $n$  est le nombre d'acides aminés. Les physico-chimistes se sont assez naturellement intéressés au mécanisme de fragmentation par CID des peptides protonés, et c'est dans ce contexte que s'inscrit la motivation initiale de cette thèse.

Cette thèse vise à contribuer au développement de méthodes intégrées à la spectrométrie de masse afin d'apporter une information structurale sur les ions moléculaires, intermédiaires réactionnels ou produits de réactions. Le laser à électrons libres (LEL) de CLIO (Centre Laser Infrarouge d'Orsay), accordable dans la gamme infrarouge dite fingerprint, s'est avéré être un outil intéressant pour dériver le spectre infrarouge d'ions au sein d'un spectromètre de masse. L'acquisition du spectre infrarouge repose sur la mesure du spectre de masse de fragmentation pour chaque longueur d'onde du laser, la fragmentation reposant sur le mécanisme dit InfraRed Multiple Photon Dissociation (IRMPD). Malgré la complexité du processus d'absorption multiphotonique, les spectres IRMPD s'interprètent assez bien par comparaison avec des spectres IR d'absorption calculés pour les différents isomères et/ou conformères. Dans quelques cas, on peut s'affranchir du calcul de chimie quantique si une signature spectrale spécifique d'un isomère est observée. Il s'avère cependant que la résolution spectrale est insuffisante pour dériver des informations structurales, notamment pour des systèmes de taille moyenne, c'est-à-dire cinq à dix acides aminés dans le cas présent.

Dans ce contexte, la mise en œuvre de plusieurs techniques de caractérisation intégrées à la spectrométrie de masse s'impose. Plusieurs équipes ont notamment combiné la spectroscopie infrarouge et la fragmentation induite par capture d'électrons, technique d'activation spécifique de la conformation, pour faciliter la caractérisation structurale. La séparation des ions par mobilité ionique, une forme de chromatographie en phase gazeuse pour les ions, a aussi été exploitée. Cette technique est dite

orthogonale à la spectrométrie de masse car la séparation repose, comme l'électrophorèse en phase condensée, sur la taille et la forme, c'est-à-dire la structure 3D, des ions. L'exploitation de données dérivées de ces multiples techniques (IRMPD, ECD, IMS) peut cependant être compliquée si elles ont été acquises sur des spectromètres de masse différents.

L'objectif ultime de cette thèse était de mettre en place une approche multimodale sur un spectromètre de masse unique, intégrant la séparation par mobilité ionique et la spectroscopie infrarouge d'ions moléculaires. Ce nouveau dispositif expérimental devrait permettre de caractériser par spectroscopie infrarouge des ions simultanément sélectionnés en masse et par mobilité ionique. D'un point de vue fondamental, ce dispositif ouvre la voie de la caractérisation spectroscopique d'isomères sélectionnés, et de corrélérer la structure 3D dérivée par mobilité ionique avec, par exemple, un motif de liaison hydrogène caractérisé par spectroscopie infrarouge.

Le premier chapitre est consacré aux méthodologies et aux instruments intégrant l'activation par laser IR à la spectrométrie de masse tandem mis en œuvre pour effectuer la spectroscopie infrarouge d'ions sélectionnés. Une particularité de nos dispositifs expérimentaux est qu'ils sont basés sur des spectromètres de masse commerciaux, contrairement à la majorité des développements actuels qui visent à effectuer la spectroscopie infrarouge hautement résolue en exploitant des pièges à ions refroidis par cryogénie. Les particularités des deux dispositifs expérimentaux, l'un basé sur un spectromètre de masse de type FT-ICR l'autre de type piège de Paul, sont présentées, en insistant sur les modes de fragmentation et de relaxation des ions de multiples collisions avec un gaz rare. Nous avons la chance de disposer au laboratoire d'un accès privilégié au laser infrarouge à électrons libres qui sont particulièrement bien adaptés pour la spectroscopie infrarouge intégrée à la spectrométrie de masse. L'essentiel des résultats de ma thèse portent cependant sur l'exploitation d'un laser de type OPO/OPA, certes moins intense que le LEL, mais qui utilisé avec un laser auxiliaire à CO<sub>2</sub> permet de dériver des informations structurales importantes via la spectroscopie des élongations NH et OH.

Le second chapitre est dédié à la caractérisation structurale des fragments ioniques  $a_n$  de peptides. L'objectif principal était de caractériser les réarrangements structuraux associés à la formation de ces ions lors de la fragmentation de peptides protonés par dissociation induite par collisions (CID). Plus précisément, il s'agissait d'identifier un diagnostic infrarouge précis de structures dérivant d'une

permutation de séquence de la chaîne peptidique. Sur la base de résultats antérieurs du groupe avec celui de B. Paizs basés sur la spectroscopie IR avec le LEL, il semblait qu'une permutation de séquence était observée dans le cas de l'ion  $a_n$  d'un peptide de type oligoglycine. Cependant, la résolution du spectre n'était pas suffisante pour exclure la formation d'autres isomères et, surtout, aucune signature vibrationnelle spécifique de la structure permutée n'avait été observée dans la gamme spectrale du LEL. La spectroscopie dans la gamme des élongations NH a donc été exploitée pour caractériser les structures dérivant d'une permutation de séquence de la chaîne peptidique ceci pour les ions  $a_n$  dérivant d'oligoglycines, mais aussi d'évaluer l'influence de chaînes latérales d'autres résidus sur le mécanisme de réarrangement des ions  $a_n$ . Une attention particulière a été portée sur la caractérisation des conditions expérimentales de fragmentation et leur influence sur la dynamique du réarrangement, et par conséquent sur la population de différents isomères des ions  $a_n$ .

Le troisième chapitre est également consacré au mécanisme de réarrangement de fragments peptidiques. Il s'agit des ions  $b_n$ , dont les plus petits représentants ( $n \leq 5$ ) ont été beaucoup étudiés par spectroscopie infrarouge en phase gazeuse combinée à la chimie quantique ces dernières années. Dans le cas des ions  $b_2$ , une signature spectrale est observée dans la gamme 1800-2000  $\text{cm}^{-1}$  dans la plupart des cas, confirmant que la structure présente un cycle oxazolone du côté C-terminal du fragment. Lorsque la taille augmente, même si aucune signature spectrale n'a pu être identifiée, la disparition de la bande caractéristique de l'oxazolone laisse penser que l'on forme de nouveaux isomères et notamment des structures macrocycliques dérivant d'une attaque nucléophile du groupe amino N-terminal sur le carbonyle de l'oxazolone du côté C-terminal. Cette structure macrocyclique est à ce jour la seule hypothèse envisagée pour interpréter la similarité des spectres de masse de fragmentation d'une série de peptides dérivant les uns des autres par une permutation de séquence. L'objectif initial était la caractérisation par spectroscopie infrarouge d'ions  $b_n$  de plus grande taille ( $n=6-9$ ). L'assignation des spectres est difficile et n'a pas été menée à terme. Nous sommes cependant allés plus loin, en caractérisant par spectroscopie infrarouge la structure des complexes formés entre ces ions  $b_n$  et la molécule d'ammoniac. Il a été montré dans une publication récente que la spécificité de la formation de ces adduits avec les ions  $b_n$  ( $n=6-9$ ) pourrait être due au fait que ces ions adoptent une structure macrocyclique. La modélisation de ces adduits, comme des ions  $b_n$  ( $n=6-9$ ), a été faite par notre collègue

B. Paizs qui a développé à cette occasion une approche de dynamique moléculaire de type Born Oppenheimer (BOMD) basée sur un potentiel calculé par fonctionnelle de la densité.

Le quatrième chapitre est consacré aux premiers résultats de spectroscopie infrarouge sur des ions à la fois sélectionnés par spectrométrie de masse et par mobilité ionique. La technique de mobilité ionique mise en œuvre est de type « Differential Ion Mobility spectrometry » (DIMS) qui permet une sélection des ions au niveau de la source ElectroSpray, et donc en amont du piège à ions. Nous aurions souhaité pouvoir exploiter l'IMS sur des ions fragments de peptides, mais la technique DIMS ne le permettait pas. Nous avons choisi d'explorer la séparation et la caractérisation d'isomères de monosaccharides, systèmes qui ont été abondamment étudiés par mobilité ionique ces dernières années. Un prototype DIMS développé par le groupe de G.L. Glish (UNC, USA) a été installé sur l'un de nos spectromètres de masse. Une description du dispositif expérimental et sa mise en œuvre sont exposées dans ce chapitre, et les premiers résultats obtenus sur la séparation des monosaccharides cationisés ( $\text{Li}^+$ ,  $\text{Na}^+$ ,  $\text{K}^+$ ) sont particulièrement encourageants en termes de résolution. Dans le cas des complexes de  $\text{Li}^+$ , la structure des ions sélectionnés par spectrométrie de masse et par mobilité ionique a été sondée par réaction ion-molécule et spectroscopie IR. L'analyse de ces résultats combinés à ceux de DIMS est cohérente avec les calculs de structure et de spectre infrarouge, et une signature spectrale spécifique des anomères du glucose a été observée.

Le cinquième chapitre s'inscrit dans le prolongement du précédent et propose une analyse plus détaillée des spectres infrarouges des complexes  $\text{Li}^+$ -monosaccharides nus ou monohydratés, basée sur les spectres d'absorption IR prédits pour différents isomères de basse énergie. L'exploration de l'espace conformationnel est assez difficile, et nous n'avons mis en œuvre qu'en fin de thèse une recherche conformationnelle s'appuyant sur un algorithme de type Monte Carlo. Nos résultats préliminaires sont cependant satisfaisants puisque les spectres observés sont en très bon accord avec le spectre prédit pour l'isomère le plus bas en énergie. Notre motivation était aussi de comprendre l'évolution des spectres DIMS en fonction de l'agent ionisant ( $\text{Li}^+$ ,  $\text{Na}^+$ ,  $\text{K}^+$ ) dans le cas des anomères du glucose. Il s'avère en effet que les complexes associés sont particuliers. Dans le cas du  $\beta$ -glucose, notamment, plusieurs variétés structurales des complexes de  $\text{Li}^+$  sont observées dans une faible gamme d'énergie, ce qui

laisserait penser que leurs énergies relatives fluctuent avec l'agent ionisant, ce qui pourrait être à l'origine des tendances observées en DIMS.







# 1 IR SPECTROSCOPY INTEGRATED TO MASS SPECTROMETRY: INSTRUMENTS AND METHODOLOGY

1	IR SPECTROSCOPY INTEGRATED TO MASS SPECTROMETRY: INSTRUMENTS AND METHODOLOGY	
	9	
1.1	Introduction.....	11
1.2	Two experimental set-ups.....	12
1.3	IRMPD with two lasers. ....	19
1.4	IRMPD Spectroscopy: Practical details.....	26
1.5	IRMPD Spectroscopy at FELIX versus CLIO .....	32
1.6	Different groups developing IR Spectroscopy .....	35
1.7	Bibliography.....	38

## 1.1 Introduction

In this chapter, the methodology and the instruments used for performing the IR spectroscopy of mass-selected ions during my PhD training will be described. The aim of the thesis work is to characterize the structure of molecular ions in the gas phase via a combination of mass spectrometry, infrared spectroscopy, DFT calculations, ion-molecule reactions and ion mobility spectrometry (IMS). The IMS set-up will be described in chapter 4.

The idea is to selectively isolate the ions of interest using mass spectrometry and then allow them to react with a neutral gas or irradiate them with infrared light. Since the earliest works on photodissociation of trapped ions in mass spectrometers [1,2], different instrumental approaches have been developed. Linear or quadrupolar radio-frequency ion-traps as well as Penning ion traps have been used, and many recent developments aim at trapping ions at low temperature. In our laboratory at Orsay, the choice of using commercial tandem mass spectrometers has been made, and experiments are performed at room temperature.

Our experimental set-ups are based on two commercial tandem mass spectrometers, both equipped with an Electrospray Source Ionization (ESI). One instrument, a Bruker Esquire 3000, is based on a quadrupole ion-trap (QIT). The second instrument, a Bruker Apex IV, is based on a 7 tesla Fourier Transform Ion Cyclotron Resonance mass spectrometer. There are practical advantages for using commercial instruments. In the context of this work the most important one is that they both provide a conventional way to perform the collisional activation of mass-selected ions. This is particularly important for probing the structure of CID fragments which are, for example, reactive intermediates involved in the peptide sequencing process.

Using one or the other mass spectrometer, ions can be thermalized using ion traps pressurized with rare gas. This aspect will be discussed in details in Chapter 2. In the case of the QIT, ions are thermalized by multiple low energy collisions in the Paul Trap using Helium as a buffer gas. In the case of the hybrid 7-Teslas FT-ICR mass spectrometer, thermalization of the molecular ions can be

performed in the Argon pressurized linear hexapole ion trap of the so-called Qh unit located between the electrospray source and the ICR cell.

Each tandem mass spectrometer is coupled with two tunable infrared lasers and an auxiliary CO<sub>2</sub> laser. The first laser is the Free Electron Laser of the Centre Laser Infrarouge d'Orsay (CLIO), which is part of the laboratory. This laser is tunable in the mid-infrared from  $\sim 100$  to  $\sim 2000$  cm<sup>-1</sup>. It is routinely used to derive IR spectra of gas-phase ions in the 800-2000 cm<sup>-1</sup> range. The second tunable infrared laser is a tabletop Optical Parametric Oscillator/Amplifier (OPO/OPA) laser. It is efficiently tunable in the 2500-4000 cm<sup>-1</sup> near-infrared spectral range, which is useful for characterizing the NH and OH stretching modes, and in particular their spectral shifts which are characteristic of hydrogen-bonding motifs. A comparison of the performance in terms of spectroscopic resolution of the two mass spectrometers has been recently proposed for CLIO [3] and OPO/OPA [4]. These studies show that the bandwidth are very similar for ions thermalized with Ar or He.

An important factor to convince people of using IR activation for analytical purpose is the irradiation time. When using the IR Free Electron Laser, irradiation time is typically on the order of few 100 ms. Tabletop laser is less powerful in comparison with Free Electron Lasers and the irradiation time may have to be increased up to 1s depending on the dissociation energy threshold of the molecular ion. In this case, an auxiliary CO<sub>2</sub> laser can be used for enhancing the fragmentation yield. The intrinsic technical aspects of the instruments that have been mentioned here will be detailed in the next sections.

## 1.2 Two experimental set-ups

### 1.2.1 Quadrupole Ion Trap mass spectrometer

One of our tandem mass spectrometer is based on a Quadrupole Ion Trap (QIT). Wolfgang Paul was awarded the Nobel Prize in Physics in 1989 for his work on ion trap techniques, based on radio-frequency electric field, such as the QIT. Since the development of these ion-traps, several reviews have appeared describing the novelties and the performances of the Paul Ion Traps [5-9].

Our QIT mass spectrometer (Bruker, Esquire 3000+) is equipped with a conventional external electrospray ionization source [10]. A scheme of our mass spectrometer which integrates the QIT, also

called Paul trap, is schematized in Figure 1-1. The continuous flow of electrosprayed ions is guided through octapoles towards the QIT where ion manipulation takes place, and then before ions are sequentially ejected towards a conventional electron multiplier detector.

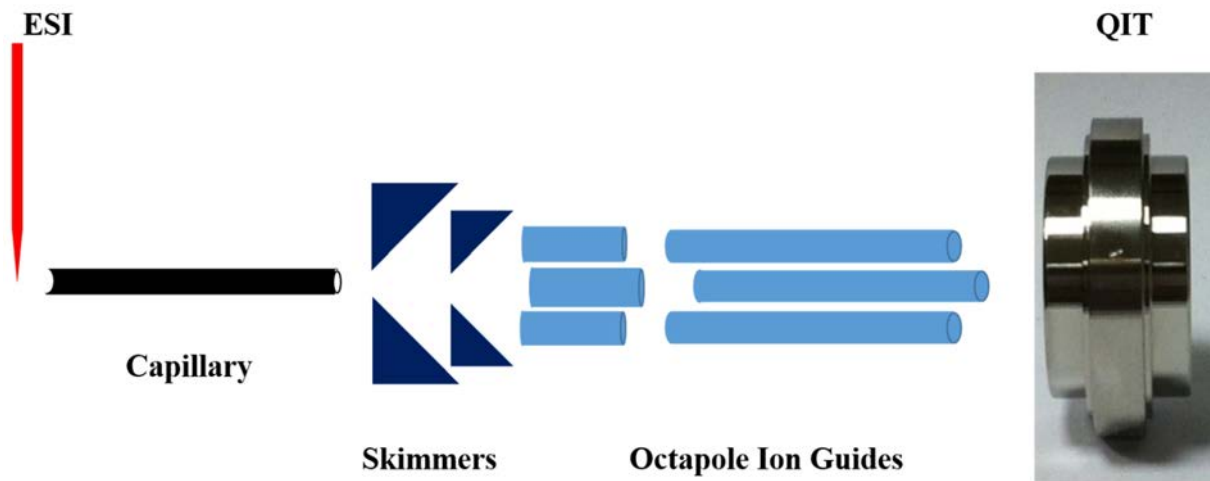


Figure 1-1: Schematic view of our Quadrupole Ion Trap mass spectrometer (Bruker Esquire 3000+). Three parts can be distinguished: The electrospray ionization (ESI) source, the transport and focusing section, and the QIT itself.

All the MS steps are performed within the QIT, which includes the trapping, the mass-selection, and the activation. The QIT unit is formed by one ring electrode (Figure 1-2) and two end-cap electrodes. An RF electric field is applied to the ring and the two end-cap electrodes are connected at ground potential. This oscillatory electric field between the two sets of electrodes allows for the trapping of the ions. The common picture used to interpret this phenomenon is an effective pseudo-potential electric well with a saddle shape. Wolfgang Paul proposed a mechanical analog with a steel ball as a particle, which is useful to interpret the dynamic trapping: it is the rotation of the saddle along its axis that can prevent the steel ball from falling. Efficiency depending on the mass of the steel ball, the frequency of the rotation of the saddle can be adjust in order to allow for the trapping.

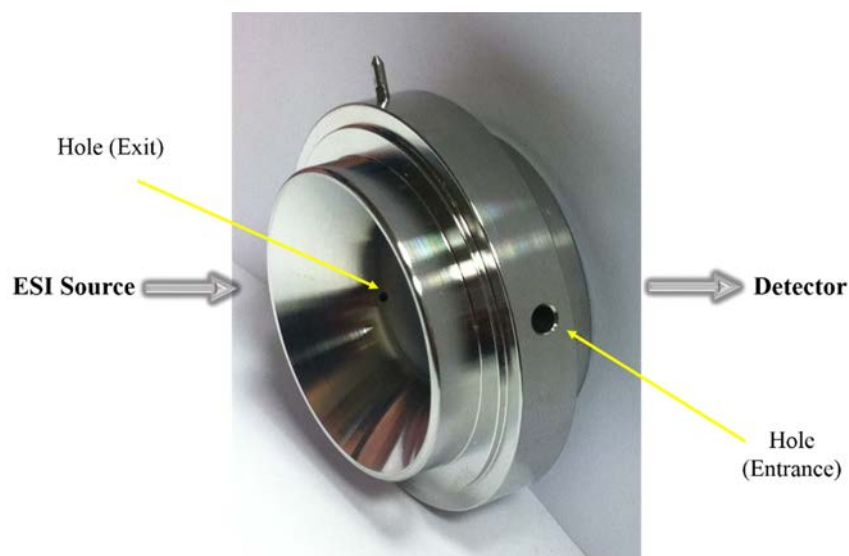


Figure 1-2 : Detailed view of the Ring Electrode. Ions are trapped within the trap by the potential difference established between the two endcap and the ring electrodes. Two holes have been drilled in the ring electrode ( $\varnothing \sim 2\text{mm}$ ) allowing for the IR irradiation of the ions.

Electrosprayed ions pass through a hole in the entrance endcap electrode, and are accumulated in the QIT. An auxiliary DC voltage is also applied to the exit endcap electrode during ion accumulation. Since the first development of the QIT, helium buffer gas has been introduced into the trap to reduce the ions' kinetic energy. The importance of the helium pressure, which is estimated to be on the order of  $10^{-3}$  mbar in the QIT of our instrument, has been shown to be critical for trapping large ions produced by ESI or MALDI sources [5-7]. The resulting kinetic energy damping improves the mass resolving power and also increases the sensitivity.

The temperature of the trapped ions is an important issue for IR spectroscopy, not only for the spectroscopic resolution but also since it determines the population of the different isomers. The temperature of ions trapped in a QIT has been first estimated by Gronert [8]. It was derived from the measurement of the equilibrium constant associated with formation/dissociation of an ion-molecule complex between the thiophenolate anion and 2,2,2-trifluoroethanol. This reaction had been chosen because it has a high temperature dependence, as shown earlier by Sieck and Meot-Ner [9]. The thiophenolate was isolated in the QIT and allowed to react with the neutral reagent. Mass spectra were recorded as a function of reaction time period (ranging from 100 to 5000 ms). Comparing the calculated

equilibrium constant with that reported by Sieck and Meot-Ner [9], the effective temperature of the trapped ions was found to be close to 300 K. This confirms that there is equilibrium between the molecular ions and the QIT electrodes at room temperature, occurring via the multiple collisions with the helium gas.

The collisional cooling process of the ion in a QIT was investigated in details by Remes *et al.* [10]. The QIT was maintained at a fixed temperature varying from 25 K to room temperature. Under normal storage conditions, and at a pressure of  $10^{-3}$  mbar, an ion experiences  $\sim 20$  collisions per millisecond, and one can thus assume that the temperature of the ions is that of the ion trap after few milliseconds [11]. The information was derived by monitoring the fragmentation of the ions using collisional activation, and also a two laser pulses technique proposed by Asamoto and Dunbar [12]. Using this two laser pulses technique, the pseudo first-order collisional cooling rate was  $334 \text{ s}^{-1}$  for the n-butylbenzene ion, at a pressure of  $5.8 \cdot 10^{-4}$  Torr, and a temperature of 295 K. It was shown that the collisional cooling rate of the ions increases almost linearly with the helium pressure. It is important to stress that, as for the temperature measurement experiment of Gronert [8], the estimation of the pressure inside the trap is a key factor. Glish and coworkers estimated that the pressure inside the trap is  $\sim 14$  times higher than that in the vacuum chamber containing the pressure gauge [10]. Finally, the effect of the ion cooling on the activation energy required for fragmenting the ions was also investigated. Using CID activation, it was shown that the activation energy had to be increased significantly when the temperature was lowered from 295K to 25K. This shows the effect of the temperature of the ions on the effective fragmentation energy threshold.

Another important factor to be considered to carry out infrared spectroscopy of trapped ions is the size of the ion cloud, which affects the overlap with the laser. The order of magnitude of the IR beam waist in our experiment is one millimeter [13]. While the ion cloud can be quite large in an ICR trap, IRMPD experiments at CLIO suggest that the IR FEL beam overlaps with 100% of the ion cloud in the QIT, since a complete depletion of the parent signal can be observed using a single CLIO macropulse [13]. A more systematic investigation of the overlap between the laser and the ion cloud was proposed by Glish and coworkers [14]. Different parameters that could influence the position of the ion cloud in

the trap have been investigated. This study reveals that the trapping frequency and the trapping voltage are two important parameters. The trapping voltage allows for the control of the position of the ions in the axial direction. While a high value improves the ion/laser overlap, it also increases the low-mass cutoff. Hence, if low-mass fragments have to be detected, a tradeoff has to be found.

### 1.2.2 FT-ICR tandem mass spectrometer

The second mass spectrometer used during the thesis work is a hybrid 7 Teslas FT-ICR tandem mass spectrometer (Bruker, APEX IV). The FT-ICR mass spectrometer is schematized in Figure 1-3. It is called “hybrid” because there is a Qh interface between the high pressure ion source region and the high vacuum region containing the ICR cell. This Qh interface consists of a linear quadrupole for mass-selection, and of a linear hexapole ion trap. The latter is fitted in a pressurized ( $\sim 10^{-3}$  mbar of Argon) cell and its purpose is fourfold. The primary purpose is ion accumulation. Hence, weakly abundant species from a complex mixture can be mass-selected using the quadrupole, and then accumulated in the hexapole ion trap. Second, collision induced dissociation (CID) can be performed in the linear ion trap. The kinetic energy of the ions can be tuned by adjusting the DC voltage applied on the eight RF rods. Typical DC voltages used for CID range for 1 to 10V. Third, as in the case of the QIT, thermalization of the ions is ensured through multiple collisions of the ions with the argon buffer gas. As a result, thermalized ions are injected in the high vacuum region of the ICR cell [10]. This is important since only radiative cooling could occur in this low pressure region. Finally, ion-molecule reactions can also be performed between the trapped ions and neutral seeded in the Argon line.

The third component of the mass spectrometer is the Ion Cyclotron Resonance (ICR) cell which is located in the ultra-high vacuum part of the instrument. The pressure in this part is routinely on the order of  $\sim 5 \cdot 10^{-10}$  mbar on our instrument. These low pressure conditions have to be maintained in order to minimize ion-molecule collisions which would perturb the trajectory of the ions and in turn the ion detection.

The main advantage of the addition of the Qh interface is to avoid the introduction of neutral molecules into the low vacuum ICR region. Nevertheless, collisional activation of the ions can also be

performed in the ICR cell, using the so-called sustained off-resonance irradiation collision induced dissociation (SORI-CID) technique. For this purpose, the mass spectrometer is equipped with one pulsed and one leaking valve gas inlets connected to the high vacuum region.

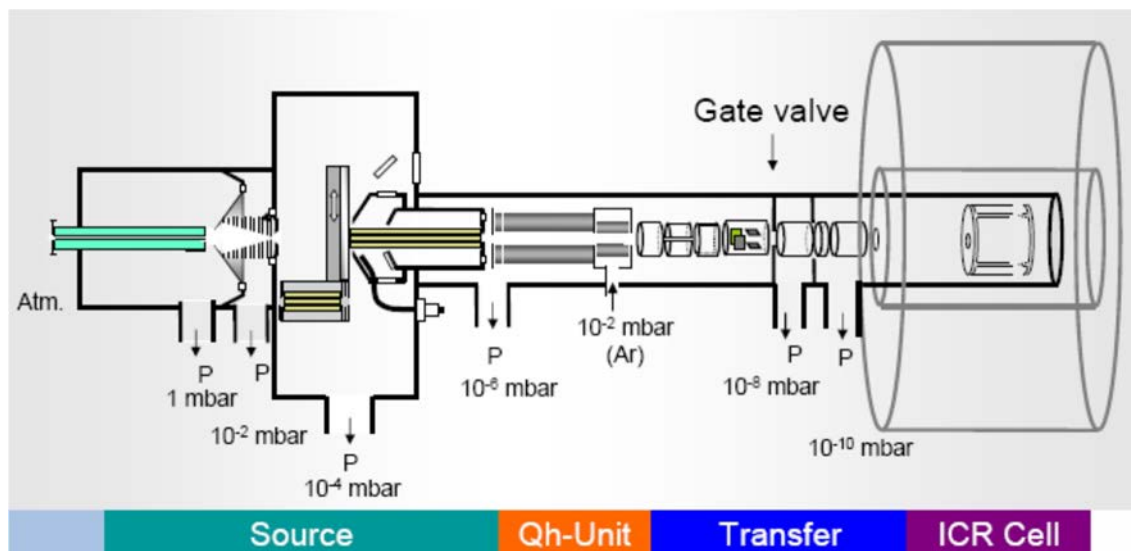


Figure 1-3 : Schematic view of our FT-ICR mass spectrometer (Bruker APEX IV). The source, the Qh-unit (Quadrupole and hexapole), the transfer optics and the ICR cell are shown. The typical pressure of each region is specified in mbar.

The first FT-ICR experiment was performed by Comisarow and Marshall [15] in the 70's, based on earlier developments in the 1930's. Since then, significant improvements have been made, especially in terms of resolution and mass range [16-18]. The ICR technique relies on the cyclotron motion of an ion in a magnetic field which is characterized by a cyclotron frequency ( $\nu$ ) which depends on the magnetic field strength  $B$  and mass-to-charge ratio ( $m/z$ ). The formulae is given below where the charge  $q = z \times e$ :

$$2\pi\nu = qB/h$$

If the direction  $z$  is defined by the magnetic field, ions are trapped in the  $(x,y)$  plane. In practice, a Penning ion trap is also made of two electric electrodes at a DC potential of few volts for trapping the ions along the  $z$  axis. As a result, the ion motion does not only consist of the cyclotron motion, but is the combination of three components [17]. The magnetic field of our FT-ICR mass spectrometer is 7.4 Tesla, which allows for a high mass resolution which is proportional to magnetic field strength.

$$n / \Delta n_{(50\%)} = -qB_{(0)} / n \Delta \omega_{(50\%)}$$

Ion manipulation, including trapping, mass-selection, ejection, and mass-analysis, is essentially based on the cyclotron motion. The working principle of ion detection is illustrated in Figure 1-4. Different configurations have been proposed for the ICR cell, and the Bruker infinity cell has a cylindrical shape, made of two sets of electrodes or plates: two “detection plates” and two “excitation plates”. Due to the cyclotron motion of the charged particles, an alternative image current can be detected on the two detection plates (Figure 1-4). For this purpose, ions are excited to a large cyclotron orbit radius using a resonant RF excitation voltage applied to “excitation electrodes”. In practice, a broadband frequency RF signal is used for the excitation over a large frequency range (*i.e.*  $m/z$  range), and a transient image current is detected, which is a combination of the image current of all individual ions. Hence, the mass spectrum can be derived by Fourier transform of the image current, as proposed by Comisarow and Marshall in 1974 [15]. Mass selection in the ICR cell can be achieved using a dedicated broadband excitation signal in order to increase the orbital radius of all ions except for those with a given frequency ( $m/z$ ) range. As a result all the non-desired ions are neutralized on the electrodes.

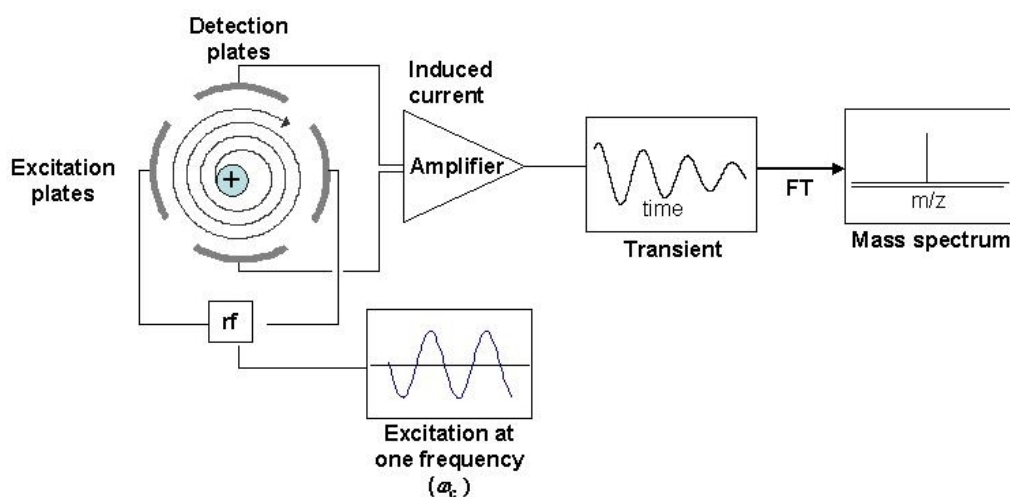


Figure 1-4 : Detection and analysis of the ions in the ICR cell. The cyclotron orbit radius of the ions can be increased by applying an RF excitation on the “excitation plates”. An induced time-dependent image current can be detected on the “detection plates”. Mass spectrum can be derived using Fourier transform methods applied on the so-called transient image current.

For performing IRMPD spectroscopy, the laser beam is mildly focused [19] and aligned along the magnetic field axis. A detailed discussion of the ion-laser overlap issue is also provided [19]. The beam waist is on the order of one millimeter. The irradiation time is slightly higher but comparable to that of the QIT.

## 1.3 IRMPD with two lasers.

### 1.3.1 IRMPD principles

Since the beginning of mass spectrometry, gas-phase physical chemists have continuously showed a particular interest for the structures, energetics, and chemistry of gas phase ions. Infrared spectroscopy has long been considered as a method of choice for structural characterization. IR absorption spectra are derived by monitoring the ratio between the transmitted infrared light ( $I_T$ ) and incident infrared light ( $I_0$ ). Such direct absorption spectroscopy usually requires  $10^{10}$  ion/cm<sup>3</sup> or higher density number [20]. Direct absorption spectroscopy is thus impossible in a Paul or in a Penning ion trap where the maximum number of ions is  $10^6$  ions, within a small volume (few mm<sup>3</sup>). Alternatively photon absorption can be probed by monitoring the IR induced fragmentation of the trapped ions.

One important paper in the context of infrared spectroscopy of trapped ion is the one of Beauchamp in 1978 [21] showing for the first time that isolated trapped ions in an ICR ion trap could be fragmented using an infrared cw CO<sub>2</sub> laser. It is worth to say that dissociation threshold for typical molecular ions is on the order of 1 eV, *i.e.* an order of magnitude larger than that of an infrared photon. One immediately sees that multiple photons have to be absorbed in order to induce ion dissociation. This photon absorption is considered to proceed stepwise, and it is named “InfraRed Multiple Photon Dissociation” (IRMPD).

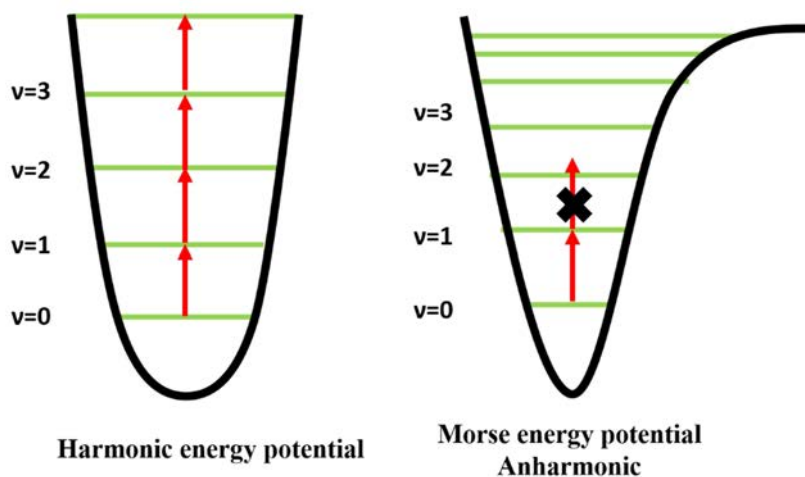


Figure 1-5: Multiple Photon Absorption through a single IR active vibrational mode assuming that the potential is harmonic (left) or anharmonic (right).

The energy potential associated with the vibrational pumping mode is shown in Figure 1-5. This vibrational mode is called “resonant mode” or “pumping mode”, because the energy is pumped into the molecular ion through this vibrational mode. If the energy potential associated with this mode is assumed to be harmonic, multiple IR photons could be absorbed consecutively. Nevertheless, due to the anharmonicity of the potential, only few photons can be sequentially absorbed depending on the laser spectral width relative to the anharmonicity, This is often referred to the “anharmonic bottleneck”.

Figure 1-6 illustrates the general understanding of the non-coherent multiple photon absorption process. Assuming that the anharmonicity associated with the pumping mode is large compared to the width of the laser, only one photon could be resonantly absorbed by the pumping mode. Prior to the subsequent photon absorption, it is assumed that there is de-excitation ( $v=1 \rightarrow 0$ ) of the pumping mode and redistribution of the internal energy into the other vibrational modes of the molecular ion. This diffusion of the energy is known as Intramolecular Vibrational Redistribution (IVR) [22], and it is crucial for allowing subsequent photon absorptions. After partial or complete (*i.e.* statistical redistribution of the energy) IVR, the resonant mode can absorb another photon through the first vibrational transition ( $v=0 \rightarrow 1$ ). The multiple photon absorption process can be seen as successive cycles involving IR absorption in the pumping mode followed by IVR. As a result, there is a stepwise increase of the internal energy of the ion as shown in the bottom panel of Figure 1-6.

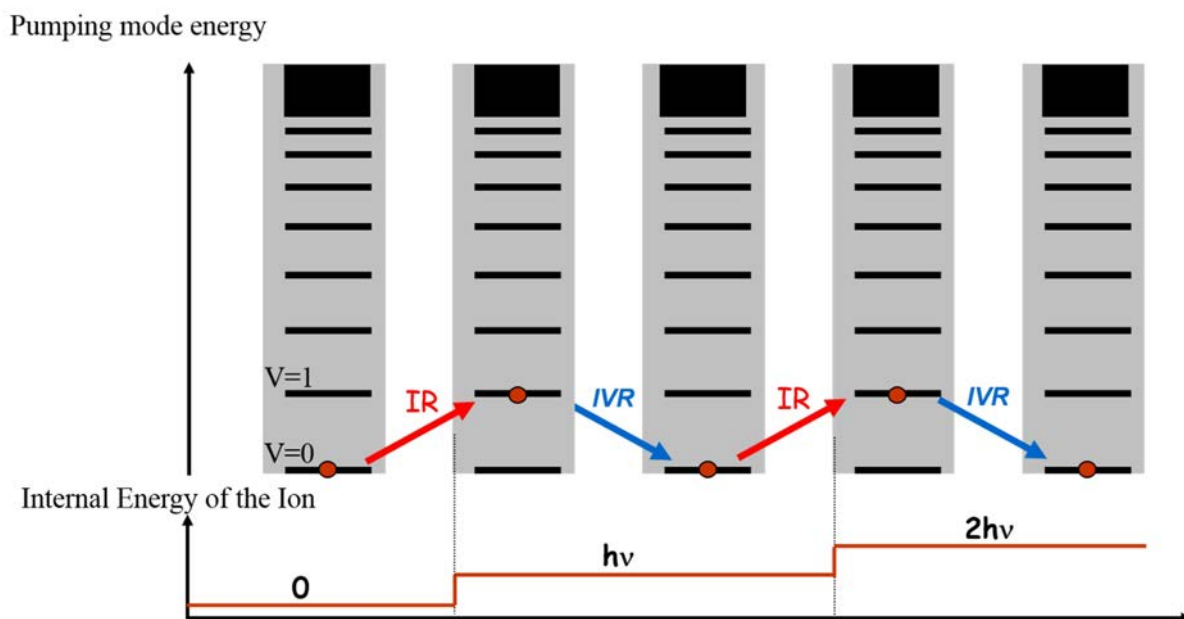


Figure 1-6 : Schematic representation of the multiple photon absorption process. It is assumed that this energy raise can be understood as successive cycles involving resonant one photon absorption (red arrows) and intramolecular vibrational energy redistribution (IVR, represented as arrows in blue). This can be represented using the vibrational energy levels of the “pumping mode” as a function of time as in the top panel. The evolution of total energy of the ion as a function of time is given in the bottom panel.

The nature of the absorption of multiple IR photons has been intensively discussed in the literature in the seventies [23,24]. Highly intense lasers were used to investigate whether the fragmentation of neutral molecule could be isotopically selective or not. It was suggested that the multiple photon absorption mechanism proceeds through three steps, evolving with the density of vibrational states. The earlier steps of the process were supposed to follow a coherent multiphoton absorption process [23,24], and the laser peak power was shown to be critical [25]. This coherent multiple absorption process was named “IR MultiPhoton Dissociation” (IRMPD) [24]. In order to make the distinction with this coherent IRMPD process, the incoherent IRMPD process at play in our case is thus named “IR multiple photon dissociation”.

In general, IRMPD spectra are compared to IR absorption spectra predicted for the lowest energy structures, as done in this manuscript. The first attempt of modeling the multiple photon absorption process by a molecular system irradiated by an IR FEL was proposed by von Helden and coworkers [26]. Gas phase neutral C<sub>60</sub> was irradiated with the FELIX IR FEL and thermal emission of

electrons was monitored. It was observed that the excitation was much more efficient when the IR radiation was chirped to lower frequencies during the macropulse. A model was used to understand this phenomena.

More recently, Parneix and coworkers [27,28] proposed a model of the kinetic of the energy absorption and distribution (IVR) during the macropulse of an IR FEL. All the steps including absorption, stimulated emission, spontaneous emission, and dissociation were taken into account. Monte Carlo simulations of the IRMPD process relied on anharmonic potential energy surfaces calculated using quantum chemical calculations.

### 1.3.2 IR-Free Electron Laser (FEL)

In 1976 was published the first paper related to IR Free Electron Lasers (FEL) by the group of Smith at Stanford [29]. They showed that amplification of infrared radiation of a CO<sub>2</sub> laser could be achieved with relativistic free electrons passing through a spatially periodic transverse magnetic field called undulator. A year later, the same group showed that IR photons can be generated and amplified using free electrons passing through the undulator which was placed within an optical cavity [30]. Indeed, photon emission relies on the deviation of the trajectory of quasi-relativistic electrons. The electrons beam was tuned at 24 MeV and an IR beam centered at 3.417  $\mu\text{m}$  with a width of 0.008  $\mu\text{m}$  and an average power of 360 mW was obtained. As stressed in the introduction [30], the electron medium is unique in the sense that it allows a wide tunability and constitutes at the same time the amplification medium. Nowadays, the FELs under operation produce Ultra Violet and Infrared up to far IR light. X-ray production is currently being developed [31].

A schematic view of the Infrared FEL is provided in Figure 1-7. The trajectory of the electron beam is modified when it passes through the magnetic cavity or undulator, where the photon emission occurs. The IR FEL beam is then extracted through a hole in one of the cavity mirrors. The amplification and the coherence of the IR FEL beam is the subtle result of the interaction of the electrons and emitted light stored in the optical cavity. The wavelength of the IR FEL beam depends on the energy of the electrons and of the period and strength of the magnetic field.

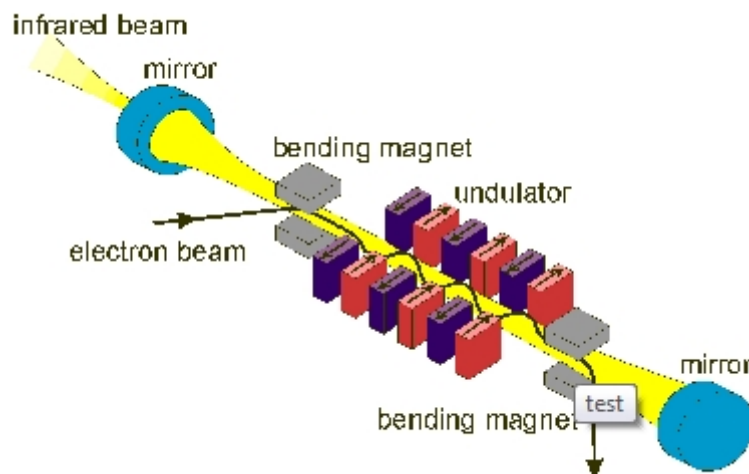


Figure 1-7 : Magnetic cavity of the CLIO IR FEL. Two magnetic benders (or electrostatic dipoles) are used to direct the electron beam (in black) into the undulator and extract it towards a beam dump at the exit of the undulator (north and south poles in violet and red, respectively). Under the influence of the alternative magnetic field, the quasi relativistic electrons bundle onto a snaking path which is at the origin of the photon emission. The interaction between the electrons and IR photons (yellow) beams is at the origin of the IR beam amplification.

The temporal structure of the IR FEL shown in Figure 1-8 is induced by that of the electron beam. The CLIO laser produces trains of IR pulses, called macropulses, at 25 Hz. These macropulses are composed of picosecond long pulses at 62.5 MHz. It should be noted that two consecutive picopulses are separated by 16 nanoseconds, which is the order of magnitude of the lifetime of excited vibrational state which typically ranges from picosecond to nanosecond [32,33]. It is thus conceivable that there is enough time for IVR to proceed between two consecutive pico-pulses. The efficient non-coherent multiple photon absorption process [22] observed with IR FEL may thus not only due to its high intensity, but also to its pulsed structure.

For a given electron energy, continuous tunability can be obtained from  $\lambda$  to  $2\lambda$  with a relatively constant laser power. The laser meanpower is routinely higher than 1 W which corresponds to macropulse (picopulse) energy of 40 mJ (80  $\mu$ J). The bandwidth of the IR FEL strongly depends on the laser cavity length. Bandwidth of 10-20  $\text{cm}^{-1}$  in the 800-2000  $\text{cm}^{-1}$  range is generally used.

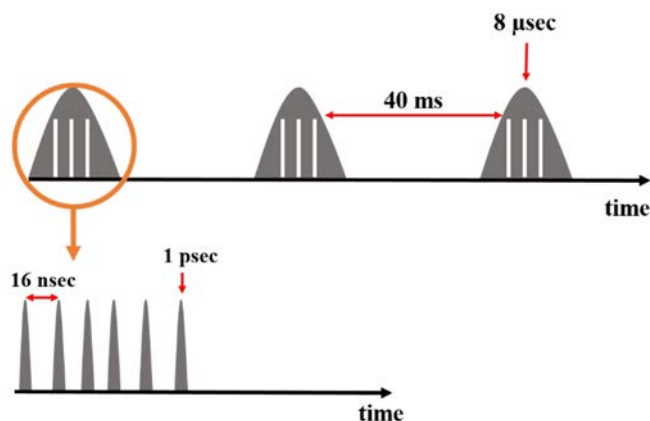


Figure 1-8 : Temporal structure of the CLIO IR FEL at Orsay. Trains of pulses (called macropulses) are delivered at 25 Hz as illustrated in the top of the Figure. Each individual macropulse is composed of  $\sim 1$  pico-second pulses separated by 16 nanoseconds as illustrated in the bottom of the Figure.

The operation of the FEL at CLIO started in 1991, and J.-M. Ortega, currently in charge of CLIO, was one of the initiators. Currently, the CLIO FEL is mainly used for IRMPD spectroscopy. The development towards long-wavelength is an important research topic [31]. CLIO has an important characteristic, which could be used for two-photon IRMPD experiments: there are two independent undulators which allow for lasing simultaneously at two different wavelengths [34]. Beside the IRMPD set-ups, there are two others. One uses the IR FEL for Second Harmonic Generation (SHG) experiments for probing adsorption phenomena on surfaces [35] with applications in Electrochemistry [36]. The second experimental set-up couples Atomic Force Microscopy (AFM) with IR CLIO FEL which provides another dimension to AFM. Applications are mainly in biological systems such as bacteria [37] and phenomena at the sub-cellular level [38].

### 1.3.3 Benchtop IR OPO/OPA laser system.

Tabletop lasers are also coupled to our mass spectrometers to explore the XH (X=C, N, and O) between 2500 and 4000  $\text{cm}^{-1}$ . The exploration of this spectral range strongly relies on the pioneering work of Lee and coworkers [39,40] on weakly bound molecular clusters. Our OPO/OPA laser system (LaserVision) is made of an OPO stage (Optical Parametric Oscillator) based on a single KTA crystal, and of an OPA stage (Optical Parametric Amplifier) made of four KTP crystals (Figure 1-9). The pump laser is an Nd:YAG laser, where the neodymium-doped yttrium aluminium garnet ( $\text{Nd:Y}_3\text{Al}_5\text{O}_{12}$ ) crystal

is the lasing medium. Our Nd:YAG is pumped by a flashlamp, and the spectral width is  $\sim 5 \text{ cm}^{-1}$  which essentially determines the resolution of the OPO/OPA laser system. The repetition rate of the Nd:YAG is different for the two set-ups: it is 25 Hz (Innolas Spitlight 600, 550 mJ per pulse, 4-6 ns pulse duration) at the FT-ICR, and 10 Hz (Continuum Surlite II, 550 mJ per pulse, 1064 nm, 4-6 ns pulse duration) at the QIT.

As shown in Figure 1-9, the 1064 nm beam (in red) of the YAG is split. About one third is frequency doubled (532 nm, in green) and used for generating a signal (13400-11400  $\text{cm}^{-1}$ ) and an idler (5400-7400  $\text{cm}^{-1}$ ) with the OPO stage. Only the idler is sent to the OPA stage. The amplification is based on difference frequency mixing (DFM) between the OPO idler and the 1064 nm beam. This allows for the generation of a mid-IR beam tunable from 2000 to 4000  $\text{cm}^{-1}$ .

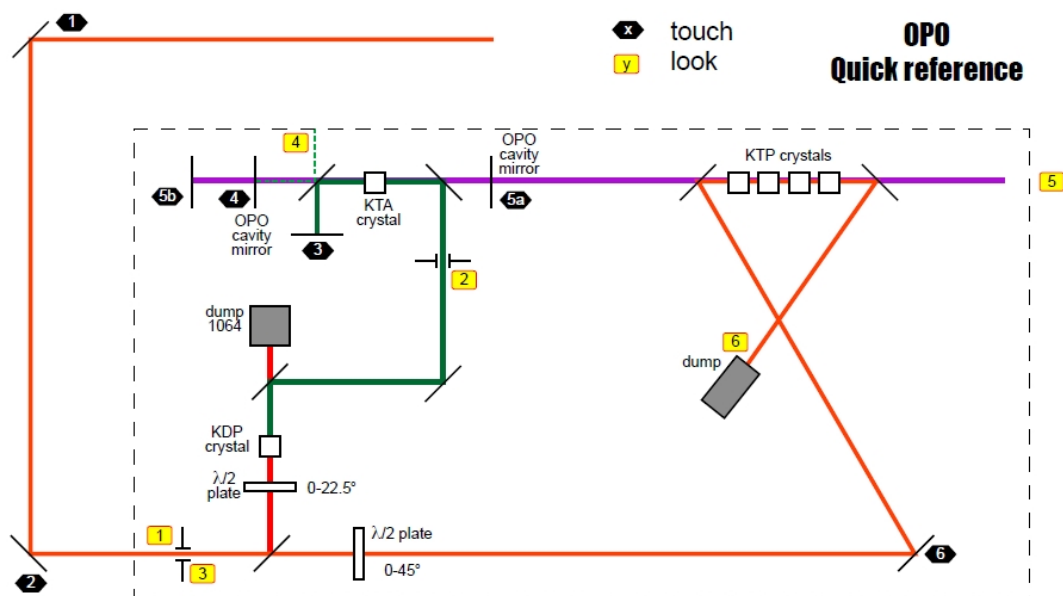


Figure 1-9: Representation of the Laservision OPO/OPA laser system used in this work. The wavelength is tuned by rotating the KTA crystal of the Optical Parametric Oscillator (OPO) stage. The amplification is achieved in the Optical Parametric Amplifier (OPA) stage made of four KTP crystals.

The energy/pulse is maximum near 3  $\mu\text{m}$  and then significantly drops going to larger wavelength. An energy/pulse of  $\sim 12 \text{ mJ}$  at 3600  $\text{cm}^{-1}$  can be easily obtained on a daily basis. In order to scan the 3400-3800  $\text{cm}^{-1}$  spectral range, the OPO/OPA system is optimized at 3675  $\text{cm}^{-1}$  (see below). In practice, we optimize the relative positions of the four OPA crystals in order to maximize the

energy/pulse. Then, to explore a lower energy range, the OPA crystals have to be re-optimized at a fixed lower energy value.

Overall, the wavelength range offered by the IR FEL is nicely complemented by that of the OPO/OPA laser system. Nevertheless, the intensity and the pulse structure of the former are better suited for IRMPD spectroscopy of strongly bound ions. On the other hand, a study of monohydrated protonated uracil performed with our FT-ICR set-up [41] clearly showed that the resolution in the OPO/OPA range is better than that in the IR FEL one. In practice, only IR spectra of weakly bound ion such as hydrated complex [39] or tagged ions [42,43] can be recorded with such OPO/OPA laser system. Nonetheless, as earlier shown by Y.T. Lee and coworkers, an auxiliary CO<sub>2</sub> laser can be used for enhancing the photo-fragmentation efficiency, thus allowing for gas phase IR spectroscopy of strongly bound ions [44,45]. Finally, it is important to mention that the 5-8  $\mu\text{m}$  range can be explored using the Laservision system. For this purpose, an AgGaSe<sub>2</sub> crystal is placed about 1 meter of the exit of the OPA stage, and the mid-IR beam is generated through Difference Frequency Mixing (DFM) on this crystal. The energy per pulse is low, but IR spectra of H<sub>2</sub>-tagged ions have been recorded successfully by the group of M.A. Johnson [46].

#### 1.4 IRMPD Spectroscopy: Practical details

The main advantage of the QIT over the FT-ICR mass spectrometer is that MS<sup>n</sup> experiments can be easily carried out. As a result, IR spectroscopy can be performed on fragment ions at steps MS<sup>2</sup>, MS<sup>3</sup>, MS<sup>4</sup>, etc... IR spectroscopy using the IR FEL is performed at fixed wavelength, which is changed by steps of typically 5 cm<sup>-1</sup>. The Fragmentation mass spectrum is an average of 5 to 10 scans. A stepwise change of the wavelength is not available with the OPO/OPA laser. The wavelength is thus scanned continuously, and we make sure that the fragmentation mass spectrum is the result of an average over a scan over a wavelength window of less than 5 cm<sup>-1</sup>, *i.e.* the bandwidth of the OPO/OPA laser. Typically, if 30 seconds are needed to record the averaged fragmentation mass-spectrum, a suitable speed would be on the order of 0.1 cm<sup>-1</sup>/second. The time to record an IR spectrum over the 3400-3750 cm<sup>-1</sup> range is thus typically 1 hour, the same order of magnitude as for recording the 800-2000 cm<sup>-1</sup> spectrum using the IR FEL.

### 1.4.1 MS<sup>3</sup> experiment using a Quadrupole Ion Trap set-up.

We herein give details on the practical procedure for an MS<sup>3</sup> experiment where a precursor ion formed by ESI is fragmented by CID, and one of its fragments is mass-selected and subsequently irradiated by an IR laser. Using the commercial software, one can set the  $m/z$  of the ions to be mass-selected, and the CID collision voltage to be applied. If the IR activation is to be done in an MS<sup>3</sup> experiment, we simply “click” on the CID MS<sup>3</sup> step of the window menu, and set the corresponding collision voltage to zero.

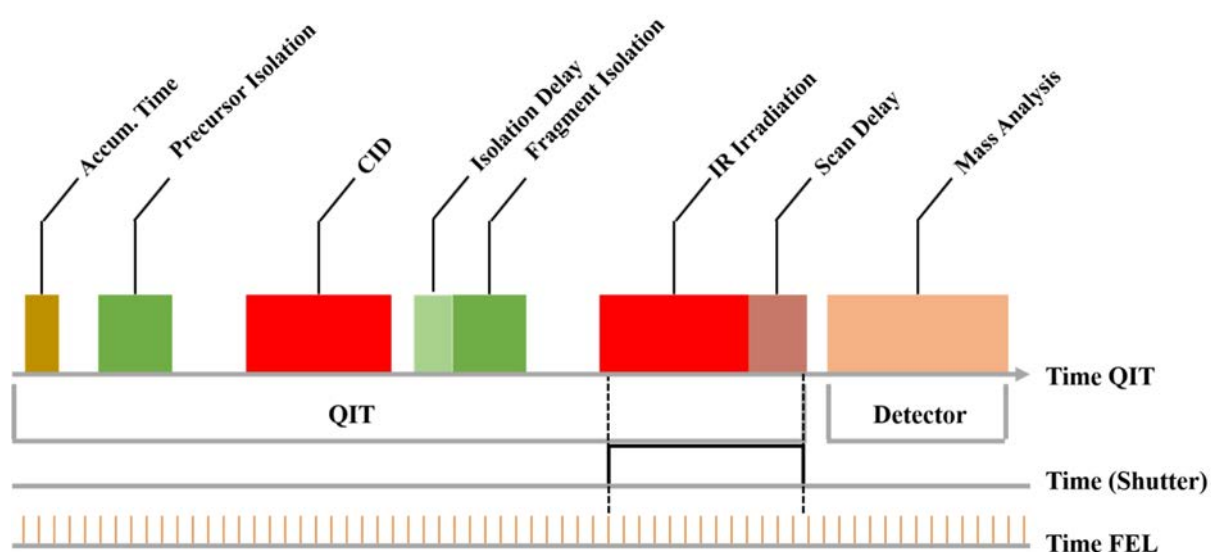


Figure 1-10: Duty cycle associated with an MS<sup>3</sup> sequence performed with our QIT. Electrosprayed ions are injected in the trap during the “accumulation time”. Then, precursor ions are mass-selected, and fragmented through CID. Following their mass-selection, specific  $m/z$  fragments are irradiated with the IR laser. Ions are then ramped extracted from the QIT towards the detector for mass analysis. All these operations can be controlled with the commercial software, which also allows to control different delay times such as “isolation delay” before mass-selection or “scan delay” prior to the mass analysis.

The corresponding duty cycle of this MS<sup>3</sup> experiment is given in Figure 1-10. First, the QIT is continuously filled with ions formed by Electrospray during what is called the “accumulation time”, which is typically set to 1 to 50 ms. Precursor ions can then be mass-selected and subsequently fragmented by CID. Two parameters can be adjusted: the collision voltage and the duration of the activation. Fragment ions of interest are then mass-selected and irradiated with the IR beam. The irradiation time is controlled with a mechanical shutter, which is synchronized with both the QIT and the IR FEL macropulses. In practice, an output trigger of the mass spectrometer is used, and an external

electronic device allows the opening of the shutter right after an IR FEL macropulse. Different delays can be used following the accumulation, the fragmentation and also before the mass-detection. The opening time of the shutter can be adjusted manually and, as illustrated in Scheme, the “scan delay” can be used to irradiate the ions for time period longer than the maximum allowed by the software. Then, ions are ramped extracted towards the detector.

#### 1.4.2 MS<sup>3</sup> experiment using the FT-ICR set-up.

MS<sup>3</sup> experiments can also be performed using the FT-ICR set-up. The first three operations (accumulation, mass-selection, and CID) are performed in the Qh interface (See Figure 1-11). The quadrupole parameters are set so as to mass-select precursor ions, which are transferred to the linear hexapole ion trap.

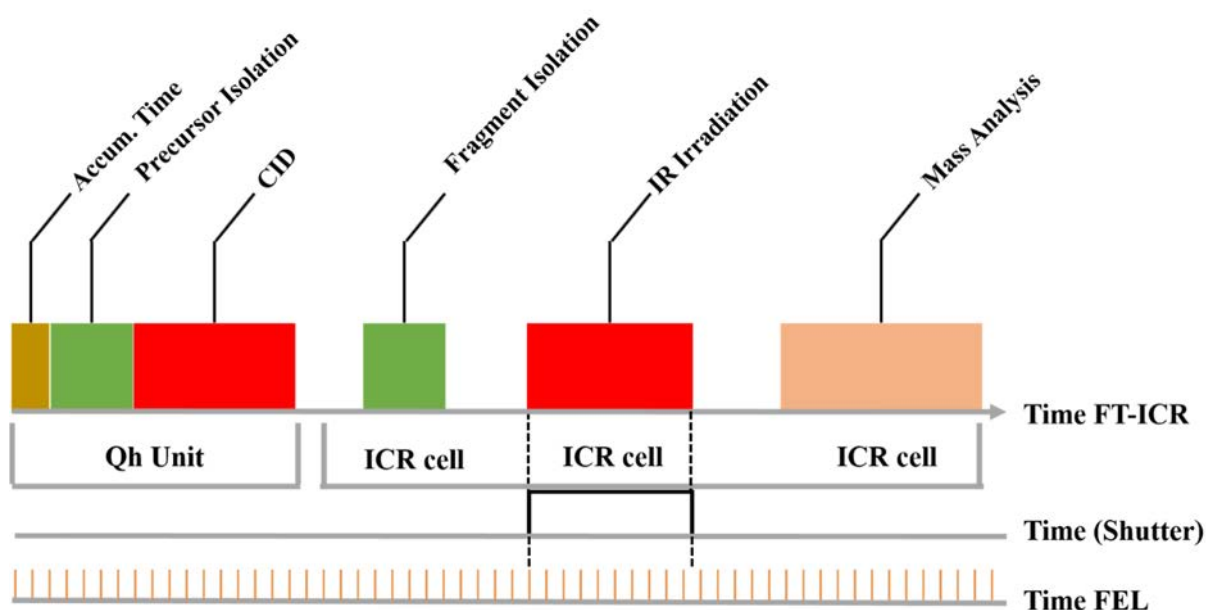


Figure 1-11: Duty cycle associated with an MS<sup>3</sup> sequence performed with our FT-ICR mass spectrometer. The accumulation time, the precursor ion isolation and the CID process are carried out in the Qh unit. The subsequent fragment isolation, its irradiation with the IR laser and the mass analysis are carried out in the ICR cell.

That is, in contrast to the case of the QIT, only the mass-selected precursor ions are accumulated, and then activated in the linear hexapole ion trap. Another difference with the QIT concerns the CID process. Using the QIT, only the precursor ions are resonantly excited using an RF excitation. In the

linear ion trap of the Qh interface of the FT-ICR mass spectrometer, the activation energy is provided by adjusting the DC voltage of the six rods forming the trap. As a result, sequential fragmentation can be observed. Then, ions are pulse extracted towards the high vacuum region of the ICR cell where they are irradiated. As for the QIT, a mechanical shutter controls the irradiation time, except that there is no external electronic device. The pulse sequence program can be easily modified in order to open the mechanical shutter right after a macropulse, which is critical to control the number of macropulses when short irradiation times are used.

### 1.4.3 Combination with an auxiliary CO<sub>2</sub> laser.

Infrared spectroscopy can be performed in our FT-ICR mass spectrometer using either the IR FEL or the OPO/OPA laser. Both infrared lasers can be combined with an auxiliary CO<sub>2</sub> laser for enhancing the fragmentation yield. The idea is that multiple CO<sub>2</sub> photons can be absorbed following the resonant absorption of one (or few) photon(s) delivered by the tunable laser. For this purpose, a broadband CO<sub>2</sub> laser (BFI Optilas, Evry, France) is used in pulse mode. With the IR FEL or the OPO/OPA tuned on a vibrational transition of the ion, a significant enhancement of the fragmentation signal can be observed by irradiating the ions using a few ms long CO<sub>2</sub> pulse following each pulse of the tunable laser, the delay being about 1  $\mu$ s (Figure 1-12). In practice, we first tune the CO<sub>2</sub> pulse length in order to get a fragmentation signal at about 1% using the CO<sub>2</sub> laser only.



Figure 1-12: Synchronization of the tunable infrared lasers (red) with the auxiliary cw CO<sub>2</sub> laser (yellow). A few  $\mu$ s after irradiation by the infrared tunable laser, ions are irradiated with a pulse of the cw CO<sub>2</sub> laser. The CO<sub>2</sub> laser pulse is typically few milliseconds long.

An amplification effect, however, can only be observed if the tunable infrared laser overlaps with the auxiliary CO<sub>2</sub> laser in the ion cloud region. A steering mirror with a hole of 2mm (Figure 1-13)

is used for this purpose. This steering mirror is located in front of the ICR cell long the ICR axe. The CO<sub>2</sub> laser passes through the hole of the steering mirror while the tunable laser is reflected (red spot in Figure 1-13) next to the hole.

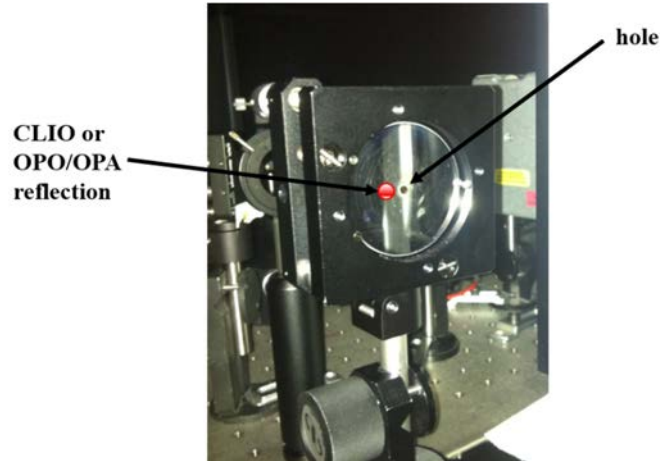


Figure 1-13 : A mirror with a hole is used in order to get the overlap of the tunable (IR FEL or IR OPO/OPA) laser and the auxiliary CO<sub>2</sub> laser with the ion cloud in the ICR cell. The CO<sub>2</sub> laser passes through the hole while the infrared lasers are reflected (red spot) next to it.

Figure 1-14 shows the IR FEL and OPO/OPA optical paths just before the entrance into the high vacuum region containing the ICR cell. A fixed mirror is used to reflect the OPO/OPA beam towards the steering mirror. A second retractable mirror is used to reflect the CLIO beam towards the same steering mirror. When changing the configuration from one tunable laser to the other, only the orientation of the steering mirror has to be slightly corrected.

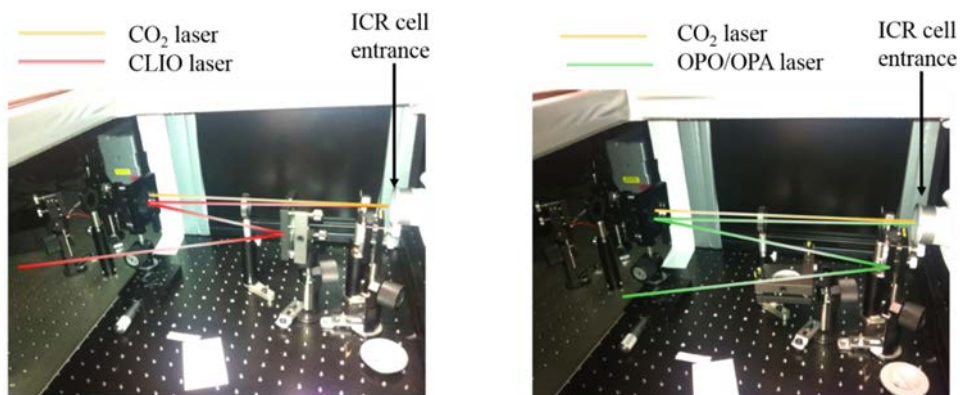


Figure 1-14 : Optical paths of CLIO IR FEL (red) and IR OPO/OPA (green) lasers. One can switch from one configuration to the other using a retractable mirror. The tunable laser can be combined with the auxiliary CO<sub>2</sub> laser (yellow).

The benefit of using the auxiliary CO<sub>2</sub> laser is illustrated in the case of the  $b_2$  ion of protonated GGG (Figure 1-15). As for other small and/or strongly bound ions, no fragmentation is observed using only the OPO/OPA laser. As illustrated in the middle panel, the CO<sub>2</sub> pulse length is adjusted up to the fragmentation threshold. Then, when the two lasers are combined, one can observe (bottom panel) a significant enhancement of the IR induced efficiency. The observed fragmentation when the ions are irradiated with the two lasers (OPO+CO<sub>2</sub>) is larger than the sum of the fragmentation observed with each laser. This is the expected synergy effect: ions which are vibrationally excited ion with the tunable laser, but not enough to fragment, can be further excited by the CO<sub>2</sub> laser thus leading to their fragmentation.

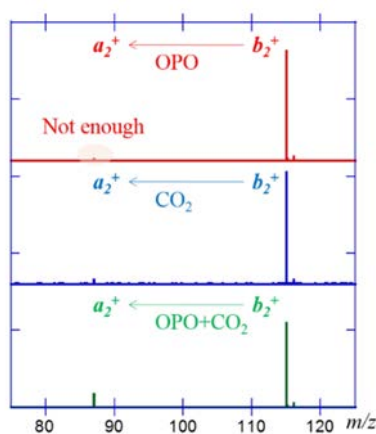


Figure 1-15 : Infrared photodissociation mass spectra of the  $b_2$  ion of protonated triglycine. The infrared photodissociation is negligible when using only the OPO/OPA laser (top panel) or the cw CO<sub>2</sub> laser (middle panel). An enhanced infrared photodissociation signal is observed (bottom panel) when both lasers are used at the same time.

Our favorite molecular ion for optimizing the alignment of the laser is protonated phosphotyrosine ( $m/z$  262). This system is interesting because it has highly IR active vibrational modes in the IR fingerprint region ( $1265\text{ cm}^{-1}$ ) and in the OH region ( $3665\text{ cm}^{-1}$ ) [47] which can be used for aligning the IR FEL and OPO/OPA laser, respectively. Furthermore, it has a phosphate group which is characterized by a strongly IR active mode on resonance with the CO<sub>2</sub> laser. Hence, this molecular ion can be used for aligning the three lasers. The fragmentation mass spectrum in Figure 1-16 is recorded after 500 ms of irradiation time at  $3665\text{ cm}^{-1}$ . Typically, fragmentation yield of 50 to 70% can be observed as illustrated in Figure 1-16.

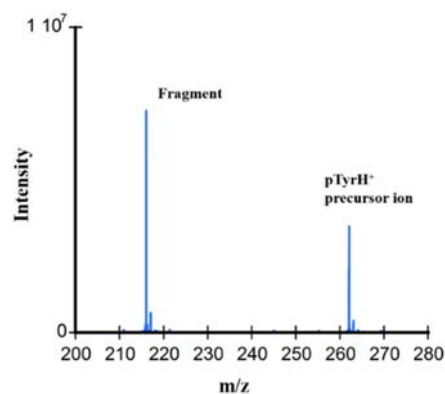


Figure 1-16 : Mass spectrum of protonated phosphotyrosine after 500 ms of irradiation time at  $3665\text{ cm}^{-1}$  with the tabletop OPO/OPA laser.

## 1.5 IRMPD Spectroscopy at FELIX versus CLIO

Two European infrared Free Electron Laser facilities are heavily used for performing IRMPD spectroscopy of molecular ions in the  $1000\text{-}2000\text{ cm}^{-1}$  spectral range. One is the CLIO IR FEL, the other is at the FELIX facility which has recently been relocated in Nijmegen in the Netherlands. The temporal structures of the two FELs are very similar, except for the fact that the repetition rate at FELIX can take different values.

The first IRMPD spectrum of molecular ions using the FELIX FEL was published in 2000 [48]. A quadrupole ion trap coupled to a time-of-flight detector equipped with a multichannel plate detector was used. The QIT was only used to store the ions during the irradiation time. In 2004, an FT-ICR mass spectrometer has been installed. The important technical aspects are given in several review papers [20,49,50]. It is important to know that some technical differences exist between the FT-ICR mass spectrometers installed at CLIO and that at FELIX.

At first, the FT-ICR mass spectrometer at FELIX was not equipped with an ESI source, and molecular ions were formed in the ICR cell [50]. Ions could be formed by electron ionization (EI) and subsequent chemical ionization (CI). Alternatively, ions could also be formed through laser induced ablation/ionization on a solid metal target placed next to the ICR cell along the magnetic [51]. This set-up was used to generate transition metal mono-cation. Then, a pulse of neutral was admitted in the high

vacuum chamber, and metal-neutral complexes could be formed. It is important to stress that ions formed through these processes cannot be thermalized by multiple low energy collisions due to the high vacuum conditions inside the ICR trap. Since then, an ESI source has been installed. Nevertheless, Electrosprayed ions or their fragments are not thermalized through multiple collisions with a rare gas (see below).

### 1.5.1 Irradiation set-ups.

The coupling of the FT-ICR mass spectrometer with the IR FEL beam at CLIO and FELIX is slightly different. Under our experimental conditions, the infrared laser beam is collinear with the magnetic field axis, and a single pass is used for irradiating the trapped molecular ions. A different configuration had to be used at FELIX since the UV-visible laser used for ablation/ionization is aligned along the B axis. As a result, the FELIX IR beam enters off-axis and is reflected within the ICR cell where the inner side of the electrodes is coated with a suitable material allowing for multiple reflections of the IR beam within the ICR cell. The infrared laser beam is thus nearly perpendicular to the B axis. It should be noted that while less than 1s irradiation time periods are routinely used with our FT-ICR, typical irradiation time reported for FT-ICR experiments at FELIX are typically higher (3-5 seconds).

### 1.5.2 Different fragmentation methods within the ICR cell.

A second difference between the two FT-ICR set-ups concerns the activation methods used to generate the fragments. As discussed above, conventional low energy activation can be performed in the Qh interface of our hybrid FT-ICR through multiple collisions with argon. Due to the absence of such Qh interface on the FELIX FT-ICR, alternative activation methods have to be used. Two approaches can be used for activating the ions within the ICR cell. Ion fragmentation can be induced using a cw CO<sub>2</sub> laser, or using the Sustained Off-Resonance Ionisation (SORI) CID approach [52,53]. SORI-CID experiments require the use of a background gas [53] or a pulsed gas [52] of nitrogen or rare gas in the ICR cell. The collisional energy is provided by exciting the ions using an RF excitation at a frequency slightly different from the cyclotron frequency as described in the first SORI-CID report [54]. As a result, ions experience multiple collisions with the background gas eventually leading to their fragmentation. It is important to stress that the internal energy of the fragment ions generated using

either of these methods may be high due to the relatively low pressure conditions during SORI-CID ( $10^{-7}$  mbar) or cw  $\text{CO}_2$  excitation ( $10^{-10}$  mbar), which may contribute to mass peak broadening. Alternative method for fragmenting the ions using the FELIX FT-ICR set-up has been used recently for Electrosprayed ions. This is the subject of the next section.

### 1.5.3 In-source fragmentation

Tandem Mass-spectrometry traditionally derives structural information from fragmentation mass spectra. Organic molecules, for example, can be characterized by comparing the fragmentation patterns with reference mass spectra [55] available in chemistry data bases [56,57]. These reference mass spectra have been recorded under specific experimental conditions (Electron Impact at 70 eV). Since the development of soft ionization sources such as ESI, fragmentation mass spectra are obtained using collision induced dissociation (CID), which can be achieved different ways depending on the mass spectrometer.

Fragmentation occurring in the high pressure “source region” can also be exploited. It has been used in particular for inducing the fragmentation in the context of proteomics [58-60]. Using an FT-ICR instrument, the advantage of this in-source fragmentation is that it is much more efficient than SORI CAD [54] or IRMPD using  $\text{CO}_2$  laser [61]. The fragmentation observed in the “source region” is the result of the collisions of the molecular ions with the molecules in the high pressure region of the source.

In the context of this work, Siu and coworkers [62,63] have used the “in-source” fragmentation to fragment the protonated GGG peptide and generate the  $a_2$  fragment ion. The aim of this study was to characterize the structure of the  $a_2$  fragment ion by Infrared multiple photon dissociation. As it will be discussed later, the high pressure of water/methanol in the electrospray source may catalyze proton transfers and thus facilitate specific rearrangements of the molecular ions [44,63].

It is worth to mention that ions formed through “in source fragmentation” have been studied in details by Armentrout and coworkers [64]. Their purpose was to derive the dissociation energy of  $\text{Ca}^{2+}(\text{H}_2\text{O})_x$ , and the smallest clusters ( $x = 1, 2$ ) could only be formed by “in source fragmentation”. TCID experiments were carried out. This technique provides the bonding energy of the ions by

monitoring the collision cross section of the dissociation reaction products as a function of the collision with rare gas. A special attention was paid on the comparison of the bonding energies derived from clusters directly formed or generated by “in source fragmentation”. It was shown that their set-up allows for thermalization of the ions. Nevertheless, this set-up is very specific, and the collision energy is given through six electrodes placed within the source hexapole. These electrodes are used to modify the DC bias of the hexapole allowing for the soft “in-source” fragmentation [65].

## 1.6 Different groups developing IR Spectroscopy

IR spectroscopy of gas phase ions on the 800-2000  $\text{cm}^{-1}$  energy range often provides important structural information, and IR-FEL's have been shown to be particularly well suited for this purpose. The CO stretching range region, as illustrated in this thesis, and also the amide II (NH bending) region are often highly structurally diagnostic for peptide and their fragments. Unfortunately, there are only two IR tunable FEL's which can be used for IR spectroscopy of mass-selected ions. These two FEL's are located at CLIO (Orsay, France) and FELIX (Nijmegen, The Netherlands). The third IR-FEL facility has recently opened at the Frith Haber institute in Berlin offers similar characteristics. A key common feature of these three FEL's is that the energy of the photons can be changed rapidly by modifying the undulator gap.

An alternative to the FEL for IR spectroscopy of gas phase ions is the OPO/OPA spectra such as the one made in this work. As said above, the intensity of this laser systems is not sufficient for driving IRMPD process for straight bond ions. To circumvent this limitation, an analog  $\text{CO}_2$  laser can be used for enhancing the photo-dissociation signal.

The so-called “ion messenger” is a technique of choice for performing IR spectroscopy of ions. The idea is to form a weakly bond complex between the ion and a “messenger”, which can either be a rare gas atom or a molecule. This technique has been first proposed by W.T. Lee [39,40] who showed that upon excitation with a relatively low-power benchtop laser, loss of the messenger could be observed when laser was tuned on resonance with an IR active vibrational mode of the ion. The lower in the ion-

messenger bounding energy, the lower is the perturbation of the ion structure, and thus the smaller is the spectral-shift of the vibrational modes [42].

Different approaches can be used for forming the ion-messenger complexes. In a joint paper on spectroscopy of  $\text{Li}(\text{H}_2\text{O})(\text{Ar})^+$  complex [66], two approaches used in the group of M. A. Duncan and J. M. Lisy are compared. Water seed in argon carrier gas is used in the two cases. In the group of J.M. Lisy,  $\text{Li}^+$  from an alkali metal ion gun are injected into a fully expanded neutral molecular beam, and the backing pressure of argon is greater than 400 Torr. The cooling of the clusters occurs through evaporative loss of Argon. In the case of M. A. Duncan,  $\text{Li}^+$  cations are formed in the nozzle throat through a laser impact on a metal rod. It is assumed that the cluster growth and the cooling occur through collisions. A similar pulsed supersonic beam expansion combined with an electron impact ion source is used in the group of O. Dopfer [67]. Metal clusters can also be formed using a similar set-up, and reactive intermediates associated with reactions of these metal clusters with neutral seeded in the carrier gas can be studied [68].

Ion-messenger complexes can also be formed in a helium-cryogenically cooled ion trap, where the temperature of the ions can be as low as 4-5 K [69]. These cooled ion-trap development are mostly based on the work of D. Gerlich [70]. These ion-traps are filled with Helium which ensures the collisional cooling, and ion-He complexes may eventually be formed [69]. By seeding heavier rare gases [71],  $\text{H}_2$  or  $\text{D}_2$  [72] in the helium line, tagged ions can be formed with a better efficiency.

Isomer specific spectroscopy is currently a hot topic. Two kinds of approaches based on cryogenically cooled ion trap have been proposed. They are both based on double resonance techniques. The first one is based on the combination of two lasers, which can be IR-UV [73] or IR-IR [72]. The second approach, is based on the combination of Ion Mobility Spectrometry (IMS) to filter isomers which are then spectroscopically interrogated with IR or UV [74] lasers.

Rizzo's group has developed a conformer-selective infrared-ultraviolet double resonance photofragmentation spectroscopy. These experiments are carried out with an ion trap cooled with a He cryostat which allows for well resolved electronic photodissociation spectroscopy with the UV laser.

This method has been used in particular for peptide and peptide fragment ions [73,75]. Recently, they have been able to record the IR spectrum of several conformers of a decapeptide [75]. First they monitor the fragmentation efficiency as a function of the ultra-violet laser energy. Then, the UV laser is tuned on one of the observed electronic transitions. This transition is supposed to be isomer specific. Right before the UV irradiation, the ions are irradiated with an OPO/OPA laser thus leading to a depletion of the UV photofragmentation signal if the IR laser is on resonance with a vibrational transition of the selected isomer. The IR spectrum of this isomer is recorded by monitoring the fragmentation yield as a function of the IR energy.

The double resonance principle is exploited by the groups of Johnson and Asmis but here a combination of two infrared lasers is used [72,76]. In the group of Asmis, a cooled ion trap is used to tag the ions, in order to facilitate the IR induced dissociation. The same technique based on Electro sprayed ions is used in the group of Johnson, but it should be noticed that tagged ions were generated in a supersonic jet in their first double resonance IR-IR paper [77]. In these experiments, one IR laser is tuned on resonance with IR band specific of one isomer. Ions are irradiated with a second infrared laser, which is scanned, providing the specific isomer infrared spectrum by monitoring the photofragmentation signal. This technique has been applied to peptides [78] and anions [46] by Johnson. On interest in the context of this work, Johnson and coworkers have recorded the IR spectra of conformer selected amino-acid and peptides generated by Electrospray.

The ultimate goal of this PhD was to develop a setup for performing IR spectroscopy of mobility selected isomers. Several groups are working in the same directions. The first report on experimental data based on the combination of laser (a CO<sub>2</sub> laser) and IMS was from Dugourd and Jarrold [79]. More recently, this approach has been pursued by Rizzo and coworkers. They recently reported UV spectra of mobility selected ions [74,79]. As discussed in the chapter 4 (Sugar+IMS), a home-built Differential Ion Mobility Spectrometer developed by Gary Glish group in North Carolina was implemented to the QIT in order to efficiently separate and characterize isobaric monosaccharide complex.

## 1.7 Bibliography

- (1) Dunbar, R. C. *Int. J. Mass spectrom.* **2000**, *200*, 571.
- (2) Duncan, M. A. *Int. J. Mass spectrom.* **2000**, *200*, 545.
- (3) Hernandez, O.; Paizs, B.; Maitre, P. *international Journal of Mass Spectrometry and Ion Processes* **2014**, *Submitted*.
- (4) Hernandez, O.; Isenberg, S.; Steinmetz, V.; Glish, G. L.; Maitre, P. *to be submitted* **2014**, *Submitted*.
- (5) Vanberkel, G. J.; Glish, G. L.; McLuckey, S. A. *Anal. Chem.* **1990**, *62*, 1284.
- (6) Chambers, D. M.; Goeringer, D. E.; McLuckey, S. A.; Glish, G. L. *Anal. Chem.* **1993**, *65*, 14.
- (7) Lennon, J. D.; Glish, G. L. *Anal. Chem.* **1997**, *69*, 2525.
- (8) Gronert, S. *J. Am. Soc. Mass. Spectrom.* **1998**, *9*, 845.
- (9) Sieck, L. W.; Meotner, M. *J. Phys. Chem.* **1989**, *93*, 1586.
- (10) Remes, P. A.; Glish, G. L. *Int. J. Mass spectrom.* **2007**, *265*, 176.
- (11) March, R. E. *Int. J. Mass spectrom.* **2000**, *200*, 285.
- (12) Asamoto, B.; Dunbar, R. C. *J. Phys. Chem.* **1987**, *91*, 2804.
- (13) Mac Aleese, L.; Simon, A.; McMahon, T. B.; Ortega, J. M.; Scuderi, D.; Lemaire, J.; Maitre, P. *Int. J. Mass spectrom.* **2006**, *249*, 14.
- (14) Remes, P. M.; Glish, G. L. *J. Phys. Chem. A* **2009**, *113*, 3447.
- (15) Comisarow, M. B.; Marshall, A. G. *J. Mass Spectrom.* **1996**, *31*, 586.
- (16) Amster, I. J. *J. Mass Spectrom.* **1996**, *31*, 1325.
- (17) Marshall, A. G. *Int. J. Mass spectrom.* **2000**, *200*, 331.
- (18) Marshall, A. G.; Hendrickson, C. L.; Jackson, G. S. *Mass Spectrom. Rev.* **1998**, *17*, 1.
- (19) Bakker, J. M.; Besson, T.; Lemaire, J.; Scuderi, D.; Maitre, P. *J. Phys. Chem. A* **2007**, *111*, 13415.
- (20) Oomens, J.; Sartakov, B. G.; Meijer, G.; Von Helden, G. *Int. J. Mass spectrom.* **2006**, *254*, 1.
- (21) Woodin, R. L.; Bomse, D. S.; Beauchamp, J. L. *J. Am. Chem. Soc.* **1978**, *100*, 3248.
- (22) Lehmann, K. K.; Scoles, G.; Pate, B. H. *Annu. Rev. Phys. Chem.* **1994**, *45*, 241.
- (23) Ambartzumian, R. V.; Furzikov, N. P.; Gorokhov, Y. A.; Letokhov, V. S. *Opt. Lett.* **1977**, *1*, 22.
- (24) Grant E, R.; Coggiola M, J.; Lee Y, T.; Schulz P, A.; Sudbo Aa, S.; Shen Y, R. In *State-to-State Chemistry*; AMERICAN CHEMICAL SOCIETY: 1977; Vol. 56, p 72.
- (25) Black, J. G.; Yablonovitch, E.; Bloembergen, N.; Mukamel, S. *Phys. Rev. Lett.* **1977**, *38*, 1131.
- (26) von Helden, G.; Holleman, I.; Meijer, G.; Sartakov, B. *Opt. Express* **1999**, *4*, 46.
- (27) Parneix, P.; Basire, M.; Calvo, F. *J. Phys. Chem. A* **2013**, *117*, 3954.
- (28) Calvo, F.; Falvo, C.; Parneix, P. *J. Phys. Chem. A* **2014**, *118*, 5427.
- (29) Elias, L. R.; Fairbank, W. M.; Madey, J. M. J.; Schwettman, H. A.; Smith, T. I. *Phys. Rev. Lett.* **1976**, *36*, 717.
- (30) Deacon, D. A. G.; Elias, L. R.; Madey, J. M. J.; Ramian, G. J.; Schwettman, H. A.; Smith, T. I. *Phys. Rev. Lett.* **1977**, *38*, 892.
- (31) Ortega, J. M.; Glotin, F.; Prazeres, R.; Berthet, J. P.; Dazzi, A. *Appl. Phys. Lett.* **2012**, *101*.
- (32) Callegari, A.; Merker, U.; Engels, P.; Srivastava, H. K.; Lehmann, K. K.; Scoles, G. *J. Chem. Phys.* **2000**, *113*, 10583.
- (33) Felker, P. M.; Zewail, A. H. *J. Chem. Phys.* **1985**, *82*, 2961.
- (34) Prazeres, R.; Glotin, F.; Insa, C.; Jaroszynski, D. A.; Ortega, J. M. *European Physical Journal D* **1998**, *3*, 87.

- (35) Pluchery, O.; Humbert, C.; Valamanesh, M.; Lacaze, E.; Busson, B. *PCCP* **2009**, *11*, 7729.
- (36) Vidal, F.; Tadjeddine, A.; Humbert, C.; Dreesen, L.; Peremans, A.; Thiry, P. A.; Busson, B. *J. Electroanal. Chem.* **2012**, *672*, 1.
- (37) Dazzi, A.; Prazeres, R.; Glotin, E.; Ortega, J. M. *Opt. Lett.* **2005**, *30*, 2388.
- (38) Policar, C.; Waern, J. B.; Plamont, M.-A.; Clede, S.; Mayet, C.; Prazeres, R.; Ortega, J.-M.; Vessieres, A.; Dazzi, A. *Angewandte Chemie-International Edition* **2011**, *50*, 860.
- (39) Okumura, M.; Yeh, L. I.; Lee, Y. T. *J. Chem. Phys.* **1985**, *83*, 3705.
- (40) Okumura, M.; Yeh, L. I.; Myers, J. D.; Lee, Y. T. *J. Chem. Phys.* **1986**, *85*, 2328.
- (41) Bakker, J. M.; Sinha, R. K.; Besson, T.; Brugnara, M.; Tosi, P.; Salpin, J. Y.; Maitre, P. *J. Phys. Chem. A* **2008**, *112*, 12393.
- (42) Hammer, N. I.; Diken, E. G.; Roscioli, J. R.; Johnson, M. A.; Myshakin, E. M.; Jordan, K. D.; McCoy, A. B.; Huang, X.; Bowman, J. M.; Carter, S. *J. Chem. Phys.* **2005**, *122*, 10.
- (43) Headrick, J. M.; Bopp, J. C.; Johnson, M. A. *J. Chem. Phys.* **2004**, *121*, 11523.
- (44) Bythell, B. J.; Hernandez, O.; Steinmetz, V.; Paizs, B.; Maitre, P. *Int. J. Mass spectrom.* **2012**, *316*, 227.
- (45) Durand, S.; Rossa, M.; Hernandez, O.; Paizs, B.; Maitre, P. *J. Phys. Chem. A* **2013**, *117*, 2508.
- (46) Kamrath, M. Z.; Relph, R. A.; Guasco, T. L.; Leavitt, C. M.; Johnson, M. A. *Int. J. Mass spectrom.* **2011**, *300*, 91.
- (47) Scuderi, D.; Bakker, J. M.; Durand, S.; Maitre, P.; Sharma, A.; Martens, J. K.; Nicol, E.; Clavaguera, C.; Ohanessian, G. *Int. J. Mass spectrom.* **2011**, *308*, 338.
- (48) Oomens, J.; van Rooij, A. J. A.; Meijer, G.; von Helden, G. *Astrophysical Journal* **2000**, *542*, 404.
- (49) Polfer, N. C.; Oomens, J.; Moore, D. T.; von Helden, G.; Meijer, G.; Dunbar, R. C. *J. Am. Chem. Soc.* **2006**, *128*, 517.
- (50) Valle, J. J.; Eyler, J. R.; Oomens, J.; Moore, D. T.; van der Meer, A. F. G.; von Helden, G.; Meijer, G.; Hendrickson, C. L.; Marshall, A. G.; Blakney, G. T. *Rev. Sci. Instrum.* **2005**, *76*, 7.
- (51) Moore, D. T.; Oomens, J.; van der Meer, L.; von Helden, G.; Meijer, G.; Valle, J.; Marshall, A. G.; Eyler, J. R. *ChemPhysChem* **2004**, *5*, 740.
- (52) Tirado, M.; Rutters, J.; Chen, X.; Yeung, A.; van Maarseveen, J.; Eyler, J. R.; Berden, G.; Oomens, J.; Polfer, N. C. *J. Am. Soc. Mass. Spectrom.* **2012**, *23*, 475.
- (53) Polfer, N. C.; Oomens, J.; Suhai, S.; Paizs, B. *J. Am. Chem. Soc.* **2007**, *129*, 5887.
- (54) Gauthier, J. W.; Trautman, T. R.; Jacobson, D. B. *Anal. Chim. Acta* **1991**, *246*, 211.
- (55) Paizs, B.; Suhai, S. *Mass Spectrom. Rev.* **2005**, *24*, 508.
- (56) Steen, H.; Mann, M. *Nature Reviews Molecular Cell Biology* **2004**, *5*, 699.
- (57) Nesvizhskii, A. I.; Vitek, O.; Aebersold, R. *Nature Methods* **2007**, *4*, 787.
- (58) Loo, J. A.; Edmonds, C. G.; Smith, R. D. *Science* **1990**, *248*, 201.
- (59) Loo, J. A.; Edmonds, C. G.; Smith, R. D. *Anal. Chem.* **1993**, *65*, 425.
- (60) Zhai, H.; Han, X. M.; Breuker, K.; McLafferty, F. W. *Anal. Chem.* **2005**, *77*, 5777.
- (61) Little, D. P.; Speir, J. P.; Senko, M. W.; Oconnor, P. B.; McLafferty, F. W. *Anal. Chem.* **1994**, *66*, 2809.
- (62) Verkerk, U. H.; Siu, C.-K.; Steill, J. D.; El Aribi, H.; Zhao, J.; Rodriguez, C. F.; Oomens, J.; Hopkinson, A. C.; Siu, K. W. M. *Journal of Physical Chemistry Letters* **2010**, *1*, 868.
- (63) Verkerk, U. H.; Zhao, J. F.; Lau, J. K. C.; Lam, T. W.; Hao, Q.; Steill, J. D.; Siu, C. K.; Oomens, J.; Hopkinson, A. C.; Siu, K. W. M. *Int. J. Mass spectrom.* **2012**, *330*, 254.
- (64) Carl, D. R.; Moision, R. M.; Armentrout, P. B. *J. Am. Soc. Mass. Spectrom.* **2009**, *20*, 2312.
- (65) Carl, D. R.; Moision, R. M.; Armentrout, P. B. *Int. J. Mass spectrom.* **2007**, *265*, 308.
- (66) Vaden, T. D.; Lisy, J. M.; Carnegie, P. D.; Pillai, E. D.; Duncan, M. A. *PCCP* **2006**, *8*, 3078.

- (67) Andrei, H. S.; Nizkorodov, S. A.; Dopfer, O. *Angewandte Chemie-International Edition* **2007**, *46*, 4754.
- (68) Savoca, M.; Langer, J.; Harding, D. J.; Palagin, D.; Reuter, K.; Dopfer, O.; Fielicke, A. *J. Chem. Phys.* **2014**, *141*.
- (69) Chakrabarty, S.; Holz, M.; Campbell, E. K.; Banerjee, A.; Gerlich, D.; Maier, J. P. *Journal of Physical Chemistry Letters* **2013**, *4*, 4051.
- (70) Gerlich, D. *Phys. Scr.* **1995**, *T59*, 256.
- (71) Goebbert, D. J.; Wende, T.; Bergmann, R.; Meijer, G.; Asmis, K. R. *J. Phys. Chem. A* **2009**, *113*, 5874.
- (72) Leavitt, C. M.; Wolk, A. B.; Fournier, J. A.; Kamrath, M. Z.; Garand, E.; Van Stipdonk, M. J.; Johnson, M. A. *Journal of Physical Chemistry Letters* **2012**, *3*, 1099.
- (73) Wassermann, T. N.; Boyarkin, O. V.; Paizs, B.; Rizzo, T. R. *J. Am. Soc. Mass. Spectrom.* **2012**, *23*, 1029.
- (74) Papadopoulos, G.; Svendsen, A.; Boyarkin, O. V.; Rizzo, T. R. *Faraday Discuss.* **2011**, *150*, 243.
- (75) Nagornova, N. S.; Guglielmi, M.; Doemer, M.; Tavernelli, I.; Rothlisberger, U.; Rizzo, T. R.; Boyarkin, O. V. *Angewandte Chemie-International Edition* **2011**, *50*, 5383.
- (76) Relph, R. A.; Elliott, B. M.; Weddle, G. H.; Johnson, M. A.; Ding, J.; Jordan, K. A. *J. Phys. Chem. A* **2009**, *113*, 975.
- (77) Elliott, B. M.; Relph, R. A.; Roscioli, J. R.; Bopp, J. C.; Gardenier, G. H.; Guasco, T. L.; Johnson, M. A. *J. Chem. Phys.* **2008**, *129*.
- (78) Kamrath, M. Z.; Garand, E.; Jordan, P. A.; Leavitt, C. M.; Wolk, A. B.; Van Stipdonk, M. J.; Miller, S. J.; Johnson, M. A. *J. Am. Chem. Soc.* **2011**, *133*, 6440.
- (79) Hudgins, R. R.; Imai, M.; Jarrold, M. F.; Dugourd, P. *J. Chem. Phys.* **1999**, *111*, 7865.





## 2 REARRANGEMENT CHEMISTRY OF $a_n$ IONS.

2	REARRANGEMENT CHEMISTRY OF $\alpha_n$ IONS.....	43
2.1	Introduction.....	45
2.2	Results and discussion.....	49
2.3	$\alpha_2$ Fragment of protonated YGGFL: Evidence for side-chain proton transfer catalysis. ....	53
2.4	$\alpha_3$ Fragment of protonated tetraglycine : QIT versus FT-ICR. ....	64
2.5	Conclusions.....	73
2.6	Annexes. ....	74
2.7	Bibliography.....	76

## 2.1 Introduction.

Mass spectrometry is a powerful analytical technique used in many field of research and in particular in proteomics for deriving the primary sequence of peptide or proteins [1,2]. These compounds are transferred to the gas phase by soft ionization techniques [3,4]. The resulting (multi)protonated protein or peptide of interest is activated by multiple low energy collisions with rare gas atoms (He or Ar) eventually leading to the fragmentation. This fragmentation technique is called Collision Induced Dissociation (CID). As a result, several fragment ions are formed depending on the cleavage of the backbone and the side chain of the peptide. The fragmentation of the peptide backbone is illustrated in Figure 2-1. Most common peptide fragment ions resulting from the backbone bond fragmentation in the CID process are  $a_n$ ,  $y_n$ , and  $b_n$  ions [5,6]. The subscript of the fragment peptides indicates the number of residues that compose the fragment.

Cleavage at the peptide bond between the second and third residues leads to  $b_2$  and/or  $y_2$  ions depending on the number of charges and their localization.  $a_n$  ions such as the  $a_2$  ion can be directly formed [7] or can also be formed by CID of the  $b_n$  ions [8]. Protonated peptides can successively fragment by losing residues of the C-terminal side leading to series of  $b_n$  ions. The difference in  $m/z$  of two consecutive ions within a series allows for residue identification. This fragmentation mechanism is known as “direct fragmentation pathway”. Nevertheless, multiple other fragments are observed [9-11]. Several studies have been carried out in order to provide more insights into the fragmentation pathways of peptides.

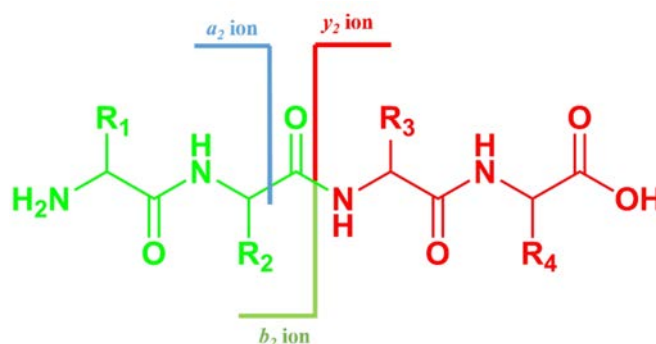


Figure 2-1 : General formula of a tetrapeptide. Activation by multiple low energy collisions can lead to the fragmentation of the peptide bonds forming the  $b_2$  (green line) and  $y_2$  (red line) ions. Subsequent fragmentation of  $b_2$  ion releasing a C=O molecule yield the corresponding  $a_2$  ions (blue line).

This chapter is dedicated to the structural characterization of  $a_n$  ions. Bela Paizs and coworkers [12] proposed a fragmentation mechanism where  $a_n$  ions are formed from the fragmentation of  $b_n$  ions (Figure 2-2). A CO molecule is released from the corresponding  $b_n$  ion leading to a linear imine-protonated structure [8,11,13,14]. The resulting structure has an iminium group which is a strong electrophile group. Fragment  $a_n$  ions contain nucleophilic groups which can potentially attack on the iminium carbon, thus leading to rearrangement chemistry. The questions addressed in this chapter are: what is the structure of  $a_n$  ions? Does it depend on the size (n) of the ion? Is there any permutation of sequence during the rearrangement chemistry?

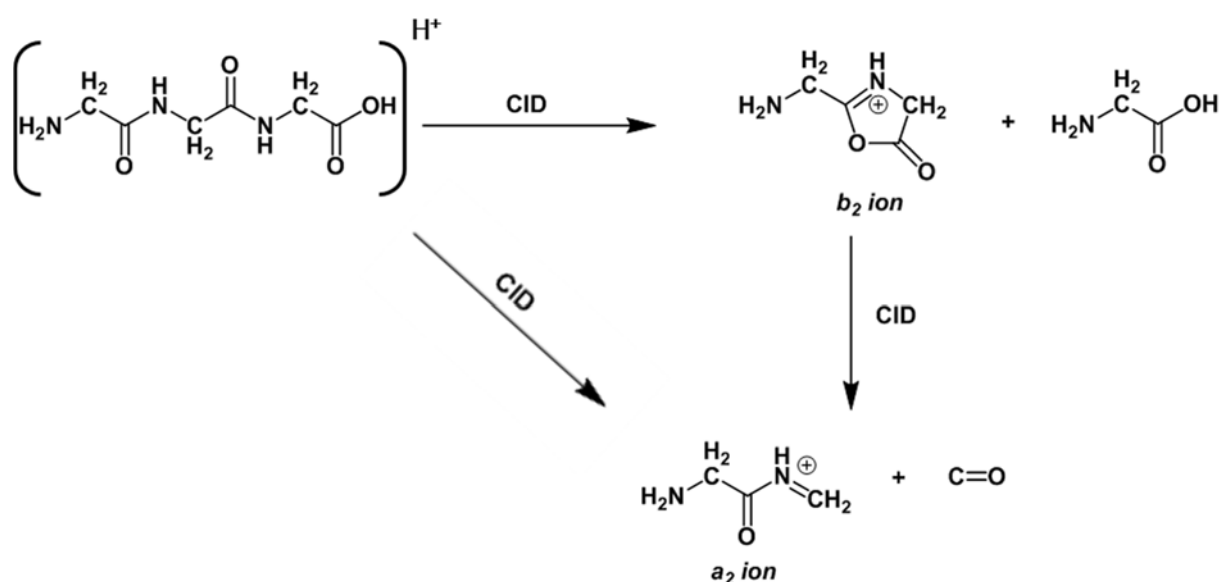


Figure 2-2 : Fragmentation of the backbone of a protonated tripeptide by multiple low energy collisions leading to the formation of a  $b_2$  ion which is assumed to have an oxazolone structure. The  $b_2$  ion can undergo further CID-induced fragmentation leading to the corresponding protonated-imine linear  $a_2$  ion [11]. The corresponding  $a_2$  ion can be also formed directly by fragmentation of the protonated peptide backbone.

The rearrangement chemistry can be initiated by a nucleophilic attack from the N-terminal amino group of the  $a_2$  to the carbon center of the C-terminal imine group forming a 5-membered cyclic structure [15-17]. Siu and coworkers combined density functional theory and threshold collision induced dissociation to characterize the  $a_2$  ion structure of protonated GGG [17]. The dissociation mechanism of protonated GGG to  $b_2$ ,  $b_2$  to  $a_2$ ,  $b_2$  to  $a_1$ , and  $a_2$  to  $a_1$  was studied. This study shows that the 5-membered ring formed as a result of the head-to-tail nucleophilic attack is 8.9 kcal mol<sup>-1</sup> more energetically

favorable than the linear immonium one (Figure 2-3). The energetic barrier for this process was calculated to be 11.9 kcal mol<sup>-1</sup>.

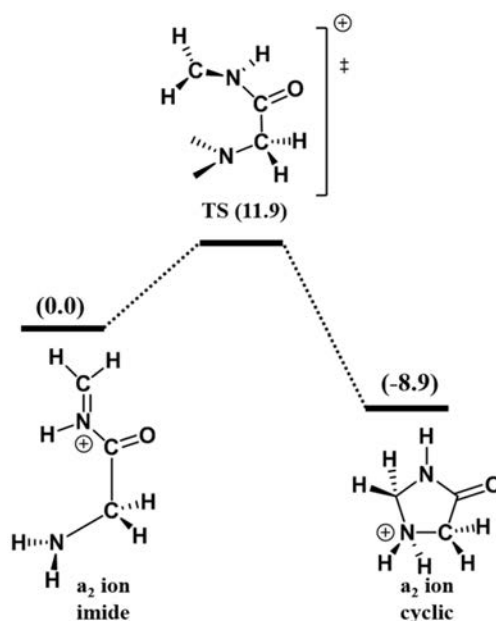


Figure 2-3 : Head-to-tail cyclization mechanism of the  $a_2$  ion leading to a more energetically favorable 5-membered ring structure. The energy barrier associated with this mechanism was calculated to be 11.9 kcal mol<sup>-1</sup>. The theoretical calculations were carried out by Siu and coworkers [17]. Gibbs free energies at 298 K in parenthesis are given in kcal mol<sup>-1</sup>.

Infrared action spectroscopy applied on peptide fragment has been shown to be particularly useful for characterization of  $b_n$  ions structure. In particular, it was shown that oxazolone structure has an infrared signature between 1800 and 2000 cm<sup>-1</sup> spectral range [18-21]. Much less attention, however, has been paid to  $a_n$  ions.

An interesting work was published by Siu and coworkers on the  $a_2$  ion composed by Glycine residues [15]. Tandem mass spectrometry, infrared spectroscopy, and DFT calculations were combined to probe the fragment ion structure. The recorded infrared spectrum revealed the presence of two different fragment structures. The infrared band observed at 1825 cm<sup>-1</sup> was shown to be characteristic of the 5-membered cyclic ring and a smaller band observed at 1727 cm<sup>-1</sup> possibly indicated the presence of a second isomer (Figure 2-4).

Different results were obtained combining the same techniques and using the same samples by Maître and coworkers [16]. In this case, only the 5-membered cyclic  $a_2$  ion structure was found to be

formed as evidenced by the band at  $1825\text{ cm}^{-1}$ . On the other hand, no band characteristic of the so-called “rearranged imine-amide” structure was observed. This structure is called “rearranged” because a  $\text{CH}_2$  group initially on the C-terminal side has moved to the N-terminal side.

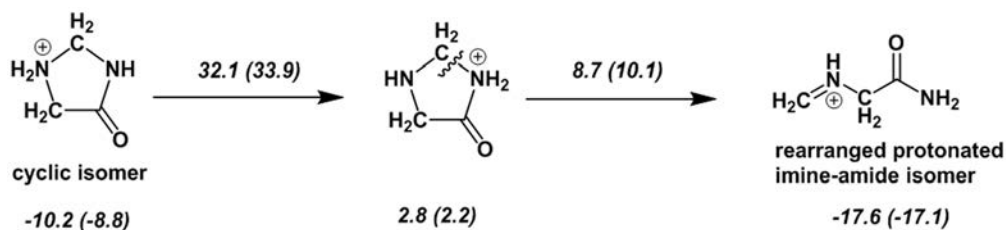


Figure 2-4 : Interconversion of cyclic  $a_2$  ion structure composed by Glycine residues into the rearranged imine-amide isomer. The 1-3 proton transfer and the reopening of the cycle are required prior to the formation of the rearranged imine-amide isomer [16]. ZPE-corrected energies and Gibbs free energies at 298 K in parenthesis are given in  $\text{kcal mol}^{-1}$ .

The aim of this chapter is to better understand under which conditions (peptide size, peptide sequence) sequence permutation occurs during the rearrangement chemistry of  $a_n$  ions. First, the structure of the  $a_2$ ,  $a_3$ , and  $a_4$  ions of protonated oligoglycines will be studied. These ions have been already studied using the CLIO IR FEL coupled to QIT mass spectrometer [16]. On this basis, a rearranged imine-amide structure was proposed for the  $a_4$  ion. Nevertheless, the IR spectrum was not well resolved, and no clear infrared signature of rearranged imine-amide structure could be observed [16]. For this purpose, the infrared spectrum was recorded in the X-H (X= O, H, and C) region where complementary information about the fragment ion structures can be obtained. The infrared spectra of  $a_2$  and  $a_3$  ion from protonated GGG and GGGG respectively were also recorded. The idea was to show the consistency of the results obtained with OPO/OPA tabletop laser coupled FTICR with CLIO laser coupled to QIT [16].

The infrared spectrum reported in this chapter were recorded using a Fourier Transform Ion Cyclotron Resonance Mass spectrometer (FT-ICR) while the  $1000\text{-}2000\text{ cm}^{-1}$  region was recorded using a Quadrupole Ion Trap mass spectrometer [16]. The infrared spectra of the  $a_3$  ion of protonated GGGG recorded using the FT-ICR mass spectrometer and the QIT have been recorded to ensure that results do not depend on the mass spectrometer device. The results obtained in this chapter are fully consistent to those obtained previously [16].

The influence of side chains in the rearrangement mechanism of small  $a_n$  ions was also studied. We were also motivated by understanding the influence of experimental conditions on the  $a_2$  fragment ion structure. A detailed discussion on the activation and thermalization conditions is provided. Theoretical IR spectra presented in this chapter are derived from structures published earlier where more details about the strategy for the structure search can be found [16,22].

## 2.2 Results and discussion.

### 2.2.1 Rearrangement chemistry of the $a_2$ ion of GGGH<sup>+</sup>.

The fragmentation pathways leading to the formation of  $a_n$  ions have been studied in details experimentally and theoretically [8,11-14]. It has been shown in particular a loss of a CO molecule is observed upon collisional excitation of  $b_2$  ions leading to  $a_2$  fragment ions. Assuming that the  $b_2$  ions have an oxazolone structure, theoretical calculations clearly show that a concerted one step mechanism would lead to an  $a_2$  ion with a protonated imine structure [12]. Nevertheless, alternative structures have been proposed for  $a_n$  ions [17]. This potential structural variety has motivated IR spectroscopic studies of  $a_n$  ions.

The elementary steps of the rearrangement mechanism and the energy associated with this process are given in Figure 2-5. This protonated imine structure (**A**) was taken as the reference structure for the relative energies [16]. Two competitive protonation sites were considered in the initial imine structure: the amino nitrogen of the N-terminal amine group (**B**) and the nitrogen of the C-terminal imine group (**A**). The N-terminal amino group was found to be the preferred protonation site [16], but the protonated imine isomer is only 2.9 kcal mol<sup>-1</sup> higher in energy. The latter isomer can undergo cyclization upon nucleophilic attack from the N-terminal amino group to the carbon center of the iminium group leading to a 5-membered ring (**C**). The corresponding transition state (**TS**<sub>1</sub>) for this reaction was calculated at 9.0 kcal mol<sup>-1</sup>. The ionizing proton can migrate to the second amine group of the 5-membered ring isomer (**D**), thus inducing a weakening of the CH<sub>2</sub>-NH<sub>2</sub><sup>+</sup> bond. The subsequent ring opening (**D**→**E**) step leads to the formation of the so-called the rearranged “imine-amide” structure (**E**).

Overall, starting from structure **A**, which is supposed to be initially formed from  $b_2$  ion, one can see that there is a rearrangement of the peptide backbone, with the  $\text{CH}_2$  group initially on the C-terminus in **A** formally transferred to the N-terminus side in **E**. It was thus proposed to call this structure “imine-amide” referring to the fact that there is an “imine” (“amide”) on the N-terminus (C-terminus) side. This rearranged “imine-amide” structure (**E**) was predicted to be the lowest energy structure, not only for the  $a_2$ , but also for the  $a_3$  and  $a_4$  ions of protonated oligoglycine [16].

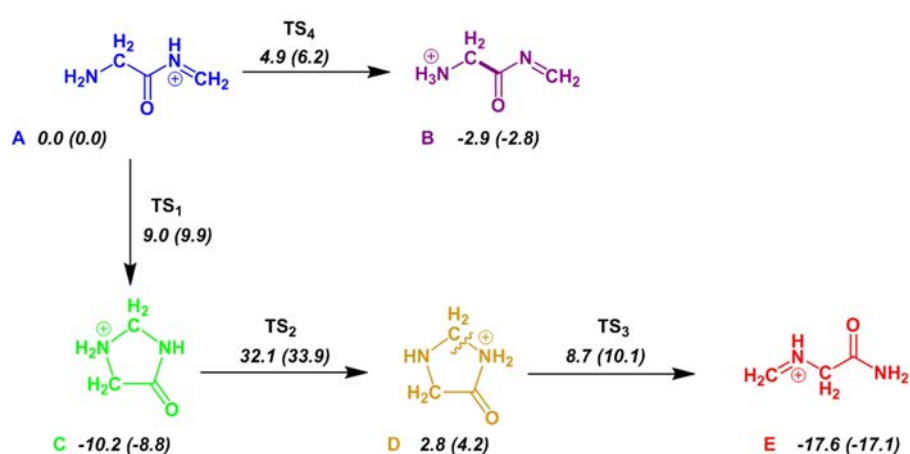


Figure 2-5 : Various  $a_2$  ion structures derived from rearrangement reactions starting from structure **A** which is generated directly from the  $b_2$  ion of protonated GGG. a) C-terminal imine-protonated linear form, b) N-terminal amino-protonated linear form, c) 5-membered ring isomer protonated at the secondary amine, d) 5-membered ring isomer protonated at the amide nitrogen and e) rearranged protonated imine-amide structure. Relative ZPE-corrected energies and Gibbs free energies at 298 K (in parentheses) are given in kcal mol<sup>-1</sup>. The energies were computed at the B3LYP/6-31+G (d,p) level.

While the rearranged imine-amide structure is preferred thermodynamically, it is important to consider the kinetic of its formation. As can be seen in Figure 2-5, the rate-limiting step from **A** to **E** is the 1-3 proton transfer within the 5-membered ring (**C**→**D**). The corresponding transition state (**TS<sub>2</sub>**) has been located [16] and it lies at high energy (32.1 kcal mol<sup>-1</sup>) with respect to structure **A**. The question is thus whether this high energy TS can be overcome allowing for the formation of the rearranged imine-amide structure, and IR spectroscopy seems to be a suitable technique to answer this question.

## 2.2.2 Infrared Spectra of $a_2$ ion of GGG.

IR spectra in the 3200-3700  $\text{cm}^{-1}$  energy range of the  $a_2$  of protonated triglycine are shown in Figure 2-6. The experimental IRMPD spectrum is given in the top panel. Two unresolved bands at 3295 and 3335  $\text{cm}^{-1}$ , and an additional band at 3450  $\text{cm}^{-1}$  can be distinguished. IR absorption spectra of the five structures discussed above are given in the five lower panels of Figure 2-6.

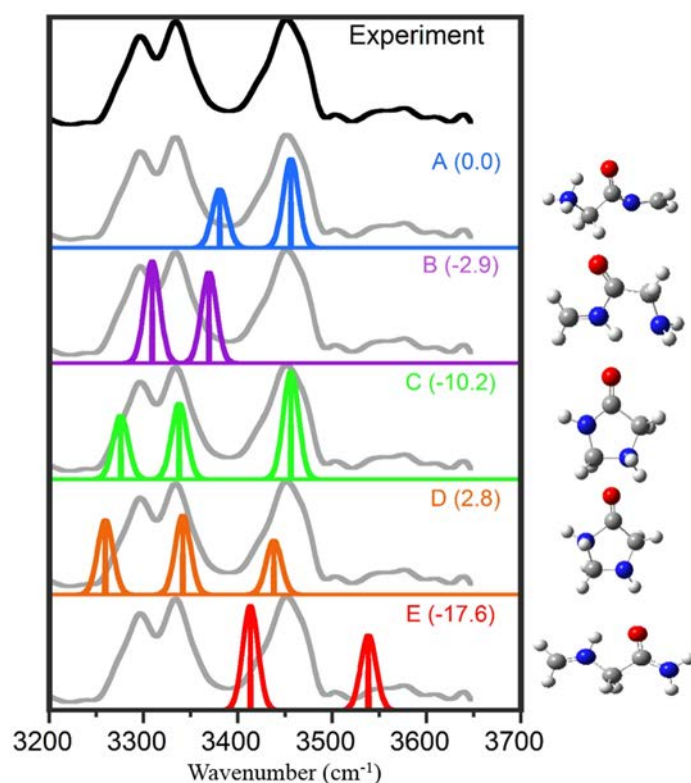


Figure 2-6 : Experimental (top panel) and calculated (A-E) Infrared spectra of the  $a_2$  ion of protonated GGG in the 3200-3700  $\text{cm}^{-1}$  range. Theoretical structures are provided on the right side of their corresponding calculated infrared spectrum. Relative energies are given in  $\text{kcal mol}^{-1}$  in parentheses. All the harmonic frequencies and energies were computed at the B3LYP/6-31+G (d,p) level and scaled by a factor of 0.955. The harmonic IR absorption bands were convoluted by a Gaussian profile (fwhm=20  $\text{cm}^{-1}$ ).

Only two infrared features are predicted for the **A**, **B**, and **E** isomers in the considered energy range. Furthermore, these three structures have a predicted band near 3400  $\text{cm}^{-1}$  (at 3380, 3369, and 3415  $\text{cm}^{-1}$  for structure **A**, **B**, and **E**, respectively) where no experimental band is observed. In the case of the rearranged structure **E**, there is also a predicted band near 3550  $\text{cm}^{-1}$  in a region where no IR band is observed. One can thus safely conclude that none of these three structures is formed experimentally. The predicted IR spectra of structures **C** and **D** are both in good agreement with the experimental one.

Nevertheless, structure **D** is predicted much higher in energy than structure **C**, it is thus very unlikely to be formed under our experimental conditions.

A band assignment is provided in Table 2-1 assuming that only the cyclic **C** isomer is formed. The positions of the three observed experimental infrared bands are in a good agreement with those predicted for the **C** isomer. Using a single scaling factor value of 0.955, only the experimental band observed at 3295  $\text{cm}^{-1}$  is slightly underestimated. The band centered at 3450  $\text{cm}^{-1}$  can be assigned to the free NH stretching mode of the amide group predicted at 3456  $\text{cm}^{-1}$ . The band centered at 3335  $\text{cm}^{-1}$  corresponds to the  $\text{NH}_2$  asymmetric stretching mode of the amine group predicted at 3337  $\text{cm}^{-1}$ . The last band observed at 3295  $\text{cm}^{-1}$  can be assigned to the  $\text{NH}_2$  symmetric stretching mode of the amine group calculated at 3275  $\text{cm}^{-1}$ .

Vibrational Mode	C structure ( $\text{cm}^{-1}$ )	Exp ( $\text{cm}^{-1}$ )
free NH st	3456	3450
$\text{NH}_2$ as st	3337	3335
$\text{NH}_2$ s st	3275	3295

Table 2-1 : Band assignment for the  $a_2$  ion of protonated GGG. The band assignment is indicated in the first column. The infrared frequencies in the second column correspond to the calculated harmonic frequencies of the **C** structure. The experimental infrared frequencies are given in the third column.

IR spectroscopy in the 3200-3700  $\text{cm}^{-1}$  thus suggests that only the N1-Protonated 4-imidazolidinone (**C**) is formed under our experimental conditions. These conclusions are consistent with those of Bythell *et al.* [16] based on the analysis of the 1000-2000  $\text{cm}^{-1}$  spectral range. As said above, the structural assignment proposed by Verkerk *et al.* [15] for the same  $a_2$  ion and based on the 1000-2000  $\text{cm}^{-1}$  IR spectra is different. They observed two bands in the CO stretching range: beside the band characteristic of structure **C**, they observed a band at 1727  $\text{cm}^{-1}$  which was assigned to the rearranged imine-amide structure **E**.

As discussed in the methodology section, it is important to stress that different experimental conditions were used for generating the  $a_2$  ion. While conventional low energy CID was used in the present work, fragmentation leading to the  $a_2$  ion was achieved in the high pressure region of the source

[23] by adjusting the voltage between the capillary exit and the ion guides [15]. As discussed by the same group of authors, it is likely that the 1,3-proton transfer within the 5-membered ring (**C**→**D**) could be catalyzed by water or methanol, and this hypothesis is supported by theory [24,25]. It was thus likely that this apparent discrepancy between results and conclusions of Bythell *et al.* [16] based and those of Verkerk *et al.* [15] is essentially due to the differences in the experimental conditions associated with the fragmentation process. This has motivated us to investigate the potential catalytic effect of a side-chain on the 1,3-proton transfer, and also to probe different factors associated with the CID process under our experimental conditions.

## 2.3 $a_2$ Fragment of protonated YGGFL: Evidence for side-chain proton transfer catalysis.

In order to probe the potential catalytic effect of the side-chain of a residue on the rearrangement chemistry of an  $a_2$  fragment ion, the YGGFL peptide was chosen. Considering the quite large gas phase basicity ( $\sim 350$  kcal mol<sup>-1</sup>) of the phenol group, it could potentially play a role in the rearrangement chemistry of the  $a_2$  fragment ion. The IR spectrum has been recorded in the 1000-2000 and 3400-3800 cm<sup>-1</sup> spectral ranges, and the rearrangement reactions have been explored with quantum chemical methods. Structures (**A**–**E**) above discussed for the  $a_2$  ion of protonated triglycine were also considered here.

### 2.3.1 IR spectra in the 1000-2000 cm<sup>-1</sup> range: Evidence for rearrangement.

The experimental IR spectra of the  $a_2$  ion of protonated YGGFL are shown in the top panel of Figure 2-7. Seven bands were observed near 1185, 1295, 1340, 1525, 1615, 1735 and 1810 cm<sup>-1</sup>. In addition, a weaker band can also be distinguished at 1685 cm<sup>-1</sup>. It should also be noted that the band with a maximum at 1735 cm<sup>-1</sup> has an asymmetric shape, with a shoulder on its blue side at 1750 cm<sup>-1</sup>.

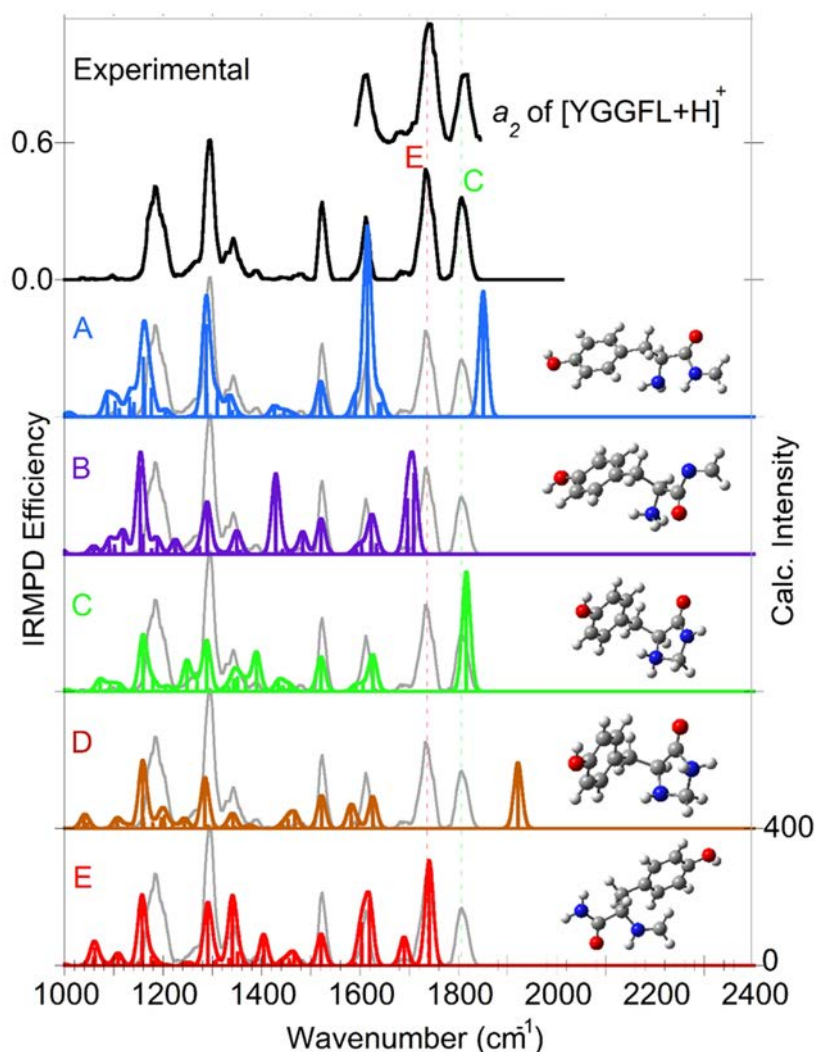


Figure 2-7 : Experimental (top panel) and calculated (A-E) Infrared spectra of the  $a_2$  ion of protonated YGGFL in the 1000-2000  $\text{cm}^{-1}$  range. Theoretical structures are provided on the right side of their corresponding calculated infrared spectrum. All the harmonic frequencies were computed at the B3LYP/6-31+G (d,p) level of theory and scaled by a factor of 0.98. The harmonic IR absorption bands were convoluted by a Gaussian profile (fwhm=20  $\text{cm}^{-1}$ ).

The fwhm of the two bands centered at 1295 and 1525  $\text{cm}^{-1}$  is less than 20  $\text{cm}^{-1}$ , which is the typical bandwidth observed when the IR-FEL is on resonance with a single IR vibrational mode [26]. The other bands are broader, which is typically the signature of multiple IR active modes overlapping with the IR-FEL and/or multiple conformers or isomers with slightly different IR band positions. In order to facilitate comparison with the experimental IRMPD spectra, the simulated IR absorption spectra given in Figure 2-7 are generated by convoluting each calculated IR absorption band with a Gaussian profile with a fwhm of 20  $\text{cm}^{-1}$ .

It follows from inspection of the experimental and theoretical spectra displayed in Figure 2-7 that the range between 1650 and 1850  $\text{cm}^{-1}$  is the most diagnostically useful part of the IRMPD spectrum. In particular, two strong bands are observed at 1735 and 1810  $\text{cm}^{-1}$ . Inspection of the theoretical bands calculated for the five candidate structures (**A–E**) in this spectral range clearly suggest that at least two isomers are formed simultaneously.

The intense experimental bands at 1735 and 1810  $\text{cm}^{-1}$  match the absorption bands predicted for the rearranged protonated imine-amide **E** (1740  $\text{cm}^{-1}$ ) and cyclic **C** isomers (1816  $\text{cm}^{-1}$ ) respectively. For isomer **E**, the normal mode is associated with the C-terminal amide CO stretch, whilst it is the ring CO stretch in the case of the ring **C** isomer. The assignment of the weaker band at 1685  $\text{cm}^{-1}$  is less clear. This band could be assigned to the N-terminal imine C=N stretch of the **E** isomer predicted at 1690  $\text{cm}^{-1}$ . This assignment would be consistent with the fact that the calculated intensity of this absorption band is smaller than that of the 1816  $\text{cm}^{-1}$  absorption band. The formation of the **B** isomer can easily be excluded since the predicted band at 1460  $\text{cm}^{-1}$  is not observed in the experimental IR spectrum. Furthermore the relative **B** isomer energy is relatively high which makes more unlikely its formation. Based on our data for the  $a_2$  ion of protonated YGGFL one can conclude that under our experimental conditions, a mixture of isomers **C** and **E** is formed.

The IR spectrum below 1650  $\text{cm}^{-1}$  does not allow for a clear structural assignment since all isomers have similar absorption bands in this range characteristic of the tyrosine side-chain. The predicted absorption bands in the 1170-1180  $\text{cm}^{-1}$  energy range for all the considered isomer structures can be associated with the tyrosine C—O—H bend which gives rise to the IR band at 1185  $\text{cm}^{-1}$ . Similarly the IRMPD band at 1295  $\text{cm}^{-1}$  can be safely assigned to the tyrosine C—OH stretch. The IRMPD band at 1525  $\text{cm}^{-1}$  also matches the predicted position (1521  $\text{cm}^{-1}$ ) of an in-plane ring deformation of the tyrosine side chain. The two IR signatures in the amide I region (1740 and 1816  $\text{cm}^{-1}$ ) seem to be clear evidences of the presence of the **E** and **C** isomers, however the band assignment below 1650  $\text{cm}^{-1}$  is more subtle. The IR spectrum of the  $a_2$  ion of protonated YGGFL was also recorded in the 3400-3600  $\text{cm}^{-1}$  energy range in order to test the hypothesis of the formation of the **C** and **E** isomers.

### 2.3.2 IR spectra in the 3400-3800 $\text{cm}^{-1}$ : IR signature of rearranged imine-amide structure.

IR spectra of the  $a_2$  fragment ion of protonated YGGFL in the 3400-3700  $\text{cm}^{-1}$  spectral range are shown in Figure 2-8. Five infrared features can be distinguished in the experimental infrared spectrum (top panel). The two most intense bands are centered at 3640 and 3430  $\text{cm}^{-1}$ . Three additional weaker bands are centered at 3540, 3515, and 3460  $\text{cm}^{-1}$ . The calculated IR absorption spectra of structures **A-E** are given in Figure 2-8. The experimental infrared band observed at 3640  $\text{cm}^{-1}$  is predicted at nearly the same position for all isomers: this band is characteristic of the tyrosine OH stretch. Comparison between theoretical and experimental results suggests that the three bands centered at 3540, 3460, and 3430  $\text{cm}^{-1}$  cannot be explained assuming that only one single isomer is formed.

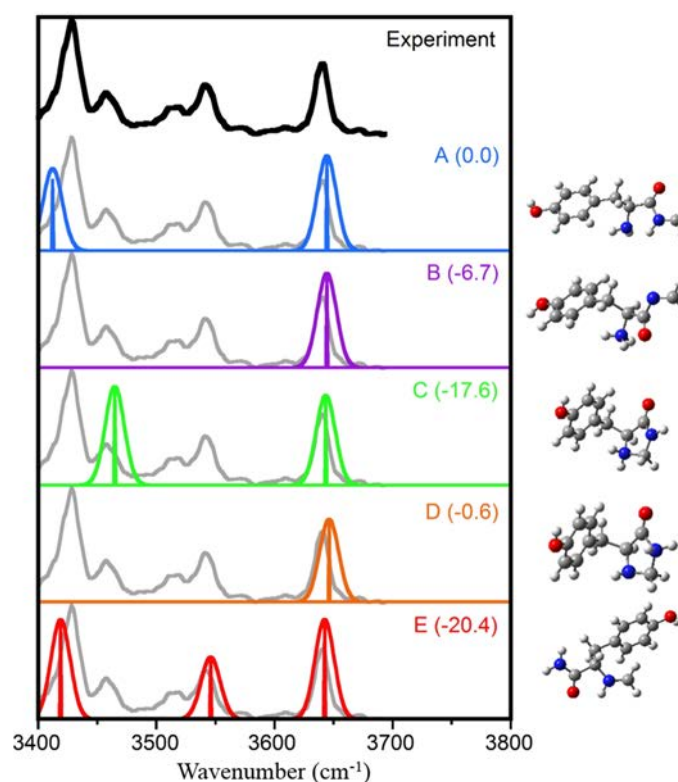


Figure 2-8 Experimental (top panel) and calculated (**A-E**) Infrared spectra of the  $a_2$  ion of protonated GGG in the 3200-3700  $\text{cm}^{-1}$  range. Theoretical structures are provided at the right side of their calculated infrared spectrum. The relative ZPE corrected-energies are given in  $\text{kcal mol}^{-1}$  in parentheses. All the harmonic frequencies were computed at the B3LYP/6-31+G(d,p) level and scaled by a factor of 0.955. The harmonic IR absorption bands were convoluted by a Gaussian profile (fwhm=20  $\text{cm}^{-1}$ ).

The most important conclusion of this work is that the band observed at 3540  $\text{cm}^{-1}$  is an IR signature of the protonated imine-amide structure (**E**). No other isomer has a predicted band in the 3500-

3600  $\text{cm}^{-1}$  energy window. The normal mode associated with the predicted band at 3545  $\text{cm}^{-1}$  for isomer **E** corresponds to the antisymmetric NH stretching mode of the amide  $\text{NH}_2$  group on the C-terminal side. The experimental band centered at 3430  $\text{cm}^{-1}$  nicely matches with the predicted band at 3418  $\text{cm}^{-1}$  of the **E** structure.

Inspection of Figure 2-8 also suggests that the experimental band centered at 3460  $\text{cm}^{-1}$  could be interpreted considering the formation of isomer **C**. Indeed, this structure has a predicted band at 3465  $\text{cm}^{-1}$ . On this basis, an assignment on the observed bands is proposed in Table 2-2 assuming the presence of both **E** and **C** isomers.

Vibrational Mode	C structure ( $\text{cm}^{-1}$ )	E structure ( $\text{cm}^{-1}$ )	Exp ( $\text{cm}^{-1}$ )
OH st Tyr	3645	3645	3640
$\text{NH}_2$ as st (E)		3545	3540
			3515
amide ring NH st (C)	3465		3460
$\text{NH}_2$ s st (E)		3418	3430

Table 2-2: Band assignment for the  $a_2$  ion of protonated YGGFL. The band assignment is indicated in the first column. The infrared frequencies in the second and third column correspond to the calculated harmonic frequencies of the C and E structures, respectively. The experimental infrared frequencies are shown in the fourth column.

### 2.3.3 Potential energy surface: Evidence for proton-transfer catalysis.

The potential energy profile associated with the rearrangement reaction of the  $a_2$  ion of protonated YGGFL is given in Figure 2-9. In order to simply visualize the effect of the tyrosine side-chain on the energetics, the corresponding profile for the  $a_2$  ion of protonated triglycine is also given in Figure 2-9 (light grey). The C-terminal imminium **A** structure, which is supposed to be directly formed from the corresponding  $b_2$  ion, is taken as the reference energy. As in the case of the  $a_2$  GG ion, the **B** structure (not shown) corresponding the proton transfer from the C-terminal imine group (**A**) to the N-terminal amino group is lower in energy than **A**, and the energy difference is -6.7  $\text{kcal mol}^{-1}$ . As can be seen in Figure 2-9, the relative energies of structures **A-E** of the  $a_2$  ion of protonated YGGFL are slightly different from those of the  $a_2$  GG ion. But the main difference between the two systems is the energy barrier associated with the 1,3-proton transfer within the 5-membered ring.

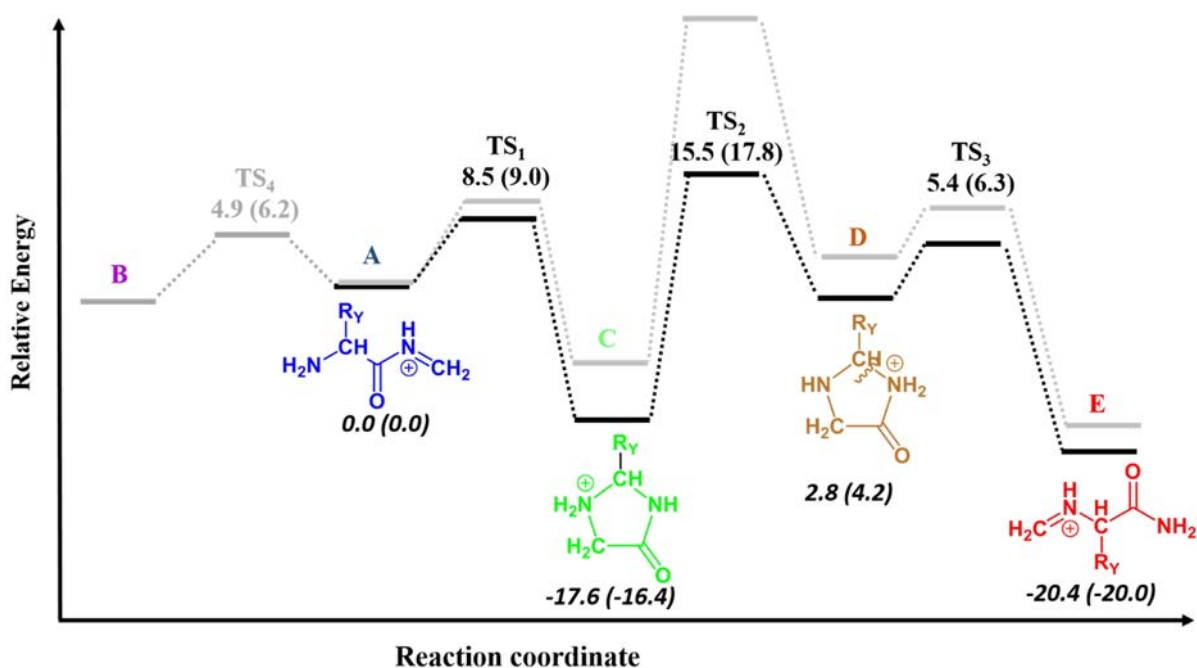


Figure 2-9 Potential energy profile associated with the rearrangement reaction of the  $a_2$  ion of protonated YGGFL. For comparison, the corresponding profile of the  $a_2$  ion of protonated triglycine is given in light grey. In the two cases, the **A** structure is taken as the reference energy. Relative ZPE-corrected energies (Gibbs free energies at 298 K) are given in kcal mol<sup>-1</sup>. The energies were computed at the B3LYP/6-31+G (d,p) level of theory [16].

The activation energy for the corresponding step **C**→**D** is predicted to be 15.5 kcal mol<sup>-1</sup> in the present case, which is significantly less than that (32.1 kcal mol<sup>-1</sup>) calculated in the case of the  $a_2$  ion of protonated GGG. The catalytic role of the tyrosine side-chain on the 1,3-proton transfer **C**→**D** is reflected by the structure of the **TS**<sub>2</sub> of  $a_2$  ion of protonated YGGFL shown in Figure 2-10. The proton is bridged by the  $\delta$  carbon (1.329 Å) of the benzyl group and the amide nitrogen (1.497 Å). As mentioned above, this catalytic effect could be anticipated considering the gas phase basicity of the phenol group (~350 kcal mol<sup>-1</sup>) and that of the amide group (~360 kcal mol<sup>-1</sup>).

It should be noted, however, that no stationary point where the proton is attached to the phenol group could be located. Another way to show the importance of the catalytic effect of the tyrosine side-chain is to consider the 1,3-transfer of the proton on the opposite site of the 5-membered ring (b in Figure 2-10). No interaction between the transferred proton and the tyrosine side-chain is possible, and the calculated energy barrier for this process is found to be exactly the same than that for the  $a_2$  ion of protonated GGG.

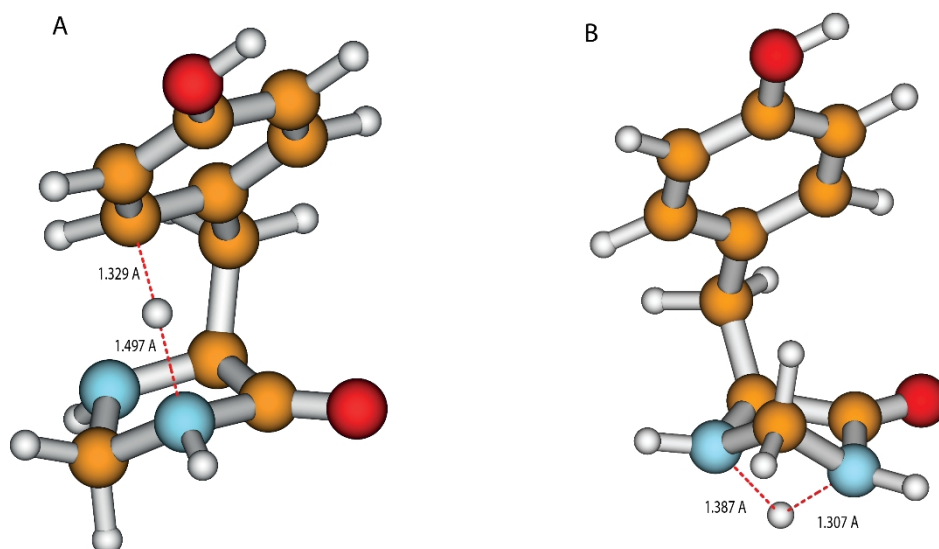


Figure 2-10 : 1-3 proton transfer transition structures for the  $a_2$  ion of protonated YGGFL. In structure a) the proton transfer is catalyzed by the Tyrosine side chain. In structure b) this proton transfer is not catalyzed by the side chain.

The main difference between the two potential energy surfaces associated with the rearrangement chemistry of the  $a_2$  ion of protonated YGGFL and GGG (Figure 2-9) is consistent with the structural assignments based on the IR spectra. The rate limiting step is the same in the two cases, and the corresponding energy barrier is much lower in the former than in the latter case.

From the systematic study of  $a_2$ ,  $a_3$ , and  $a_4$  ions of protonated oligoglycine, it was concluded that under our experimental CID conditions, rearrangement of  $a_n$  ions could occur only if the rate limiting step activation energy is on the order of 10-15 kcal mol<sup>-1</sup> [16]. Hence, in the case of the  $a_2$  ion of protonated GGG, the energy barrier for the **C**→**D** proton transfer (32.1 kcal mol<sup>-1</sup>) prevents for the formation of the rearranged imine-amide structure **E**. In the case of the  $a_2$  ion of protonated YGGFL, however, the barrier height is sufficiently low to allow for the formation of rearranged imine-amide structure **E**.

#### 2.3.4 Quantifying the isomer populations.

From the above discussion, it is clear that **C** and **E** isomers are formed and trapped under our experimental condition. The question is then: can we extract valuable information from the relative intensities of the IR-isomer specific bands characteristic of each isomer? Before answering this question, we will first go back to the definition of the “IRMPD intensities”.

If the parent and fragment abundances are noted as P and F, respectively, the interaction of the IR photon ( $h\nu$ ) with the parent ions can be written as equation (1). The number of P ions trapped is on the order of  $10^6$ , while the number of IR photons within each pico-pulse is on the order of  $10^{15}$ . As a result, it is reasonable to consider that IR photo-induced reaction should follow a pseudo first order model. Note that all our IRMPD spectra correspond to the representation of IRMPD efficiency as a function of the photon energy, where the IRMPD efficiency is defined as  $-\ln\left(\frac{P(t)}{P(t=0)}\right) = kt$ , which in practice is defined as  $-\ln\left(\frac{P(t)}{P(t)+F(t)}\right)$ .



The parent ion abundance should thus follow a mono exponential decay as a function of time  $P(t) = P(t=0)e^{-kt}$ . As noted above, the kinetic constant “ $k$ ” depends on the IR cross section of the parent at a specific wavelength. If two (or more) isomers are present, each with a specific IR cross section, the evolution of the parent abundance P as a function of time should not follow a simple exponential decay. In the present case, where two isomers **C** and **E** are formed, one should consider the population of the two parent isomers at  $t=0$  ( $P_C(0)$  and  $P_E(0)$ ), and the corresponding pseudo-first order kinetic constants ( $k_C$  and  $k_E$ ) at a given wavelength. The total abundance of the parent ions ( $P(t)$ ) should thus follow a bi-exponential decay:

$$P(t) = P_C(0)e^{-k_C t} + P_E(0)e^{-k_E t}$$

This principle has been first used by Williams and coworkers [27,28] for providing clear evidence of population of two isomers.

This approach has been used in the present case for deriving the population of the two isomers **C** and **E**. For this purpose, the IRMPD efficiency of the  $a_2$  ion of protonated YGGFL has been monitored as a function of time at three fixed wavelength (Figure 2-11). As discussed above, isomers **C** and **E** have isomer specific IR absorption at  $3460$  and  $3430 \text{ cm}^{-1}$ , respectively. The evolution of  $P(t)$  has thus been investigated at these two isomer-specific wavelengths. In addition, the evolution of the parent ion

abundance has also been monitored at  $3640\text{ cm}^{-1}$ , which is characteristic of the tyrosine OH stretching mode, and thus a common band for the two isomers.

In the two first cases, the evolution of  $P(t)$  can be nicely fitted using the above bi-exponential function and assuming that the initial populations of isomers C and E ( $P_C(0)$  and  $P_E(0)$ , respectively) were 40 and 60%, respectively. As expected, when the laser is tuned at  $3460\text{ cm}^{-1}$ , *i.e.* on resonance with a C-specific band, the best fit was obtained with the  $k_C$  value ( $0.049\text{ s}^{-1}$ ) being an order of magnitude larger than that of  $k_E$  ( $0.004\text{ s}^{-1}$ ). Conversely, when the laser is on resonance with an IR mode of isomer E,  $k_E$  ( $0.067\text{ s}^{-1}$ ) was found significantly larger than  $k_C$  ( $0.004\text{ s}^{-1}$ ). Finally, when the photon energy was tuned on resonance with the tyrosine stretching mode at  $3640\text{ cm}^{-1}$ , a complete depletion of the  $a_2$  ion was observed.

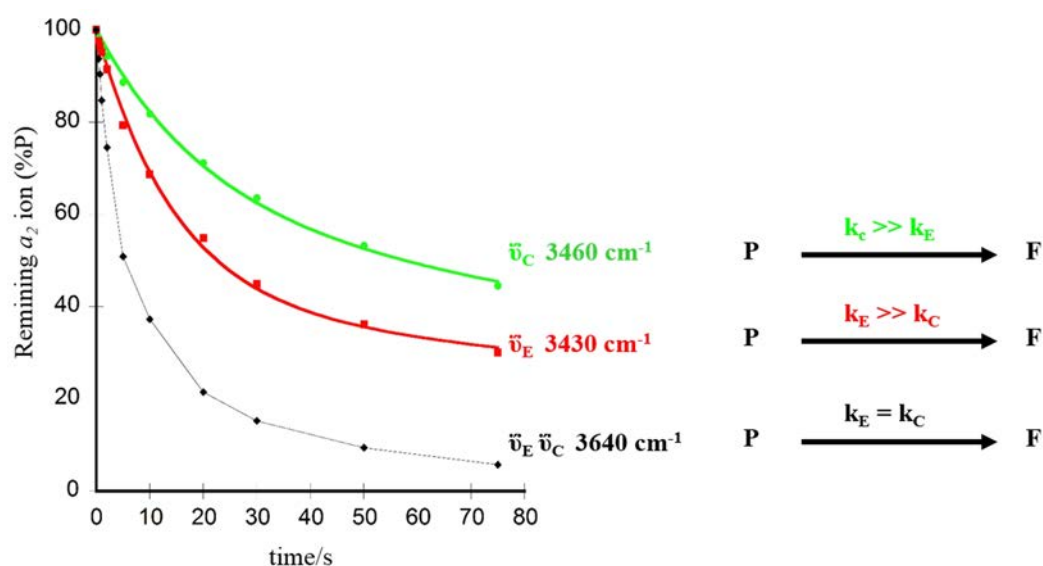


Figure 2-11: Depletion of the  $a_2$  ion of protonated YGGFL induced by isomer selective photo-dissociation. The depletion of the  $a_2$  ion is monitored as a function of the irradiation time. The green, red, and black lines represent the  $a_2$  ion depletion produced at  $3460\text{ cm}^{-1}$ ,  $3430\text{ cm}^{-1}$ , and  $3640\text{ cm}^{-1}$ .

From this kinetic study, it can thus be concluded that the percentages of the 5-membered ring structure (C) and the rearranged protonated imine-amide isomer (E) are  $\sim 40\%$  and  $\sim 60\%$ . It should be emphasized that the same relative abundances were found using two isomer-specific bands in the C=O stretching region [22]. It is probably important to stress that the present experimental data were acquired using the OPO/OPA coupled with the FT-ICR mass spectrometer, while that the IR FEL study was

conducted using the QIT mass spectrometer. The consistency of these results using our two set-ups is a positive result. Nevertheless, one should keep in mind that the CID conditions are different from one instrument to the other. In particular, the CID time period is never clearly specified in the experimental section. As far as IRMPD studies are concerned, it can be assumed that CID conditions were tuned in order to maximize the abundance of the ions of interest, but no specific care has been taken of the potential impact of different parameters on the ion population.

### 2.3.5 Controlling the rearrangement chemistry.

In this context, various experiments have been carried out using the FT-ICR set-up in order to evaluate the effect of the CID conditions on the isomer population of the  $a_2$  ion of protonated YGGFL. The  $b_2$  ion was formed in the high pressure region of the ESI source and then mass-selected in the quadrupole of the Qh interface and accumulated in the hexapole ion-trap where they were activated through multiple collisions with Argon. As discussed just above, under our experimental conditions, two **C** and **E** isomers are formed and the respective percentages are 40 and 60%. Nevertheless, it would be interesting to better define what do we mean by “our experimental conditions” using the hybrid FT-ICR. We usually use moderate CID activation voltage on the order of 5 to 8 volts. The CID time duration is on the order of few hundred of ms. These two parameters were varied in order to evaluate their effect on the relative populations of **C** and **E** isomers.

Varying the CID activation voltage was found to have no effect on the relative population (annex). On the other hand, an effect on the relative populations was observed by varying the activation time from 0.5 to 3 seconds has (Figure 2-12). This was evidenced by recording the infrared spectra in the 3400-3600  $\text{cm}^{-1}$  spectral range where characteristic bands of **C** and **E** isomers have been characterized at 3460 and 3430  $\text{cm}^{-1}$ , respectively. As can be seen in Figure 2-12, the infrared band corresponding to the **C** structure decreases when increasing the CID time period [29].

These results suggest that under our experimental conditions the interconversion of isomer **C** into the lowest energy **E** structure occurs relatively slowly. The reaction is driven by the proton transfer from the amine group to the amide group in the 5-membered ring structure (**C**). Since this proton transfer

TS energy is relatively high ( $15 \text{ kcal mol}^{-1}$ ), it is probably not surprising to see an effect at the second time scale. These results indicate that the time scale for collisional activation process is very important in the peptide dissociation process [29].

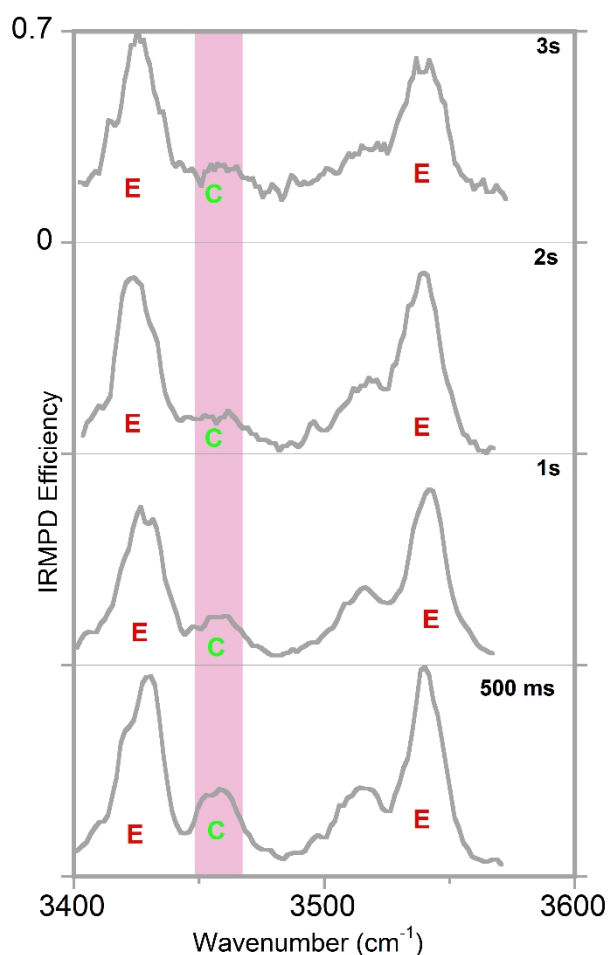


Figure 2-12: Infrared spectra of the  $a_2$  fragment ion of protonated YGGFL in the  $3400\text{-}3600 \text{ cm}^{-1}$  spectral range using the FT-ICR. The infrared spectra were recorded after fragmentation of the precursor  $b_2$  ion at different collision activation times: a) 3s, b) 2s, c) 1s and d) 500 ms. Bands labelled C and E can be assigned to the 5-membered ring (C) and rearranged protonated imine-amide isomers (E) respectively.

## 2.4 $a_3$ Fragment of protonated tetraglycine : QIT versus FT-ICR.

### 2.4.1 Structure and isomerization processes.

Structure characterization of larger  $a_n$  ions can be more challenging. The number of low-energy rearrangement pathways increases with the size of the fragment ion since it contains more nucleophilic centers which can potentially react with the initially formed protonated imine **A** structure. This is illustrated in Figure 2-13 where three low-energy pathways [16] associated with three nucleophilic additions on the iminium carbon of **A** are displayed. The linear protonated imine **A** structure was used as the reference energy structure. It should be noted however that protonation on the N-terminal amino group is slightly more favorable ( $0.6 \text{ kcal mol}^{-1}$ ).

Starting from structure **A**, the head-to-tail cyclisation ultimately leading to the rearranged imine-amide **M** structure corresponds to the reaction pathway **I** in Figure 2-13. As in the case of the  $a_2$  ions of oligoglycine, the **M** structure is predicted to be the lowest energy isomer ( $-14.2 \text{ kcal mol}^{-1}$ ), but its formation is likely to be prevented by the high energy barrier ( $41.2 \text{ kcal mol}^{-1}$ ) associated with the proton transfer within the 8-membered ring (step **I**→**J**).

The second type of reaction can be initiated by the nucleophilic attack of the N-terminal carbonyl oxygen at the carbon center of the protonated imine resulting in the formation of a 7-membered ring structure (**L**). This structure has one cis amide bond and one imine group. The imine group and the N-terminal amino group are the two competitive protonation sites, the former being  $0.6 \text{ kcal mol}^{-1}$  more favorable than the latter. The energy barrier associated with this cyclization process is  $10.5 \text{ kcal mol}^{-1}$ . Based on the above discussion, from a kinetic point of view, it thus seems that the **L** isomer, which is the second most energetically favored isomer, could be formed and this structure was found to be the structure formed under the QIT conditions based on the combination of quantum chemistry and IR spectroscopy data [16].

The third reaction pathway is initiated by the nucleophilic attack of the N-terminal carbonyl of the oxygen of the **A** isomer structure at the C-terminal carbonyl carbon. According to theory, a concerted one-step reaction leads to the formation of a proton-bound dimer (PBD) between  $\text{NH}=\text{CH}_2$  and 2-

(aminomethyl)-5-oxazolone moieties. It was found that this PBD, which is higher in energy than structure **A**, can undergo a reassociation reaction by a nucleophilic attack from the N-terminal amine oxazolone nitrogen to the carbon center of the imine group leading to a new oxazolone containing structure (**F**). Following a proton transfer to the N-terminus amine nitrogen group, the lowest energy structure along this pathway was found to be structure **G** (-3.5 kcal mol<sup>-1</sup>). As can be seen in Figure 2-13, the activation barrier of the rate-limiting step associated with this reaction pathway III (14.2 kcal mol<sup>-1</sup>) is only slightly higher than that (10.5 kcal mol<sup>-1</sup>) leading to 7-membered ring structure (**L**). As a result, isomers formed along pathway III, especially structure **G** which is only slightly higher in energy than **M**, could potentially be formed under our experimental conditions.

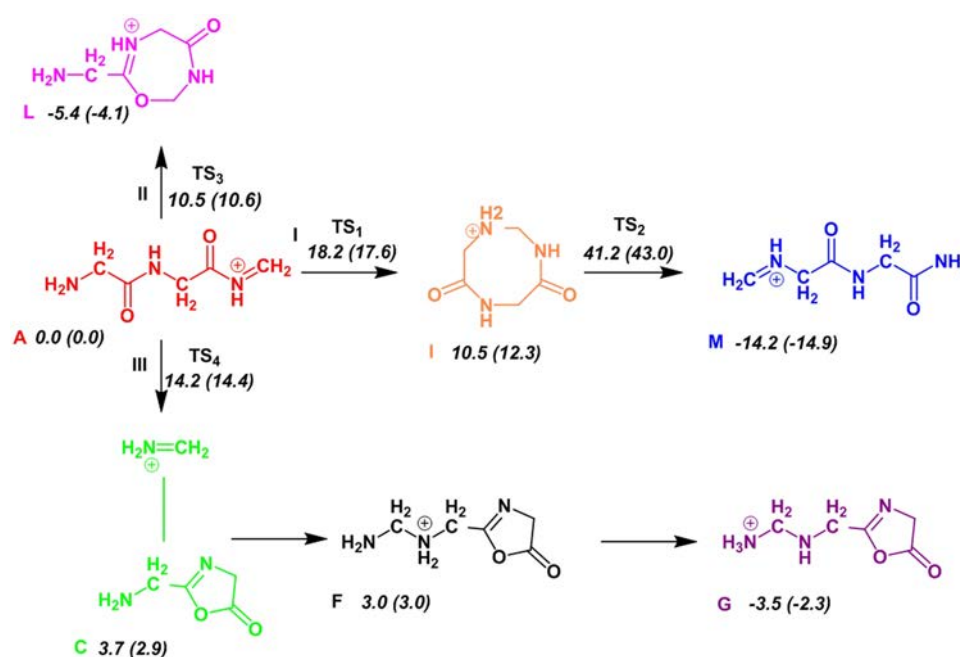


Figure 2-13 : Various *a*<sub>3</sub> ion structures derived from rearrangement reactions starting from structure **A** which is generated directly from the *b*<sub>3</sub> ion of protonated GGGG. Relative ZPE-corrected energies and Gibbs free energies at 298 K (in parentheses) are given in kcal mol<sup>-1</sup>. The calculations were carried out at the B3LYP/6-31+G (d,p) level.

## 2.4.2 IR spectra in the 3400-3800 cm<sup>-1</sup>

IR spectra in the 3200-3800 cm<sup>-1</sup> spectral range of the *a*<sub>3</sub> fragment ion of protonated tetraglycine are shown in Figure 2-14. The experimental spectrum is shown in the top panel where two infrared features can be observed. The first one is an asymmetric and broad (fwhm=25 cm<sup>-1</sup>) band centered at

3435 $\text{cm}^{-1}$  with a shoulder on its blue side at 3450  $\text{cm}^{-1}$ . The second infrared band centered at 3390  $\text{cm}^{-1}$  is narrower, with a bandwidth (fwhm  $\sim 15 \text{ cm}^{-1}$ ) which is typically observed when only one vibrational mode is excited with the laser [26].

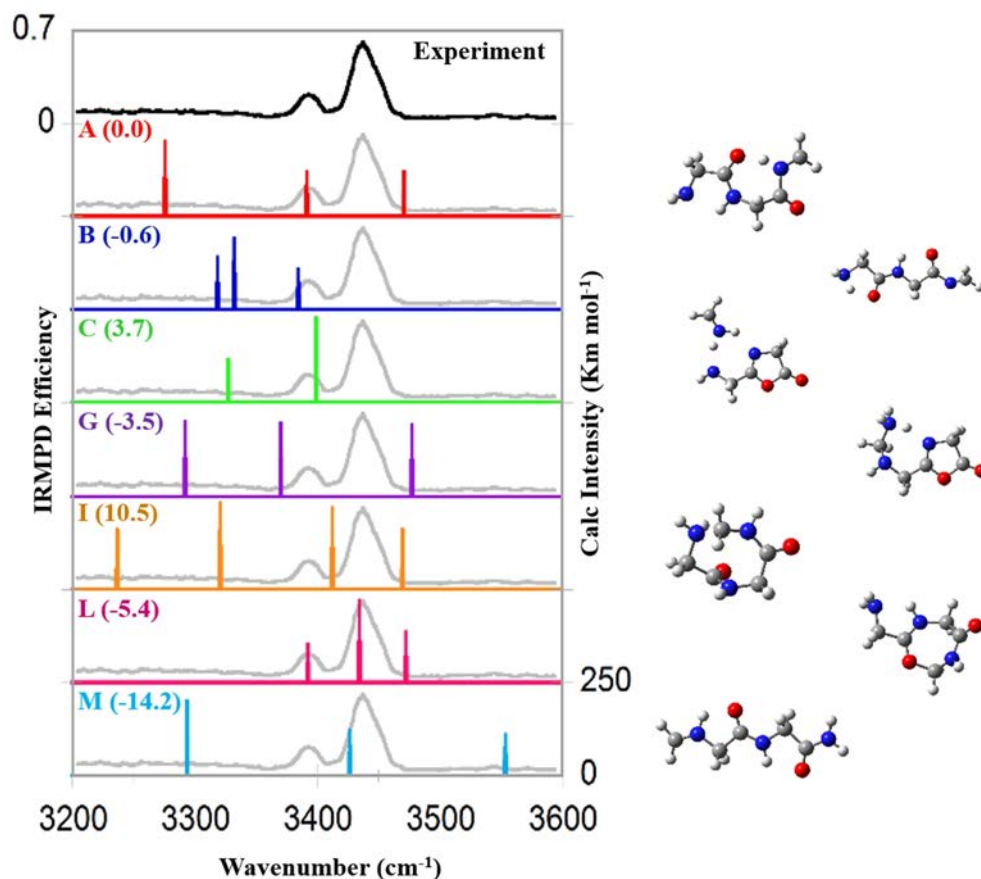


Figure 2-14: Infrared spectra of the  $a_3$  fragment ions of protonated tetraglycine in the 3200-3600  $\text{cm}^{-1}$  spectral range. The top panel corresponds to experimental IRMPD spectra recorded using a hybrid FT-ICR (black line). The calculated IR spectra (stick bars in different colors) of the lowest-energy structures are compared with the experimental infrared spectrum in grey in the lower panels. The representations of the calculated structures are given on the right side of the figure. The energies were computed at the B3LYP/6-31+G (d,p) level of theory. The harmonic frequencies were scaled by a factor of 0.955.

The 800-2000  $\text{cm}^{-1}$  range of the IR spectra had been explored previously [16]. On this basis, it had been concluded that only the **L** structure is formed. The predicted IR absorption spectrum of this **L** structure and of all the other low-energy structures discussed just above are given in Figure 2-14. As can be seen in this Figure, all but the **L** structure have predicted bands in region where no IRMPD bands were observed experimentally. In particular, no band is observed near 3550  $\text{cm}^{-1}$ , *i.e.* the diagnostic band for the rearranged imine-amide **M** structure. Formation of the other structures than **L** can be discarded

since no experimental infrared bands are observed below 3370  $\text{cm}^{-1}$  where the OPO/OPA laser power is still high.

Assuming that only the 7-membered ring **L** isomer is formed, an assignment of the experimental infrared features can be proposed (Table 2-3). The experimental band centered at 3435  $\text{cm}^{-1}$  can be assigned to the amide NH stretching mode. The shoulder near 3450  $\text{cm}^{-1}$  could be due to the  $\text{NH}_2$  asymmetric stretching mode which is predicted at 3470  $\text{cm}^{-1}$ . Finally, the band at 3390  $\text{cm}^{-1}$  can be assigned to the  $\text{NH}_2$  symmetric stretch. Overall, the agreement in terms of band position is good, with a maximum discrepancy of  $\sim 20 \text{ cm}^{-1}$ .

Vibrational Mode	L structure ( $\text{cm}^{-1}$ )	Exp ( $\text{cm}^{-1}$ )
$\text{NH}_2$ as st	3470	3435
NH st	3434	
$\text{NH}_2$ s st	3391	3390

Table 2-3 : Band assignment for the  $a_3$  ion of protonated GGGG. The band assignment is indicated in the first column. The infrared frequencies in the second column correspond to the calculated harmonic frequencies of the **L** structure. The experimental infrared frequencies are given in the third column.

Our conclusions are thus consistent with those based on the analysis of the mid-IR region [16]: the  $a_3$  ion has a 7-membered ring **L** structure. As already mentioned above, the spectra of the  $a_2$ ,  $a_3$ , and  $a_4$  fragments of polyglycine recorded in the 1000-2000  $\text{cm}^{-1}$  spectral range have been obtained using the Quadrupole Ion Trap (QIT) [16]. On the other hand, the infrared spectra in the X-H (X=N, C, O) stretching region were recorded using the FT-ICR set-up in order to illustrate the similarity of the IR spectra recorded with the two set-ups. Since the processes leading to the formation of the fragment ions are quite different from one set-up to the other, it is important to keep in mind that different isomer population could depend on the experimental conditions.

### 2.4.3 IRMPD spectra recorded with the FT-ICR or QIT set-ups.

For this purpose the infrared spectrum of the  $a_3$  fragment ion of protonated GGGG has been recorded with the FT-ICR spectra and it is compared with the infrared spectra of the same  $a_3$  fragment ion recorded with the QIT [16] in Figure 2-15.

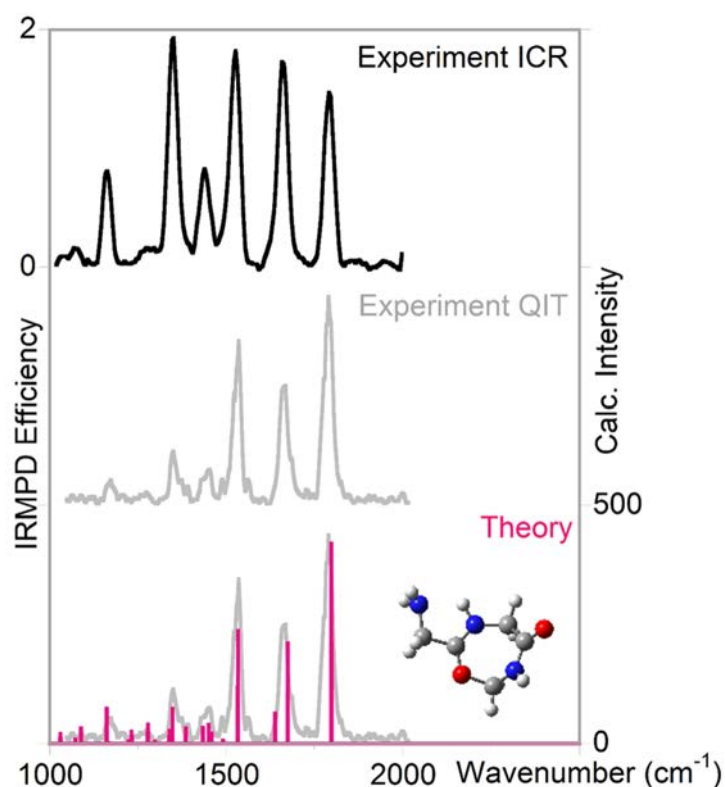


Figure 2-15: Infrared spectra of the  $a_3$  fragment ion of protonated tetraglycine in the 1000-2000  $\text{cm}^{-1}$  spectral range. The two top panels correspond to experimental IRMPD spectra recorded using a hybrid FT-ICR (black) and a quadrupole ion-trap (grey). The calculated IR absorption spectrum (stick bars in color) of the lowest energy structure together with a representation of this structure are given in the bottom panel. The theoretical infrared spectrum was computed at the B3LYP/6-31 G (d,p) level of theory and the harmonic frequencies were scaled by a factor of 0.98.

The infrared spectra recorded using the two set-ups in the 1000-2000  $\text{cm}^{-1}$  spectral range are very similar and both nicely match with the predicted spectrum of the 7-membered ring **L** isomer. The band positions and the bandwidth are very similar. This strongly suggests that the temperature of the ions is similar in the two cases. The only slight difference is the relative band intensity.

The reason for this small difference is probably due to the complex nature of the multiple photon absorption process and in particular that ions are trapped at quite different pressures. Due to the relatively high Helium pressure in the QIT, the remaining non fragmented but yet excited ions are thermalized at room temperature prior to the next IR macro pulse since the repetition rate of the IR-FEL is 25 Hz. In the case of the hybrid FT-ICR, however, ions are only thermalized in the linear hexapole ion-trap prior to their transfer into the ICR cell where they are irradiated. As a result, ions cannot be thermalized prior

to each train of IR Pico pulses due to the low pressure in the Penning ion-trap ( $10^{-9}$ - $10^{-10}$  mbar). One would thus expect that the IR activation regimes are slightly different from one instrument to the other, which may be in part at the origin of the differences in relative IRMPD intensities.

#### 2.4.4 $a_4$ ion of GGGG.

The largest  $a_n$  ion included in this study was the  $a_4$  ion of GGGGG. The same nucleophilic additions of the  $a_3$  ion of protonated GGGG were considered in the case of the  $a_4$  ion of protonated pentaglycine [16]. The linear protonated imine **A** structure was also used as the reference energy structure. The corresponding reaction pathways are showed in Figure 2-16. In this rearrangement chemistry, the rearranged protonated imine-amide structure (**M**) was calculated as the lowest energy structure ( $-14.0$  kcal mol $^{-1}$ ).

It is important to stress that the activation barrier of the rate-limiting step associated with this process is calculated at  $10.7$  kcal mol $^{-1}$ . This activation barrier is much lower in comparison to the activation barrier associated with the rearrangement pathway of the  $a_2$  and  $a_3$  fragment ions of glycine residues ( $32.1$  and  $41.2$  kcal mol $^{-1}$  respectively) [16] and that of the  $a_2$  ion of protonated YGGFL ( $15.5$  kcal mol $^{-1}$ ) [22]. As a result, rearranged protonated imine-amide isomer **M** can be potentially formed under our experimental conditions.

This was the conclusion of the mid-IR ( $1000$ - $2000$  cm $^{-1}$ ) study. It should be noted however, that the IR spectrum consisted essentially in one broad band. Formation of other structures could not be excluded. Furthermore, no isomer-specific band of the rearranged imine-amide isomer could be identified in the  $1000$ - $2000$  cm $^{-1}$  spectral range.

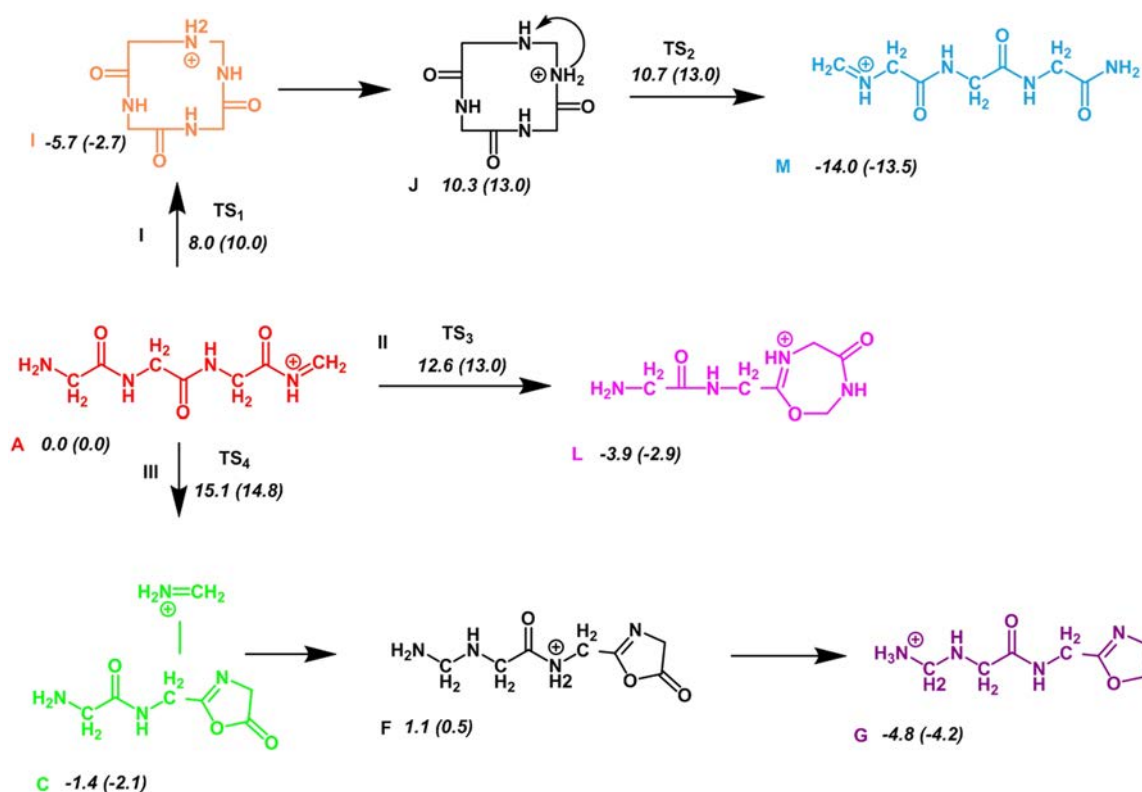


Figure 2-16: Various  $a_4$  ion structures derived from rearrangement reactions starting from structure A. Relative ZPE-corrected energies and Gibbs free energies at 298 K (in parentheses) are given in kcal mol<sup>-1</sup>. The calculations were carried out at the B3LYP/6-31+G (d,p) level of theory.

#### 2.4.5 Infrared Spectroscopy of the $a_4$ ion of GGGGG.

IR spectra in the 3200-3600 cm<sup>-1</sup> spectral range of the  $a_4$  fragment ion of protonated pentaglycine are shown in Figure 2-17. The experimental spectrum is shown in the top panel where three infrared features can be observed. The first low intense feature is observed at 3540 cm<sup>-1</sup>. An intense and symmetric feature is also observed at 3430 cm<sup>-1</sup> with a bandwidth of ~25 cm<sup>-1</sup>. A low intense band can also be observed at 3330 cm<sup>-1</sup>. Comparing the experimental spectrum and theory, one can conclude that the observed infrared spectrum cannot be explained assuming the formation of a single isomer type.

As can be seen in this Figure, the band observed at ~3540 cm<sup>-1</sup> is a clear-cut diagnostic of the rearranged imine-amide structure. This ~3540 cm<sup>-1</sup> band can only be assigned to the rearranged imine-amide structure (M), which is predicted at 3546 cm<sup>-1</sup>. This infrared signature of the rearranged imine-amide structure has also been observed in the case of another  $a_4$  ion (of YGGFL) [30], as well as in the case of the YG  $a_2$  ion [31]. This ~3540 cm<sup>-1</sup> band is observed at higher frequency than typical amide

NH stretching bands which are observed near  $3450\text{ cm}^{-1}$  or even at lower frequency if they are involved in hydrogen bond. The most intense band observed near  $\sim 3430\text{ cm}^{-1}$  can be assigned to three closely spaced IR absorption bands predicted at  $3421$ ,  $3432$  and  $3458\text{ cm}^{-1}$  corresponding also to the same isomeric structure (**M** isomer). Interestingly, there is a weak band observed at  $\sim 3330\text{ cm}^{-1}$  which cannot be assigned if only the rearranged imine-amide structure is considered.

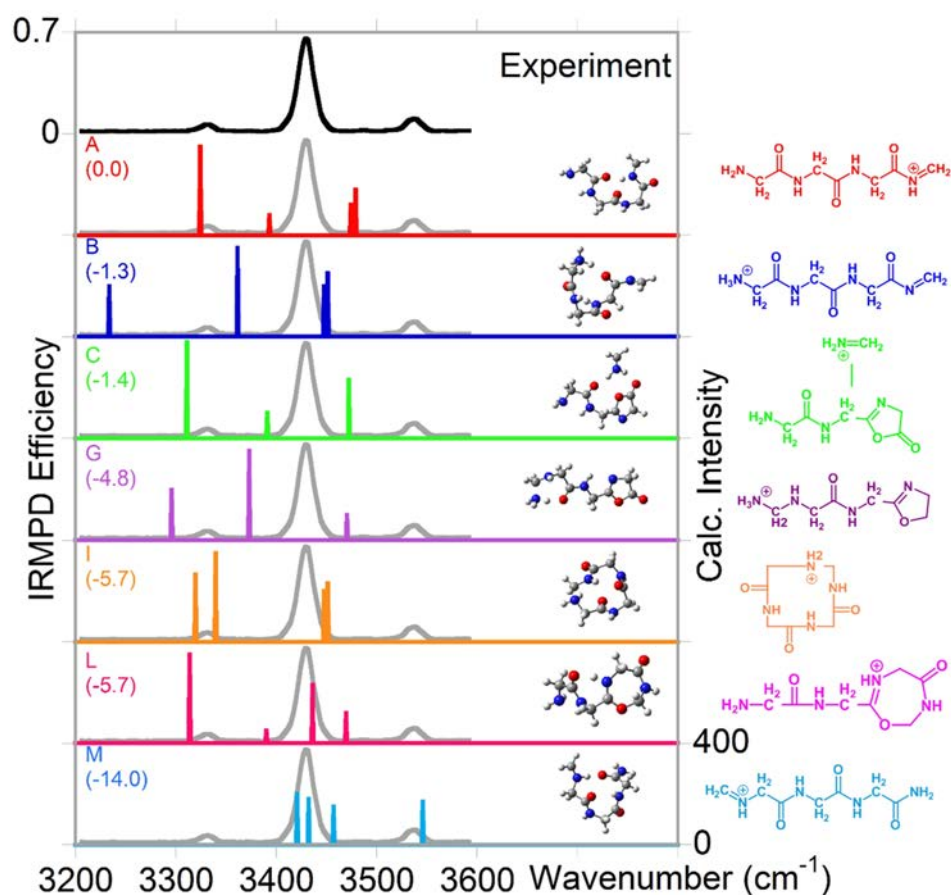


Figure 2-17: Infrared spectra of the  $a_4$  fragment ions of protonated pentaglycine in the  $3200\text{--}3600\text{ cm}^{-1}$  spectral range. The top panel corresponds to experimental IRMPD spectra recorded using a hybrid FT-ICR (black line). The calculated IR spectra (stick bars in different colors) of the lowest-energy structures are compared with the experimental infrared spectrum in grey in the lower panels. The representations of the calculated structures are given on the right side of the figure. All the harmonic frequencies were computed at the B3LYP/6-31+G (d,p) level of theory and corrected by a scaling factor of 0.955.

While the  $\sim 3540\text{ cm}^{-1}$  band is a clear-cut signature of the rearranged imine-amide structure, the band observed at  $\sim 3330\text{ cm}^{-1}$  is likely to be the signature of other isomers formed under our experimental

conditions. Interestingly, on the basis of the IR fingerprint spectrum it had been concluded that although the rearranged imine-amide structure is likely to be the predominant structure for the  $a_4$  ions, one could also conceive that a smaller fraction of other isomers could also be formed [16]. Based on the comparison of the experimental 1000-2000  $\text{cm}^{-1}$  IR spectrum with the corresponding theoretical IR absorption spectra, it was proposed that macrocyclic structures such as **I** and/or an amino-protonated imine **B** structure could also be formed. The predicted IR absorption spectrum of isomer **B** does not match with the observed IR spectrum in the 3200-3600  $\text{cm}^{-1}$  range. On the other hand, the band observed at  $\sim 3330 \text{ cm}^{-1}$  nicely matches with two predicted IR absorption band of the macrocyclic structure **I** at 3320 and 3340  $\text{cm}^{-1}$ . Formation of **A**, **B**, **C**, **G**, and **L** isomers can be discarded since their predicted infrared spectra are rather different in comparison with the experimental one.

Based on our results, a detailed assignment of the observed bands is proposed in Table 2-4. The first observed band correspond to the asymmetric  $\text{NH}_2$  stretching mode of the C-terminal amide group of the rearranged imine-amide structure. The intense band centered at 3430  $\text{cm}^{-1}$  corresponds to the symmetric terminal amine NH stretch, and two amide NH stretches of the rearranged protonated imine amide structure. The last observed band at 3330  $\text{cm}^{-1}$  corresponds to the asymmetric NH stretch of the protonated amine and to an amide NH stretch, respectively.

Vibrational Mode	I structure ( $\text{cm}^{-1}$ )	M structure ( $\text{cm}^{-1}$ )	Exp ( $\text{cm}^{-1}$ )
$\text{NH}_2$ as st		3545	3540
Amine ter NH st		3458	
Amide NH st	3451		3430
Amide NH st	3446		
Amide NH st		3432	
Amide NH st	3340		
$\text{NH}_2$ as st	3320		3330
Amide NH st		3421	

Table 2-4 : Band assignment for the  $a_4$  ion of protonated GGGGG. The band assignment is indicated in the first column. The infrared frequencies in the second and third columns correspond to the calculated harmonic frequencies of the **I** and **M** structures. The experimental infrared frequencies are given in the third column.

## 2.5 Conclusions.

This gas phase infrared spectroscopic study further confirms that  $a_n$  ions present a large structural variety. Spectroscopic investigation in the NH stretching region presented here is fully consistent with the conclusions based on the IR “fingerprint” region. In the case of oligoglycine peptides, under our experimental conditions, it unambiguously shows that  $a_2$  and  $a_3$  ions have a 5- and a 7-membered ring structure, respectively. In the case of the  $a_4$  ions, spectroscopy in the NH stretching region allows for a clear-cut conclusion regarding the formation of a rearranged imine-amide structure. A band observed near  $3550\text{ cm}^{-1}$  is a clear signature of the C-terminal amide formed upon the permutation of primary sequence.

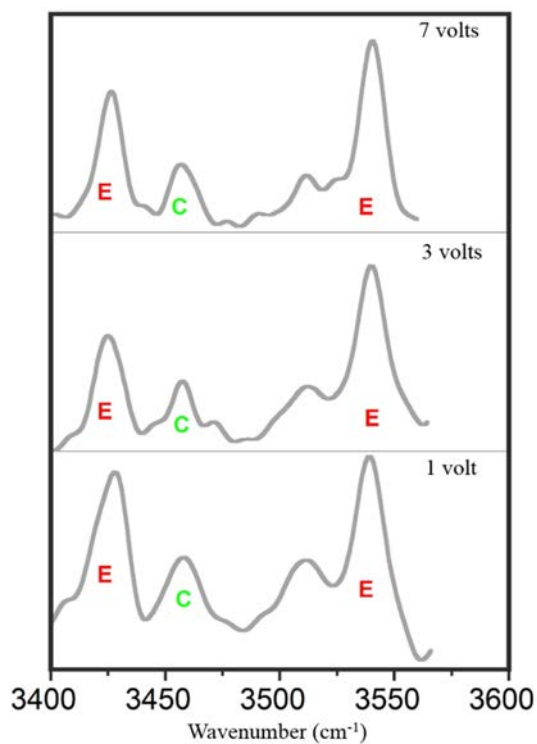
Infrared spectroscopy is also used to better characterize the dynamics of the formation of this rearranged imine-amide structure in the case of the YG  $a_2$  ion. Using two couples of infrared signatures of the co-existing 5-membered ring and rearranged structures (**C** and **E** in the text), the evolution of the isomer population can be monitored. It is shown in particular that increasing the time period for collisional activation up to 3 seconds leads to a complete isomerization into the rearranged imine-amide structure.

It is also shown in this chapter that similar IR spectra of the same ion can be recorded using a QIT and a hybrid FT-ICR provided that ions are collisionally cooled prior to the interrogation with the IR laser. In a context of increasing use of IR spectroscopy for characterizing isomer population, this result raises the question of a better definition of the experimental conditions associated with the collisional thermalization and also of the collisional activation conditions used to generate the ions.

## 2.6 Annexes.

GGG, GGGG, and GGGGG were dissolved in MeOH:H<sub>2</sub>O = 30:70 with 2% of acetic acid with a final concentration of 50  $\mu\text{mol L}^{-1}$ . They were sprayed with conventional ESI conditions into the FT-ICR mass spectrometer. The precursor  $b_n$  ions ( $n=2, 3, \text{ and } 4$ ) were mass-selected in the quadrupole and fragmented by multiple low energy collisions with a bath gas of Ar in the linear hexapole. The Ar pressure in the linear hexapole was  $\sim 10^{-3}$  mbar. Fragment ions were then pulse-driven into the ICR cell. Then, the corresponding  $a_n$  ions ( $n=2, 3, \text{ and } 4$ ) were mass-selected and subjected to the infrared light. As discussed in chapter 1, two infrared lasers were combined: OPO/OPA tabletop laser and a cw CO<sub>2</sub> laser. Depending on the system, the irradiation time were:

- $a_2$  ion from protonated GGG: 1 second of irradiation time with 40 ms of CO<sub>2</sub> laser.
- $a_2$  ion from protonated YGGFL: 1 second of irradiation time with 15 ms of CO<sub>2</sub> laser.
- $a_3$  ion from protonated GGGG: 1 second of irradiation time with 10 ms of CO<sub>2</sub> laser.
- $a_4$  ion from protonated GGGGG: 1 second of irradiation time with 8 ms of CO<sub>2</sub> laser.



Annex 2-1 : Infrared spectra of the  $a_2$  fragment ion of protonated YGGFL in the 3400-3600  $\text{cm}^{-1}$  spectral range using the FT-ICR. The infrared spectra were recording after fragmentation of the precursor  $b_2$  ion at different collision activation energies: a) 7 v, b) 3 v, c) 1 v. Bands labelled C and E can be assigned to the 5-membered ring (C) and rearranged protonated imine-amide isomers (E) respectively.

## 2.7 Bibliography

- (1) Hunt, D. F.; Yates, J. R.; Shabanowitz, J.; Winston, S.; Hauer, C. R. *Proceedings of the National Academy of Sciences of the United States of America* **1986**, *83*, 6233.
- (2) Biemann, K. *Biomedical and Environmental Mass Spectrometry* **1988**, *16*, 99.
- (3) Karas, M.; Hillenkamp, F. *Anal. Chem.* **1988**, *60*, 2299.
- (4) Fenn, J. B.; Mann, M.; Meng, C. K.; Wong, S. F.; Whitehouse, C. M. *Science* **1989**, *246*, 64.
- (5) Roepstorff, P.; Fohlman, J. *Biomedical Mass Spectrometry* **1984**, *11*, 601.
- (6) Nesvizhskii, A. I.; Vitek, O.; Aebersold, R. *Nature Methods* **2007**, *4*, 787.
- (7) Vachet, R. W.; Ray, K. L.; Glish, G. L. *J. Am. Soc. Mass. Spectrom.* **1998**, *9*, 341.
- (8) Yalcin, T.; Csizmadia, I. G.; Peterson, M. R.; Harrison, A. G. *J. Am. Soc. Mass. Spectrom.* **1996**, *7*, 233.
- (9) Bleiholder, C.; Osburn, S.; Williams, T. D.; Suhai, S.; Van Stipdonk, M.; Harrison, A. G.; Paizs, B. *J. Am. Chem. Soc.* **2008**, *130*, 17774.
- (10) Harrison, A. G.; Young, A. B.; Bleiholder, C.; Suhai, S.; Paizs, B. *J. Am. Chem. Soc.* **2006**, *128*, 10364.
- (11) Paizs, B.; Suhai, S. *Mass Spectrom. Rev.* **2005**, *24*, 508.
- (12) Paizs, B.; Szlavik, Z.; Lendvay, G.; Vekey, K.; Suhai, S. *Rapid Commun. Mass Spectrom.* **2000**, *14*, 746.
- (13) Yalcin, T.; Khouw, C.; Csizmadia, I. G.; Peterson, M. R.; Harrison, A. G. *J. Am. Soc. Mass. Spectrom.* **1995**, *6*, 1165.
- (14) Johnson, R. S.; Martin, S. A.; Biemann, K. *Int. J. Mass Spectrom. Ion Processes* **1988**, *86*, 137.
- (15) Verkerk, U. H.; Siu, C.-K.; Steill, J. D.; El Aribi, H.; Zhao, J.; Rodriquez, C. F.; Oomens, J.; Hopkinson, A. C.; Siu, K. W. M. *Journal of Physical Chemistry Letters* **2010**, *1*, 868.
- (16) Bythell, B. J.; Maitre, P.; Paizs, B. *J. Am. Chem. Soc.* **2010**, *132*, 14766.
- (17) El Aribi, H.; Rodriquez, C. F.; Almeida, D. R. P.; Ling, Y.; Mak, W. W. N.; Hopkinson, A. C.; Siu, K. W. M. *J. Am. Chem. Soc.* **2003**, *125*, 9229.
- (18) Yoon, S. H.; Chamot-Rooke, J.; Perkins, B. R.; Hilderbrand, A. E.; Poutsma, J. C.; Wysocki, V. H. *J. Am. Chem. Soc.* **2008**, *130*, 17644.
- (19) Oomens, J.; Young, S.; Molesworth, S.; van Stipdonk, M. *J. Am. Soc. Mass. Spectrom.* **2009**, *20*, 334.
- (20) Bythell, B. J.; Erlekam, U.; Paizs, B.; Maitre, P. *ChemPhysChem* **2009**, *10*, 883.
- (21) Chen, X.; Tirado, M.; Steill, J. D.; Oomens, J.; Polfer, N. C. *J. Mass Spectrom.* **2011**, *46*, 1011.
- (22) Bythell, B. J.; Hernandez, O.; Steinmetz, V.; Paizs, B.; Maitre, P. *Int. J. Mass spectrom.* **2012**, *316*, 227.
- (23) Verkerk, U. H.; Zhao, J. F.; Lau, J. K. C.; Lam, T. W.; Hao, Q.; Steill, J. D.; Siu, C. K.; Oomens, J.; Hopkinson, A. C.; Siu, K. W. M. *Int. J. Mass spectrom.* **2012**, *330*, 254.
- (24) Bohme, D. K. *Int. J. Mass Spectrom. Ion Processes* **1992**, *115*, 95.
- (25) Rodriguez-Santiago, L.; Sodupe, M.; Oliva, A.; Bertran, J. *J. Phys. Chem. A* **2000**, *104*, 1256.
- (26) Mac Aleese, L.; Simon, A.; McMahon, T. B.; Ortega, J. M.; Scuderi, D.; Lemaire, J.; Maitre, P. *Int. J. Mass spectrom.* **2006**, *249*, 14.
- (27) Prell, J. S.; Chang, T. M.; Biles, J. A.; Berden, G.; Oomens, J.; Williams, E. R. *J. Phys. Chem. A* **2011**, *115*, 2745.
- (28) Prell, J. S.; Chang, T. M.; O'Brien, J. T.; Williams, E. R. *J. Am. Chem. Soc.* **2010**, *132*, 7811.
- (29) Vachet, R. W.; Bishop, B. M.; Erickson, B. W.; Glish, G. L. *J. Am. Chem. Soc.* **1997**, *119*, 5481.
- (30) Wassermann, T. N.; Boyarkin, O. V.; Paizs, B.; Rizzo, T. R. *J. Am. Soc. Mass. Spectrom.* **2012**, *23*, 1029.
- (31) Bythell, B. J.; Hernandez, O.; Steinmetz, V.; Paizs, B.; Maitre, P. *Int. J. Mass Spectrom.* **2012**, *316*, 227.





### 3 MIDDLE SIZE $b_n$ IONS: ION-MOLECULE REACTION AS A DIRECT EVIDENCE OF MACROCYCLE FORMATION.

3	MIDDLE SIZE $b_n$ IONS: ION-MOLECULE REACTION AS A DIRECT EVIDENCE OF MACROCYCLE FORMATION. ....	79
3.1	Introduction.....	81
3.2	Methods .....	88
3.3	Intra-peptide hydrogen bond interactions.....	91
3.4	Results and discussion.....	92
3.5	Conclusions.....	114
3.6	Annexes .....	115
3.7	Bibliography.....	119

### 3.1 Introduction

As introduced in chapter 2 ( $a_n$  ions), peptide sequence can be derived from mass spectrometry [1,2]. In the most common MS/MS experiments, protonated protein or peptides are activated by multiple low energy collisions to induce the dissociation (CID) process [2,3]. The resulting fragment peaks are used to deduce the peptide sequence via bioinformatic tools [4]. In some cases, however, carbonyl and amide groups contained in peptides can undergo nucleophilic attack modifying the amino acid sequence. Thus, the resulting fragmentation spectrum can lead to a false positive identification [5]. A large variety of peptide fragments are currently known [6,7] but the structure and reactivity of  $b_n$  ions have received significant attention. This fragment ions are obtained from the fragmentation of the peptide backbone upon multiple low energy collisions. Figure 3-1 illustrates the peptide bond fragmentation. Depending on the protonation site, either  $b_n$  or  $y_n$  ions are formed [3].

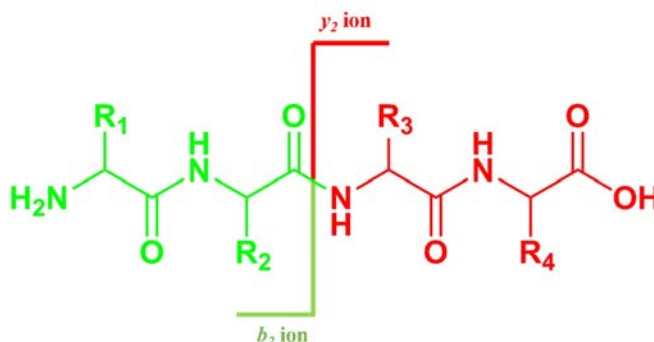


Figure 3-1 : General formula of a tetrapeptide. Activation by multiple low energy collisions can lead to the fragmentation of the peptide bonds forming the  $b_2$  (green line) and  $y_2$  (red line) ions.

Identification of the resulting peaks is one of the most common problems. Only about 10% of the available information in a mass spectrum is duly exploited. Moreover, fragment ions are formed as a result of different fragmentation pathways which lead to different ion intensities. The relative intensities are often underestimated. A better understanding of peptide fragmentation mechanism can provide answers to these important questions.

Understanding the reaction pathways associated with the formation and rearrangement chemistry of the fragment  $b_n$  ions has been the subject of numerous studies. In the case of the small size  $b_n$  ions, two types of structures have been proposed. An acylium  $b_n$  structure would be formed following

the cleavage of the C(O)-N<sup>+</sup>H<sub>2</sub> bond, but it has been early realized that this bond cleavage is followed by or concerted with a nucleophilic addition on the strongly electrophilic acylium CO<sup>+</sup> group. As shown in Figure 3-2, two nucleophilic groups can be considered for a *b*<sub>2</sub> ion. The addition of the carbonyl oxygen (route 1) leads to the formation of a 5-membered ring, known as oxazolone [8-11], protonated on the ring nitrogen. Proton transfer may occur from the ring to the N terminal amino group. The formation of the oxazolone structure for *b*<sub>2</sub> ions is supported by several studies combining quantum chemical calculations and IRMPD spectroscopy [12-16]. A second type of structure resulting from the nucleophilic attack of the N-terminal amino group on the CO<sup>+</sup> group has been envisaged (route 2 on Figure 3-2). It leads to a 6-membered ring structure known as diketopiperazine [17,18].

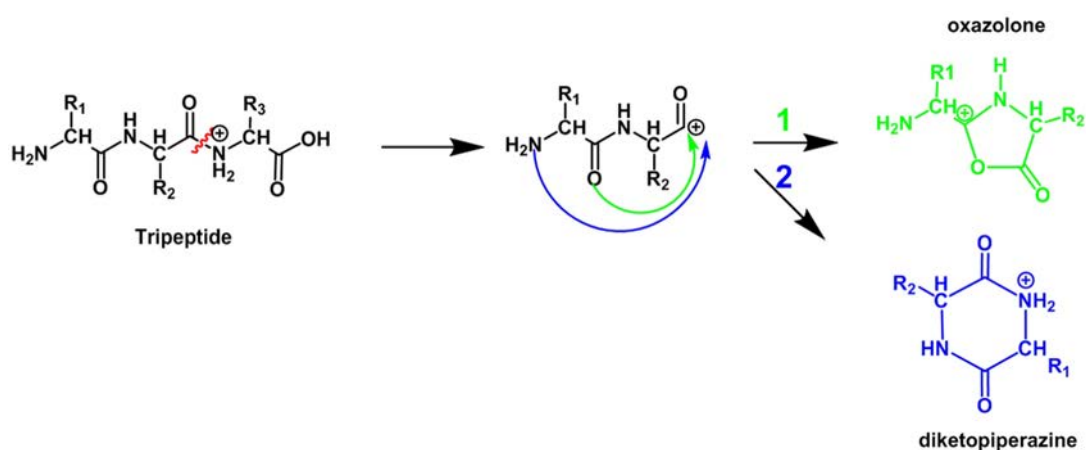


Figure 3-2: Fragmentation of protonated tripeptide induced by multiple low energy collisions. Starting from the hypothetical (unstable) acylium structure of the *b*<sub>2</sub> ion, two alternative structures can be formed: an oxazolone structure (green structure) or a diketopiperazine through a head-to-tail nucleophilic attack (blue structure).

There is no doubt that IRMPD spectroscopy is a suitable technique for structural characterization. If the 800-2000 cm<sup>-1</sup> is considered, it provides direct information on the functional groups of the gas phase molecular ion. The success of IRMPD spectroscopy in the case of the *b*<sub>n</sub> ion is due to the fact that the oxazolone isomer has a clear diagnostic IR feature. This is illustrated in Figure 3-3 where the theoretical IR absorption spectra of oxazolone and diketopiperazine of the *b*<sub>2</sub> ion formed by glycine residues are given. As can be observed in this Figure, an IR signature of oxazolone structures is predicted in the 1800-2000 cm<sup>-1</sup> energy range, which corresponds to the carbonyl stretching mode of

the 5-membered ring structure. The observation of a band in this spectral range is an unambiguous signature of the oxazolone. Diketopiperazine structure of  $b_2$  ions can also be easily detected by IRMPD spectroscopy since two closely-spaced IR features are predicted in the 1600-1800  $\text{cm}^{-1}$  range. It has been shown in particular that diketopiperazine structure of  $b_2$  ions can be formed depending on peptide length and identity of terminal residue in the departing fragment [19,20].

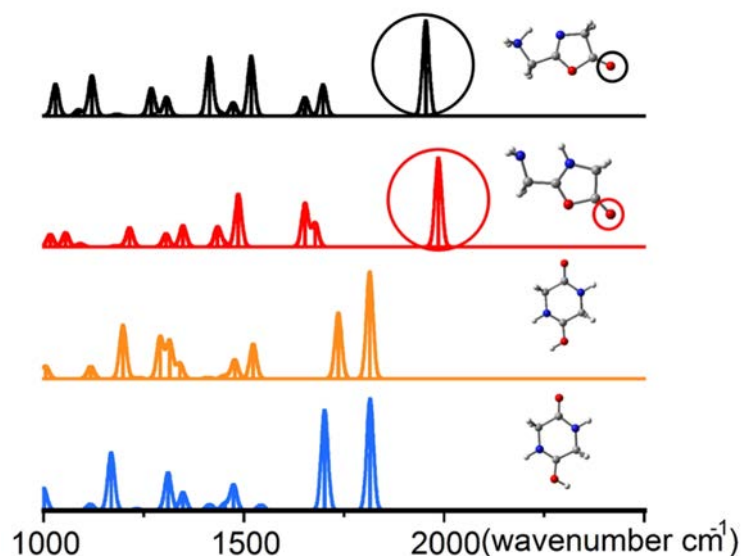


Figure 3-3: Predicted harmonic IR spectra of two diketopiperazine and two oxazolone structures corresponding to the  $b_2$  ion of protonated GGG peptide. The highlighted IR bands correspond to the IR signature of the C=O stretching mode of oxazolone structures.

Simultaneous formation of diketopiperazine and oxazolone for some small fragment  $b_n$  ions [11,12,14,20-22] has been evidenced. Overall, it has been shown that for peptides containing basic residues or composed by proline,  $b_2$  ions with diketopiperazine structure or a mixture of diketopiperazine and oxazolone structures can be formed. It is important to note that theoretical calculations show that diketopiperazine structure is more energetically stable than oxazolone structure [22]. If the kinetics is considered, however, the formation of diketopiperazine requires a trans-cis isomerization of the first amide bond upon the cycle formation, and this step is the rate limiting step. The associated kinetic barrier may thus prevent the formation of the diketopiperazine structure under low energy multiple collisions induced dissociation (CID) [23,24]. It seems, however, that basic side chains can facilitate the trans-cis isomerization thus allowing the diketopiperazine formation [22].

If larger  $b$  ions are considered, the rearrangement chemistry is more complex. This can be simply understood by considering the increasing number of nucleophilic site which can attack the acylium  $\text{CO}^+$  site. There is in particular increasing evidence for the formation of macrocyclic structures for large  $b$  ions. This was first evidenced by tandem mass spectrometry. Boyd and coworkers [25,26] demonstrated using tandem mass spectrometry that  $b$  ions generated from Lysine-containing peptides often eliminates internal amino acid residues. Several experimental studies suggested that internal loss can be observed as a consequence of the head-to-tail nucleophilic attack from the N-terminal amino group to the C-terminal carbonyl group [27,28]. The formation of macrocyclic structure was first suggested by Harrison *et al.* [29] based on the comparison of the CID mass spectra of protonated cyclic-YAGFL and a series of C-ter amidated pentapeptides with a permuted sequence (YAGFL-NH<sub>2</sub>, AGFLY-NH<sub>2</sub>, GFLYA-NH<sub>2</sub>, FLYAG-NH<sub>2</sub>, LYAGF-NH<sub>2</sub>). It was found that all the linear and the cyclic protonated pentapeptides have very similar breakdown graphs.

These results lead to the hypothesis of the formation of a cyclic-YAGFL pentapeptide (Figure 3-4) upon collisional activation of protonated linear peptides. This so-called macrocycle would be formed as a result of a head-to-tail nucleophilic attack of the N-terminal amino group on the oxazolone CO group. Assuming that the proton can migrate from one amide nitrogen to another, the macrocyclic structure could reopen at a different amide bond, leading to the formation of a new oxazolone structure. Then, assuming a regular sequential loss on the C terminal side, elimination of internal residues could be conceived.

Infrared “action” spectroscopy and theory calculations were used to characterize large  $b$  ion structures [15,31-33]. The structure of the  $b_4$  ion of Leu-enkephalin, for example, was studied by Polfer and coworkers [32]. It was suggested that a mixture of macrocyclic and linear oxazolone structures was formed. Nevertheless, the IR spectrum was extremely congested in the CO stretching range of interest. An interesting aspect of this study was to discuss the influence of the time scale of the experiment on the  $b_4$  ion IR spectrum. The time delay before the irradiation in the ICR cell was varied and some changes were observed in the infrared spectrum. By extending this delay, a depletion of the band at 1930  $\text{cm}^{-1}$  corresponding to the N-ring protonated oxazolone structure and simultaneous enhancement of the band

at 1780  $\text{cm}^{-1}$  related with the N-terminal protonated oxazolone were observed. It was proposed that this result gives qualitative insights into the proton mobility along the fragment ion structure which is extremely important in the peptide fragmentation pathways [34]. Another interesting aspect of this work was to compare the IR spectra of  $b_2$ ,  $b_3$  and  $b_4$  ions from Leu-enkephalin formed under similar experimental conditions [32]. In the case of the  $b_2$  and  $b_3$  ions, an IR feature in the 1800-2000  $\text{cm}^{-1}$  energy range is observed, thus showing that these smaller size  $b_n$  ions have an oxazolone structure.

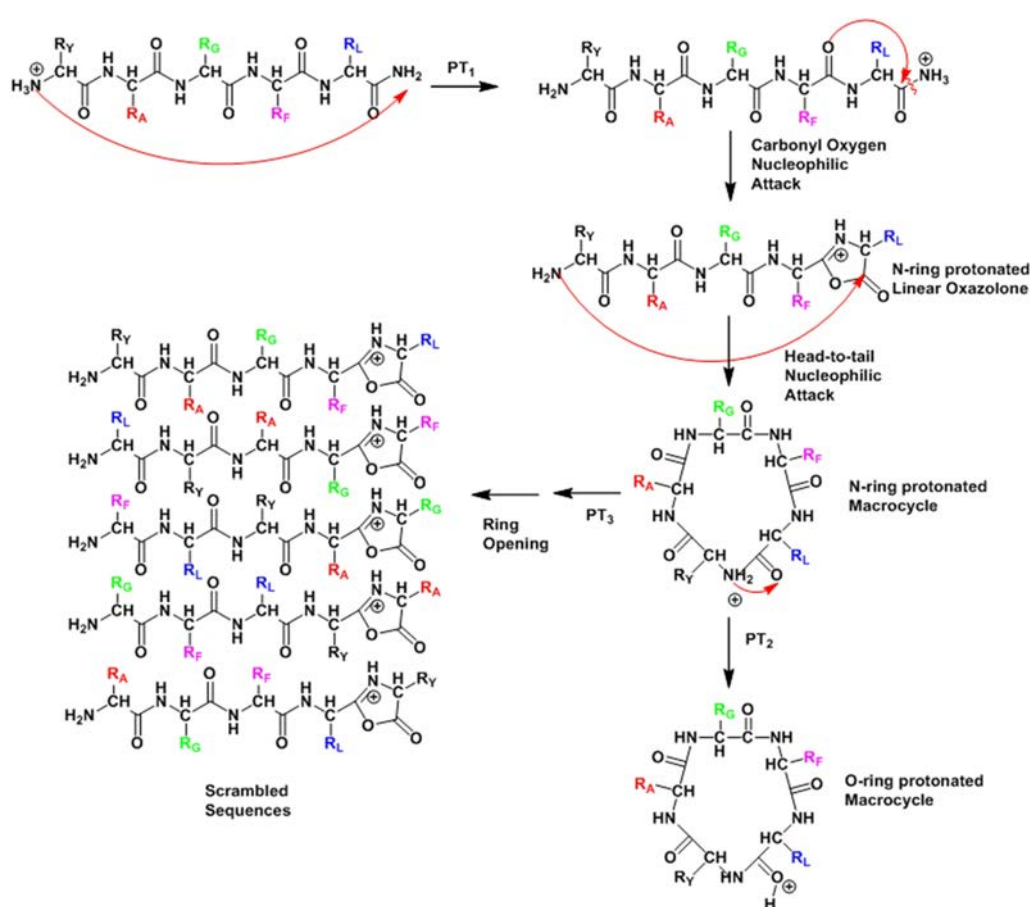


Figure 3-4: Rearrangement mechanism derived from Harrison and coworkers[30]. After formation of a linear oxazolone structure, a head-to-tail nucleophilic attack could occur leading to a macrocyclic structure. Following proton transfer from one amide N to another, the macrocyclic structure can reopen at different places giving rise to linear oxazolone structures with permuted sequence.

It was particularly important to show that the formation of a macrocyclic structure for  $b_n$  ions, and thus potentially peptide scrambling, could occur for tryptic peptides, *i.e.* peptides generated using

tryptic enzyme. Several  $b_n$  ions derived from such peptides have been studied, and in particular the  $b_5$  ion of protonated GGGGGR peptide [35]. In this case it was concluded that only the O-protonated macrocyclic structure was formed. This structure was shown to be the lowest energy structure at the B3LYP/6-31+G(d,p) level of theory. Macrocyclic structures protonated on an amide N atom were found to be  $\sim 13$  kcal/mol higher in energy. The transition state associated with the oxazolone to macrocycle interconversion was found to lie  $\sim 25$  kcal/mol higher in energy. The oxazolone structure protonated on the N-terminal amino group (ring N) was found to lie  $\sim 12$  ( $\sim 9$ ) kcal/mol higher in energy than the O-protonated macrocyclic structure. It should be stressed that the structural identification was based on a very good agreement between the shape of the experimental and predicted spectra for the macrocyclic structure.

However, no clear-cut signature of the macrocyclic structure, could be observed in the 800-2000  $\text{cm}^{-1}$ . It was earlier proposed that a band centered at 1430  $\text{cm}^{-1}$  which corresponds to the  $\text{CO-H}^+$  stretching mode [15] could be an IR signature of the macrocyclic structure. Nevertheless, this spectral region is very congested in the case of peptide fragments, and it was later shown that no diagnostic could be derived from signal in this region.

In this context, the NH stretching region of  $b_n$  ions was explored [36-42] since it may also provide IR signatures of specific structural motifs, especially those associated with hydrogen-bonding. In addition, IR spectra in this spectral range provide clear information on the protonation site, as shown for the smaller  $b_2$  ions [36,40]. A comparative study of the IR spectra in the NH stretching regions of the  $b_4$  ions of oligoglycine, oligoalanine, and YGGFL was performed [42]. The two first systems have very similar spectra in this spectral range, and their spectra recorded in the 800-2000  $\text{cm}^{-1}$  clearly suggest that these two  $b_4$  ions have an oxazolone structure. Their spectra in the NH stretching region can be assigned using the calculated spectra of oxazolone structure [42].

The spectrum of the  $b_4$  ion of protonated YGGFL, on the other hand, is different from the two others. It is in particular characterized by a band observed near 3238  $\text{cm}^{-1}$  [42]. Similar band positions have also been reported for one of the four isomers of the  $b_4$  of YGGFL studied using double resonance

IR/UV technique in a cold ion trap [38]. As a result, the room temperature IR spectrum of the  $b_4$  of YGGFL ion could also be assigned to a linear N-terminal amide-protonated oxazolone structure (structure (a) in Figure 3-5). However, an alternative assignment could also be proposed because the corresponding IR spectrum nicely matches with the predicted IR absorption spectrum of a macrocyclic structure (structure (b) in Figure 3-5).

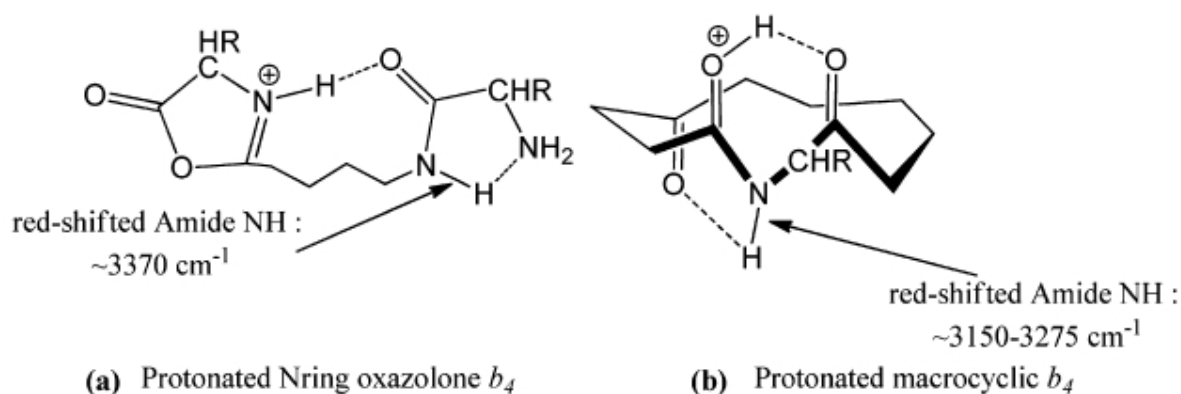


Figure 3-5: Hydrogen bonding motifs found for the lowest energy structures of a) Protonated N ring oxazolone Isomer and b) protonated Macrocyclic Isomer of  $b_4$  fragment ion [42].

An alternative to IR spectroscopy for identifying macrocyclic  $b_n$  structures has been proposed by Somogyi, Harrison and Paizs. They showed that middle size  $b_n$  fragment ions undergo selective complex formation through their gas phase reaction with ammonia molecule [43]. Their first intention was to probe the kinetics of the hydrogen to deuterium exchange (HDX) reactions with a variety of peptide fragment ions. The protonated AAAAAAAYA peptide was considered, for example, and all the peptide fragments formed in the hexapole collision cell of a hybrid FT-ICR instrument were injected into the ICR cell and allowed to react with  $\text{ND}_3$ .

In the course of these experiments, it was realized that in the case of the middle size  $b_n$  ions ( $n=5-10$ ), in addition to the various HDX products, ammonia adducts were also formed. The formation of these ion- $\text{ND}_3$  adducts seems to be specific of the middle size  $b_n$  ions. One could conceive that it is a size effect since only HDX were observed for smaller size  $b_n$  ions. But it is not the case since other middle size peptide fragments such as  $y$ ,  $a$ ,  $a^*$ ,  $y^0$ , and  $b^0$  ions do not form stable ammonia complexes.

Since no internal residue loss is observed for N-terminal acetylated peptide, the same experiment was carried out with such peptide and no stable complex with ND<sub>3</sub> was observed. These results further support the hypothesis of the formation of macrocyclic structure for the middle sized  $b_n$  ions. And it was concluded that the formation of a stable complex with ND<sub>3</sub> is an isomer specific reaction with macrocyclic isomer.

In this chapter, we present our results on middle size  $b_n$  ions ( $n=6-9$ ) of protonated polyalanine. Our aim was to characterize the structure of the complex formed between  $b_n$  ion and the ammonium molecule. IR spectra of these complexes were recorded, and compared to the IR absorption spectra calculated for the lowest energy structure for each complex size. As expected, the structures correspond to an NH<sub>4</sub><sup>+</sup> ammonium molecule interacting with a neutral cyclic peptide. This means that a proton transfer occurs from the  $b_n$  ion to the ammonia molecule. The resulting NH<sub>4</sub><sup>+</sup> ammonium group is bound through hydrogen bonds with amide CO groups. The bare  $b_n$  ions were also investigated using a combination of infrared spectroscopy and theoretical calculations. In these cases, a satisfactory agreement between experimental and theoretical spectra could be found in the NH stretching region. In the case of the  $b_6$  ion [41], the optimized structure clearly shows that the proton is shared by two CO groups, and this structure can thus be called a Zundel type structure. Besides the middle size  $b_n$  ions ( $n=6-9$ ) of protonated polyalanine, the protonated cyclic-YAGFL system, which is a model of a macrocyclic  $b_5$  ion, was also studied.

## 3.2 Methods

All the experiments were carried out with our hybrid FT-ICR tandem mass spectrometer. IR spectroscopy was performed in both the 1000-2000 and 3200-3800 cm<sup>-1</sup> wavenumber regions using the CLIO Free Electron Laser and the OPO/OPA laser, respectively. In the latter case, the CO<sub>2</sub> auxiliary laser was used for enhancing the photofragmentation efficiency.

The series of middle size  $b_6$ ,  $b_7$ ,  $b_8$ , and  $b_9$  ions were obtained from fragmentation of protonated AAAAAAMA, AAAAAAAYA, AAAAAAAAYA, and AAAAAAAAAYA, respectively. Two methods could be used for fragmenting the ions and then forming the ammonia complexes with

ammonia. After mass-selection of the protonated peptide in the quadrupole, fragmentation could be achieved in the hexapole ion trap, and the fragments could then be pulse driven into the ICR cell where ion-molecule reactions were performed under a constant pressure of  $\text{NH}_3$ . The  $b_n$ - $\text{NH}_3$  adducts of interest were then mass-selected in the ICR cell before irradiation with the tunable laser. The associated duty cycle is relatively long, due to the reaction time associated with the ion-molecule reaction in the low pressure region of the ICR cell.

The alternative for fragmenting the ions and then forming the ammonia complexes with ammonia is to fragment the ion in the source region and then perform the ion-molecule reaction in the hexapole ion trap. The  $b_n$  ions of interest formed in the source region can be selectively isolated in the quadrupole and then allowed to react in the hexapole with  $\text{NH}_3$  seeded in the Argon line. The ion-molecule reaction efficiency is significantly higher than in the low pressure region of the ICR cell. Ions are then pulse-extracted into the ICR cell where the  $b_n$ - $\text{NH}_3^+$  adducts of interest are mass-selected before the irradiation with the tunable laser.

Ion fragmentation can occur even under soft ionization conditions. Since the first investigation on the electrospray ionization process [44,45], significant improvements have been proposed [46,47] for guiding the ions from the exit of the capillary to the low pressure region of the mass spectrometer. In the case of the Appolo source mounted on the FT-ICR instrument, ions pass through two ion funnels before reaching the hexapole guide. The typical DC voltages applied in the source region are displayed in Figure 3-6. The optimization of these source DC parameters is case dependent, and it is in particular a trade-off between an enhancement of ion transmission and minimization of fragmentation. Indeed, in the high pressure source region, ions experience multiple collisions with the gas molecules.

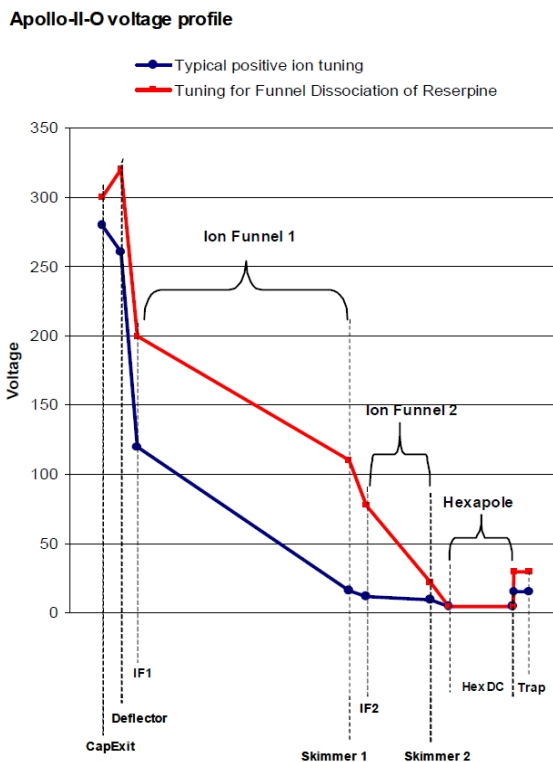


Figure 3-6: Voltage settings corresponding to the electrospray APPOLO source of the FT-ICR mass spectrometer. Typical ion source voltages are represented in blue color. The suitable voltages to perform fragmentation of molecular ions are shown in red color.

In the present case, protonated AAAAAAMA, AAAAAAYA, AAAAAAYA, and AAAAAAYA are stable enough so that in-source fragmentation can be easily avoided. The corresponding  $b_6$ ,  $b_7$ ,  $b_8$ , and  $b_9$  ions can be easily obtained by raising the skimmer 1 potential, which has the net effect of accelerating the ions between the two funnels. Typical mass spectra obtained under the two source voltage conditions are given in Figure 3-7 for the AAAAAAMA system. Under “soft source voltage” conditions, only the  $MH^+$  ion is observed while significant fragmentation can be observed by increasing the skimmer 1 DC voltage.

The drawbacks of the in-source fragmentation have been critically discussed in the previous chapter. Water and methanol solvent molecules, present at high pressure in the source region, may catalyze proton transfers [48] which can be involved in rate limiting steps of the fragmentation process leading to the  $b_n$  ions. Performing the ion-molecule reactions under the low pressure conditions of the ICR cell or in the higher pressure ( $\sim 10^{-3}$  mbar) region of the hexapole ion trap may also be lead to

different adduct structures. These two issues are discussed in the next sections in the case of the formation of the  $b_6$  ion and in the case of the formation of the complexes between a model cyclic YAGFL peptide and ammonia, respectively.

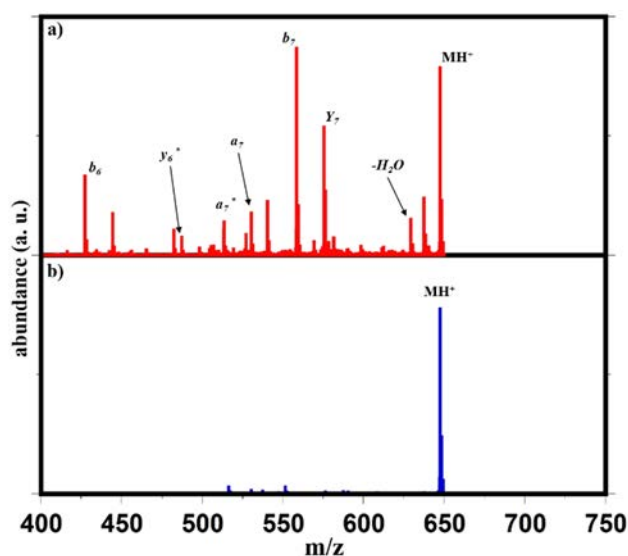


Figure 3-7: Mass spectra of electrosprayed  $A_6MA$  peptide. The mass spectrum recorded with "source fragmentation" voltage settings (a) is compared to that using "soft source voltage" conditions (b).

### 3.3 Intra-peptide hydrogen bond interactions.

Hydrogen bonding is the key factor that determines the secondary structure of peptide and proteins [49-53]. Side chains may also be involved, but we will focus here on the interactions between the backbone functional groups. Hydrogen bonding occurs between the amide NH donor and an amide CO acceptor [50]. As a result, as illustrated in Figure 3-8, hydrogen bonded cycles are formed, and the different types of hydrogen bonds are named  $C_n$ , where  $n$  is the number of atoms involved in the corresponding cycle [54].

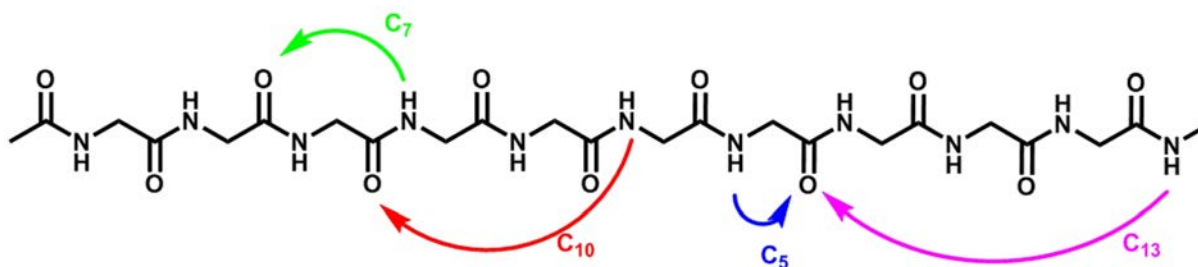


Figure 3-8: Different types of hydrogen bonding motifs giving rise to the formation of hydrogen bonded cycles containing 5, 7, 10 and 13 atoms, and called C<sub>5</sub>, C<sub>7</sub>, C<sub>10</sub>, and C<sub>13</sub>, respectively.

Both theoretical and experimental data pinpointed these HB interactions as the key for the stabilization of secondary protein structure. In particular,  $\gamma$ -turn structures are stabilized by C<sub>7</sub> HB interactions [51-53]. On the other hand, only the C<sub>10</sub> hydrogen bond intramolecular interactions can take place in the  $\beta$ -turns structure [49-53]. The amide II absorption frequency is very sensitive to the chemical environment providing a direct picture of intramolecular interactions involving the NH groups. Previous IR spectroscopic studies on short capped peptides have also established the dependence of the amide stretching frequency on the hydrogen bond interactions [55-57]. In particular, it was observed that C<sub>7</sub> hydrogen bond interactions induce the largest red-shift in the amide NH stretching frequency (75-175 cm<sup>-1</sup>). The C<sub>7</sub> hydrogen bonds were thus found to be associated to the strongest intramolecular interactions. The hydrogen bond strength was found to decrease from C<sub>7</sub>, C<sub>10</sub>, C<sub>5</sub> to NH- $\pi$  interactions.

### 3.4 Results and discussion.

#### 3.4.1 IRMPD of $b_6$ ion: Zundel-type H-bonding.

The bare structure of the  $b_6$  ion of protonated A<sub>6</sub>MA was investigated by IR spectroscopy and theory calculations. More precisely, the B3LYP calculations and molecular dynamics simulations (AMBER [58]) were used to determine the energetically most favored structures. These calculations were performed by B. Paizs resulting in two equienergetic and equivalent structures (Figure 3-9) of macro-cyclic  $b_6$  which can be transformed into each other by a 180° rotation. These structures feature a strong ionic HB between amide oxygens of the Ala1 and Ala4 residues forming a HB-bridge between the two oxygen atoms. These structures feature typical Eigen-type HB, *e.g.* the ionizing proton is

attached to one of the bridge oxygens. This asymmetric arrangement is characterized by a short OH bond (1.107 Å) and a long HB (1.305 Å). As can be seen in Figure 3-9, these two macrocycle structures are also stabilized by two  $C_{10}$  and two  $C_7$  hydrogen bond interactions [54].

In order to further investigate the potential energy surface, the transition structure for the proton transfer between the two calculated structures (Figure 3-9a and 3-9b) was also characterized. The calculations indicate that the ionizing proton in the TS is equally shared by the two bridging amide oxygens in a Zundel-type-H-bonding which is given in Figure 3-9. The TS has a  $C_2$  symmetry. After zero-point energy correction, this TS is more energetically favored than the two equienergetic structures shown in Figure 3-9a and 3-9b (-4.18 kJ mol<sup>-1</sup>). It can thus be concluded that the PES along the PT is flat and that the ionizing proton explores a relatively shallow single-well potential characteristic of Zundel-type H-bonding.

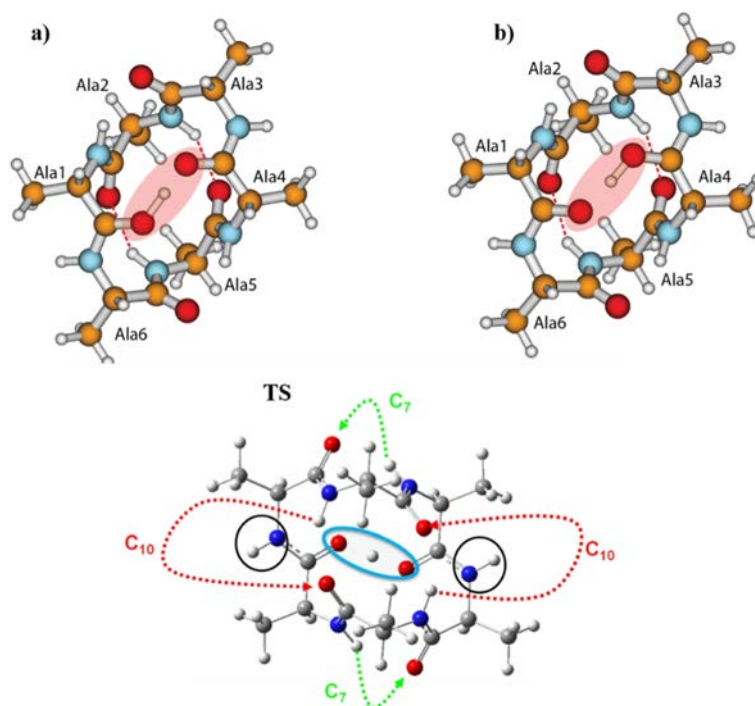


Figure 3-9: Computed structures for the all-Ala  $b_6$  ion. The ionic H-bond and the shared proton are indicated by a pink background. The four hydrogen bond interactions are indicated by dotted arrows ( $C_{10}$  in red and  $C_7$  in green) in the TS picture.

In this context Born-Oppenheimer molecular dynamics (BOMD) simulations were carried out by B. Paizs in order to follow the dynamical behavior of the ionizing proton between the two bridging

oxygens. Figure 3-10 displays interatomic distances between the ionizing proton and the two bridging oxygens and between the bridging oxygens for one of the trajectories initiated from the structure of the  $b_6$  ion given in Figure 3-9a. The ionizing proton explores the vicinity of both oxygens with numerous swaps between the pillar oxygen atoms thus corroborating the hypothesis of the Zundel-type H-bond.

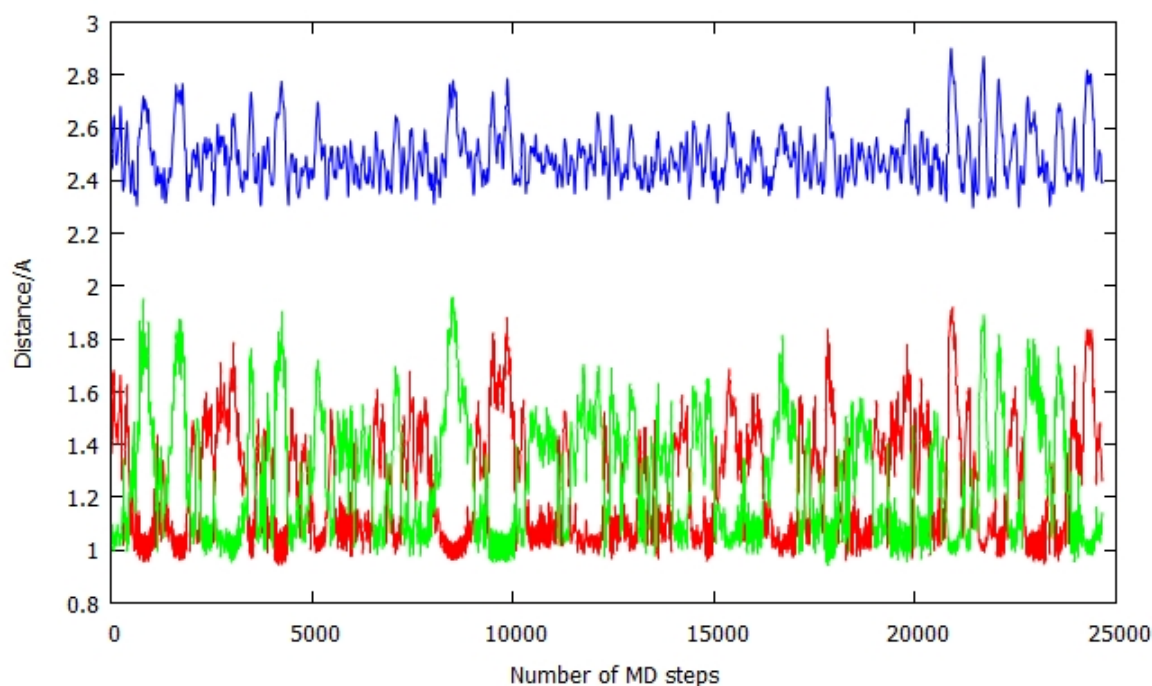


Figure 3-10: Time evolution of the  $H(O(Ala_1)...H$  (green)-- $O(Ala_4)...H$  (red) and  $O(Ala_1)...O(Ala_4)$  (blue) interatomic distances (in Å) during a BOMD trajectory initiated with structure given in Figure 3-9a plotted as a function of time i.e. the number of steps during the MD simulation.

An infrared spectrum of the  $b_6$  ion could be derived from BOMD trajectories. The IR absorption spectrum was calculated by Fourier-transforming the time autocorrelation function of the first time derivative of the dipole moment, thus taking into account the anharmonic effects associated with the large-amplitude motion of the proton. Similar approaches have been used for calculating IR absorption spectra of molecular ions based on dynamical calculations [59,60].

The IR spectra of the  $b_6$  ions are given in Figure 3-11. As can be seen in this Figure, as far as the NH stretching range is concerned, the shape of the experimental spectrum (a) is well reproduced by the calculated spectrum at the BOMD level. Considering the level of computation (B3LYP/6-31g(d)) for the energies and gradients for the BOMD trajectories, the same scaling factor values were used for

the BOMD and harmonic IR spectra. The harmonic IR absorption spectra of both the Eigen-type minimum and Zundel\_type TS are given in Figure 3-11. These two harmonic spectra are significantly different from each other, and also from the BOMD spectrum which is expected when strongly anharmonicities are at play.

An assignment can be proposed based of the normal modes determined at the harmonic levels. The band observed at  $3455\text{ cm}^{-1}$  can be assigned to the free NH which is predicted at  $3470\text{ cm}^{-1}$  at the BOMD level. The band centered at  $3375\text{ cm}^{-1}$  can be assigned to the stretching mode of the two NH groups involved as hydrogen bond donor in the  $C_{10}$  hydrogen bond ring. Due to the symmetry breaking when going from the Zundel\_type TS (c) to the Eigen-type minimum (b), there is a splitting of the three sets of twofold degenerate free NH or NH involved in a  $C_7$  or  $C_{10}$  hydrogen bond. As can be noticed in Figure 3-11, this splitting is much larger in the case of the  $C_7$  NH than in the two other cases.

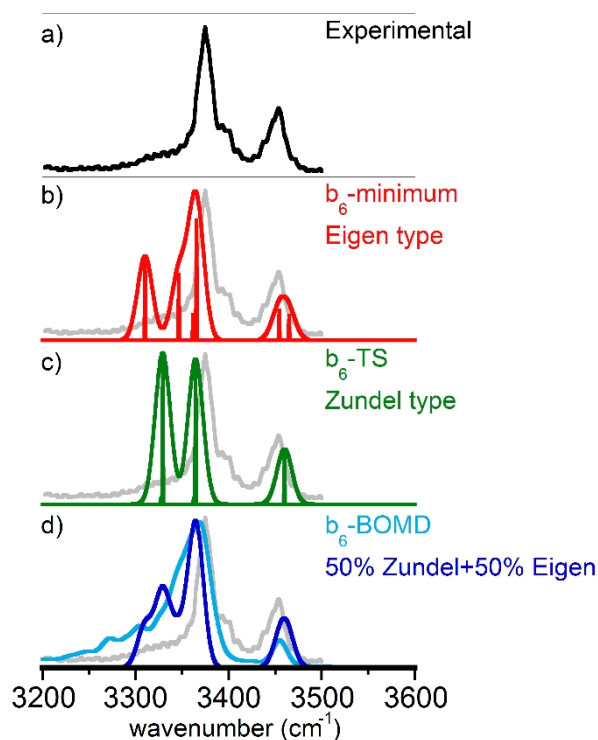


Figure 3-11: Experimental IRMPD spectrum (black) and theoretical absorption spectrum (blue) of the  $b_6$  ion in the  $3200\text{--}3600\text{ cm}^{-1}$  range. The theoretical spectrum was computed at the BOMD(B3LYP/6-31G\*\*) level of theory and scaled by a factor of 0.955.

If one compares the predicted harmonic IR spectra of the Eigen-type and Zundel-type structures (Figure 3-11b and 3-11c, respectively), the two nearly degenerate C<sub>7</sub> NH stretches (~3329 cm<sup>-1</sup>) splits into two bands predicted at ~3310 and ~3347 cm<sup>-1</sup>. The asymmetric band with a maximum at ~3375 cm<sup>-1</sup> thus reflects the fact that the ionizing proton oscillates between the two oxygen pillars, which results in a broadening of the C<sub>7</sub> NH stretching band in the 3200-3350 cm<sup>-1</sup> region. Interestingly, these frequency splitting are consistent with the structural changes from the TS to the minimum structure. While the two C<sub>10</sub> hydrogen bond distances are essentially the same in the Eigen-type and Zundel-type structures (~2.07 Å), the C<sub>7</sub> NH...O distances significantly change: 2.08 and 2.00 Å in the former, in contrast with two equivalent 2.04 Å bonds in the latter.

The main difference between the harmonic and BOMD spectra is the intensity in the C<sub>7</sub> NH stretching region. A naive interpretation of the shape of the observed IR spectrum could be proposed on the basis of the difference discussed above between the harmonic spectra of the Eigen-type and Zundel-type structures. If the BOMD IR spectrum could be interpreted as an average of the IR spectra along the trajectories, one could easily conceive that the intensity of the C<sub>7</sub> NH stretching is lower than those of the free and C<sub>10</sub> NH stretching. In the two latter cases, the band position does not significantly change from the Eigen-type to the Zundel-type structures. As a result, a larger average intensity would be expected as compared to that associated with the C<sub>7</sub> NH stretching which have significantly different frequencies in one structure and the other. This interpretation is illustrated in chart D of Figure 3-11 where an average spectrum of the two harmonic spectra is shown.

Assignment	Experiment	BOMD
NH st (C <sub>7</sub> )	shoulder	shoulder
NH st (C <sub>10</sub> )	3375	3380
NH st (Free)	3455	3470

Tableau 3-1 : Assignment of the IR spectrum of the b<sub>6</sub> ion in the NH stretching region. Positions of the observed bands and predicted BOMD(B3LYP/6-31G\*\*) bands are given in columns 2 and 3, respectively. The BOMD(B3LYP/6-31G\*\*) frequencies were scaled by a factor of 0.955.

The agreement between the experimental and BOMD spectra in the 1000-2000  $\text{cm}^{-1}$  energy range (Figure 3-12) is much less satisfactory. Overall, the relative predicted intensities are significantly different from those found experimentally. The difficulty for determining the IR spectrum in this spectral range is expected on the basis of the literature data on the proton shared systems [61]. As clearly shown by Johnson and coworkers [61], the frequency of the OH stretching mode significantly changes going from an Eigen\_type to a Zundel\_type proton bound system. And this frequency shift was found to be correlated with the difference in proton affinities of the two groups involved in the proton sharing. When this difference is large, the OH stretching mode is red-shifted in the 3500  $\text{cm}^{-1}$  region. For Zundel\_type systems, *i.e.* corresponding to a small difference in proton affinity, the mode corresponding to the proton shift from one donor to the other can be found in the 1000-2000  $\text{cm}^{-1}$  region. It is thus likely to be the case here. A longer time for the trajectory might be needed to improve the modeling of the IR spectrum in this spectral range.

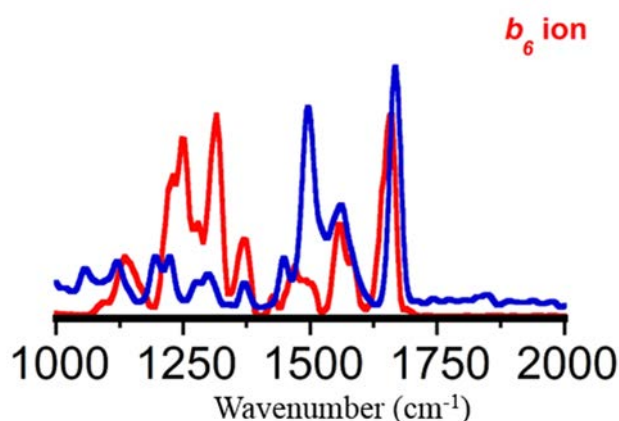


Figure 3-12 Experimental IRMPD spectrum (red) and theoretical absorption spectrum (blue) of the  $b_6$  ion in the 1000-2000  $\text{cm}^{-1}$  range. The theoretical spectrum was computed at the BOMD(B3LYP/6-31G\*\*) level of theory and scaled by a factor of 0.98.

Protonated  $A_6$ MA peptide was isolated and fragmented under conventional CID conditions in the Qh unit of the FTICR mass spectrometer. Then the  $b_6$  fragment ion was isolated and subjected to the IR light in the ICR cell in order to record the IR spectrum. As it was said before, in-source fragmentation may induce the rearrangement mechanism which can lead to different ion structures [39,48].

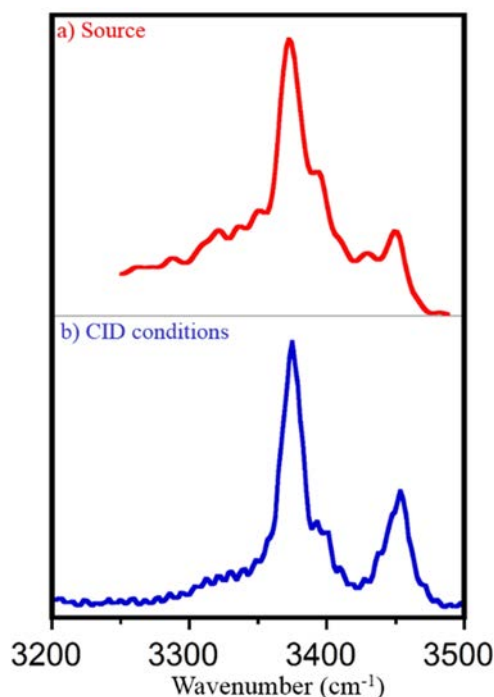


Figure 3-13: IR spectra of the  $b_6$  ion of protonated  $A_6MA$ . The  $b_6$  ion was formed in the source region (red) or in the hexapole ion trap (blue).

For this purpose, the IR spectrum of  $b_6$  ion of protonated  $A_6MA$  was obtained after in-source fragmentation of the precursor ion and also after conventional CID conditions. The similarity of the two spectra allows us to assume that the same isomer population is formed under the two experimental conditions.

### 3.4.2 Formation of an ammonia adduct with a model cyclic peptide

Following the previous study performed by Somogyi, Harrison, and Paizs [43], we first focused our attention on the characterization of the structure of the complex formed between ammonia and a synthetic cyclic penta-peptide. The protonated cyclic YAGFL,  $[c\text{-YAGFL+H}]^+$ , could be generated with a high abundance, and was allowed to react in the ICR cell with ammonia maintained at a constant pressure ( $\sim 10^{-8}$  mbar) using a leak valve for introducing ammonia. This pressure is a trade-off between ion-molecule efficiency and mass-resolution. The mass spectrum recorded after three seconds of ion-molecule reaction is given in Figure 3-14.

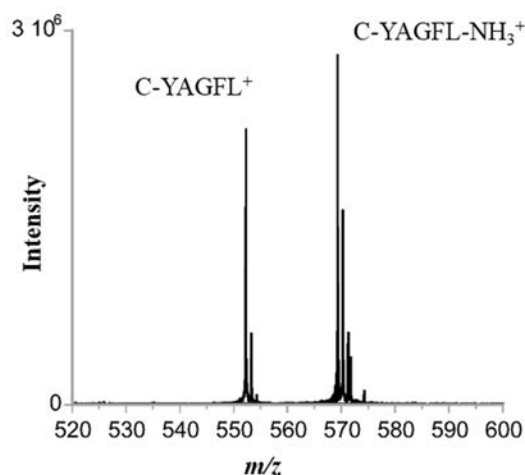


Figure 3-14: Mass spectrum recorded after three seconds of ion-molecule reaction between of protonated cyclic-YAGFL peptide and  $\text{NH}_3$  in the ICR cell maintained at a pressure of  $\sim 10^{-8}$  mbar.

The adduct formation efficiency,  $\sim 50\%$  after three seconds of reaction delay, is comparable to that observed by Somogyi, Harrison and Paizs for several middle size  $b_n$  ions [43]. Following the mass-selection of the  $[\text{c-YAGFL}+\text{NH}_3+\text{H}]^+$  adduct in the ICR cell, IR spectroscopy could be performed. Nevertheless, the duty cycle was quite long due to the long reaction delay in the ICR cell. Two other methods were thus used for generating the  $[\text{c-YAGFL}+\text{NH}_3+\text{H}]^+$  adducts.

The IR spectra of the  $[\text{c-YAGFL}+\text{NH}_3+\text{H}]^+$  generated three different ways are given in Figure 3-15. In panel (a) is the IR spectrum recorded when the  $[\text{c-YAGFL}+\text{H}]^+$  ions were mass-selected in the quadrupole of the Qh interface, and allowed to react with  $\text{NH}_3$  in the ICR cell. In order to reduce the ion-molecule reaction delay, we thought that it would be more efficient to perform this reaction in the hexapole ion trap of the Qh interface which is pressurized with Ar at a pressure of  $\sim 10^{-3}$  mbar. For this purpose,  $\text{NH}_3$  was simply seeded in the Ar line. The corresponding IR spectrum is given in panel (b) of Figure 3-15. As can be seen in this Figure, the spectrum of the two  $[\text{c-YAGFL}+\text{NH}_3+\text{H}]^+$  species are identical.

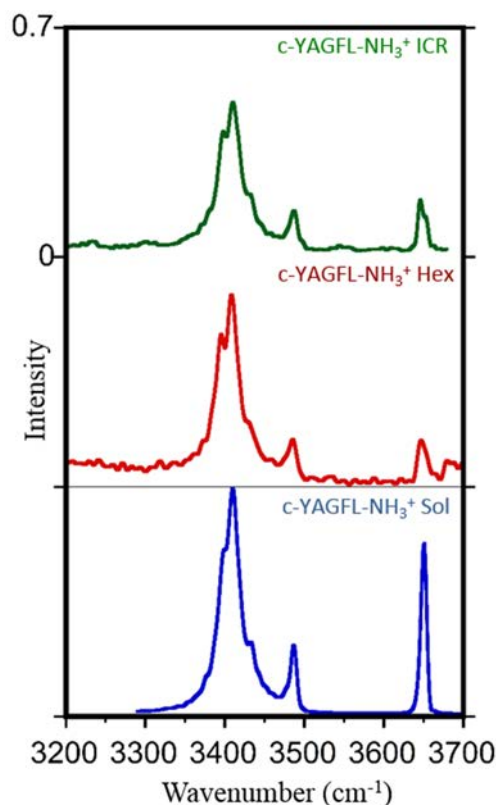


Figure 3-15: IR spectra of the  $[c\text{-YAGFL}+\text{NH}_3+\text{H}]^+$  adduct. The complex was formed by ion-molecule reaction in the ICR cell (a), in the linear hexapole (b), and in solution and then sprayed into the FTICR mass spectrometer (c).

The third IR spectrum given in panel (c) of Figure 3-15 corresponds to an  $[c\text{-YAGFL}+\text{NH}_3+\text{H}]^+$  adduct formed in solution. As it will be discussed later and confirmed through the comparison of experimental and theoretical spectra, the adduct formed between a  $b_n$  ion and  $\text{NH}_3$  can be seen as a neutral cyclic peptide interacting with  $\text{NH}_4^+$ . A solution of the cyclic c-YAGFL and an ammonia salt was thus prepared and used for the Electrospray ionization. The corresponding IR spectrum is very similar to the two others (panel c in Figure 3-15) in the 3300-3500  $\text{cm}^{-1}$  spectral region. It should be noted however that while the position of the band near  $\sim 3650 \text{ cm}^{-1}$  is the same as in the two other cases, the corresponding intensity is much larger. This difference might be due to a different optimization of the OPO/OPA laser system and/or to a different level of water on the optical table.

### 3.4.3 [cyclic-YAGFL+NH<sub>3</sub>+H<sup>+</sup>] predicted structure and IR spectrum.

DFT calculations were performed on the  $[c\text{-YAGFL}+\text{NH}_3+\text{H}]^+$  ion. Two views of the lowest energy structure are given in panels (b) or (c) in Figure 3-16, along with a schematic view of the

hydrogen bonding associated with this structure. As can be seen in Figure 3-16a, the lowest energy structure corresponds to an ammonium  $\text{NH}_4^+$  ion bound to the cyclic peptide backbone through three oxygen atoms (light blue oxygen atoms). As can be seen in panel b of Figure 3-16, one ammonium NH points towards the outside of the structure and is thus not involved in hydrogen bonding. The NH stretching modes associated with the three ammonium NH groups involved in hydrogen bonding with the amide CO are predicted to be strongly red-shifted. The IR region which was probed in the present work was restricted to the  $3200\text{-}3800\text{ cm}^{-1}$  spectral range. We did not try to probe the broad bands associated with these strongly red-shifted NH bands. Conversely, the formation of the complexes could be characterized by the band associated with the free ammonium NH which is predicted at  $3405\text{ cm}^{-1}$ .

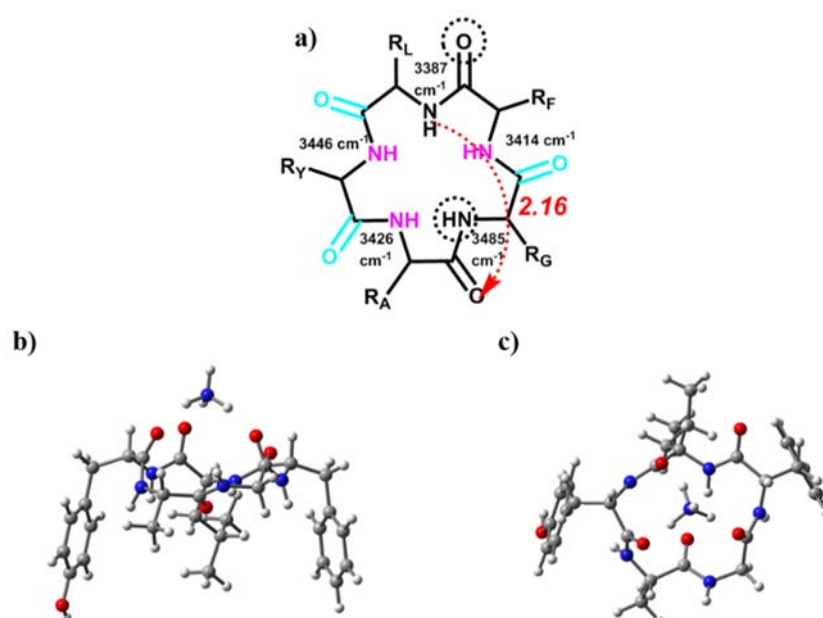


Figure 3-16: Three representations of the lowest energy structure of the  $[\text{c-YAGFL}+\text{NH}_3]^+$  ion. In (a), only the backbone of the cyclic peptide is shown. The three amide CO groups involved in HB with the ammonium are represented in light blue. The free NH and carbonyl groups are marked with a dotted circle. The intra-peptide  $\text{C}_{10}$  hydrogen bond is shown with a red dashed arrow in (a). The infrared frequencies provided in Figure 3-16a correspond to the predicted IR amide A (NH stretching) modes. The predicted IR frequencies were computed at the B3LYP/6-31+G (d,p) level of theory and scaled with a factor of 0.955. Two views of the optimized structures are given in (b) and (c).

Five amide CO and five amide NH are available for intra-peptide hydrogen bonding. One CO is involved in an intra-peptide  $\text{C}_{10}$  hydrogen bond (red dotted arrow) with an amide NH. The hydrogen bond distance is  $2.16\text{ \AA}$ . The theoretical frequency associated with this NH group is predicted at  $3387\text{ cm}^{-1}$ . Out of the four remaining amide NH groups, one is not involved in intra-peptide interactions. It is

represented by the dotted circle in Figure 3-16. As a result, the frequency associated with the NH stretching mode of this amino group is predicted at  $3485\text{ cm}^{-1}$ . The three remaining NH groups are involved in intra-peptide interactions with the  $\pi$ -electrons of the aromatic rings (pink NH groups). Similar NH- $\pi$  interactions have been characterized for gas phase neutral peptides [55] or ionized peptides [62-64]. The predicted frequencies for these amino groups in the present case are  $3446$ ,  $3426$  and  $3414\text{ cm}^{-1}$ .

A comparison between the experimental infrared spectrum of the  $[c\text{-YAGFL}+\text{NH}_3+\text{H}]^+$  complex and the predicted IR absorption spectrum of the lowest energy structure in the  $3200\text{-}3600\text{ cm}^{-1}$  is provided in Figure 3-17. Overall, the experimental IRMPD spectrum is well simulated using the IR absorption bands predicted for the lowest energy structure  $c\text{-YAGFL-NH}_3^+$  complex. Three experimental features can be distinguished. Two narrow bands are observed near  $\sim 3490$  and  $\sim 3650\text{ cm}^{-1}$ . A more intense and broad centered at  $\sim 3410\text{ cm}^{-1}$  can also be observed, with two shoulders at  $\sim 3400$  and  $\sim 3430\text{ cm}^{-1}$ .

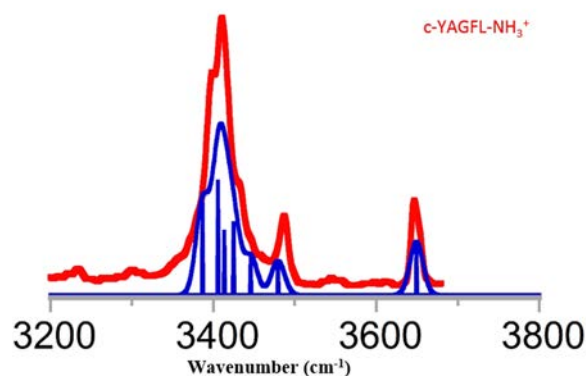


Figure 3-17: Experimental (red) and calculated (blue) infrared spectra of the  $[c\text{-YAGFL}+\text{NH}_4^+]$  complex. The harmonic frequencies were computed at the B3LYP/6-31+G (d,p) level and corrected by a scaling factor of 0.955. The harmonic IR absorption bands were convoluted by a Gaussian profile (fwhm= $20\text{ cm}^{-1}$ ).

Assuming the formation of the lowest energy structure under our experimental conditions, a band assignment given in Table 3-2 can be proposed. The experimental band observed at  $\sim 3650\text{ cm}^{-1}$  can be assigned to the OH stretching mode of the Tyrosine predicted at  $3649\text{ cm}^{-1}$ . The second narrow band at  $\sim 3490\text{ cm}^{-1}$  can be also assigned to the “free” NH stretching mode of the cyclic backbone which is predicted at  $3485\text{ cm}^{-1}$ . As expected, multiple IR active transition are predicted in the vicinity of the

broad band centered at  $\sim 3410\text{ cm}^{-1}$ . First, the “free” NH stretching mode of the  $\text{NH}_4^+$  group is predicted at  $3405\text{ cm}^{-1}$ . Second, the stretching mode of the NH group involved in a hydrogen bond with the the  $\pi$ -electron cloud of the phenylalanine side chain is predicted at  $3414\text{ cm}^{-1}$ . The shoulder on the blue side of the broad and intense band is consistent the two predicted NH stretching modes of the Alanine and Tyrosine residues. These two NH groups are influenced by the  $\pi$ -electron cloud of the Tyrosine, and the corresponding stretching modes are predicted at  $3446$  and  $3426\text{ cm}^{-1}$ , respectively. Finally the shoulder at the red side of the broad and intense band can be assigned to the NH stretching mode of the glycine residue which is involved in the  $\text{C}_{10}$  intra-peptide hydrogen bond. It is predicted at  $3387\text{ cm}^{-1}$ . The three bands corresponding to the  $\text{NH}_4^+$  NH groups involved in hydrogen bonding with the peptide CO are predicted at low frequencies ( $3070\text{-}3062\text{ cm}^{-1}$ ). This region of the IR spectrum has not been explored with our tabletop OPO/OPA laser. In this region, the laser power is relatively low thus preventing for an efficient photo-fragmentation signal.

Vibrational Mode	Theory ( $\text{cm}^{-1}$ )	Exp. ( $\text{cm}^{-1}$ )
Tyr OH st	3649	3650
Free NH st	3485	3490
$\pi(\text{Tyr})\text{-HB NH st}$	3446	3430
	3426	
$\pi(\text{Phe})\text{-HB NH st}$	3414	3410
Free $\text{NH}_4^+$ NH st	3405	
$\text{C}_{10}$ HB NH st	3387	3400
HB $\text{NH}_4^+$ NH st	3071	n/a
	3066	n/a
	3062	n/a

Table 3-2 : Band assignment for the  $[\text{c-YAGFL}+\text{NH}_3+\text{H}]^+$  complex. A description of the normal mode is indicated in the first column. The infrared frequencies in the second column correspond to the calculated harmonic frequencies of theoretical structure presented in Figure 3-16. The experimental infrared frequencies are shown in the third column.

The  $1000\text{-}2000\text{ cm}^{-1}$  infrared spectra of the complex formed between the cyclic YAGFL peptide and  $\text{NH}_4^+$  is given in Figure 3-18. Four infrared bands can be observed in the experimental IR spectrum. Amide I and amide II bands are centered at  $1695$  and  $1515\text{ cm}^{-1}$ , respectively. The width (fwhm) for these two IR features is about  $\sim 40\text{ cm}^{-1}$ . This is expected since amide CO and NH groups are involved in different hydrogen bonding interactions. It should be noted, however, that the spectral resolution in

the CLIO range is not sufficient for explaining the small spectral shifts of the CO stretching and NH bending modes. Below  $1300\text{ cm}^{-1}$ , two weaker infrared features are observed. The band centered at  $1280\text{ cm}^{-1}$  corresponds to the C-C stretching mode. The other, centered at  $1190\text{ cm}^{-1}$ , can be assigned to the OH bending mode of the Tyrosine.

Overall, the experimental and theoretical results are consistent, and allow for a structural characterization of the complex formed between a protonated cyclic YAGFL peptide and  $\text{NH}_4^+$ . It confirms in particular that there is a proton transfer from the peptide to the ammonia. The resulting  $\text{NH}_4^+$  is predicted to lie in the center of the cyclic peptide, and the complex is stabilized by three ionic hydrogen bonds between  $\text{NH}_4^+$  NH and amide CO acceptor groups. A band predicted near  $\sim 3410\text{ cm}^{-1}$  is characteristic of the free  $\text{NH}_4^+$  NH group. From the predicted position of the NH stretching mode associated with the intra-peptide  $\text{C}_{10}$  hydrogen bond, one can anticipate that  $\text{C}_{10}$  and  $\text{C}_7$  NH modes should be observed below  $3400\text{ cm}^{-1}$  for the complexes formed between ammonia and large  $b_n$  ions.

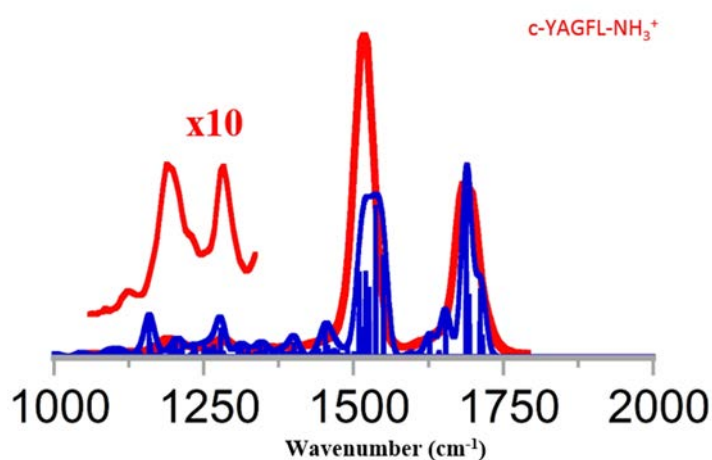


Figure 3-18: Experimental (red) and calculated (blue) infrared spectra of the  $c\text{-YAGFL-NH}_3^+$  ion. The harmonic frequencies were computed at the B3LYP/6-31+G (d,p) level and corrected by a scaling factor of 0.98. The harmonic IR absorption bands were convoluted by a Gaussian profile (fwhm=20  $\text{cm}^{-1}$ ).

#### 3.4.4 Complex formed between middle size $b_n$ and $\text{NH}_3$ : mass spectrometry and IR spectra.

Our goal was to probe the structure of the complexes formed by middle size  $b_n$  ions and ammonia which have been observed by Somogyi, Harrison and Paizs [43]. In this earlier study, these complexes were formed by allowing the middle size  $b_n$  fragment ions with the  $\text{NH}_3$  background gas in the ICR cell.

As discussed above, in order to reduce the duty cycle of the experiments,  $b_n$  fragment ions were generated in the source region and ion-molecule reactions were performed in the relatively high pressure region of the hexapole ion trap of the Qh interface of the FT-ICR. The  $b_n$  ions ( $n=6-9$ ) containing only alanine residues were studied. The mass spectra after three seconds of ion-molecule reaction with the  $\text{NH}_3$  gas are given in Figure 3-19. Beside the isotopic mass characteristic of the  $b_n$  ions, a second  $m/z$  signal at +17 can be observed, characteristic of the formation of the complex between the  $b_n$  ion and the  $\text{NH}_3$  molecule.

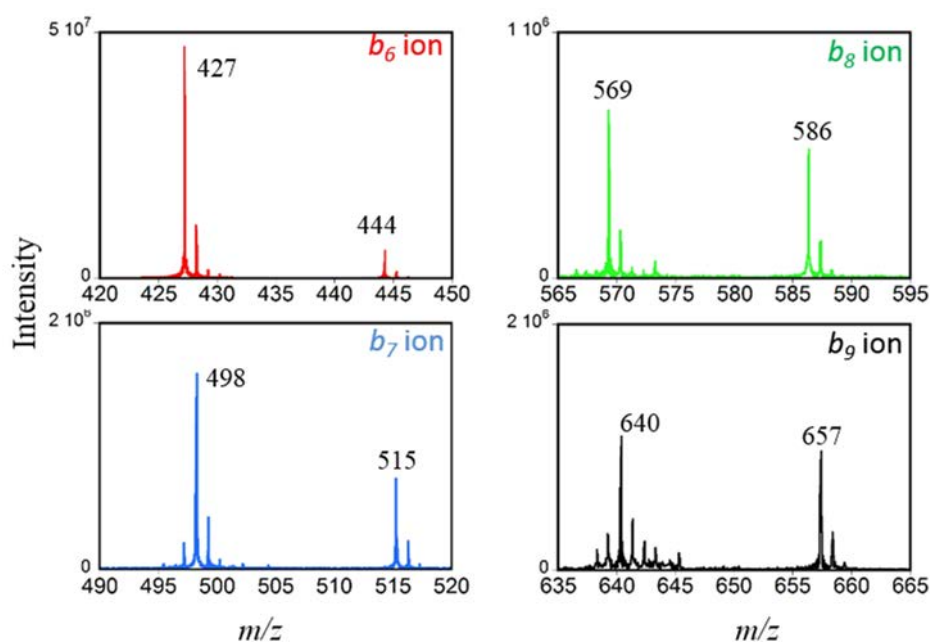


Figure 3-19: Mass spectra of the middle size  $b_n$  ( $n=6-9$ ) ions composed by alanine residues. The  $b_n$  ions were allowed to react with ammonia gas during three seconds in the hexapole ion trap of the hybrid FT-ICR mass spectrometer.

The IR spectra of the  $b_n$ - $\text{NH}_3$  complexes in the  $1000-2000\text{ cm}^{-1}$  and  $3200-3600\text{ cm}^{-1}$  energy ranges are given in Figure 3-20. As can be seen in this Figure, the IR spectra in the “fingerprint” region are rather similar. The two intense IR features are observed near  $1520$  and  $1670\text{ cm}^{-1}$  correspond to the so-called amide II and I bands. A higher resolution would be needed to derive structural information from these bands. In addition, the respective band assignment is difficult because the amide carbonyl stretches are coupled through the backbone, and there is no one-to-one correspondence between one frequency and one carbonyl stretch. The amide II region suffers the same type of drawback because the NH bending motions are coupled through the backbone C-N stretches [54].

Weaker IR features can also be observed below  $1400\text{ cm}^{-1}$ . In the case of the  $b_9$  adduct, a distinct infrared feature is observed at  $\sim 1455\text{ cm}^{-1}$  which is not observed in the other  $1000\text{--}2000\text{ cm}^{-1}$  IR spectra. It should finally be noted that no infrared features are observed between  $1800\text{--}2000\text{ cm}^{-1}$  characteristic of a free oxazolone CO stretching mode was observed in any case.

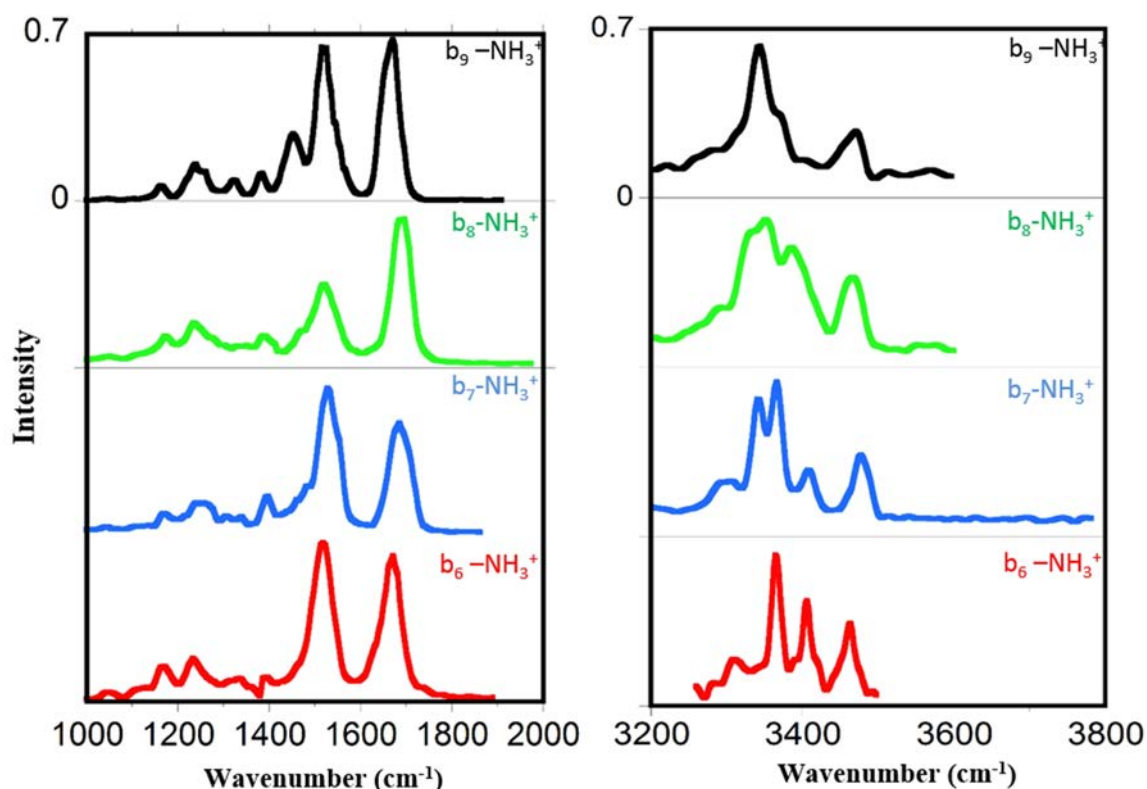


Figure 3-20: Experimental IR spectra of the middle size  $b_n\text{-NH}_3^+$  complexes recorded in the  $1000\text{--}2000$  spectral region (a) and in the N-H stretching region (b). All the experimental IR spectra were recorded using the FT-ICR mass spectrometer coupled with the OPO/OPA laser systems, in conjunction with the auxiliary  $\text{CO}_2$  laser.

The  $3200\text{--}3600\text{ cm}^{-1}$  region of the IR spectra is more informative because there is less coupling between the NH stretching and other modes [65]. As can be seen in Figure 3-20, the four experimental IR spectra in this energy range are rather different. It can be seen in particular that IR bands of the  $b_8\text{-NH}_3^+$  and  $b_9\text{-NH}_3^+$  complexes are red-shifted and broader with respect to those of the  $b_6\text{-NH}_3^+$  and  $b_7\text{-NH}_3^+$  systems. In addition, the IR features in the two latter cases are well resolved. The following

discussion on the structural characterization of the  $b_n+\text{NH}_3$  adducts will essentially be based on the 3200-3600  $\text{cm}^{-1}$  IR spectra.

### 3.4.5 IRMPD spectroscopy of the $b_9+\text{NH}_3^+$ complex: Highly symmetric structure.

Different representations of the calculated lowest energy structure of the  $b_9\text{-NH}_3$  ion are given in Figure 3-21. This structure is highly symmetric and belongs to the  $C_3$  point group. The peptide backbone forms a macrocycle ring which is bound to an  $\text{NH}_4^+$  moiety lying at the center of the ring. Three equivalent ionic hydrogen bonds are formed between ammonium NH donor and amide CO acceptor groups. The corresponding NH-OC bond distance is 1.79 Å, and the predicted frequencies are 3081 and 3040  $\text{cm}^{-1}$ , *i.e.* out of the energy range scanned here.

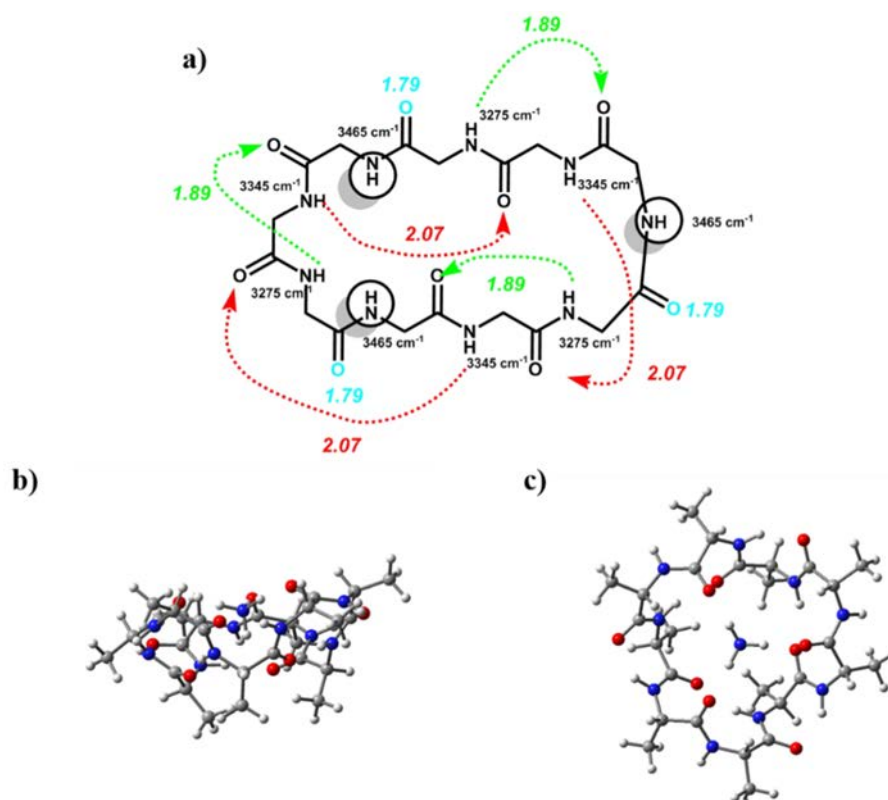


Figure 3-21: Three representations of the lowest energy structure ( $C_3$  symmetry) formed between the  $b_9$  fragment ion of protonated  $\text{A}_9\text{YA}$  and  $\text{NH}_3$ . In the schematic view (a), only the backbone of the peptide is shown. The three free amide NH and CO groups are marked with a circle. The three equivalent  $C_7(C_{10})$  hydrogen bonds are shown with a green (red) dashed arrow. The three equivalent carbonyl groups bonded to the  $\text{NH}_4^+$  ion are displayed in blue color. The hydrogen bond distances and the corresponding NH stretching frequencies are given in (a). The predicted IR frequencies were computed at the B3LYP/6-31+G (d,p) level of theory and scaled with a factor of 0.955. Two views of the lowest energy predicted structure are given in (b) and (c).

The cyclic peptide structure is characterized by three equivalent  $C_7$  and three equivalent  $C_{10}$  hydrogen bonding networks (panel (a) in Figure 3-21). The NH-OC bond distance is shorter for a  $C_7$  (1.89 Å) than for a  $C_{10}$  (2.07 Å) hydrogen bond. The corresponding NH stretching modes are predicted at 3275 and 3345  $\text{cm}^{-1}$ , respectively. The three remaining amide NH can be considered as “free” and the corresponding stretching modes are predicted at 3465  $\text{cm}^{-1}$ . These results are consistent with the frequency shifts of the NH modes involved in intra-peptide hydrogen bond interactions reported in previous studies for neutral systems [54].

The experimental 3200-3600  $\text{cm}^{-1}$  spectrum of the  $b_9+\text{NH}_3^+$  complex is compared with the predicted IR absorption spectrum of the lowest energy structure in Figure 3-22. The experimental spectrum is dominated by an intense and broad band with a maximum near  $\sim 3345 \text{ cm}^{-1}$ , and a shoulder on its blue side near  $\sim 3370 \text{ cm}^{-1}$ . A weaker and asymmetric band with a maximum near  $\sim 3465 \text{ cm}^{-1}$  is also observed. Finally a less intense shoulder is observed at  $\sim 3275 \text{ cm}^{-1}$ .

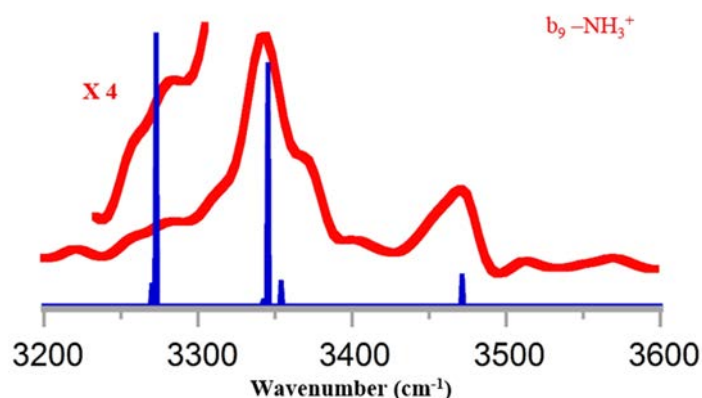


Figure 3-22: Experimental (red) and calculated (blue sticks) infrared spectra of the  $b_9+\text{NH}_3^+$  ion in the 3200-3600  $\text{cm}^{-1}$  spectral range. The harmonic frequencies were computed at the B3LYP/6-31+G (d,p) level and scaled with a factor of 0.955.

An assignment of the experimental features is proposed in Table 3-3 assuming the unique formation of the lowest energy structure with a  $C_3$  symmetry. The band observed at  $\sim 3465 \text{ cm}^{-1}$  can be assigned to the three degenerate “free” NH stretching modes which are predicted at 3472  $\text{cm}^{-1}$ . The intense and broad band observed at  $\sim 3345 \text{ cm}^{-1}$  can be assigned to the NH stretching modes of the three amide NH groups involved in  $C_{10}$  intra-peptide hydrogen bonds which are predicted at 3345  $\text{cm}^{-1}$ . The blue-side shoulder observed at  $\sim 3370 \text{ cm}^{-1}$  can be assigned to the NH stretching mode of the  $\text{NH}_4^+$  ion

predicted at 3354 cm<sup>-1</sup>. It can be noticed that the position of this band is red-shifted as compared to that of the “free” NH<sub>4</sub><sup>+</sup> NH group of the complex formed between the model cyclic peptide and NH<sub>4</sub><sup>+</sup>. Indeed, as can be seen in Figure 3-21b, in the case of the *b*<sub>9</sub> fragment, the NH<sub>4</sub><sup>+</sup> is embedded in the cage structure formed by the cyclic peptide, and it is thus not as free as in the model case discussed previously. Finally, the IR shoulder observed at 3275 cm<sup>-1</sup> can be assigned to the NH stretching mode of the amide NH groups involved in the C<sub>7</sub> intra-peptide interaction predicted at 3275 cm<sup>-1</sup>.

Vibrational Mode	Theory (cm <sup>-1</sup> )	Exp (cm <sup>-1</sup> )
Free NH st	3472	3465
Free NH <sub>4</sub> <sup>+</sup> NH st	3354	3370 (sh)
<b>C<sub>10</sub></b> HB NH st	3345	3345
<b>C<sub>7</sub></b> HB NH st	3273	3275 (sh)
HB NH <sub>4</sub> <sup>+</sup> NH st	3081	n/a
HB NH <sub>4</sub> <sup>+</sup> NH as st	3081	n/a
HB NH <sub>4</sub> <sup>+</sup> NH s st	3040	n/a

Table 3-3 : Band assignment for the *b*<sub>9</sub>-NH<sub>4</sub><sup>+</sup> ion. The band assignment is indicated in the first column. The infrared frequencies in the second column correspond to the calculated harmonic frequencies of the theoretical structure presented in figure 3-21. The experimental infrared frequencies are showed in the third column.

The experimental and theoretical spectra in the 1000-2000 cm<sup>-1</sup> energy range are given in Figure 3-23. The amide I band centered at 1665 cm<sup>-1</sup> is relatively narrow, in agreement with theory which predicts that the nine amide CO stretches are nearly degenerate. The amide NH bending frequencies, however, are predicted over a larger frequency range, in agreement with the broader and asymmetric amide II feature with a maximum at ~1520 cm<sup>-1</sup>. One interesting IR feature is the one observed at ~1455 cm<sup>-1</sup>. On the basis of the theoretical results, this IR band can be assigned to the NH<sub>4</sub><sup>+</sup> umbrella mode predicted at 1475 cm<sup>-1</sup>. Finally, it is worth to stress that no IR features are observed in the 1800-2000 cm<sup>-1</sup> energy range characteristic of oxazolone structure.

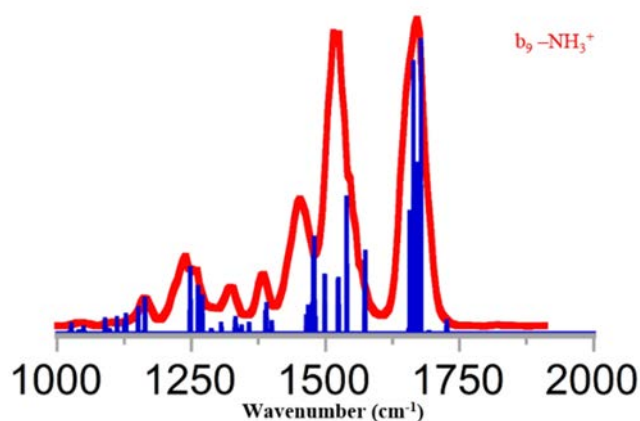


Figure 3-23: Experimental (red) and calculated (blue) infrared spectra of the  $b_9\text{-NH}_3^+$  complex in the 1000-2000  $\text{cm}^{-1}$  spectral range. The harmonic frequencies were computed at the B3LYP/6-31+G(d,p) level and scaled with a factor of 0.98.

### 3.4.6 IRMPD spectroscopy of the $b_n\text{-NH}_3^+$ ( $n = [6, 8]$ ) complexes.

Calculations performed for the  $b_n\text{-NH}_3^+$  ( $n = [6-8]$ ) ions resulted in macrocyclic structures similar to that of the  $b_9\text{-NH}_3^+$  complex ion in which the peptide backbone forms a macrocycle ring coordinated to an  $\text{NH}_4^+$  moiety. Schematic representations of the backbone of the three  $b_n\text{-NH}_3^+$  complexes are given in Figure 3-24. The macrocyclic structure is bound to the  $\text{NH}_4^+$  moiety through three oxygen atoms (in light blue) lying at the center of the ring.

These  $b_n\text{-NH}_3^+$  structures are stabilized by  $\text{C}_{10}$  and  $\text{C}_7$  hydrogen bonding networks as shown in Figure 3-24. The number of intra-peptide hydrogen bonds not only depends on the 3D conformation of the macrocycle ring, but also on the backbone size. Three hydrogen bonds (2  $\text{C}_{10}$  and 1  $\text{C}_7$ ) are observed in the case of the  $b_6\text{-NH}_3^+$  and  $b_7\text{-NH}_3^+$  and four (2  $\text{C}_{10}$  and 2  $\text{C}_7$ ) in the case of the  $b_8\text{-NH}_3^+$  complex. It is important to recall that six hydrogen bonds (3  $\text{C}_{10}$  and 3  $\text{C}_7$ ) were formed in the  $b_9\text{-NH}_3^+$  structure. Alternative structures for these complexes presenting more intra-peptide HB may exist, and calculations are still in progress.

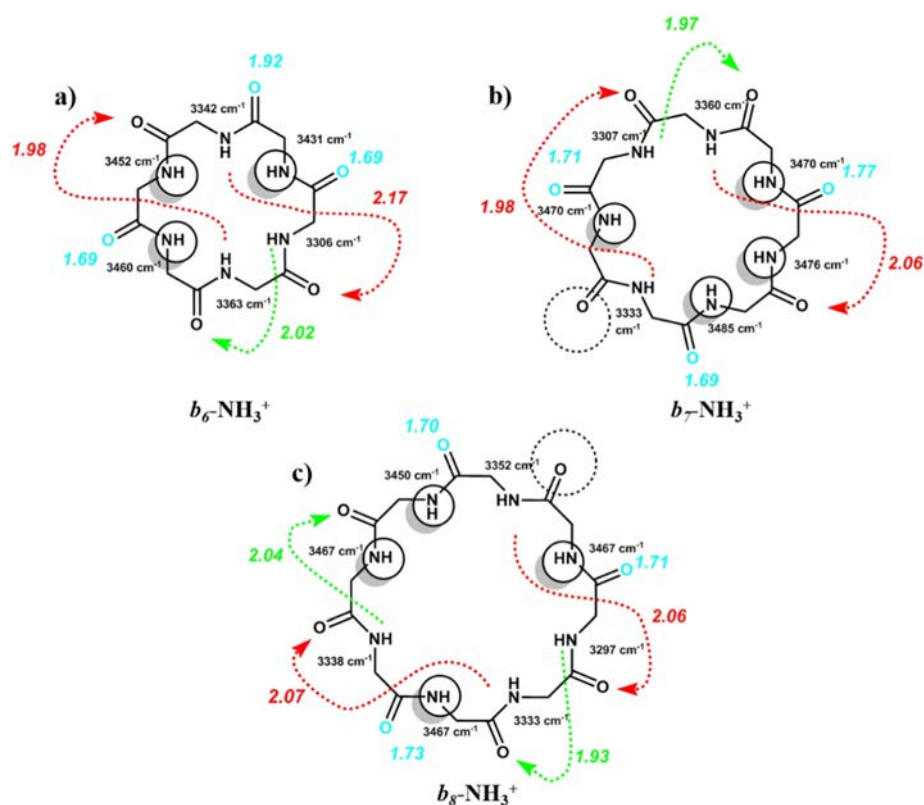


Figure 3-24: Schematic views of the lowest energy structure complex formed between the  $b_6$ ,  $b_7$ , and  $b_8$  fragment ion of Alanine residues and  $\text{NH}_3$ . Only the backbone of the peptide is shown. The free amide NH and CO groups are marked with a circle. The  $C_7$  and  $C_{10}$  hydrogen bonds are shown with a green and red dashed arrow, respectively. The carbonyl groups bonded to the  $\text{NH}_3^+$  ion are displayed in blue color. The hydrogen bond distances and the corresponding NH stretching frequencies are given in  $\text{cm}^{-1}$  and  $\text{\AA}$ , respectively. The predicted IR frequencies were computed at the B3LYP/6-31+G (d,p) level of theory and scaled with a factor of 0.955.

As can be seen in Figure 3-24, the  $C_7$  hydrogen bond distance decreases when increasing the number of the residues of the backbone *i.e.* the flexibility of the peptide. The  $b_6\text{-NH}_3^+$  complex exhibits a  $C_7$  hydrogen bond whose distance is 2.02  $\text{\AA}$ , while in the case of the  $b_7\text{-NH}_3^+$  and  $b_8\text{-NH}_3^+$  the  $C_7$  distances are shorter (1.97 and 1.93  $\text{\AA}$ , respectively). An even shorter distance is observed for the  $b_9\text{-NH}_3^+$  where the  $C_7$  hydrogen bond distance is 1.89  $\text{\AA}$ . As a direct consequence of these intra-peptide interactions, the  $b_6\text{-NH}_3^+$  structure exhibits three “free” amide NH groups while the  $b_7\text{-NH}_3^+$  and the  $b_8\text{-NH}_3^+$  structures exhibit four “free” amide NH groups. Another important structural characteristic is that only in the case of the  $b_7\text{-NH}_3^+$  and  $b_8\text{-NH}_3^+$  complexes one carbonyl oxygen atom remains “free”.

After ion-molecule reaction in the linear hexapole of the FTICR mass spectrometer, the  $b_n\text{-NH}_3^+$  complexes were isolated and subjected to the IR light in order to record the IRMPD spectra of the  $b_n$

series. As it was said before the experimental IRMPD spectra in the 3200-3600  $\text{cm}^{-1}$  energy range will be discussed because this energy region provides more diagnostic structural information than the “fingerprint” region for this kind of complexes. Comparison between experimental IRMPD spectra of the  $b_n\text{-NH}_3^+$  ions and theoretical spectra in the X-H (X = C, O, and N) are given in Figure 3-25. Overall, experiment and theory are in good agreement.

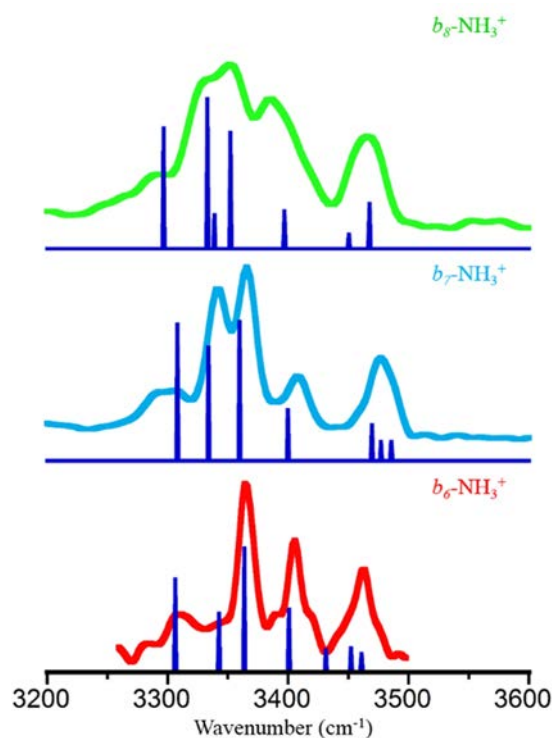


Figure 3-25: Experimental (red, light blue and green) and calculated (blue) infrared spectra of the  $b_6\text{-NH}_3^+$ ,  $b_7\text{-NH}_3^+$ , and  $b_8\text{-NH}_3^+$  complex in the 3200-3600  $\text{cm}^{-1}$  spectral range. The harmonic frequencies were computed at the B3LYP/6-31+G(d,p) level and scaled with a factor of 0.955.

The three IRMPD spectra present a common IR feature near 3470  $\text{cm}^{-1}$  which can be assigned to the “free” amide NH stretching mode. As can be seen in this Figure, IR bands observed in the  $b_8\text{-NH}_3^+$  IRMPD spectrum are red shifted in comparison with those of the  $b_7\text{-NH}_3^+$  and  $b_6\text{-NH}_3^+$  complexes. This reflects the fact that  $C_7$  hydrogen bonds are stronger when the peptide size increases. The IR band assignment of the three  $b_n\text{-NH}_3^+$  complexes is provided in Table 3-4. It is rather complicated to establish a tendency between the IR frequency of the amide NH stretching frequencies and the intra-peptide hydrogen bond distances, except in the case of the  $C_7$  hydrogen bonds.

Modes	$b_6\text{-NH}_3^+$	$b_7\text{-NH}_3^+$	$b_8\text{-NH}_3^+$
free NH st	3460	3475	3465
free $\text{NH}_4^+$ NH st	3405	3410	3390
$\text{C}_{10}$ HB NH st	3365 5 (1.98)	3365 (2.06)	3355 (2.06)
	3340 (2.17)	3340 (1.98)	
$\text{C}_{10}\text{-C}_7$ HB NH st			3330 (2.07 2.04)
$\text{C}_7$ HB NH st	3310 (2.02)	3300 (1.97)	3290 (1.93)

Table 3-4 Band assignment of the  $b_n\text{-NH}_3^+$  complex ions. The vibrational modes are indicated in the first column. The experimental band positions of  $b_6\text{-NH}_3^+$ ,  $b_7\text{-NH}_3^+$ , and  $b_8\text{-NH}_3^+$  complex in the 3200-3600  $\text{cm}^{-1}$  are given in the second, third and fourth column, respectively. The hydrogen-bond distances associated with the experimental bands are given in Å in parentheses.

Structural information can be derived from the IR frequency associated with the “free”  $\text{NH}_4^+$  NH stretch. A picture of the four  $b_n\text{-NH}_3^+$  complexes is given in Figure 3-26. In the case of the  $b_6\text{-NH}_3^+$  and  $b_7\text{-NH}_3^+$  the IR band assigned to this vibrational mode is observed at 3405 and 3410  $\text{cm}^{-1}$ , respectively. This band is slightly red-shifted in the IRMPD spectrum of the  $b_8\text{-NH}_3^+$  (3390  $\text{cm}^{-1}$ ) and even more red-shifted in the case of the  $b_9\text{-NH}_3^+$  complex (3370  $\text{cm}^{-1}$ ). This difference can be explained by the position of the  $\text{NH}_4^+$  with respect to the macrocyclic ring. In the case of the  $b_6$ ,  $b_7$ , and  $b_8$  complexes, the  $\text{NH}_4^+$  is at the “surface” of the macrocyclic structure and one  $\text{NH}_4^+$  NH group is free. In the case of the  $b_9$  complex, however, the  $\text{NH}_4^+$  is completely “inside” of the cavity which means that the  $\text{NH}_4^+$  NH stretch is not completely “free” leading to a lower vibrational frequency (3370  $\text{cm}^{-1}$ ).

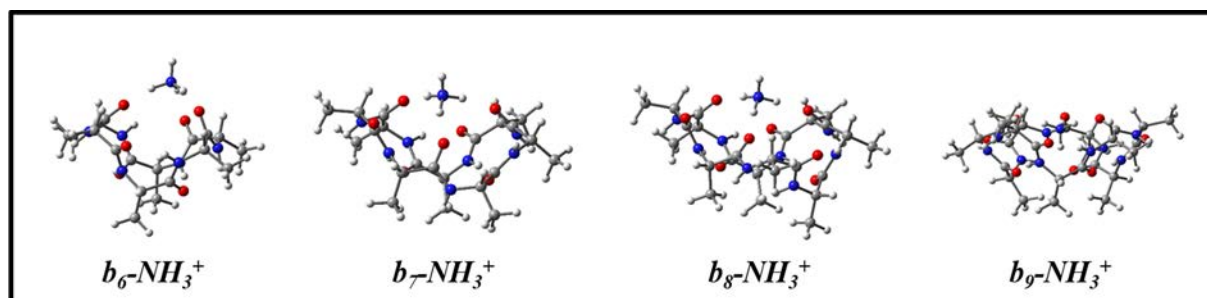


Figure 3-26 Comparative pictures of the middle size  $b_n\text{-NH}_3^+$  ions.

### 3.5 Conclusions

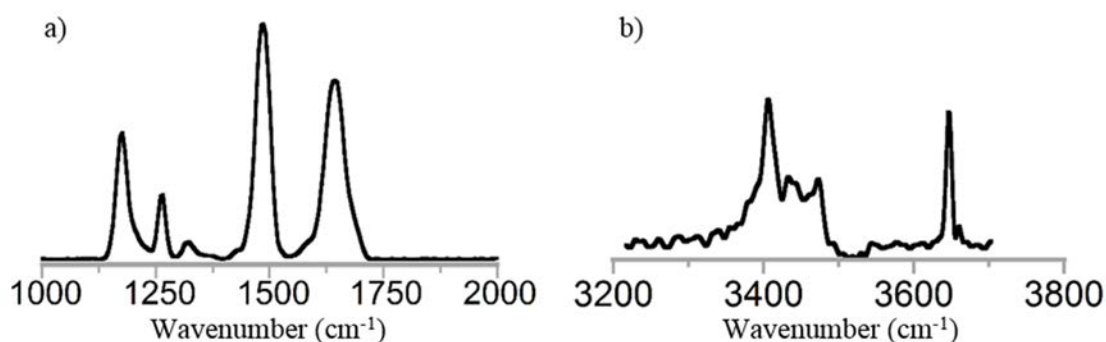
Our spectroscopic study combined with the quantum chemical calculations performed by B. Paizs provide a consistent picture of the structure of the complexes formed upon reaction of  $b_n$  peptide fragment ions with ammonia in the gas phase. A host-guest structure can be proposed for the  $b_n$ -NH<sub>3</sub><sup>+</sup> adducts where an ammonium cation is coordinated to three amide CO groups of a macrocyclic peptide, as suggested in the original paper of Somogyi, Harrison, and Paizs [43]. With this respect, the study of the model cyclic YAGFL peptide was interesting since the IR spectrum of an adduct formed in solution with an ammonium salt was found to be similar to those formed in the gas phase between the protonated c-YAGFL and ammonia.

The experimental spectra of the  $b_n$ -NH<sub>3</sub><sup>+</sup> adducts and also of the complex formed between a cyclic peptide and NH<sub>4</sub><sup>+</sup> nicely match with the corresponding predicted IR absorption spectra. The bands observed in the NH stretching region are more structurally diagnostic than those observed in the mid-IR region. Consistent with the predicted structures showing that the NH<sub>4</sub><sup>+</sup> cation is only bound through three ionic hydrogen bonds to three amide CO groups, a band characteristic of the “free” NH<sub>4</sub><sup>+</sup> NH stretching mode was observed in all cases. For the largest  $b_n$  ion studied here ( $b_9$ ) this band is slightly red-shifted suggested that for larger size ions, tetra-coordination of the ammonium cation could occur.

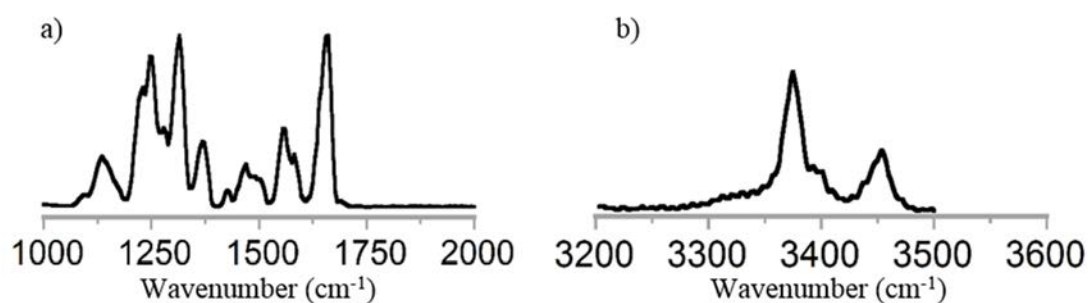
The structure of the  $b_n$ -NH<sub>3</sub><sup>+</sup> adducts is also characterized with intra-peptide hydrogen bonds. Two types of NH bands are observed for each system, and the assignment based on the predicted IR absorption spectra suggests that they correspond to C<sub>10</sub> and C<sub>7</sub> cyclic hydrogen bonds. With this respect, the case adduct formed with the  $b_9$  ion is particularly interesting because a highly symmetric structure is predicted for the corresponding ammonia complex, the structure displaying three equivalent sets of C<sub>7</sub>, C<sub>10</sub>, and free NH groups. Our spectral resolution, however, prevents from a clear derivation of structural information from a structurally diagnostic IR band. These macrocyclic structures are still very challenging for both theory and experiments.

Dynamics calculations based on energies and gradients determined at a hybrid density functional level (B3LYP) have been carried out by B. Paizs for exploring the potential energy surfaces of the systems. While convincing results were obtained for the ammonia complexes, the modelisation of the bare  $b_n$  ion, and more precisely of the IR spectra in the mid-IR range still require additional calculations. Results are only discussed in the case of the  $b_6$  ion, and the analysis of the NH stretching region suggests that a Zundel-Type ionic hydrogen bonding may be formed, where the proton would be equally shared between two amide CO groups of a cyclic peptide.

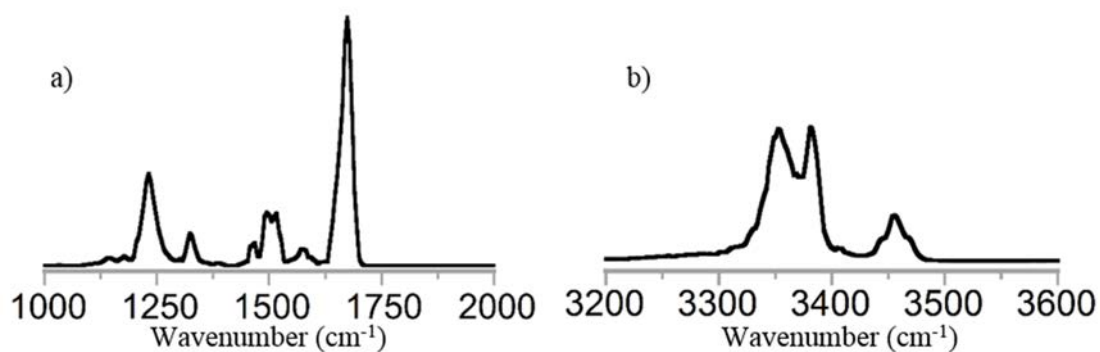
### 3.6 Annexes



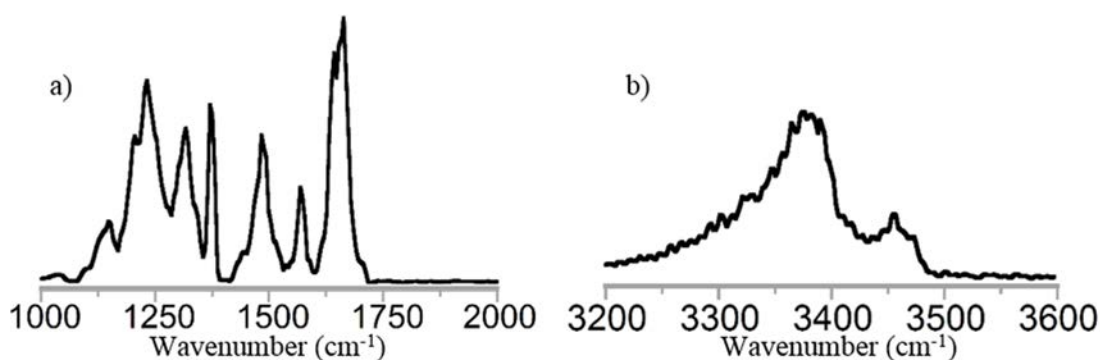
Annex 1: IR spectra in the 1000-2000  $\text{cm}^{-1}$  a) and 3200-3800  $\text{cm}^{-1}$  b) energy ranges of the protonated cycle-YAGFL ion.



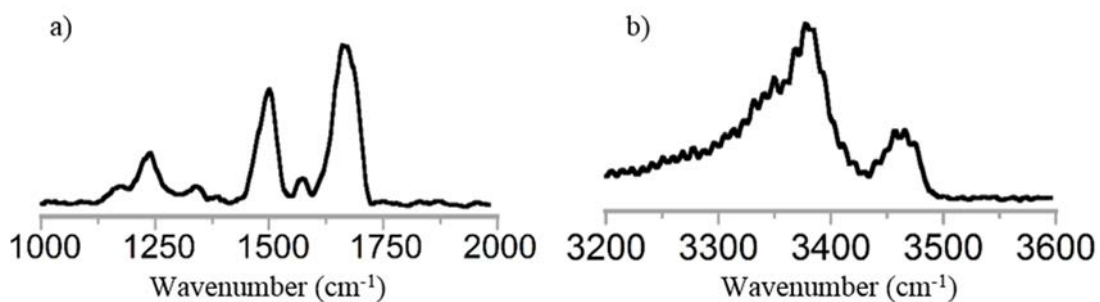
Annex 2: IR spectra in the 1000-2000  $\text{cm}^{-1}$  a) and 3200-3600  $\text{cm}^{-1}$  b) energy ranges of the  $b_6$  fragment ion of the protonated  $A_6MA$  peptide.



Annex 3: IR spectra in the 1000-2000  $\text{cm}^{-1}$  a) and 3200-3600  $\text{cm}^{-1}$  b) energy ranges of the  $b_7$  fragment ion of the protonated  $A_7YA$  peptide.



Annex 4: IR spectra in the 1000-2000  $\text{cm}^{-1}$  a) and 3200-3600  $\text{cm}^{-1}$  b) energy ranges of the  $b_8$  fragment ion of the protonated  $A_8YA$  peptide.



Annex 5: IR spectra in the 1000-2000  $\text{cm}^{-1}$  a) and 3200-3600  $\text{cm}^{-1}$  b) energy ranges of the  $b_9$  fragment ion of the protonated  $A_9YA$  peptide.

Vibrational Modes	Theory (cm <sup>-1</sup> )	Exp (cm <sup>-1</sup> )
	3461	
Free NH st	3452	3460
	3431	
Free NH <sub>4</sub> <sup>+</sup> NH st	3400	3405
<b>C<sub>10</sub></b> HB NH st	3363	3365
	3342	3340
<b>C<sub>7</sub></b> HB NH st	3306	3310
	3142	n/a
HB NH <sub>4</sub> <sup>+</sup> NH st	2909	n/a
	2870	n/a

Table-Annex 1: Band assignment for the *b<sub>6</sub>*-NH<sub>4</sub><sup>+</sup> ion. The band assignment is indicated in the first column. The infrared frequencies in the second column correspond to the calculated harmonic frequencies of the theoretical. The experimental infrared frequencies are showed in the third column

Vibrational Modes	Infrared frequency (cm <sup>-1</sup> )	Exp (cm <sup>-1</sup> )
	3485	
Free NH st	3476	3475
	3470	
	3470	
Free NH <sub>4</sub> <sup>+</sup> NH st	3400	3410
<b>C<sub>10</sub></b> HB NH st	3360	3365
	3334	3340
<b>C<sub>7</sub></b> HB NH st	3309	3300
	3106	n/a
HB NH <sub>4</sub> <sup>+</sup> NH st	2967	n/a
	2937	n/a

Table-Annex 2: Band assignment for the *b<sub>7</sub>*-NH<sub>4</sub><sup>+</sup> ion. The band assignment is indicated in the first column. The infrared frequencies in the second column correspond to the calculated harmonic frequencies of the theoretical structure. The experimental infrared frequencies are showed in the third column.

Vibrational Modes	Infrared frequency (cm <sup>-1</sup> )	Exp (cm <sup>-1</sup> )
	3468	
Free NH st	3468	3465
	3468	
	3451	
Free NH <sub>4</sub> <sup>+</sup> NH st	3398	3390
C <sub>10</sub> HB NH st	3353	3355
C <sub>10</sub> -C <sub>7</sub> HB NH as st	3339	
		3330
C <sub>10</sub> -C <sub>7</sub> HB NH st	3333	
		3290
C <sub>7</sub> HB NH st	3297	
	3062	n/a
HB NH <sub>4</sub> <sup>+</sup> NH st	3022	n/a
	3010	n/a

Table-Annex 3: Band assignment for the *b<sub>8</sub>*-NH<sub>4</sub><sup>+</sup> ion. The band assignment is indicated in the first column. The infrared frequencies in the second column correspond to the calculated harmonic frequencies of the theoretical structure. The experimental infrared frequencies are showed in the third column.

## 3.7 Bibliography

- (1) Hunt, D. F.; Yates, J. R.; Shabanowitz, J.; Winston, S.; Hauer, C. R. *Proceedings of the National Academy of Sciences of the United States of America* **1986**, *83*, 6233.
- (2) Biemann, K. *Biomedical and Environmental Mass Spectrometry* **1988**, *16*, 99.
- (3) Roepstorff, P.; Fohlman, J. *Biomedical Mass Spectrometry* **1984**, *11*, 601.
- (4) Paizs, B.; Suhai, S. *Mass Spectrom. Rev.* **2005**, *24*, 508.
- (5) Paizs, B.; Van Stipdonk, M. *J. Am. Soc. Mass. Spectrom.* **2008**, *19*, 1717.
- (6) Dancik, V.; Addona, T. A.; Clauser, K. R.; Vath, J. E.; Pevzner, P. A. *Journal of Computational Biology* **1999**, *6*, 327.
- (7) Taylor, J. A.; Johnson, R. S. *Anal. Chem.* **2001**, *73*, 2594.
- (8) Harrison, A. G. *Mass Spectrom. Rev.* **2009**, *28*, 640.
- (9) Yalcin, T.; Csizmadia, I. G.; Peterson, M. R.; Harrison, A. G. *J. Am. Soc. Mass. Spectrom.* **1996**, *7*, 233.
- (10) Yalcin, T.; Khouw, C.; Csizmadia, I. G.; Peterson, M. R.; Harrison, A. G. *J. Am. Soc. Mass. Spectrom.* **1995**, *6*, 1165.
- (11) Farrugia, J. M.; O'Hair, R. A. J.; Reid, G. E. *Int. J. Mass spectrom.* **2001**, *210*, 71.
- (12) Oomens, J.; Young, S.; Molesworth, S.; van Stipdonk, M. *J. Am. Soc. Mass. Spectrom.* **2009**, *20*, 334.
- (13) Bythell, B. J.; Erlekam, U.; Paizs, B.; Maitre, P. *ChemPhysChem* **2009**, *10*, 883.
- (14) Yoon, S. H.; Chamot-Rooke, J.; Perkins, B. R.; Hilderbrand, A. E.; Poutsma, J. C.; Wysocki, V. H. *J. Am. Chem. Soc.* **2008**, *130*, 17644.
- (15) Polfer, N. C.; Oomens, J.; Suhai, S.; Paizs, B. *J. Am. Chem. Soc.* **2007**, *129*, 5887.
- (16) Polfer, N. C.; Oomens, J.; Suhai, S.; Paizs, B. *J. Am. Chem. Soc.* **2005**, *127*, 17154.
- (17) Cordero, M. M.; Houser, J. J.; Wesdemiotis, C. *Anal. Chem.* **1993**, *65*, 1594.
- (18) Polce, M. J.; Ren, D.; Wesdemiotis, C. *J. Mass Spectrom.* **2000**, *35*, 1391.
- (19) Morrison, L. J.; Chamot-Rooke, J.; Wysocki, V. H. *Analyst* **2014**, *139*, 2137.
- (20) Perkins, B. R.; Chamot-Rooke, J.; Yoon, S. H.; Gucinski, A. C.; Somogyi, A.; Wysocki, V. H. *J. Am. Chem. Soc.* **2009**, *131*, 17528.
- (21) Bythell, B. J.; Somogyi, A.; Paizs, B. *J. Am. Soc. Mass. Spectrom.* **2009**, *20*, 618.
- (22) Gucinski, A. C.; Chamot-Rooke, J.; Nicol, E.; Somogyi, A.; Wysocki, V. H. *J. Phys. Chem. A* **2012**, *116*, 4296.
- (23) Armentrout, P. B.; Heaton, A. L. *J. Am. Soc. Mass. Spectrom.* **2012**, *23*, 632.
- (24) Balta, B.; Aviyente, V.; Lifshitz, C. *J. Am. Soc. Mass. Spectrom.* **2003**, *14*, 1192.
- (25) Tang, X. J.; Thibault, P.; Boyd, R. K. *Anal. Chem.* **1993**, *65*, 2824.
- (26) Tang, X. J.; Boyd, R. K. *Rapid Commun. Mass Spectrom.* **1994**, *8*, 678.
- (27) Vachet, R. W.; Bishop, B. M.; Erickson, B. W.; Glish, G. L. *J. Am. Chem. Soc.* **1997**, *119*, 5481.
- (28) Yague, J.; Paradela, A.; Ramos, M.; Ogueta, S.; Marina, A.; Barahona, F.; de Castro, J. A. L.; Vazquez, J. *Anal. Chem.* **2003**, *75*, 1524.
- (29) Harrison, A. G.; Young, A. B.; Bleiholder, C.; Suhai, S.; Paizs, B. *J. Am. Chem. Soc.* **2006**, *128*, 10364.
- (30) Bleiholder, C.; Osburn, S.; Williams, T. D.; Suhai, S.; Van Stipdonk, M.; Harrison, A. G.; Paizs, B. *J. Am. Chem. Soc.* **2008**, *130*, 17774.
- (31) Chen, X.; Yu, L.; Steill, J. D.; Oomens, J.; Polfer, N. C. *J. Am. Chem. Soc.* **2009**, *131*, 18272.
- (32) Chen, X. A.; Steill, J. D.; Oomens, J.; Polfer, N. C. *J. Am. Soc. Mass. Spectrom.* **2010**, *21*, 1313.
- (33) Chen, X.; Tirado, M.; Steill, J. D.; Oomens, J.; Polfer, N. C. *J. Mass Spectrom.* **2011**, *46*, 1011.

- (34) Wysocki, V. H.; Tsaprailis, G.; Smith, L. L.; Brecht, L. A. *J. Mass Spectrom.* **2000**, *35*, 1399.
- (35) Erlekam, U.; Bythell, B. J.; Scuderi, D.; Van Stipdonk, M.; Paizs, B.; Maitre, P. *J. Am. Chem. Soc.* **2009**, *131*, 11503.
- (36) Wang, D.; Gulyuz, K.; Stedwell, C. N.; Polfer, N. C. *J. Am. Soc. Mass. Spectrom.* **2011**, *22*, 1197.
- (37) Wang, D.; Gulyuz, K.; Stedwell, C. N.; Yu, L.; Polfer, N. C. *Int. J. Mass spectrom.* **2012**, *330*, 144.
- (38) Wassermann, T. N.; Boyarkin, O. V.; Paizs, B.; Rizzo, T. R. *J. Am. Soc. Mass. Spectrom.* **2012**, *23*, 1029.
- (39) Bythell, B. J.; Hernandez, O.; Steinmetz, V.; Paizs, B.; Maitre, P. *Int. J. Mass spectrom.* **2012**, *316*, 227.
- (40) Sinha, R. K.; Erlekam, U.; Bythell, B. J.; Paizs, B.; Maitre, P. *J. Am. Soc. Mass. Spectrom.* **2011**, *22*, 1645.
- (41) Hernandez, O.; Pulay, P.; Maitre, P.; Paizs, B. *J. Am. Soc. Mass. Spectrom.* **2014**, *25*, 1511.
- (42) Durand, S.; Rossa, M.; Hernandez, O.; Paizs, B.; Maitre, P. *J. Phys. Chem. A* **2013**, *117*, 2508.
- (43) Somogyi, A.; Harrison, A. G.; Paizs, B. *J. Am. Soc. Mass. Spectrom.* **2012**, *23*, 2055.
- (44) Fenn, J. B.; Mann, M.; Meng, C. K.; Wong, S. F.; Whitehouse, C. M. *Science* **1989**, *246*, 64.
- (45) Yamashita, M.; Fenn, J. B. *J. Phys. Chem.* **1984**, *88*, 4451.
- (46) Covey, T. R.; Thomson, B. A.; Schneider, B. B. *Mass Spectrom. Rev.* **2009**, *28*, 870.
- (47) Gabelica, V.; De Pauw, E. *Mass Spectrom. Rev.* **2005**, *24*, 566.
- (48) Verkerk, U. H.; Zhao, J. F.; Lau, J. K. C.; Lam, T. W.; Hao, Q.; Steill, J. D.; Siu, C. K.; Oomens, J.; Hopkinson, A. C.; Siu, K. W. M. *Int. J. Mass spectrom.* **2012**, *330*, 254.
- (49) Richardson, J. S. *Adv. Protein Chem.* **1981**, *34*, 167.
- (50) Toniolo, C. *CRC critical reviews in biochemistry* **1980**, *9*, 1.
- (51) Hutchinson, E. G.; Thornton, J. M. *Protein Sci.* **1994**, *3*, 2207.
- (52) Hutchinson, E. G.; Sessions, R. B.; Thornton, J. M.; Woolfson, D. N. *Protein Sci.* **1998**, *7*, 2287.
- (53) Guruprasad, K.; Rajkumar, S. *Journal of Biosciences* **2000**, *25*, 143.
- (54) Chin, W.; Piuzzi, F.; Dimicoli, I.; Mons, M. *PCCP* **2006**, *8*, 1033.
- (55) Chin, W.; Mons, M.; Dognon, J. P.; Piuzzi, F.; Tardivel, B.; Dimicoli, I. *PCCP* **2004**, *6*, 2700.
- (56) Chin, W.; Piuzzi, F.; Dognon, J. P.; Dimicoli, I.; Mons, M. *J. Chem. Phys.* **2005**, *123*.
- (57) Chin, W.; Dognon, J. P.; Piuzzi, F.; Tardivel, B.; Dimicoli, I.; Mons, M. *J. Am. Chem. Soc.* **2005**, *127*, 707.
- (58) Pearlman, D. A.; Case, D. A.; Caldwell, J. W.; Ross, W. S.; Cheatham, T. E.; Debolt, S.; Ferguson, D.; Seibel, G.; Kollman, P. *Comput. Phys. Commun.* **1995**, *91*, 1.
- (59) Cimas, A.; Vaden, T. D.; de Boer, T. S. J. A.; Snoek, L. C.; Gageot, M. P. *Journal of Chemical Theory and Computation* **2009**, *5*, 1068.
- (60) Gregoire, G.; Gageot, M. P.; Marinica, D. C.; Lemaire, J.; Schermann, J. P.; Desfrancois, C. *PCCP* **2007**, *9*, 3082.
- (61) Roscioli, J. R.; McCunn, L. R.; Johnson, M. A. *Science* **2007**, *316*, 249.
- (62) Wu, R. H.; McMahon, T. B. *ChemPhysChem* **2008**, *9*, 2826.
- (63) Gapeev, A.; Dunbar, R. C. *J. Am. Chem. Soc.* **2001**, *123*, 8360.
- (64) Dunbar, R. C.; Steill, J. D.; Oomens, J. *PCCP* **2010**, *12*, 13383.
- (65) Wieczorek, R.; Dannenberg, J. J. *J. Am. Chem. Soc.* **2003**, *125*, 14065.





4 PROBING MOBILITY SELECTED  
SACCHARIDE ISOMERS: SELECTIVE  
ION-MOLECULE REACTIONS AND  
WAVELENGTH-SPECIFIC IR  
ACTIVATION

4	PROBING MOBILITY SELECTED SACCHARIDE ISOMERS: SELECTIVE ION-MOLECULE REACTIONS AND WAVELENGTH-SPECIFIC IR ACTIVATION .....	123
4.1	Ion Mobility Spectrometry (IMS).....	125
4.2	IMS applied to sugar separation.....	129
4.3	Coupling DIMS to MS/MS.....	136
4.4	Results and discussion.....	139
4.5	Conclusions.....	149
4.6	Bibliography.....	152

## 4.1 Ion Mobility Spectrometry (IMS).

### 4.1.1 IMS: A brief overview.

Ion Mobility Spectrometry (IMS) is an analytical technique that separates ionic mixtures based on the transport properties of gas-phase ions through a carrier gas. IMS on its own has been extensively employed for the detection of explosives [1,2], drugs [3,4] and chemical-warfare agents [5,6]. It is often said that the integration of IMS to mass spectrometers [7] offers a new dimension to mass spectrometry because IMS and MS separate ions as a function of their 3D shape and  $m/z$ , respectively. Progresses in terms of IMS high-resolution allow for the separation of structural isomers, even of small molecules [8-10].

The Drift Tube Ion Mobility Spectrometry (DTIMS) is the oldest IMS technique. Ions are introduced in a drift tube where a static uniform electric field of 5-20 V/cm is applied. Ions drift along the axis of the drift cell which is on the order of 50 cm to 1 m long. The typical pressure of the buffer gas is few Torr. Under the influence of multiple collisions with the buffer gas, ions reach a terminal velocity  $v$ , and the observable is the drift time, which is the time for an ion to drift through the cell. Small ions drift faster than bigger ions which have a large collision cross section (CCS) with the buffer gas.

The principle of the separation of two ions using DTIMS is illustrated in Figure 4-1. The velocity of the ions is proportional to the electric field ( $E$ ). The proportionality constant  $K$  is called ion mobility which can be expressed as a function of the CCS ( $\Omega$ ) of the ion through the Nernst-Townsend-Einstein relationship where  $\mu$  is the reduced mass of the ion and buffer gas,  $T$  the temperature,  $k_B$  the Boltzmann constant,  $ze$  the charge of the ion, and  $N$  the number density of the buffer gas. As shown in the expression of  $K$  as a function of the CCS, the ion mobility depends on the nature of the buffer gas. Commonly used gases are Helium and Nitrogen, but other buffer gases or gas mixtures have been shown to improve ion separation [11].

$$v = K \cdot E$$

$$K = \frac{3}{16} \left( \frac{2\pi}{\mu k_B T} \right)^{1/2} \left( \frac{ze}{N\Omega} \right)$$

The relationship between  $K$  and  $\Omega$  is only true at the so-called “low electric field limit”. In fact, it is better to talk about a low intensity of  $E/N$  (reduced electric field). For this purpose, it is convenient to define the Townsend unit ( $1 \text{ Td} = 10^{-21} \text{ V m}^2$ ) [12]. And the above  $K$  formula is only true at  $E/N$  lower ratio than 2 Td.

IMS-MS instruments are not only used to separate but also to derive structural information on the 3D shape of the gas phase ions. The CCS ( $\Omega$ ) is an important concept which is routinely used in the IMS-MS community. Knowing the length of the drift cell, and measured drift time of each ions, CCS of each ions can be extracted using the two above formulae. Structural information can be derived from the CCS which can be modeled using theory. Different method can be used for predicting the CCS values of the various isomers of a given ion. Either elastic hard sphere scattering theory [13] or trajectory method [14] can be used.

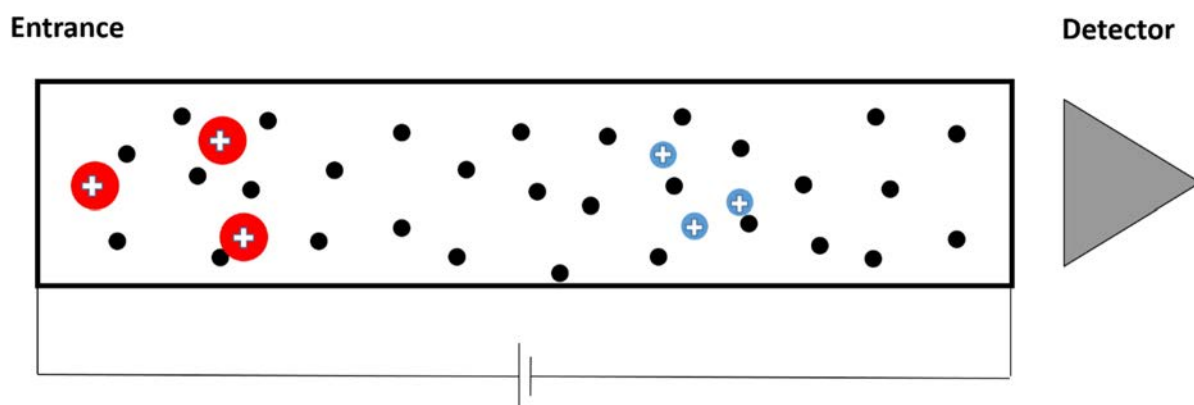


Figure 4-1 : Separation of two molecular ions with different collision cross section (CCS) by Ion Mobility Spectrometry. Black circles represent buffer gas atoms.

The SYNAPT G2 (Waters) IMS-MS instrument is based on a drift tube, but the ion separation principle is slightly different from the one in DTIMS. The technique used is called Tunable Wave Ion Mobility Spectrometry (TWIMS). As in DTIMS, ions move along the tube axis under the influence of a low electric field. In addition, “travelling electric wave” is applied to the set of electrodes which contribute to the radial confinement of the ions [15], and also improves the resolving power up to 30-40

for the latest version of the commercial instrument (SYNAPT G1) [16]. TWIMS device works under the low-field limit, and mobility data can thus be exploited to derive structural information. Due to the travelling wave applied to the electrodes, however, a calibration of the instrument is needed for deriving CCS values [17-19].

#### 4.1.2 Differential Ion Mobility Spectrometry (DIMS).

Differential ion Mobility is another IMS technique which relies on the difference in ion mobility between high and low electric field. Ions are entrained by a gas flow and an asymmetric electric field is applied perpendicular to the gas flow. Ion mobility is rather constant at low electric field, but changes for electric field values higher than 1.5 kV/cm. As illustrated in Figure 4-2, two ions may have similar mobilities at low field (green and blue), but they can evolve differently at high electric field values. By applying an asymmetric electric field, ions which could not be separated at low electric field using DTIMS or TWIMS can be separated using DIMS. A disadvantage of techniques based on asymmetric electric field is that the mobility at high electric is not well understood and still the subject of an intense debate [20]. As a result, CCS cannot be extracted and thus no structural information can be simply derived from DIMS.

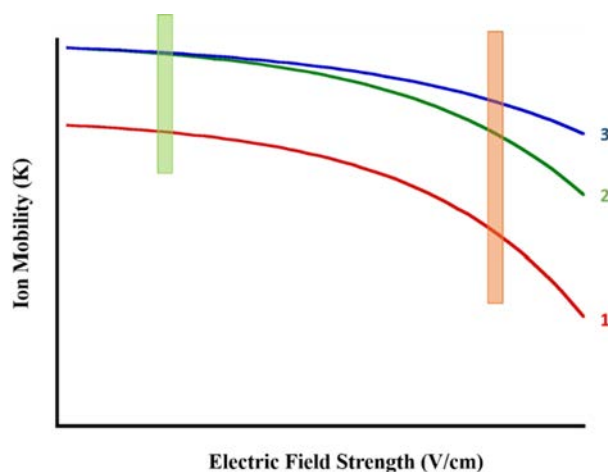


Figure 4-2: Ion mobilities of three different molecular ions as a function of the electric Field Strength. Ion 2 and ion 3 cannot be differentiated by Ion Mobility Spectrometry under low Electric Field Strength conditions (green region). The two ions can only be effectively separated under high Electric Field Strength conditions (orange region).

Two techniques based on asymmetric electric fields are used. One is called FAIMS for Field Asymmetric IMS. In this case, two concentric electrodes are used. The second one, generally called DIMS (Differential IMS), uses two parallel planar electrodes. As illustrated in Figure 4-3, ions are entrained between the two parallel plates by a gas flow, and the asymmetric RF field applied to the electrodes creates an electric field perpendicular to the electrodes. Depending on the relative mobilities at low and high electric field, ions (green) can go through the device or can be neutralized (red) on one electrode.

The mobility spectra using FAIMS or DIMS correspond to the ion intensity as a function of the compensation voltage called CV. This DC voltage is an off-set which is applied to one of the electrodes in order to select the ions of interest. An ion can go through the DIMS device if the radial displacement under low field ( $d_L$ ) is equal to that at high field ( $d_H$ ). Considering the above relationships, these two displacement values are the same when:

$$K_L \times E_L \times t_L = K_H \times E_H \times t_H$$

By changing the CV offset value, one changes the relative  $E_L$  and  $E_H$  values, and thus allow for another set of ions to go through the DIMS device.

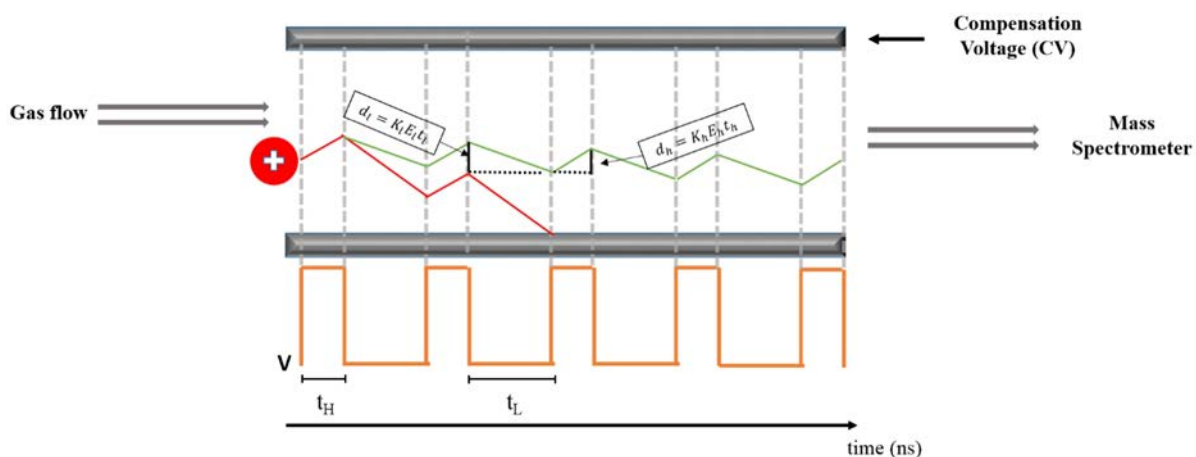


Figure 4-3: Ion trajectory within a Differential Ion Mobility Spectrometer. Molecular ions are repulsed and attracted by the effect of the alternative electric field (voltage represented in orange). A compensation voltage is necessary to maintain the molecular ions to the middle of the two electrodes (trajectory in green color). Otherwise, molecular ions collide with the electrodes (trajectory in red color).

Each IMS design has unique ion mobility characteristics and advantages when coupled with mass spectrometers. Pros and cons of all the IMS methods have been recently discussed in a review [15]. The traditional drift time IMS provides the highest resolving powers, but has a low sensitivity. FAIMS or DIMS resolutions is traditionally poor ( $R < 20$ ) but the inclusion of dopant gases in the carrier gas like He or H<sub>2</sub> can increase the resolution significantly (up to 500) [21-23]. These devices are mounted before the ESI capillary. As a result, a continuous flow of ions can be introduced in the mass spectrometer, which is critical for subsequent MS/MS and in particular for IRMPD spectroscopy in our case.

In this study the Ion Mobility experiments were carried out with a non-commercial Differential Ion Mobility Spectrometer. The Ion Mobility device was conceived and assembled in the laboratory of Professor Gary L. Glish in North Carolina. The characteristic, particularities, and some technical aspects will be provided in the next section.

## 4.2 IMS applied to sugar separation

### 4.2.1 Saccharides: isomers.

The first set of experiments using the set-up integrating the DIMS to the QIT mass spectrometer were performed with a set of saccharides, also named carbohydrates because their general formula is C<sub>m</sub>(H<sub>2</sub>O)<sub>n</sub>. They constitute an important class of biomolecules because they are actively involved in numerous biological processes like embryonic development and differentiation, and cell-cell recognition [24-26]. The structural characterization of saccharides is a first step towards the understanding of their biological activity [27]. In this context, mass spectrometry can be important. For example, collision induced dissociation (CID) has been extensively applied to differentiate the carbohydrate isomers [28-32]. As said in the introduction, the integration of ion mobility spectrometry (IMS) techniques to mass spectrometry (MS) [5, 6] has been shown to be particularly interesting for separating isomeric forms which is of particular interest for saccharides.

We chose to focus on the separation and characterization of three saccharides, namely the methylated  $\alpha$ -glucose,  $\beta$ -glucose, and  $\alpha$ -mannose (Figure 4-4). This choice was made in the perspective

of the comparison with DTIMS and TWIMS data on the same set of molecules recently published by Hill and coworkers [33].

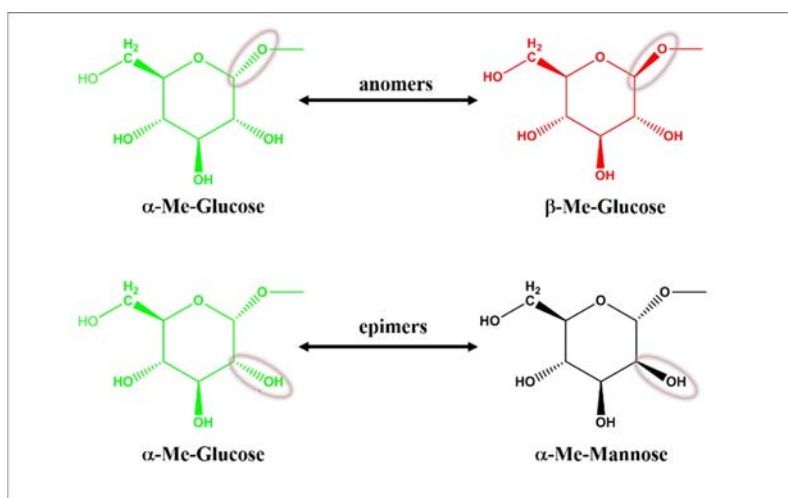


Figure 4-4: Three different methylated monosaccharide isomers.  $\alpha$ -Me-Glucose,  $\beta$ -Me-Glucose, and  $\alpha$ -Me-Mannose are represented in green, red and black colors respectively. The stereochemical relationships between these three diastereoisomers are shown by the circles.

Saccharides are polymers composed of subunits called monosaccharides, and the D-glucose shown in Figure 4-4 is a representative monomer. The general formula for monosaccharides is  $(\text{CH}_2\text{O})_n$ , and they have multiple hydroxyl groups and one carbonyl group. Monosaccharides can be classified according to essentially three characteristics: the number of carbon atoms, the position of the carbonyl group on the carbon chain, and the stereochemistry of the different carbon atoms. The systems studied here are hexoses, because they have six carbon atoms and one ketone group. For a given  $(\text{CH}_2\text{O})_6$ , multiple stereoisomers are possible due to the asymmetric character of carbon atoms C(2), C(3), C(4), and C(5).

As illustrated in Figure 4-5, reversible cyclisation of the monosaccharides may occur following the nucleophilic attack of a hydroxyl group on the ketone group. This leads to a heterocyclic ring with an oxygen bridge between two carbon atoms. Five and six-membered rings are the most common, and they are called furanose and pyranose forms, respectively. There exist in equilibrium with the straight-chain form. Upon the formation of the C(1)-O bond, the C(1) atom becomes asymmetric, and two configurations can be formed. The C(1) carbon is called anomeric, and the two cyclic forms are called

$\alpha$  and  $\beta$  anomers. The three isomers studied and shown in Figure 4-4 correspond to methylated forms of three pyranose: ( $\alpha$ - and  $\beta$ -glucose, and  $\alpha$ -mannose) which methylation occurs on the O(1)H hydroxyl group. Methylated saccharides are in general easier to investigate using mass-spectrometry, leading to less and more specific fragmentation patterns [34]. In the case of monosaccharides, protonation of the anomeric methylated group leads to an easy C(1)-OH<sup>+</sup>Me bond cleavage due to the stabilization of the carbenium ion through the well-known anomeric effect [35].

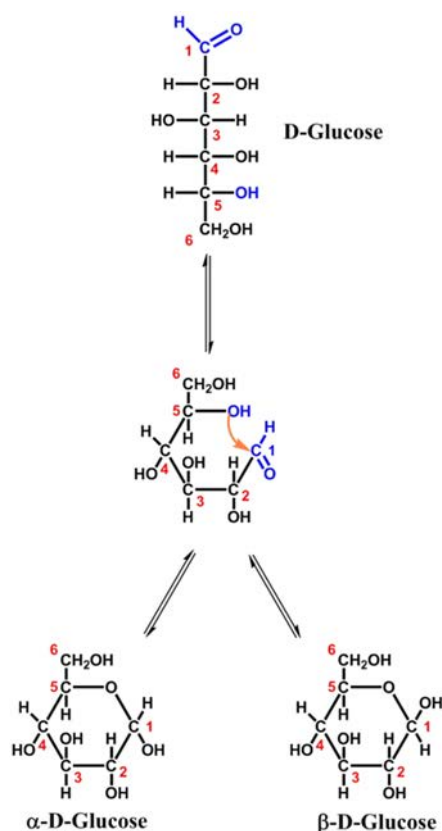


Figure 4-5: Cyclization process of D-Glucose. A nucleophilic attack from the hydroxyl group of the C(5) center to the aldehyde carbonyl group leads to a six-membered ring structure.

The separation and identification of saccharides within a mixture is challenging. Already in the case of the three monosaccharides given in Figure 4-4, it can be seen that they only differ by the chirality of the two carbon centers C(1) and C(2). The structural variety of oligosaccharides or polysaccharides is off course larger. The polymerization occurs through the formation of the so-called glycosidic bond between two monosaccharides. This bond is formed through the nucleophilic attack of one of the

hydroxylic group of one monosaccharide on the hemiacetal or hemiketal group of another monosaccharide (or a polysaccharide already formed).

The structural variety of polysaccharides first results from the fact that multiple hydroxyl groups (4 in the case of the systems studied here) are available for the nucleophilic attack. Second, depending on the experimental conditions, the nucleophilic attack can occur on the two sides of the C(1) anomer atom, leading to two sets of stereoisomers. The stereoselective control of the formation of glycosidic bonds is recognized to be extremely challenging [36,37].

The well-known anomeric effect [35] is an important factor in the chemistry at the C(1) center. For example, protonated monosaccharides formed under ESI conditions are unstable, and the loss of O(1)H<sub>2</sub> water, or O(1)HCH<sub>3</sub> methanol in our case, is observed [34]. Similarly, the formation of an oxacarbenium intermediates [35] on the route to the formation of the glycosidic bond is often discussed [38]. The structural characterization of polysaccharides implies the characterization of the relative positions of the monomers (sequence), of the position of the linkage and of the stereochemistry of the anomer carbon atoms.

#### 4.2.2 IMS applied to saccharides.

Separation and identification of oligosaccharides remain a challenge, for natural but also for synthetic carbohydrates because there are no universal reaction conditions for oligosaccharide synthesis [39]. Complex mixtures of isomeric carbohydrates constituted of monosaccharide residues have to be analyzed, and the structural identification is arduous because it consists in characterizing the anomeric configuration and the monomer stereochemistry, as well as the inter-residue linkage positions and the branching features. In this context, tandem mass spectrometry has been shown to be a promising analytical approach, which allows the selection and manipulation of isomeric species if they are pure. Information is derived from the fragmentation pattern of mass-selected ions, which often are adducts of oligosaccharides and metal cations. Interestingly, it has been observed that the smaller is the metal ion used for ionizing the sample, the larger is the fragmentation yield [40]. Using collision induced dissociation (CID), it has been shown in particular that characteristic CID fragments related to linkage

types can be obtained [28,29]. It has also been observed that the degree of branching of the oligosaccharide, which is of importance for its biology, can be correlated with its fragmentation yield [40].

An important advance in the structural characterization of oligosaccharides was achieved with the integration of ion mobility spectrometry (IMS) techniques to mass spectrometry (MS) [41,42]. Separating isomeric species as a function of their collision cross section with a buffer gas [43-46] allows for an enhancement of the resolving power of the experiment. Additionally, structural information can be derived via the comparison of measured and predicted mobilities [47] of various isomeric forms using either an exact (elastic) hard sphere scattering [13] or a trajectory method [14] calculations. These two advantages were evidenced in pioneering studies ion oligosaccharides using IMS-MS instruments featuring electrospray [37] as well as MALDI [48] ionization techniques. Tetraoses and hexaoses cationized with  $\text{Na}^+$  were studied by Bowers and coworkers [48]. Deprotonated oligosaccharides were studied by Clemmer and coworkers [37], and an interesting aspect of this work was to exploit the fragmentation occurring at the entrance of the drift tube for examining the mobility separation of oligosaccharides and also their fragments.

More systematic recent studies have shown that using low electric field mobility techniques, drift-tube ion mobility spectrometry (DTIMS) and/or, more recently, travelling wave IMS (TWIMS), [49] anomers, epimers and more generally isomeric stereoisomers can be efficiently separated using the IMS-MS approach [9,11,33,50,51]. A subsequent step towards the structural characterization of mobility- and mass-selected ions can be achieved by integrating IMS and tandem mass spectrometry (MS/MS) leading to IMS-MS/MS instruments. The principle added value is that mobility-selected precursor ions can be reacted or dissociated, followed by mass analysis of the product ions [52]. More generally, combining multiple MS/MS approaches, including electron capture dissociation and photo-induced dissociation is highly desirable [53-58].

#### 4.2.3 Alternative methods to provide structural characterization: Spectroscopic Techniques.

Gas-phase spectroscopy of ions integrated to mass spectrometry has been developed in many groups, and applications to mobility and mass-selected ions is under development. Several studies in which the coupling of UV laser with IMS based instruments have been reported recently [56,58,59]. Rizzo and coworkers [56] showed a UV spectroscopic study of mobility selected isomers of doubly protonated peptide bradykinin. The corresponding integrated set-up is based on a cold ion trap, which by itself already greatly simplifies the electronic spectra of large molecular ions [60,61]. A High-Field Asymmetric waveform IMS (FAIMS) device was used to separate conformers before injecting them into a cold ion trap [56]. An interesting output of this work was to provide spectroscopic evidence for conformational equilibrium of mobility-selected conformer.

Doubly protonated Bradykinin peptide was used as a test case. This peptide has different conformers as evidenced by ion mobility [62]. The idea was to filter each individual conformer by FAIMS and then irradiate the isolated conformer. Two problems were detected under these experimental conditions. The first one was that FAIMS device did not provide a sufficient resolution to separate the different conformers. The electronic spectrum of FAIMS-selected conformer showed a mixture of multiple structures. This result suggest that isomerization occurs after FAIMS separation and it is consistent with previous IMS studies of Clemmer [62]. It seems that isomerization occurs during the transfer of the FAIMS-selected ions into the ion-trap, not likely at the exit of the capillary.

The gas phase equilibrium of mobility-selected conformers of bradykinin  $[M+3H]^{3+}$  ions had been also studied in details by Clemmer and coworkers [62,63] using an IMS-IMS instrument, where mobility selected conformers could be energized through collisions (0-70 eV) before their injection into a second drift-tube. The home-built ion mobility spectrometry is composed by two independent drift tubes. In the middle of the two drift tubes there is a funnel to focus the diffuse ion packet which can also be used for ion activation. Two dimensional IMS-IMS-MS could be recorded where IMS-selected ions could be activated between the two drift tubes and the resulting isomer population could thus be separated in the second drift tube. When the activation was turned off, six different structures for  $[Bradikinin-3H]^{3+}$  could be distinguished. The activation energy was increased progressively. The

results showed that starting with any IMS-selected conformers, it was shown that the same quasi-equilibrium distribution was observed.

Clemmer, Reilly and coworkers [57,58] recently proposed two combinations of IMS and UV induced fragmentation for elucidating the structure of disaccharides. It was shown in particular that, in contrast with CID, irradiation at 157 nm generates unique fragments for each disaccharide ion that are useful for distinguishing them.

Another interesting recent report, by Bieske and coworkers [59], describes an IMS+UV set-up allowing for monitoring the mobility variation as a function of the excitation wavelength prior to the injection of ions into a drift tube. The case of polymethine dye HITC was studied. This molecule has multiple C=C bonds and cis-trans inter-conversion can be induced upon UV excitation. The arrival time corresponding to the HITC peak was 22.9 ms. Upon irradiating by UV laser at different energies, different arrival time distribution were found. The arrival time of the HITC ions after irradiation at 650 nm was slightly lower than 22.9 ms. However after irradiation at 765 nm, the recorded arrival time of the HITC was slightly higher. Quantum chemical calculations were carried out and it was suggested that during irradiation of the HITC at 650 nm, trans-to-cis photoisomerization occurred. Conversely a cis-to-trans interconversion was observed during irradiation at 765 nm.

Photoelectron spectroscopy of mobility-selected anions developed by Kappes and coworkers [64,65] is also particularly promising. Using this approach conformer-selective photoelectron spectroscopy of alpha-lactalbumin has been performed on multianions, demonstrating the correlation between mobility (folded versus unfolded) and gas phase adiabatic detachment energies [54].

IR spectroscopy of mobility-selected metal cationized monosaccharides is presented in this study. A differential ion mobility spectrometer (DIMS) has been mounted on the inlet of the mass spectrometer, allowing for MS/MS study of DIMS- and mass-selected isomeric ions. In contrast to DTIMS or TWIMS, structural information cannot be directly linked to the mobility parameter of DIMS. This IMS technique relies on the difference of ion mobility between high and low electric fields, and the mobility under high electric field conditions is still not understood. Conversely, DIMS provides high resolution separation

[66], and coupled with an ion-trap offers high ion sensitivity. In addition, DIMS separates ions in space rather than in time like the other IMS techniques. Thus, DIMS can be readily coupled with any type of mass analyzer, not just time-of-flight. Separation of adducts of alkali cations ( $\text{Li}^+$ ,  $\text{Na}^+$ ,  $\text{K}^+$ ) and monosaccharide methyl glycosides has been investigated, and the DIMS performance in terms of resolving power are compared with recently reported data obtained with DTIMS and TWIMS devices [33]. MS/MS experiments were performed in the case of  $\text{Li}^+$  adducts for probing the structure of DIMS selected isomers. It is shown that selective ion-molecule reactions with water can be observed, and that the yields of this reaction nicely correlate with the mobility results. Similarly, IR spectra recorded for mobility-selected ions are also consistent with the mobility results. It is shown in particular that the two glucose anomer complexes share the same IR signature, a band observed near  $\sim 3400\text{ cm}^{-1}$ . These results can be rationalized using quantum chemical modeling, and they suggest that structural differences between metal cationized monosaccharides are associated with the competition between intra-sugar hydrogen bonding and coordination to the metal cation.

### 4.3 Coupling DIMS to MS/MS.

#### 4.3.1 DIMS and MS/MS: The DIMS 3G assembly.

The planar DIMS 3G (third generation) used in this thesis work developed in the group of G.L. Glish was coupled with a Bruker Esquire 3000+. A schematic view of our experimental set-up is provided in Figure 4-6. The DIMS device is threaded to match the spray shield of a Bruker Esquire 3000, such that the spray shield can be removed and the DIMS assembly can be screwed on in its place. The electrospray is placed in front of the DIMS device. The planar electrodes are 25x6 mm separated by  $\sim 0.5\text{ mm}$ . The carrier gas used in the experiment was 100%  $\text{N}_2$ . The standard glass transfer capillary of the source was replaced with a custom flared glass transfer capillary to improve ion transmission through the DIMS assembly [67].

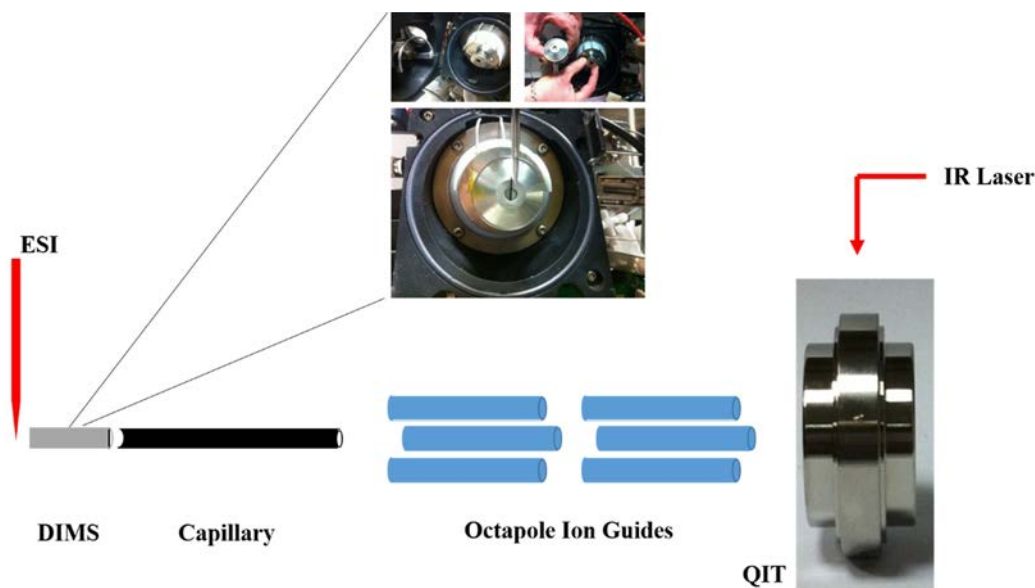


Figure 4-6: Schematic view of the DIMS device assembly integrated to our Esquire 3000+. The DIMS device is located between the needle and the Capillary within the source of the mass spectrometer. Three pictures of the DIMS device are also given.

#### 4.3.2 Radio-frequency waveform.

The radio-frequency applied to the electrodes has a bisinusoidal form (Figure 4-7) approximating a square wave. This particular form is obtained combining two sinusoidal radio-frequencies. The dispersion voltage (DV) is defined by the maximum voltage ( $V_{op}$ ) of the bisinusoidal form. The DV voltage can be adapted to find the best trade-off between separation and ion transmission. All the results obtained by Ion Mobility Spectrometry were performed using a 2 kV value of Dispersion Voltage.

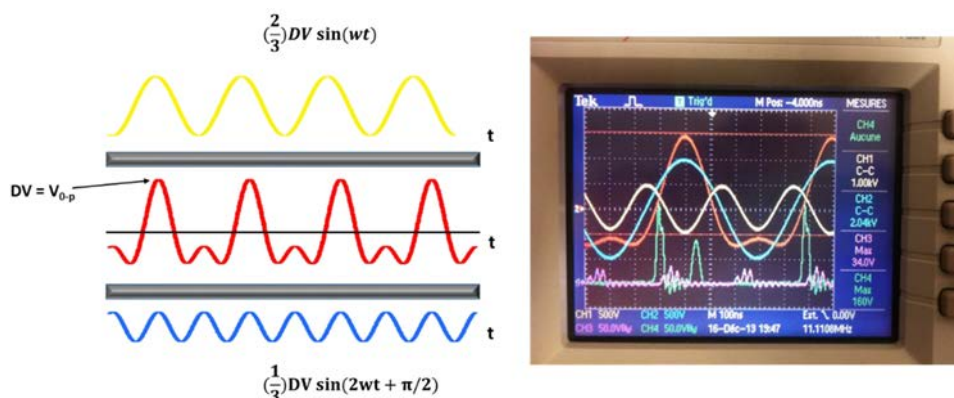


Figure 4-7: Asymmetric electric field applied to the DIMS electrodes. Two bisinusoidal Radio Frequencies (yellow and blue) are combined in order to obtain the resulting Radio frequency waveform (red). In the right panel, a screenshot of our oscilloscope is also given.

### 4.3.3 Two DIMS modes: Scanning and Static modes.

An advantage of the DIMS over the FAIMS device is that the DIMS-MS/MS instrument can be used in nearly ESI-MS/MS mode. For this purpose, the asymmetric RF voltage is turned off, and the two plate electrodes are connected to the ground. When starting with DIMS experiment, this is the first step to check the ion transmission through the DIMS device. Then, RF voltages are tuned on, and the CV is fixed. Using this “static mode”, *i.e.* fixed CV value, the DIMS device is used as an ion filter. The ion of interest can be accumulated and trapped in our QIT allowing for subsequent IRMPD spectroscopy or CID experiments. Prior to fix the CV value, the maximum transmission of the ion of interest has to be extracted from a DIMS chromatogram.

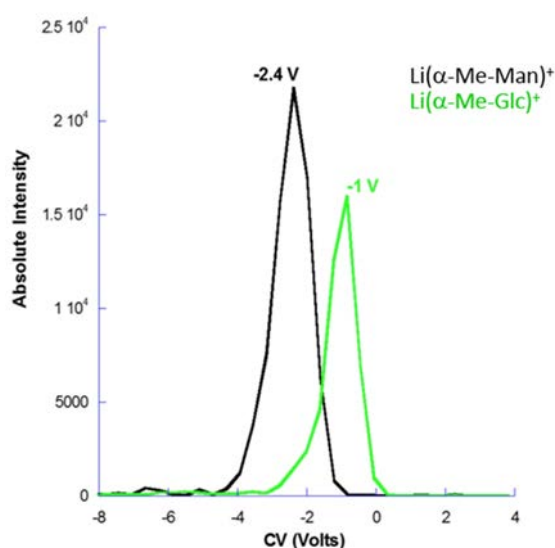


Figure 4-8 : Ion Mobility Chromatogram of two monosaccharide epimers. The absolute intensity of each epimer is monitored as a function of the Compensation Voltage (CV).

A DIMS chromatogram corresponds to the different ion abundances as a function of the CV value. For this purpose, a LabVIEW interface synchronized to the instrument control software is used to synchronize the stepwise change of the compensation voltage (CV) with the “chromatogram mode” of the mass spectrometer. Each MS/MS spectrum in the chromatogram corresponds to a CV value. The LabVIEW interface can either be used under “static mode” (fixed CV) or under “scanning mode” which allows for a stepwise change of the CV value. In Figure 4-8, the ion mobility chromatogram of two monosaccharide isomer complexes is given. The CV is scanned from -40 to 40 V, and the typical fwhm

value of a DIMS peak is less than 1 V. We generally start by scanning using steps of 0.4 V, and then the CV range of interest is scanned with steps of 0.1 V.

#### 4.3.4 Methods.

Adducts of alkali cations ( $\text{Li}^+$ ,  $\text{Na}^+$ ,  $\text{K}^+$ ) and monosaccharide methyl glycosides has been investigated. Sample solutions were prepared mixing 100  $\mu\text{M}$  saccharides (Carbosynth) and 2 mM of different alkali metal salts in  $\text{H}_2\text{O}:\text{CH}_3\text{OH}=3:7$  for electrospray ionization. MS/MS experiments were performed in the case of  $\text{Li}^+$  adducts for probing the structure of DIMS selected isomers.

IR spectroscopy has been carried out in the 2800-3800  $\text{cm}^{-1}$  spectral range after mobility-selection of the metal cations. Monohydrated ions were formed through ion-molecule reaction between DIMS-selected ions and water. The irradiation time for the three monohydrated isomers was 1 second for all monohydrated systems. The experimental IR spectra were compared with the calculated harmonic IR spectra. Theoretical spectra were computed at the B3LYP/6-31G(d,p) level of theory and the infrared frequencies were scaled by a factor of 0.955.

## 4.4 Results and discussion.

### 4.4.1 Separation of alkali saccharide complexes by DIMS.

DIMS spectra of  $\text{M}(\text{Sac})^+$  adducts of alkali cations  $\text{M}^+$  ( $\text{M}=\text{Li}^+$ ,  $\text{Na}^+$ ,  $\text{K}^+$ ) and saccharides ( $\text{Sac}=\alpha\text{-Me-Glc}$ ,  $\beta\text{-Me-Glc}$ , and  $\alpha\text{-Me-Man}$ ) obtained using our DIMS device coupled to a quadrupole ion trap are displayed in Figure 4-9. For each  $\text{M}^+$  alkali cation, in addition to the spectrum of each individual isomer, the DIMS spectrum of the isomer mixture was also recorded. The dispersion voltage DV values were 2.0 kV ( $\sim 40$  kV/cm) for the three alkali cations. This value was found to correspond to the best trade-off between ion transmission and mobility separation. As can be seen in Figure 4-9, particularly in the case of sodium adducts, different ionization efficiencies are observed for the isomers using equimolar mixtures, and the relative efficiencies vary with cation. This is probably related to the relative affinity of the methyl glycoside isomers to the alkali cation [48,68].

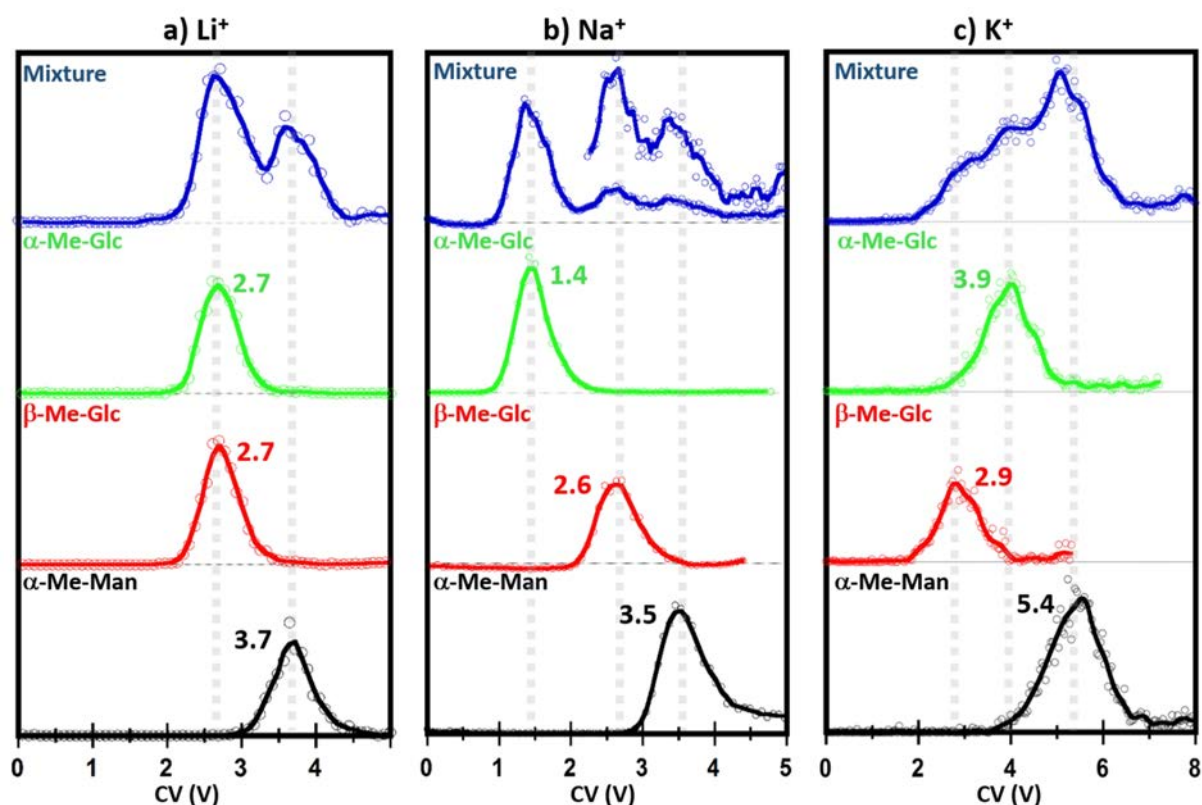


Figure 4-9: DIMS spectra of complexes of Saccharides and  $\text{Li}^+$  (a),  $\text{Na}^+$  (b), and  $\text{K}^+$  (c). In each panel, the DIMS spectrum of the individual isomer (Sac= $\alpha$ -Me-Glucose (green),  $\beta$ -Me-Glucose (red) and  $\alpha$ -Me-Mannose (black)) is given along with the spectrum recorded for the equimolar mixture (blue).

A single peak was observed for each combination of cation and saccharide, suggesting that a single conformer/isomer is formed in all cases. The peak shape observed for the individual ions in the cases of  $\text{M}^+=\text{Li}^+$  and  $\text{Na}^+$  (Figure 4-9a and 4-9b, respectively) is the same, with a fwhm value of  $\sim 0.5$  V. The larger peak width observed in the case of  $\text{K}^+$  (Figure 4-9c) may suggest that more flexible structures or mixtures of conformers are formed.

Separation between anomers and epimers is an important goal [33,69]. The comparison of the DIMS spectra recorded for the sugar mixtures clearly show that the most efficient separation could be obtained with  $\text{Na}^+$  as an ionizing agent. In particular, the complexes corresponding to the glucose anomers, and to the methyl- $\alpha$ -glucose and methyl- $\alpha$ -mannose epimers are well resolved. For the  $\text{Na}^+$  complexes, the peak separation between the two glucose anomers is 1.2 V with a peak fwhm of 0.5 V. For these anomers bound to  $\text{Na}^+$ , the DIMS resolution is 1.41, which is very close to the corresponding DTIMS 1.12 value, and larger than the TWIMS 0.44 value recently reported by Hill and coworkers.[33]

Separation of anomers, epimers and more generally isomers of methyl glycosides does not only depend on the stereochemistry of the compounds, but also on its coordination to the ionizing cation. This is clearly illustrated in Figure 4-9 which shows that the two glucose anomers have identical CV values when complexed to  $\text{Li}^+$ , while two well resolved peaks can be observed when they are complexed to  $\text{Na}^+$  or  $\text{K}^+$ . Furthermore, it is interesting to observe that the relative CV values of the two glucose anomers switch when changing the cation from  $\text{Na}^+$  to  $\text{K}^+$  (Figure 4-9b and 4-9c, respectively). Even if there is no obvious correlation between the DIMS mobility parameter (CV) and the collision cross section, as in DTIMS or even TWIMS, this observation suggests a non-trivial change of coordination when the size of the alkali cation increases.

As mentioned above, MS/MS experiments on DIMS- and mass-selected ions can afford structural information, and could also be interesting for enhancing the analytical resolving power. The CID spectra of the isomers studied here are similar, making it difficult to distinguish them. Two alternative MS/MS approaches are shown to provide unique structural information on the mobility selected methyl glycosides/ $\text{M}^+$  complexes in the case of  $\text{M}=\text{Li}$ . The first one was Ion Molecule Reaction of Ion mobility selected isomers.

#### 4.4.2 Ion-Molecule Reaction (IMR) of DIMS-Selected Ions: More insights into the structural characterization.

In an attempt to probe the structure of these  $\text{Li}^+$  adducts,  $\text{MS}^2$  experiments were carried out on DIMS selected  $\text{Li}(\text{Sac})^+$  ions. Following their mass selection, ions were allowed to react with water seeded in the He buffer gas using a set-up allowing for a control of the neutral flow [70]. The corresponding mass-spectra for a reaction time delay of three seconds are provided in Figure 4-10. While the monohydrated  $\text{Li}(\text{Sac})^+$  adducts are formed in large amount in the cases of the two glucose anomers, association reaction of water in the case of the methyl- $\alpha$ -mannose is less favorable. Only ~8% of the monohydrated adduct could be formed after three seconds.

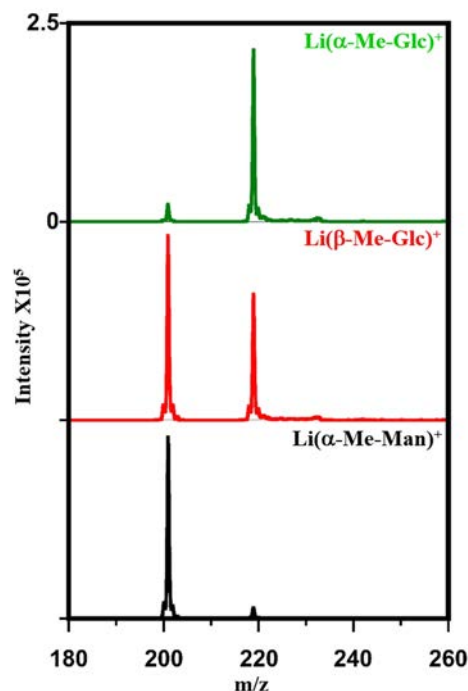


Figure 4-10:  $MS^2$  mass spectra where DIMS- and mass-selected of  $Li(Sac)^+$  ions (Sac= $\alpha$ -Me-Glucose (a);  $\beta$ -Me-Glucose (b), and  $\alpha$ -Me-Mannose (c)) ions were allowed to react for three seconds with water seeded in the He buffer gas.

These results are consistent with the shape of the DIMS spectra observed for the lithiated complexes. The fact that a single mobility peak corresponding to the two glucose anomers was observed may suggest that the two corresponding complexes have similar 3D structure which, in turn, would suggest that the  $Li^+$  coordination number is the same. Considering the strong dependency of the  $H_2O-Li^+$  binding energy on the  $Li^+$  coordination number [71], it could be conceived that the complex formed with the methyl- $\alpha$ -mannose corresponds to a larger coordination number of the metal, and thus to a weaker binding and less efficient association reaction with water.

These interesting differences led to a more detailed kinetic study. In figure 4-11 the relative intensity of each individual saccharide is plotted as a function of the reaction time with water. The formation of monohydrated saccharides is considered as a pseudo first order kinetic reaction. At first sight it can be seen that the amount of monohydrated  $Li(Sac)^+$  formed depends on the nature of the isomer. In the case of mannose, only 8% of monohydrated  $Li(Sac)^+$  is formed whereas for  $\alpha$ -glucose it

is around 90%. For  $\beta$ -glucose the equilibrium of the reaction is reached when 45% of monohydrated adduct is formed.

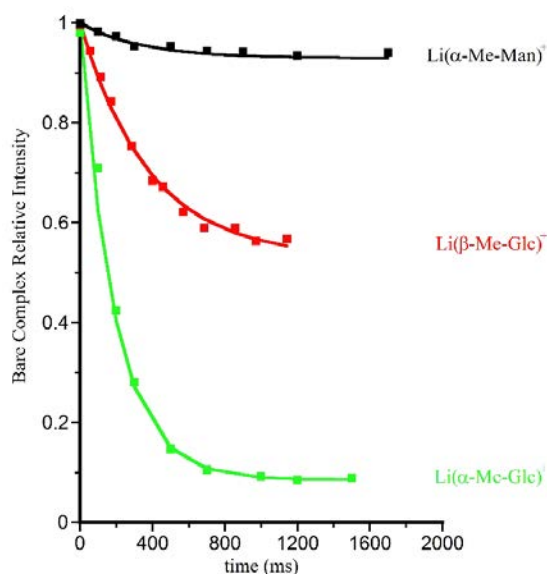


Figure 4-11: Kinetic of the hydration reaction of the three lithiated monosaccharide isomers. The intensity of the bare complexes is monitored as a function of the reaction time.

#### 4.4.3 Infrared Spectroscopy of $\text{Li}(\text{Sac})(\text{H}_2\text{O})^+$ .

Structural information on the mobility selected  $\text{Li}(\text{Sac})^+$  adducts could be derived using  $\text{MS}^3$  experiments.  $\text{Li}^+$  adducts were DIMS and mass-selected, allowed to react with water, and the mass-selected monohydrated clusters were then activated using a wavelength tunable IR laser. Reference gas phase IR spectra of electrosprayed monohydrated  $\text{Li}(\text{Sac})(\text{H}_2\text{O})^+$  complexes were first recorded using a hybrid FT-ICR, in which  $\text{Li}(\text{Sac})^+$  complexes were mass-selected in a linear quadrupole before their accumulation in a linear hexapole ion-trap pressurized with Ar seeded with water [70].

$\text{Li}(\text{Sac})(\text{H}_2\text{O})^+$  adducts could be formed, as in the quadrupole ion-trap, and then transferred in the ICR cell where they were mass-selected and interrogated with the tunable IR laser. The advantage of this set-up over the quadrupole ion-trap is that under the low pressure conditions of the ICR cell, the above discussed association/dissociation water reactions do not compete with the IR activation. As a result, well resolved IR spectra could be recorded for the  $\text{Li}(\text{Sac})(\text{H}_2\text{O})^+$  adducts (Figure 4-12),

especially in the case of the Sac=  $\alpha$ -Methyl-mannose for which the association reaction efficiency is low.

Gas phase IR spectra of DIMS selected isomers were then recorded in the 3000-3700  $\text{cm}^{-1}$  using our quadrupole ion-trap equipped with the DIMS device by setting the CV to a value to transmit the specific ion of interest and scanning the laser wavelength. As discussed recently by Clemmer, Reilly and coworkers,[58] sensitivity is an important challenge for performing IR photodissociation. With this respect, DIMS is the method of choice since using a fixed CV value, DIMS selected ions can be continuously accumulated in the quadrupole ion trap, before being subjected to MS/MS experiments [72]. The IRMPD spectra recorded for the DIMS selected  $\text{Li}(\alpha\text{-Me-Glc})(\text{H}_2\text{O})^+$  and  $\text{Li}(\beta\text{-Me-Glc})(\text{H}_2\text{O})^+$  adducts are shown in Figure 4-12a and 4-12b, respectively. Using an irradiation time of 1s, up to 10% fragmentation could be observed, providing good signal/noise. Overall, the IR spectra of mobility-selected ions compare very well with reference spectra recorded without DIMS selection using our hybrid FT-ICR (Figure 4-12).

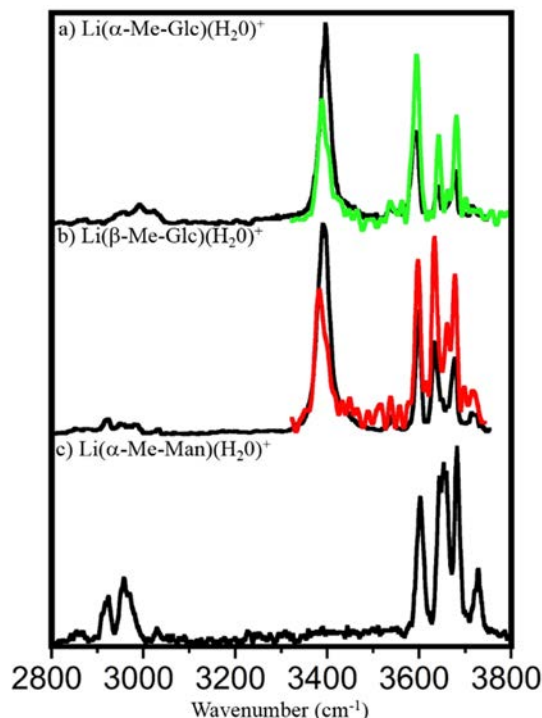


Figure 4-12: IR spectra of  $\text{Li}(\text{Sac})(\text{H}_2\text{O})^+$  ions. a) Sac= $\alpha$ -Me-Glucose; b) Sac= $\beta$ -Me-Glucose; c) Sac= $\alpha$ -Me-Mannose. Full line black spectra correspond to reference IR spectra of mass-selected electrosprayed ions recorded using a hybrid FT-ICR. IR spectra of DIMS- and mass-selected ions using a quadrupole ion trap of  $\text{Li}(\alpha\text{-Me-Glucose})(\text{H}_2\text{O})^+$   $\text{Li}(\beta\text{-Me-Glucose})(\text{H}_2\text{O})^+$  ions given in panel a (Green) and b (Red), respectively.

Well resolved bands are observed above  $3100\text{ cm}^{-1}$ . They correspond to the OH stretches of sugar and water moieties. In addition, weak bands corresponding to CH stretches near  $3000\text{ cm}^{-1}$  can also be distinguished. Considering the weak absorbance of the CH stretching modes, this observation provides evidence for the high sensitivity of IR spectroscopy. Since the laser power increases from  $3100\text{ cm}^{-1}$  to  $3700\text{ cm}^{-1}$ , it is thus likely that all weak IR absorption bands can be revealed through IR induced photodissociation under our experimental conditions.

A detailed assignment of the observed bands is provided in the following chapter. We rather would like to focus on the main difference between the spectra of the  $\text{Li}(\text{Sac})(\text{H}_2\text{O})^+$  adducts of the two anomers of glucose (Figure 4-12a and 4-12b) and the one corresponding to  $\text{Sac}=\alpha\text{-Me-Man}$  (Figure 4-12c). While no band can be observed in the  $3100\text{-}3500\text{ cm}^{-1}$  range in the latter case, a band is observed near  $\sim 3400\text{ cm}^{-1}$  in the former two cases. On the basis of spectroscopic studies of water solvated metal complexes,[73] the position of this band is characteristic of a hydrogen bonded OH stretch.

#### 4.4.4 Structure-specific band observed for glucose anomers.

The band observed near  $\sim 3400\text{ cm}^{-1}$  for both  $\text{Li}(\alpha\text{-Me-Glc})(\text{H}_2\text{O})^+$  and  $\text{Li}(\beta\text{-Me-Glc})(\text{H}_2\text{O})^+$  complexes is interesting because it is likely to be structure-specific. Structure of the present  $\text{Li}(\text{Sac})(\text{H}_2\text{O})^+$  complexes, and more generally of metal-saccharide complexes, is the result of a trade-off between the maximization of the coordination of the metal cation and the intrinsic conformational energetics of the saccharide, which is for a large part driven by hydrogen bonding. This is clearly illustrated by the work of Armentrout and coworkers [74] on the thermochemistry and structures of  $\text{Na}^+$  coordinated pentose and hexose, which had also been investigated earlier by Wesdemiotis and coworkers [68].

Density functional calculations were being carried out on the  $\text{Li}(\text{Sac})(\text{H}_2\text{O})^+$  ( $\text{Sac}=\alpha\text{-Me-Glc}$ ,  $\beta\text{-Me-Glc}$ , and  $\alpha\text{-Me-Man}$ ) complexes. These results will be discussed in more details in the next chapter. The harmonic frequencies of the lowest energy structures of each individual hydrated adduct are compared with experimental infrared spectra in Figure 4-13.

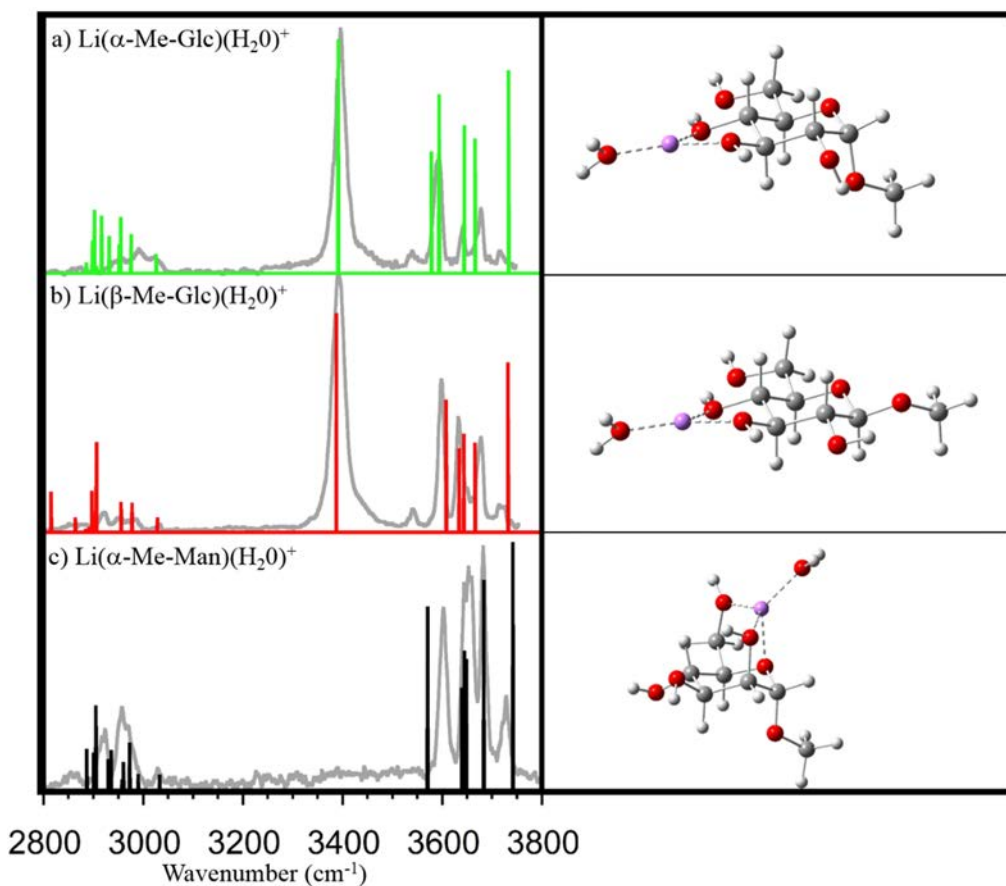


Figure 4-13: IR spectra and corresponding lowest-energy structure of  $\text{Li}(\alpha\text{-Me-Glucose})(\text{H}_2\text{O})^+$  (a),  $\text{Li}(\beta\text{-Me-Glucose})(\text{H}_2\text{O})^+$  (b), and  $\text{Li}(\alpha\text{-Me-Mannose})(\text{H}_2\text{O})^+$  complex ions (c). In each case, the experimental IR spectrum (full line, in grey) is compared with the IR absorption spectrum predicted for the lowest energy structure. Stick bars represent the intensities associated the harmonic frequencies (scaling factor=0.955) computed at B3LYP/6-31G (d,p) level of theory.

Within the large number of optimized structures, two types of low-energy structures can be distinguished. As found for  $\text{Na}^+$ -hexose, [68,74] structures with tri- or even tetradentate coordination of the sugar unit to the  $\text{Li}^+$  were found. Such structures were found to be the most favorable ones for the  $\text{Li}(\alpha\text{-Me-Man})(\text{H}_2\text{O})^+$  system, and the lowest-energy structure is given in Figure 4-13c. The Methyl- $\alpha$ -Mannose has a  ${}^4\text{C}_1$  chair conformation, and it is bonded through the axial O(2)H, hemiacetal O(5) and hydroxymethyl O(6)H oxygen atoms. The predicted IR absorption spectrum for this structure is given in Figure 4-13c. As can be seen in this Figure, the observed bands nicely match with the predicted IR absorption bands in the OH stretching region.

In the case of the two glucose anomers, however, the bonding motif associated with the lowest energy structure is different. The lowest energy structure of  $\text{Li}(\alpha\text{-Me-Glc})(\text{H}_2\text{O})^+$  is shown in Figure 4-

13a. The sugar is bound to  $\text{Li}^+$  through only two oxygen atoms, and the hydroxymethyl OH group is involved in an intra-sugar hydrogen bond. Structures with a tridentate sugar coordination, *i.e.* similar to the lowest energy structure of the  $\text{Li}(\alpha\text{-Me-Man})(\text{H}_2\text{O})^+$  system (Figure 4-13c), are found higher in energy ( $\sim 10$  kJ/mol) than the structure shown in Figure 4-13a. The lowest-energy structure found for the glucose containing complexes is characterized by a sugar unit in a  ${}^4\text{C}_1$  chair conformation bound in a bi-dentate fashion through the hydroxyl O(3) and O(4) oxygen atoms. The O(4)H is also involved in a strong hydrogen bond with the hydroxymethyl oxygen characterized by a O(4)H-O(5) distance of  $\sim 180$  pm.

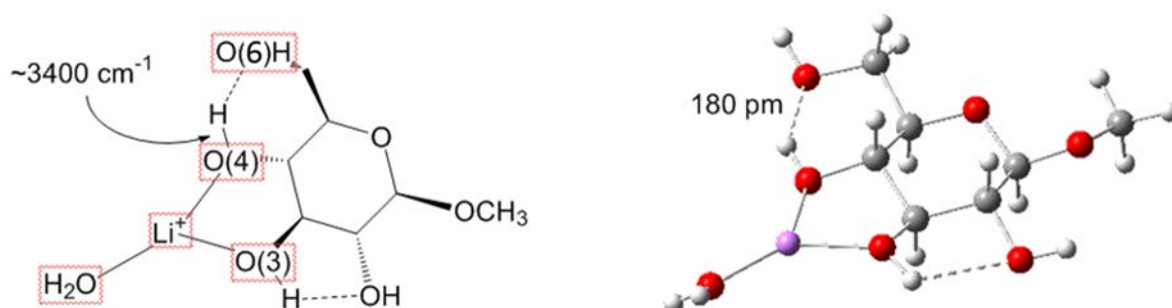


Figure 4-14: A schematic view of the lowest energy structure of  $\text{Li}(\alpha\text{-Me-Glc})(\text{H}_2\text{O})^+$  is provided in the left panel. The  $3400\text{ cm}^{-1}$  frequency corresponds to the stretching mode of the O(4)H group of the molecular ion. A picture corresponding to the same complex is provided in the right panel indicating the distance of the O(4)H...O(6)H hydrogen bond.

The predicted IR absorption spectrum for the lowest energy structure of  $\text{Li}(\alpha\text{-Me-Glc})(\text{H}_2\text{O})^+$  and  $\text{Li}(\beta\text{-Me-Glc})(\text{H}_2\text{O})^+$  is also given in Figure 4-13a and 4-13b along with the experimental spectrum (grey trace). The observed bands nicely match with the predicted IR absorption bands in the OH stretching region. In particular, an IR absorption band is predicted near  $\sim 3400\text{ cm}^{-1}$  which could explain the structure-specific IR band observed for both  $\text{Li}(\alpha\text{-Me-Glc})(\text{H}_2\text{O})^+$  and  $\text{Li}(\beta\text{-Me-Glc})(\text{H}_2\text{O})^+$  complexes. The corresponding normal mode essentially involves the O(4)-H stretching mode (Figure 4-14). The  $\sim 200\text{ cm}^{-1}$  red-shift associated with this vibrational mode is characteristic of the  $\text{Li}^+\text{-O(4)-H-O(6)}$  bonding motif where the O(4)H hydroxyl group acts simultaneously as an electron donor to  $\text{Li}^+$  and hydrogen bond donor to the hydroxymethyl OH group. Similar hydrogen bonding motifs have been characterized when progressive water solvation of metal cation has been studied in the gas phase

using IR spectroscopy [73]. Bands significantly red-shifted as compared to the free OH stretching position could be observed upon formation of the second coordination shell. It should be noted however, that these bands observed for the  $M(H_2O)_n^+$  systems[73] were significantly broader than the  $\sim 3400\text{ cm}^{-1}$  band observed for the present  $Li(Sac)(H_2O)^+$  complexes.

The structures obtained for both  $Li(\alpha\text{-Me-Glc})(H_2O)^+$  and  $Li(\beta\text{-Me-Glc})(H_2O)^+$  complexes, versus the structure of the  $Li(\alpha\text{-Me-Man})(H_2O)^+$ , together with the spectroscopic results provide a consistent picture of the DIMS and ion-molecule reaction results for the lithiated systems. As evidenced by the determination of sequential water binding energies of water to  $Li^+$ , [75] the binding energy of water to  $Li^+$  decreases when the CN of  $Li^+$  increases. One can thus expect that the binding energy of water to  $Li^+$  is stronger when it is only dicoordinated (glucose anomers complexes) than when it is tricoordinated (mannose) by the sugar. This would thus explain that the water association/dissociation equilibrium is more displaced towards the monohydrated complex in the former than in the latter case. Similarly, assuming that the sugar denticity remains unchanged in the  $Li(Sac)^+$  versus the  $Li(Sac)(H_2O)^+$ , the structures for  $M=\alpha\text{-Me-Glc}$  and  $\beta\text{-Me-Glc}$  would be similar, which would explain that the optimum CV value for the corresponding complexes are very similar. A different CV value, however, would be expected for the  $Li(\alpha\text{-Me-Man})^+$  complex which corresponds to a tricoordinated  $Li^+$  cation.

#### 4.4.5 Comparison with previous theoretical studies on metalated monosaccharides.

Our results are also consistent with those Armentrout and coworkers[74] on the thermochemistry and structures of  $Na^+$  coordinated pentose and hexose, including glucose anomers. The lowest energy structures of the  $Na(\text{hexose})^+$  involve multidentate sodium cation coordination, with the sugar in a sterically favored chair ring conformation. Of particular interest in the context of the present study is the case of the  $Na(\text{glucose})^+$  complexes. The ground state geometry of the  $\alpha$  and  $\beta$  complexes differ considerably. This result can be considered as consistent with the DIMS spectra of the sodiated systems presented in Figure 4-9b. In contrast to the case of the lithiated complexes (Figure 4-9a) where

the two glucose anomers cannot be separated, it was found that the sodiated methylated glucose anomers can be efficiently separated with our DIMS device.

The results of Armentrout and coworkers[74] together with our result thus suggest that when going from  $\text{Li}^+$  to  $\text{Na}^+$ , the bonding of the glucose anomers to the metal cation changes. In the case of the sodiated complexes, the metal-sugar interaction associated with the lowest energy structure of the  $\alpha$ -glucose anomer is very similar to the one associated with the lowest energy structure of the  $\text{Li}(\alpha\text{-Me-Glc})(\text{H}_2\text{O})^+$  and  $\text{Li}(\beta\text{-Me-Glc})(\text{H}_2\text{O})^+$  complexes. The sugar binds the metal in a bidentate fashion, and the hydroxymethyl O(6)H group is involved in a hydrogen bond with the O(4)H donor group, which in turn is bound to the metal. It should be noted that in an earlier study of the thermochemistry and structure of  $\text{Na}^+$  coordinated pentose and hexose,[68] it was found the hydroxymethyl O(6)H group was bound to the  $\text{Na}^+$  cation in the lowest energy structures. It should be stressed, however, that the relative energies of structures associated with different metal-sugar bonding schemes is very sensitive to the theoretical levels, as found for  $\text{Na}^+$ [74], and also for  $\text{Li}^+$  complexes [76]. Thus, the predicted lowest energy structures can differ from other studies depending on the theoretical level of theory used.

## 4.5 Conclusions.

To conclude, integrating DIMS and IR activation on the same tandem mass spectrometer provides two additional dimensions to the analytical technique. Our motivation for developing an innovative instrument is twofold. It ranges from understanding the correlation of the shape of a molecule with intra-molecular interactions to enhancing the resolving power of the method for separating and characterizing isomeric or isobaric molecules.

From an analytical point of view, an interesting perspective for enhancing the resolving power of the analytical method would be to use a structure-specific activation wavelength for inducing the fragmentation of DIMS-selected ions. This idea is illustrated in Figure 4-15 where two DIMS spectra of a mixture sample of the three saccharides cationized with  $\text{Li}^+$  recorded with the laser off (a) and on (b) are given. The laser was tuned at  $3400\text{ cm}^{-1}$ , *i.e.* corresponding to the IR active mode specific of the glucose complexes. The DIMS spectra of the  $m/z$  201 ( $\text{Li}(\text{Sac})^+$ ) and 219 ( $\text{Li}(\text{Sac})(\text{H}_2\text{O})^+$ ) ions given in

Figure 4-15 were recorded using an MS<sup>3</sup> sequence. DIMS- and mass-selected  $m/z$  201 ions were allowed to react with water and the resulting  $m/z$  201 and 219 ions were irradiated for 1s with the laser tuned at 3400 cm<sup>-1</sup>. As compared to the DIMS spectrum recorded with the laser off, a depletion of  $m/z$  219 signal and a simultaneous increase of the  $m/z$  201 signal can be observed in the CV range (~2.5 V) corresponding to the complexes of the glucose anomers. Conversely, the peak at CV≈3.6 V corresponding to the mannose complex, does not change. This is expected since 3400 cm<sup>-1</sup> is a structure-specific wavenumber, characteristic of the hydrogen bonding network of the Li( $\alpha$ -Me-Glc)(H<sub>2</sub>O)<sup>+</sup> and Li( $\beta$ -Me-Glc)(H<sub>2</sub>O)<sup>+</sup> complexes.

This approach could be used for identifying specific bonding motif or functional groups associated to the different peaks within a DIMS spectrum. As illustrated in Figure 4-15, an OPO/OPA table-top laser is ideally suited for probing hydrogen bonding network. Identifying specific functional groups could also be done using the 800-2000 cm<sup>-1</sup> fingerprint spectral range as available with Free Electron Laser based in our lab.

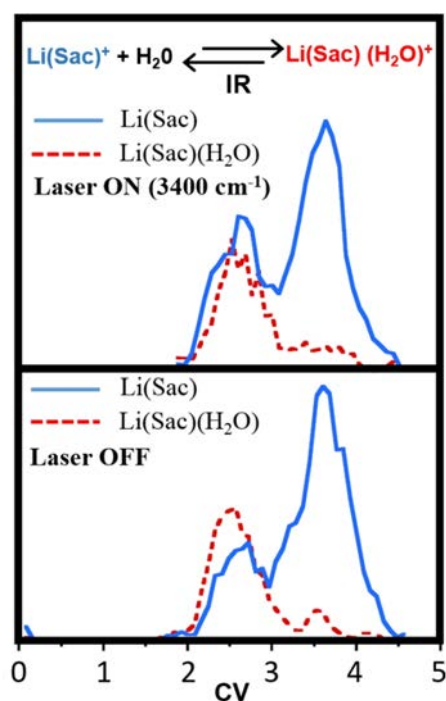


Figure 4-15: DIMS spectra for an equimolar mixture of the three saccharides in Li<sup>+</sup> solution. An MS<sup>3</sup> sequence was used where DIMS- and mass-selected  $m/z$  201 ions were allowed to react with water and the resulting  $m/z$  201 (blue) and 219 (red) ions were irradiated for 1s with the laser tuned at 3400 cm<sup>-1</sup>. (a) Laser on. (b) Laser off.

From a fundamental point of view, we herein demonstrate that the present instrument allows for the IR spectroscopic characterization of mobility- and mass-selected ions. A DIMS device coupled with an ion trap offers the advantage that DIMS-selected ions can be accumulated. As a result, ion signal is sufficient for performing MS/MS experiments and excellent signal/noise is achieved with the IR spectroscopy. As illustrated in Figure 4-13, the comparison of experimental IR spectra with the predicted IR spectra of the different isomers allows for a structural characterization of the ions of interest. Information on the hydrogen bonding network can be obtained using OPO/OPA lasers tunable in the NH-OH stretching regions as in the present case.

Pure mobility separation relies on the collision cross section of the ion with the buffer gas. Using drift-tube instruments, structural information can be derived from the comparison of experimental collision cross section against theoretical ones. While this is true when ions are submitted to low electric conditions, as of yet no clear correlation between the mobility parameter and the structure can be drawn when ions are submitted to high electric field, as under DIMS (or FAIMS). IR spectroscopy of DIMS selected ions could thus contribute to a better understanding of the ion mobility separation under asymmetric high electric field conditions.

## 4.6 Bibliography

- (1) Fetterolf, D. D.; Clark, T. D. *Journal of Forensic Sciences* **1993**, *38*, 28.
- (2) Ewing, R. G.; Miller, C. J. *Field Anal. Chem. Technol.* **2001**, *5*, 215.
- (3) Steiner, W. E.; Clowers, B. H.; Fuhrer, K.; Gonin, M.; Matz, L. M.; Siems, W. F.; Schultz, A. J.; Hill, H. H. *Rapid Commun. Mass Spectrom.* **2001**, *15*, 2221.
- (4) Kanu, A. B.; Hill, H. H. *Talanta* **2007**, *73*, 692.
- (5) Steiner, W. E.; Clowers, B. H.; Haigh, P. E.; Hill, H. H. *Anal. Chem.* **2003**, *75*, 6068.
- (6) Hoaglund-Hyzer, C. S.; Lee, Y. J.; Counterman, A. E.; Clemmer, D. E. *Anal. Chem.* **2002**, *74*, 992.
- (7) Kanu, A. B.; Dwivedi, P.; Tam, M.; Matz, L.; Hill, H. H. *J. Mass Spectrom.* **2008**, *43*, 1.
- (8) Ahonen, L.; Fasciotti, M.; af Gennas, G. B.; Kotiaho, T.; Daroda, R. J.; Eberlin, M.; Kostianen, R. *J. Chromatogr. A* **2013**, *1310*, 133.
- (9) Fasciotti, M.; Sanvido, G. B.; Santos, V. G.; Lalli, P. M.; McCullagh, M.; de Sa, G. F.; Daroda, R. J.; Peter, M. G.; Eberlin, M. N. *J. Mass Spectrom.* **2012**, *47*, 1643.
- (10) Benassi, M.; Corilo, Y. E.; Uria, D.; Augusti, R.; Eberlin, M. N. *J. Am. Soc. Mass. Spectrom.* **2009**, *20*, 269.
- (11) Dwivedi, P.; Bendiak, B.; Clowers, B. H.; Hill, H. H. *J. Am. Soc. Mass. Spectrom.* **2007**, *18*, 1163.
- (12) Creaser, C. S.; Griffiths, J. R.; Bramwell, C. J.; Noreen, S.; Hill, C. A.; Thomas, C. L. P. *Analyst* **2004**, *129*, 984.
- (13) Shvartsburg, A. A.; Jarrold, M. F. *Chem. Phys. Lett.* **1996**, *261*, 86.
- (14) Mesleh, M. F.; Hunter, J. M.; Shvartsburg, A. A.; Schatz, G. C.; Jarrold, M. F. *J. Phys. Chem.* **1996**, *100*, 16082.
- (15) Giles, K.; Pringle, S. D.; Worthington, K. R.; Little, D.; Wildgoose, J. L.; Bateman, R. H. *Rapid Commun. Mass Spectrom.* **2004**, *18*, 2401.
- (16) Giles, K.; Williams, J. P.; Campuzano, I. *Rapid Commun. Mass Spectrom.* **2011**, *25*, 1559.
- (17) Bush, M. F.; Hall, Z.; Giles, K.; Hoyes, J.; Robinson, C. V.; Ruotolo, B. T. *Anal. Chem.* **2010**, *82*, 9557.
- (18) Campuzano, I.; Bush, M. F.; Robinson, C. V.; Beaumont, C.; Richardson, K.; Kim, H.; Kim, H. I. *Anal. Chem.* **2012**, *84*, 1026.
- (19) Chawner, R.; McCullough, B.; Giles, K.; Barran, P. E.; Gaskell, S. J.; Eyers, C. E. *Journal of Proteome Research* **2012**, *11*, 5564.
- (20) Campbell, J. L.; Zhu, M.; Hopkins, W. S. *J. Am. Soc. Mass. Spectrom.* **2014**, *25*, 1583.
- (21) Shvartsburg, A. A.; Seim, T. A.; Danielson, W. F.; Norheim, R.; Moore, R. J.; Anderson, G. A.; Smith, R. D. *J. Am. Soc. Mass. Spectrom.* **2013**, *24*, 109.
- (22) Shvartsburg, A. A.; Smith, R. D. *Anal. Chem.* **2011**, *83*, 9159.
- (23) Shvartsburg, A. A.; Danielson, W. F.; Smith, R. D. *Anal. Chem.* **2010**, *82*, 2456.
- (24) Hennes, T.; Ellies, L. G. *Biochimica Et Biophysica Acta-General Subjects* **1999**, *1473*, 123.
- (25) Gorelik, E.; Galili, U.; Raz, A. *Cancer and Metastasis Reviews* **2001**, *20*, 245.
- (26) Gabius, H. J.; Andre, S.; Kaltner, H.; Siebert, H. C. *Biochimica Et Biophysica Acta-General Subjects* **2002**, *1572*, 165.
- (27) Dashnau, J. L.; Sharp, K. A.; Vanderkooi, J. M. *J. Phys. Chem. B* **2005**, *109*, 24152.
- (28) Asam, M. R.; Glish, G. L. *J. Am. Soc. Mass. Spectrom.* **1997**, *8*, 987.
- (29) Hofmeister, G. E.; Zhou, Z.; Leary, J. A. *J. Am. Chem. Soc.* **1991**, *113*, 5964.
- (30) Jiao, J.; Zhang, H.; Reinhold, V. N. *Int. J. Mass Spectrom.* **2011**, *303*, 109.
- (31) Prien, J. M.; Ashline, D. J.; Lapadula, A. J.; Zhang, H.; Reinhold, V. N. *J. Am. Soc. Mass. Spectrom.* **2009**, *20*, 539.

- (32) Prien, J. M.; Huysentruyt, L. C.; Ashline, D. J.; Lapadula, A. J.; Seyfried, T. N.; Reinhold, V. N. *Glycobiology* **2008**, *18*, 353.
- (33) Li, H. L.; Giles, K.; Bendiak, B.; Kaplan, K.; Siems, W. F.; Hill, H. H. *Anal. Chem.* **2012**, *84*, 3231.
- (34) Lindberg, B.; Lonngren, J. *Methods Enzymol.* **1978**, *50*, 3.
- (35) Salzner, U.; Schleyer, P. V. J. *J. Org. Chem.* **1994**, *59*, 2138.
- (36) Zhu, X.; Kawatkar, S.; Rao, Y.; Boons, G.-J. *J. Am. Chem. Soc.* **2006**, *128*, 11948.
- (37) Liu, Y. S.; Clemmer, D. E. *Anal. Chem.* **1997**, *69*, 2504.
- (38) Crich, D. *Acc. Chem. Res.* **2010**, *43*, 1144.
- (39) Boltje, T. J.; Buskas, T.; Boons, G.-J. *Nature Chemistry* **2009**, *1*, 611.
- (40) Cancilla, M. T.; Penn, S. G.; Carroll, J. A.; Lebrilla, C. B. *J. Am. Chem. Soc.* **1996**, *118*, 6736.
- (41) Lanucara, F.; Holman, S. W.; Gray, C. J.; Evers, C. E. *Nature Chemistry* **2014**, *6*, 281.
- (42) Both, P.; Green, A. P.; Gray, C. J.; Sardzik, R.; Voglmeir, J.; Fontana, C.; Austeri, M.; Rejzek, M.; Richardson, D.; Field, R. A.; Widmalm, G.; Flitsch, S. L.; Evers, C. E. *Nature Chemistry* **2014**, *6*, 65.
- (43) Clemmer, D. E.; Jarrold, M. F. *J. Mass Spectrom.* **1997**, *32*, 577.
- (44) Jarrold, M. F. *J. Phys. Chem.* **1995**, *99*, 11.
- (45) Vonhelden, G.; Hsu, M. T.; Kemper, P. R.; Bowers, M. T. *J. Chem. Phys.* **1991**, *95*, 3835.
- (46) Hill, H. H., Jr.; Siems, W. F.; St Louis, R. H.; McMinn, D. G. *Anal. Chem.* **1990**, *62*, 1201A.
- (47) Shvartsburg, A. A.; Mashkevich, S. V.; Baker, E. S.; Smith, R. D. *J. Phys. Chem. A* **2007**, *111*, 2002.
- (48) Lee, S.; Wyttenbach, T.; Bowers, M. T. *Int. J. Mass spectrom.* **1997**, *167*, 605.
- (49) Shvartsburg, A. A.; Smith, R. D. *Anal. Chem.* **2008**, *80*, 9689.
- (50) Clowers, B. H.; Dwivedi, P.; Steiner, W. E.; Hill, H. H.; Bendiak, B. *J. Am. Soc. Mass. Spectrom.* **2005**, *16*, 660.
- (51) Li, H. L.; Bendiak, B.; Siems, W. F.; Gang, D. R.; Hill, H. H. *Anal. Chem.* **2013**, *85*, 2760.
- (52) Hilderbrand, A. E.; Myung, S.; Barnes, C. A. S.; Clemmer, D. E. *J. Am. Soc. Mass. Spectrom.* **2003**, *14*, 1424.
- (53) Bellina, B.; Compagnon, I.; MacAleese, L.; Chirot, F.; Lemoine, J.; Maitre, P.; Broyer, M.; Antoine, R.; Kulesza, A.; Mitric, R.; Bonacic-Koutecky, V.; Dugourd, P. *PCCP* **2012**, *14*, 11433.
- (54) Vonderach, M.; Winghart, M.-O.; MacAleese, L.; Chirot, F.; Antoine, R.; Dugourd, P.; Weis, P.; Hampe, O.; Kappes, M. M. *PCCP* **2014**, *16*, 3007.
- (55) Thi Nga, L.; Pouilly, J. C.; Lecomte, F.; Nieuwjaer, N.; Manil, B.; Desfrancois, C.; Chirot, F.; Lemoine, J.; Dugourd, P.; van der Rest, G.; Gregoire, G. *J. Am. Soc. Mass. Spectrom.* **2013**, *24*, 1937.
- (56) Papadopoulos, G.; Svendsen, A.; Boyarkin, O. V.; Rizzo, T. R. *Faraday Discuss.* **2011**, *150*, 243.
- (57) Lee, S.; Valentine, S. J.; Reilly, J. P.; Clemmer, D. E. *Int. J. Mass spectrom.* **2012**, *309*, 161.
- (58) Zucker, S. M.; Lee, S.; Webber, N.; Valentine, S. J.; Reilly, J. P.; Clemmer, D. E. *J. Am. Soc. Mass. Spectrom.* **2011**, *22*, 1477.
- (59) Adamson, B. D.; Coughlan, N. J. A.; Continetti, R. E.; Bieske, E. J. *PCCP* **2013**, *15*, 9540.
- (60) Papadopoulos, G.; Svendsen, A.; Boyarkin, O. V.; Rizzo, T. R. *J. Am. Soc. Mass. Spectrom.* **2012**, *23*, 1173.
- (61) Wassermann, T. N.; Boyarkin, O. V.; Paizs, B.; Rizzo, T. R. *J. Am. Soc. Mass. Spectrom.* **2012**, *23*, 1029.
- (62) Pierson, N. A.; Valentine, S. J.; Clemmer, D. E. *J. Phys. Chem. B* **2010**, *114*, 7777.
- (63) Pierson, N. A.; Chen, L.; Valentine, S. J.; Russell, D. H.; Clemmer, D. E. *J. Am. Chem. Soc.* **2011**, *133*, 13810.
- (64) Vonderach, M.; Ehrler, O. T.; Matheis, K.; Weis, P.; Kappes, M. M. *J. Am. Chem. Soc.* **2012**, *134*, 7830.
- (65) Vonderach, M.; Ehrler, O. T.; Weis, P.; Kappes, M. M. *Anal. Chem.* **2011**, *83*, 1108.
- (66) Shvartsburg, A. A.; Smith, R. D. *Anal. Chem.* **2013**, *85*, 10.

- (67) Bushey, J. M.; Kaplan, D. A.; Danell, R. M.; Glish, G. L. *Instrumentation Science & Technology* **2009**, *37*, 257.
- (68) Cerda, B. A.; Wesdemiotis, C. *Int. J. Mass spectrom.* **1999**, *189*, 189.
- (69) Li, H. L.; Bendiak, B.; Siems, W. F.; Gang, D. R.; Hill, H. H. *Rapid Communications in Mass Spectrometry* **2013**, *27*, 2699.
- (70) Gronert, S. J. *Am. Soc. Mass. Spectrom.* **1998**, *9*, 845.
- (71) Rao, J. S.; Dinadayalane, T. C.; Leszczynski, J.; Sastry, G. N. *Journal of Physical Chemistry A* **2008**, *112*, 12944.
- (72) Hall, A. B.; Coy, S. L.; Kafle, A.; Glick, J.; Nazarov, E.; Vouros, P. J. *Am. Soc. Mass Spectrom.* **2013**, *24*, 1428.
- (73) Walters, R. S.; Pillai, E. D.; Duncan, M. A. *Journal of the American Chemical Society* **2005**, *127*, 16599.
- (74) Heaton, A. L.; Armentrout, P. B. *Journal of Physical Chemistry A* **2008**, *112*, 10156.
- (75) Rodgers, M. T.; Armentrout, P. B. *J. Phys. Chem. A* **1997**, *101*, 1238.
- (76) Hernandez, O.; Maitre, P. *Manuscript under preparation* **2014**.





## 5 PROBING THE STRUCTURE OF METAL CATIONIZED MONOSACCHARIDES: IR SPECTROSCOPY

5	PROBING THE STRUCTURE OF METAL CATIONIZED MONOSACCHARIDES: IR SPECTROSCOPY ..	157
5.1	Introduction.....	159
5.2	Conformational search: Nomenclature and method .....	159
5.3	Lithiated monosaccharides: Structure and energetics.....	169
5.4	IR spectroscopy of monosaccharide complexes. ....	181
5.5	IR spectra of monosaccharide complexes: Spectral and structural assignment.....	185
5.6	Conclusions.....	201
5.7	Annexes .....	203
5.8	Bibliography.....	209

## 5.1 Introduction.

This chapter is dedicated to the structure, energetic, and IR spectroscopy of gas phase complexes of three methylated monosaccharides (methyl- $\alpha$ -glucose, methyl- $\beta$ -glucose, methyl- $\alpha$ -mannose). We will essentially focus our attention on the lithiated complexes, and both the bare and the monohydrated complexes of these three stereoisomers will be considered. Our goal was to derive structural information from the gas phase IR spectra recorded for these six complexes. Quantum chemical calculations have been carried out on these complexes. Their structures are the result of a subtle trade-off between intra-sugar hydrogen bonding and maximization of the coordination of the lithium cation. Considering the complexity of the conformational landscape of the potential energy surface of these systems, we mainly focus our attention on the low-energy structures of the six complexes which present different structural motifs, and thus different IR absorption spectra.

## 5.2 Conformational search: Nomenclature and method

### 5.2.1 Conformation of free monosaccharides: nomenclature.

A representation of a 6-membered ring structure of a methylated hexose is given in Figure 5-1. The carbon and oxygen atom numbering derives from the linear structure where the carbonyl carbon atom is numbered C(1). After methylation of the O(1) oxygen, only four hydroxyl groups are available for hydrogen bonding which is an important driving force for conformational stabilization. Due to the possible rotation about the C(5)-C(6) angle, the flexibility hydroxymethyl O(6)H group also plays an important role in the structuration of these systems.

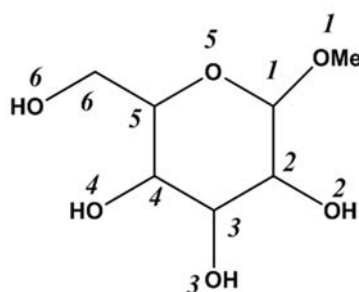


Figure 5-1 : Carbon and oxygen atoms numbering for Methyl hexose with a 6-membered ring structure. The six carbon atoms are numbered from 1 to 6 in clockwise fashion.

Hexose with a pyranose form, *i.e.* with a six-membered ring structure, can adopt different conformations including two chairs forms ( ${}^4C_1$  and  ${}^1C_4$ ) or boat conformations. A schematic representation of the two chairs and one boat conformers are given in Figure 5-2. The  ${}^4C_1$  notation refers to a chair configuration where the C(4) carbon is above the reference C(2)C(3)C(5)O plane and the C(1) carbon atom is found below it. Other conformers such as skew-boats, half-chairs and envelopes can be adopted by hexose compounds, but they are higher in energy and will not be considered further.

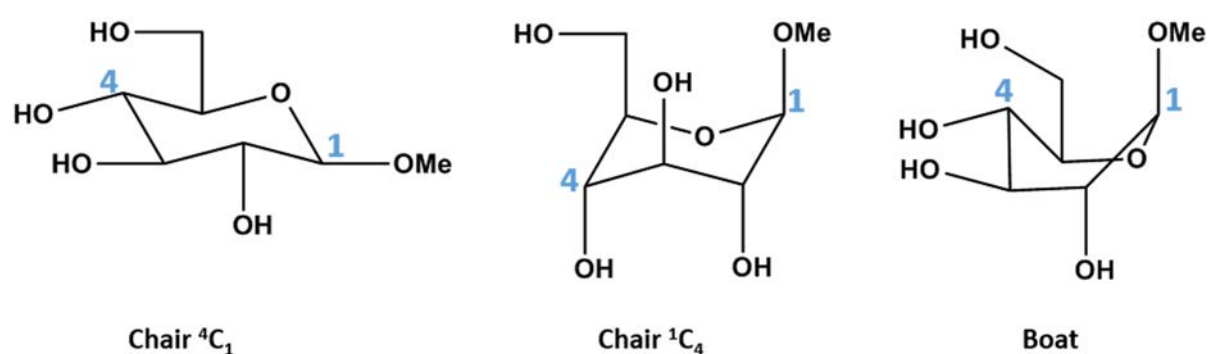


Figure 5-2: Representation of three different conformers of the methylated  $\beta$ -glucose: two chairs ( ${}^4C_1$  or  ${}^1C_4$ ) and one boat.

Conformation of hexose derivatives has been studied theoretically [1-4]. In the case of the two glucose anomers, it has been established that the lowest energy structure has a  ${}^4C_1$  chair configuration [3], in both aqueous and gas phases. Different  ${}^4C_1$  conformations have been characterized, and they essentially differ by the intramolecular hydrogen bonding network. The different conformers can thus be distinguished depending on the orientation of the hydroxyl groups and of the hydroxymethyl group [5].

The intramolecular interaction between the exocyclic  $\text{CH}_2\text{OH}$  group and the six-membered ring has been studied in details [1,2]. It has been shown in particular that low-energy structures of glucopyranose essentially derive from two types of orientation of the hydroxymethyl group each being associated with a specific hydrogen bonding motif involving the hydroxymethyl O(6)H group. A representation of the two types of conformers for the two structures of interest here can be found in Figure 5-3. The O(6)H group can interact, as a hydrogen bond donor or acceptor, with the O(4)H group,

resulting in the formation of a six-membered hydrogen-bonded ring. The second type of conformers is characterized by a five-membered HB ring resulting from the HB interaction between the O(6)H donor and the ring O(5) oxygen atom. Structures of gluco-pyranose have been characterized by Truhlar and coworkers [3] at the MP2/cc-pVDZ level of theory. In the case of each glucose anomers, it was shown that the difference in free energy at 298K of the two types of conformers differ by less than 3 kJ/mol. As noted in this paper [3], the relative energy ordering is very sensitive to the level of theory.

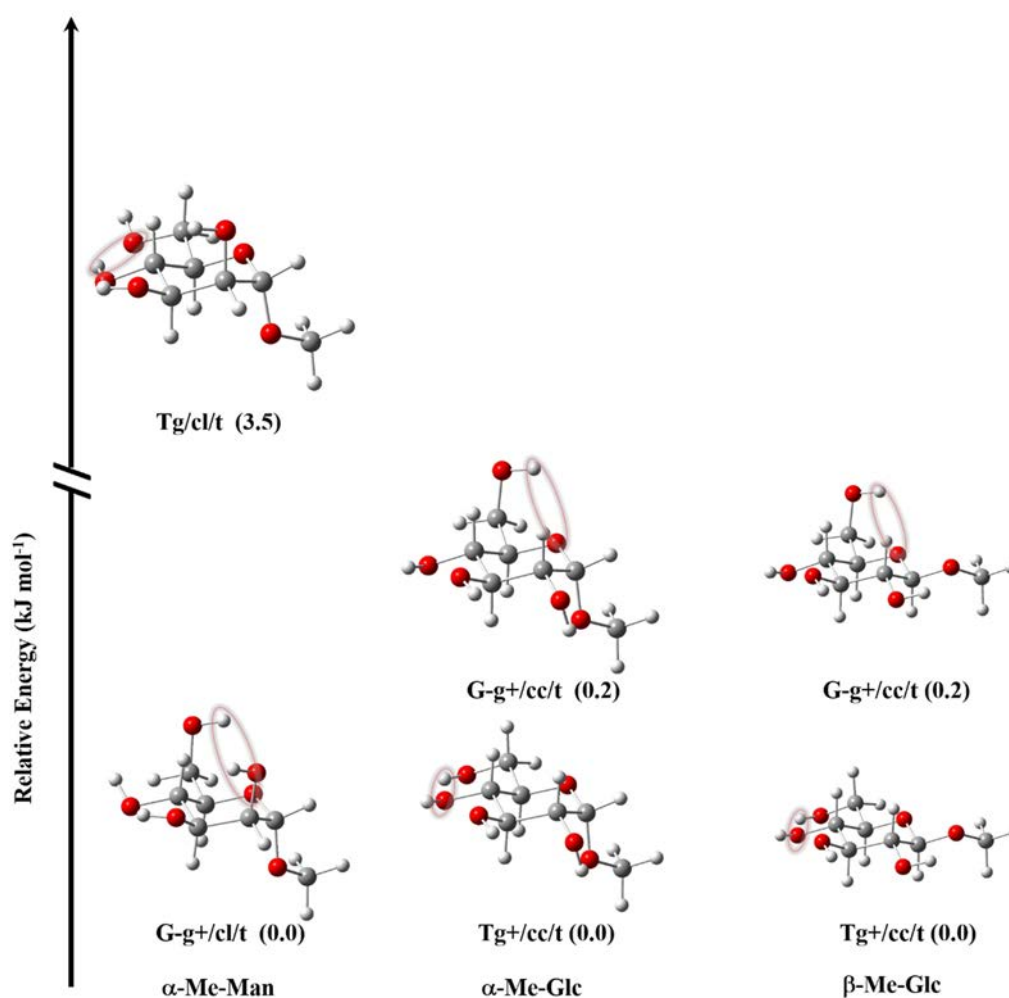


Figure 5-3: Structure and energetics associated with the two different conformations of each individual methylated monosaccharide isomers. The interaction of the exocyclic  $\text{CH}_2\text{OH}$  group with the O(5) oxygen or with the O(4)H group are represented with a blue dotted line. The stationary points were computed at the B3LYP/6-31G\*\* level of theory. The 298K relative free energies are given in  $\text{kJ mol}^{-1}$  in parenthesis.

A nomenclature of the different conformers of pyranose is proposed in a recent paper combining quantum chemical calculations (at the MP2/6-311++G(d,p) level) and Fourier transform microwave

spectroscopy coupled with laser ablation of crystalline glucopyranose [5]. This nomenclature is used in Figure 5-3. The two first symbols refer to the orientation of the exocyclic CH<sub>2</sub>OH group. Each conformer is characterized by the conformation (G<sup>+</sup>, G<sup>-</sup>, or T) associated to the O(6)C(6)C(5)O(5) torsional angle, and to that (g<sup>+</sup>,g<sup>-</sup>,t) of the H(6)O(6)C(6)C(5) torsional angle. The symbol “cl” or “cc” refers to the clockwise (cl) or counterclockwise (cc) arrangement of the cooperative network of intramolecular hydrogen bonds. Then, the last symbol (g<sup>+</sup>, g<sup>-</sup>, t) refers to the H(1)O(1)C(1)C(2) dihedral angle associated to the anomeric hydroxyl group.

Four conformers of  $\alpha$ - and three of  $\beta$ -glucose have been unequivocally identified on the basis of microwave spectroscopy in conjunction with *ab initio* calculations [5]. The energy ordering is consistent with that proposed by Truhlar and coworkers [3]. The G-g<sup>+</sup>/cc/t conformers characterized by a five-membered HB ring involving the O(6)H-O(5) bond are found to be the lowest in energy. In these structures, the hydroxymethyl C-OH bond is perpendicular to the cycle. The lowest energy structure is characterized by a six-membered hydrogen bond ring involving a hydrogen bond between the O(6)H and O(4)H groups is the Tg<sup>+</sup>/cc/t conformer. It is predicted to lie 2.8 (3.3) kJ/mol higher in energy in the case of the  $\alpha$ -anomer ( $\beta$ -anomer) if the 298K free energies at the 6-311++G(d,p) level of theory are considered.

In the present study, the starting point geometries for the structural search for the bare and monohydrated complexes were the methylated sugars in a chair (<sup>4</sup>C<sub>1</sub> or <sup>1</sup>C<sub>4</sub>) or boat conformation which are schematized in Figure 5-2. A detailed study of the conformational landscape of the free monosaccharides was out of the scope of this study. Nevertheless, different conformations of the chairs and boat structures have been characterized. In particular, two representative structures, corresponding to the replacement of the H(1) atom by the methyl group from the two abovementioned G-g<sup>+</sup>/cc/t and Tg<sup>+</sup>/cc/t conformers of  $\alpha$ - and  $\beta$ -glucose are shown in Figure 5-3. As can be seen in this Figure, the two types of structure are also very close in energy in the cases of the three methylated monosaccharides. As already noted [3], the energy ordering is very sensitive to the level of theory used. At the B3LYP/6-31G\*\* level, the Tg<sup>+</sup>/cc/t is the lowest energy structure for the methylated glucose anomers, but the G-g<sup>+</sup>/cc/t structure is nearly degenerate.

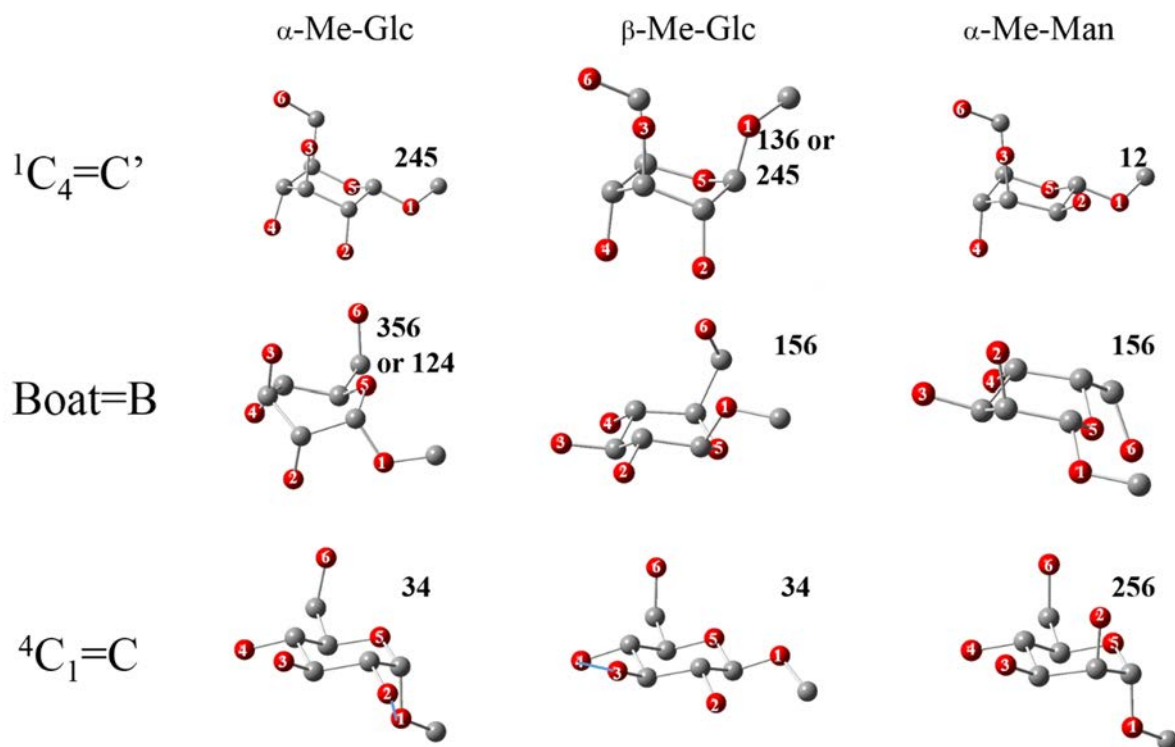


Figure 5-4: Maximum coordination number of the lowest energy structure of methylated monosaccharides ( $\alpha$ -Me-Glc,  $\beta$ -Me-Glc, and  $\alpha$ -Me-Man).

### 5.2.2 Method of calculation

The structures were optimized at the B3LYP/6-31G(d,p) level of theory. Single point MP2 calculations were then carried out using a more extended basis set (6-311+G\*\*). Gibbs free energies at 298K are considered for the relative energetics. The structures of the free sugars were first considered assuming a chair ( ${}^4C_1$  or  ${}^1C_4$ ) or a boat conformation. Then, the  $Li^+$  cation was added and different coordination sites were envisaged using various orientations of the hydroxyl and hydroxymethyl groups in order to find the best compromise between hydrogen bonding and  $Li^+$  coordination. IR absorption spectra were derived from harmonic calculations. A scaling factor of 0.955 was applied to the harmonic frequencies, as used previously to simulate the IR spectra in the X-H (X= O, N, C) stretching spectral range [6,7].

Tri- or even tetra-coordination of the metal cation with hexose has been discussed in the literature [8,9]. This can be understood considering the representation of the two chairs and one boat

conformation of the three saccharides considered here. As discussed below, the lowest energy conformer for these three systems is the  ${}^4C_1$  chair. If the methyl- $\alpha$ -mannose is considered in a  ${}^4C_1$  chair conformation, one can anticipate that a tri-coordination complex could be formed through the binding of  $\text{Li}^+$  to the O(2), O(5) and O(6) atoms (Figure 5-5a). On the other hand, if one of the glucose anomers is considered, no efficient tri-coordination of  $\text{Li}^+$  could be achieved. Alternatively, multiple or di-coordinated structures could be envisaged (Figure 5-5b).

Multiple guess structures of the  $\text{Li}^+(\text{Sac})$  di- and tri-coordinated complexes were built manually and then optimized. While low-energy tri-coordinated  $\text{Li}^+$  complex structures could be derived from the  ${}^4C_1$  chair of mannose, no such structure could be found for the glucose anomers.

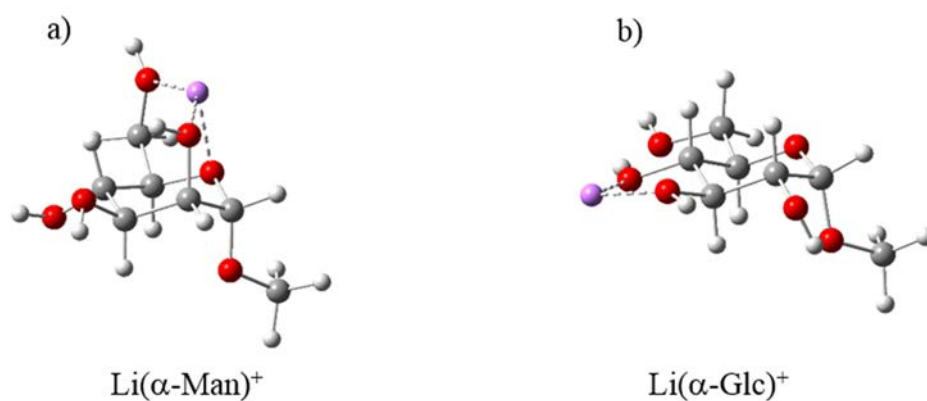


Figure 5-5 : Tri-coordination and bi-coordination complexes of  $\text{Li}(\alpha\text{-Me-Man})^+$  and  $\text{Li}(\alpha\text{-Me-Glc})^+$  respectively.

If the  ${}^4C_1$  conformation of the glucose anomers is considered, it can only act as a bidentate ligand. Some of these di-coordinated  $\text{Li}^+$  structures were found to be low in energy because  $\text{Li}^+$  coordination does not require a strong disruption of the hydrogen bonding network within the hydroxyl groups of the saccharide. In the case of  $\text{Li}^+(\text{methyl-}\alpha\text{-glucose})$  complex, for example, the lowest-energy structure corresponds to the coordination of  $\text{Li}^+$  to the O(3) and O(4) oxygen atoms (Figure 5-5b), but relatively strong O(4)H-O(6) and O(3)H-O(2) hydrogen bonds can be maintained.

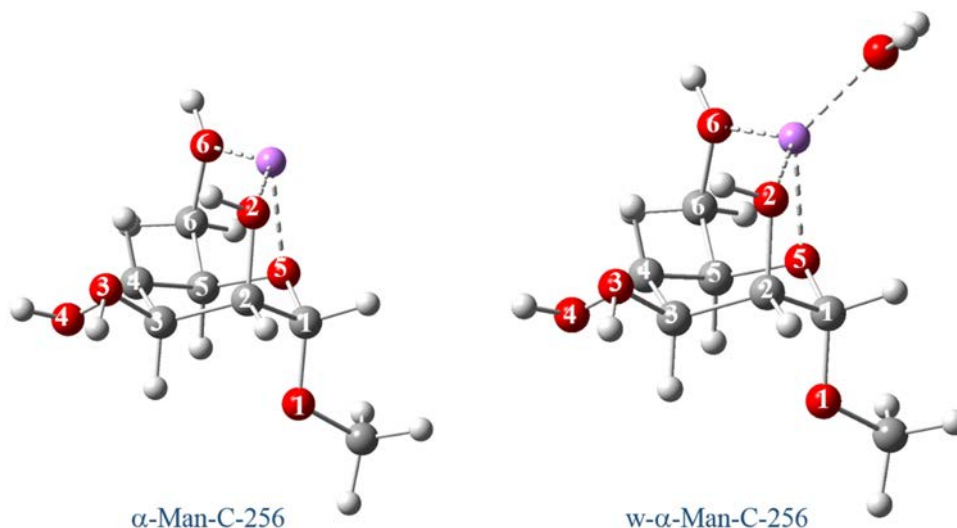


Figure 5-6 : Illustration of the nomenclature using the lowest energy structure of the  $\text{Li}^+(\text{methyl-}\alpha\text{-mannose})$  and  $\text{Li}^+(\text{methyl-}\alpha\text{-mannose})(\text{H}_2\text{O})$  complexes. The degree of coordination of the  $\text{Li}^+$  cation is specified by the three numbers “256”, specifying that the O(2), O(5), and O(6) atoms are bound to the metal center using a Li-O distance threshold of 2 Å. The  ${}^4\text{C}_1$  chair conformation of the saccharide is specified by the “C” letter.

The nomenclature used for the complexes is illustrated on the cases of the lowest energy structures of the  $\text{Li}^+(\text{methyl-}\alpha\text{-mannose})$  and  $\text{Li}^+(\text{methyl-}\alpha\text{-mannose})(\text{H}_2\text{O})$  complexes which are displayed in Figure 5-6. They are named  $\alpha\text{-Man-C-256}$  and  $w\text{-}\alpha\text{-Man-C-256}$ , respectively, where  $\alpha\text{-Man}$  is the short name for methyl- $\alpha$ -mannose. The three numbers “256” designate the oxygen atoms that are bound to the  $\text{Li}^+$  cation considering a Li-O distance threshold of 2 Å. The saccharide conformation within the complex is specified by one letter (C= ${}^4\text{C}_1$  chair, C’= ${}^1\text{C}_4$  chair, B=boat).

### 5.2.3 Free monosaccharides: structure, energetic and IR spectra

The relative energies of the two  ${}^4\text{C}_1$  and  ${}^1\text{C}_4$  chairs, and of the different boats structures were optimized at the B3LYP/6-31G\*\* level of theory. For each conformation of the ring structure, different orientations of the OH groups were used as a starting point for geometry optimization. A particular care was taken of the hydroxymethyl group. The corresponding O(6)H hydroxyl can be involved in hydrogen bonding with equatorial O(4)H, or axial O(3)H hydroxyl groups, or O(5) intracyclic oxygen, depending on the hexose conformation ( ${}^4\text{C}_1$  and  ${}^1\text{C}_4$ , respectively).

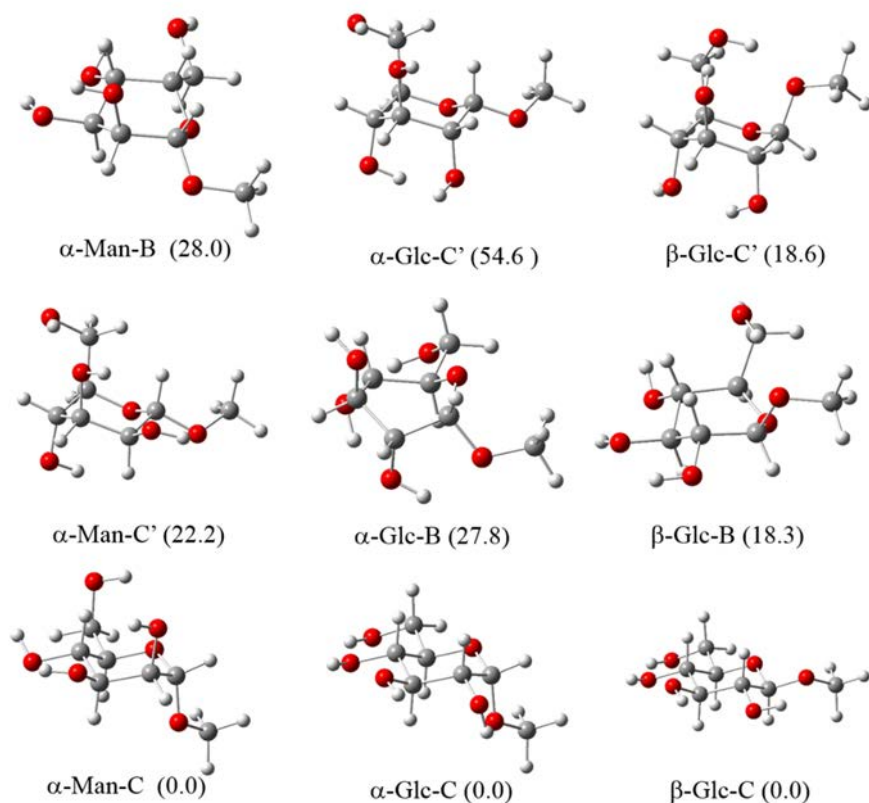


Figure 5-7: Structure and relative energies (kJ/mol) of the lowest energy structure associated with a chair ( ${}^4C_1$  or  ${}^1C_4$ ) and one boat configuration for the three methylated monosaccharides. The C, C', and B symbols in the structure names refer to the  ${}^4C_1$ ,  ${}^1C_4$ , and Boat conformers respectively. 298K Gibbs free energies were determined at the B3LYP/6-31G\*\* level of theory.

The relative energies (kJ/mol) of the lowest energy structure associated with a chair ( ${}^4C_1$  or  ${}^1C_4$ ) and one boat configuration for the three methylated monosaccharides are given in Figure 5-7. 298K Gibbs free energies were calculated at the B3LYP/6-31G\*\* level of theory. As can be seen in this Figure, the  ${}^4C_1$  configuration is found to be the lowest in energy for the three systems. Interestingly, the energy ordering of the lowest  ${}^1C_4$  and boat conformers differ from one system to another. In the case of mannose, the lowest energy  ${}^1C_4$  chair and boat conformers are predicted to lie 18.7 and 24.5 kJ/mol higher in energy, respectively. The energy ordering of the three lowest energy conformers is different for the two glucose anomers where one boat conformer is found to be lower than the lowest  ${}^1C_4$  conformer. In the case of  $\beta$ -glucose, the energy gap between the boat and  ${}^1C_4$  chair conformers is small. The relative energies of the lowest energy boat and  ${}^1C_4$  conformers are predicted to be 18.3 and 18.6 kJ mol $^{-1}$ , respectively. In the case of  $\alpha$ -glucose, the lowest energy boat conformer is predicted to be much

lower in energy ( $27.8 \text{ kJ mol}^{-1}$ ) than the lowest energy  ${}^1\text{C}_4$  chair conformers ( $54.6 \text{ kJ mol}^{-1}$ ). These are important results in the perspective of the study of the lithiated complexes, and they suggest that the structural characterization in the case of methyl- $\beta$ -glucose complexes will be more challenging.

This can be rationalized considering the number of intra-sugar hydrogen bonds. Only two hydrogen bonds can be formed when the methyl- $\alpha$ -glucose is in its  ${}^1\text{C}_4$  chair conformation, while three hydrogen bonds can be formed in the case of the methyl- $\beta$ -glucose in its  ${}^1\text{C}_4$  chair conformation.

The different hydroxyl groups of the monosaccharide structures can be involved in intra-sugar interactions, *i.e.* hydrogen bonds. Depending on the stereochemistry of the carbon atoms and of the conformer structure, the predicted hydrogen bond distance ranges from  $\sim 1.75$  to  $\sim 2.5 \text{ \AA}$ , and the corresponding OH stretching mode ranges from  $\sim 3375$  to  $\sim 3635 \text{ cm}^{-1}$ . Hydrogen bond distances and corresponding OH stretching frequencies associated with different structures derived from chair conformations are given in Table 5-1. Three classes have been distinguished depending on the relative position (equatorial-equatorial, axial-axial, or axial equatorial) of the groups (OH, O(1)Me, or CH<sub>2</sub>O(6)H) involved in the hydrogen bonds. Note that as discussed above, the O(5) atom can also be considered as a hydrogen bond acceptor in some cases.

Overall, the hydrogen bond distance decreases in the order equatorial-equatorial, axial-equatorial, and axial-axial. As expected, the red-shift of hydrogen bond donor OH group follows the same trend. This is true for the three types of hydrogen bond: between two hydroxyl groups, between the hydroxymethyl and a hydroxyl group, or between the O(1)Me and one hydroxyl group.

If two equatorial OH groups are considered, the shortest hydrogen bond is formed between the hydroxymethyl O(6)H donor and the hydroxyl O(4)H acceptor groups (Table 5-1). The hydrogen bond distance is on the order of  $1.95$ - $2.0 \text{ \AA}$ , and the corresponding OH stretching frequency is on the order of  $\sim 3550$ - $3570 \text{ cm}^{-1}$ . Note that the O(6)H-O(4) hydrogen bond leads to the formation of a favorable six membered ring motif. Other hydrogen bonds between equatorial hydroxyl groups or between the O(1)Me donor group and the O(2)H acceptor group are weaker. They are characterized by long hydrogen bonds ( $\sim 2.3$ - $2.5 \text{ \AA}$ ), and a small red-shift of the OH stretching mode of the donor OH group. When the

O(1)Me is the acceptor group, the equatorial-equatorial hydrogen bond is predicted to be weaker than when two hydroxyl groups are involved.

When the hydrogen bond involved two hydroxyl groups, the HB distance decreases from  $\sim 2.3$ - $2.4$  Å (e-e), to  $\sim 2.15$ - $2.25$  Å (a-e) and  $1.95$ - $2.1$  Å (a-a). The corresponding stretching frequency of the HB donor OH group decreases from  $\sim 3620$ - $3630$   $\text{cm}^{-1}$  (e-e) to  $\sim 3600$   $\text{cm}^{-1}$  (a-e) and  $\sim 3550$   $\text{cm}^{-1}$  (a-a). Overall, the strongest OH red-shifts are predicted when two axial groups are involved. For example, the hydroxymethyl group can be involved in short axial-axial HB interactions ( $1.77$ - $1.89$  Å). The corresponding stretching frequency of the HB donor group is strongly red-shifted ( $3375$ - $3475$   $\text{cm}^{-1}$ ). These characteristic intra-sugar interactions are only observed in the  $\beta$ -glucose isomers (Boat and  ${}^1C_4$  conformers).

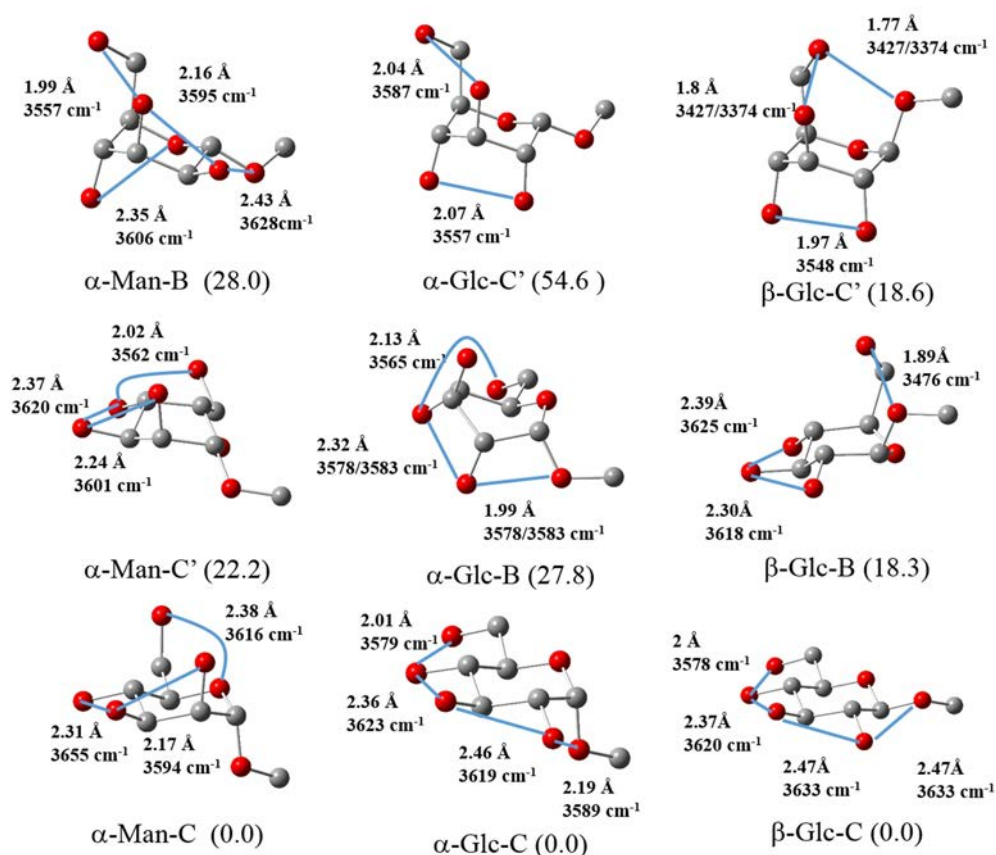


Figure 5-8: Harmonic frequencies corresponding to the NH stretching modes involved in the intra-sugar hydrogen bond interactions formed in the lowest energy structure of the free monosaccharide  ${}^4C_1$ ,  ${}^1C_4$ , and boat conformers. The corresponding HB distance are given in Å. The harmonic frequencies were calculated at the B3LYP/6-31G(d,p) level of theory and scaled by a factor of 0.955.

OH stretching frequencies of monosaccharide derivatives isolated either in the gas phase [10] or in a rare gas matrix [11] have been recorded recently. IR-UV double resonance spectroscopy has been performed on aromatic (UV chromophore) derivatives such as  $\beta$ -phenyl glucopyranosides and their hydrates [10]. The vibrational analysis of the IR spectra of  $\alpha$ -glucose trapped in argon matrix has also been performed. Comparison of the observed bands in the OH stretching region with the predicted (B3LYP/6-311++G\*\*) IR spectra suggested that the three lowest energy  ${}^4C_1$  conformers (G-g+/cc/t, G-g-/cc/t, Tg+/cc/t) of the  $\alpha$ -glucose system are populated. It was suggested that a free OH stretch should correspond to a band near  $\sim 3664\text{ cm}^{-1}$ , which is consistent with our predicted scaled value ( $3665\text{ cm}^{-1}$ ). As in our case, the largest red-shift was found to be when the hydroxymethyl O(6)H group was involved, either as a donor or acceptor, in a hydrogen bond with the O(4)H group. The corresponding observed values are  $3576$  and  $3549\text{ cm}^{-1}$ , respectively.

Equatorial-equatorial			Axial-Equatorial			Axial-Axial		
Type	Distance (Å)	Energy ( $\text{cm}^{-1}$ )	Type	Distance (Å)	Energy ( $\text{cm}^{-1}$ )	Type	Distance (Å)	Energy ( $\text{cm}^{-1}$ )
OH--OH	2.31	3655	CH <sub>2</sub> OH--O(5)	2.38	3616	CH <sub>2</sub> OH--OH	2.04	3587
	2.47	3633	OH--O(5)	2.35	3606	OH--OH	2.32	3583
OH-O(1)Me	2.47	3633	OH--OH	2.24	3601	OH-O(1)Me	1.99	3578
	2.43	3628		2.16	3595	OH-OHCH <sub>2</sub>	2.13	3565
OH--OH	2.39	3625		2.17	3594	OH--OH	2.07	3557
	2.36	3623	OH-O(1)Me	2.19	3589	CH <sub>2</sub> OH--OH	1.99	3557
	2.37	3620			OH--OH	1.97	3548	
	2.37	3620			CH <sub>2</sub> OH--O(1)Me	1.89	3476	
	2.46	3619			OH-OHCH <sub>2</sub>	1.8	3427	
	2.30	3618			CH <sub>2</sub> OH-O(1)Me	1.77	3374	
CH <sub>2</sub> OH--OH	2.01	3579						
	2	3578						
OH-OHCH <sub>2</sub>	2.02	3562						

Table 5-1 : Hydrogen bond interactions observed in the free monosaccharide  ${}^1C_4$ ,  ${}^4C_1$ , and boat conformers. The corresponding hydrogen bond distances and the predicted harmonic frequencies associated with each individual intra-sugar hydrogen bond interaction are also given.

## 5.3 Lithiated monosaccharides: Structure and energetics.

### 5.3.1 Li(Sac)<sup>+</sup> adducts: lowest energy structures.

In the following, only the lowest energy structure associated with the adducts formed with Li<sup>+</sup> and sugar in a  ${}^4C_1$ ,  ${}^1C_4$ , and boat are discussed. The lowest energy structures of these three different

structure types for the  $\text{Li}(\alpha\text{-Me-Glc})^+$ ,  $\text{Li}(\beta\text{-Me-Glc})^+$ , and  $\text{Li}(\alpha\text{-Me-Man})^+$  systems are given in Figure 5-10. The relative free energies at 298 K given in Figure 5-10 were determined at the B3LYP/6-31G\*\* level of theory. The relative energies have also been determined at the MP2/6-311+G\*\* level, and multiple isomers have been considered for each structure type and each sugar (see annex). While some differences in the relative energies can be observed, the relative energies of the lowest-energy lying isomers were found to be the same at the two levels of theory.

Overall, it can be noticed that the lowest energy structure for the three systems are different. They differ by the conformation of the sugar unit and/or its denticity. As can be seen in Figure 5-10, the lowest energy structures for  $\text{Li}(\alpha\text{-Me-Glc})^+$  and  $\text{Li}(\alpha\text{-Me-Man})^+$  have the sugar in a  ${}^4\text{C}_1$  chair conformation. It should be noted, however, that the bonding schemes between the  $\text{Li}^+$  and the  ${}^4\text{C}_1$  chair conformer of the sugar are very different for these two structures. In the case of the  $\text{Li}(\beta\text{-Me-Glc})^+$  complex, the lowest energy structure does not correspond to a  ${}^4\text{C}_1$  chair but to a boat conformation of the sugar unit.

The lowest energy structure of  $\text{Li}(\alpha\text{-Me-Man})^+$  determined at our DFT level of calculations is the  $\alpha\text{-Man-C-256}$ . As discussed above, this tridentate bonding scheme between the three O(2), O(5), and O(6) oxygen atoms of the sugar in its preferred  ${}^4\text{C}_1$  conformation with  $\text{Li}^+$  cation could be anticipated simply by considering the relative position of the oxygen atoms in the free sugar  ${}^4\text{C}_1$  conformation. This  $\text{Li}(\alpha\text{-Me-Man})^+$  structure is also characterized by an intra-sugar hydrogen bond between the axial O(2)H donor and the equatorial O(3)H acceptor groups. Other structures derived from the sugar in a  ${}^4\text{C}_1$  conformation were characterized, but they were higher in energy (see annex).

The lowest boat conformer of  $\text{Li}(\alpha\text{-Me-Man})^+$  is  $\alpha\text{-Man-B-356}$  whose relative energy is 13.0 (18.6)  $\text{kJ mol}^{-1}$  at the B3LYP/6-31G\*\* (MP2/6-311+G\*\*) level of theory. It is a three coordinated structure with the three O(3), O(5), and O(6) oxygen atoms bonded to the  $\text{Li}^+$  cation. The O(3)H--O(2) distance (2.2 Å) suggests that this structure is also stabilized by one intra-sugar hydrogen bond.

The structures derived from the  $\alpha$ -mannose in a  ${}^1\text{C}_4$  conformation are predicted to be high in energy. The lowest energy  ${}^1\text{C}_4$  structure is the  $\alpha\text{-Man-C}'\text{-12}$  which is predicted to be 66.1 (70.7)  $\text{kJ/mol}$

above the lowest-energy  $\alpha$ -Man-C-256 structure. This could be anticipated because the  $\text{Li}^+$  cation can only bind two oxygen atoms when the methylated  $\alpha$ -mannose is its  ${}^1\text{C}_4$  chair conformation which is, in addition, a high energy conformer with respect to the  ${}^4\text{C}_1$  chair. The  $\alpha$ -Man-C'-12 structure is also characterized by two intra-sugar hydrogen bonds. One between the equatorial O(2)H group, which is bound to  $\text{Li}^+$ , and the axial O(3)H acceptor group. The corresponding HB distance is 2.08 Å. The O(3)H group is a donor-acceptor (DA) group since it also acts as a HB donor with the hydroxymethyl O(6)H group. The corresponding HB distance is short (1.78 Å) as in the free  ${}^1\text{C}_4$  conformer.

The lowest energy  ${}^4\text{C}_1$  structure of the  $\text{Li}(\alpha\text{-Me-Glc})^+$  system is an illustration of the trade-off between intra-sugar hydrogen bonding and  $\text{Li}^+$  coordination as driving forces for the energy stabilization. The lowest energy structure is the  $\alpha$ -Glc-C-34 one, where the  $\alpha$ -Glucose is in its low-energy  ${}^4\text{C}_1$  conformation. As discussed above, when  $\alpha$ -Glucose is in its low-energy  ${}^4\text{C}_1$  conformation, one cannot find three oxygen atoms to efficiently bind the  $\text{Li}^+$  cation. This is confirmed by our quantum chemical calculation. In the lowest energy  $\alpha$ -Glc-C-34 structure of  $\text{Li}(\alpha\text{-Me-Glc})^+$ , the sugar moiety is only bound to  $\text{Li}^+$  through the two equatorial oxygen O(3) and O(4) atoms (Figure 5-10).

The fact that a bidentate ( $\alpha$ -Glc-C-34) structure is the lowest energy structure for the  $\text{Li}(\alpha\text{-Me-Glc})^+$  complex is non intuitive, and two arguments may be considered to understand this finding. First, as discussed above, for the free sugar, the  ${}^4\text{C}_1$  conformation is the lowest energy conformer and the  ${}^1\text{C}_4$  and lowest energy boat are much higher in energy (35.9 and 54.9 kJ/mol, respectively). Second, there seems to be a synergistic effect between the  $\text{Li}^+$  coordination and the intra-sugar hydrogen bonding. This hydrogen bonding pattern is somewhat similar to that observed between water molecules of the first and second shell of metal cation [12] (Figure 5-9). It seems that the hydrogen bond is reinforced when the hydrogen bond donor is coordinated to a metal cation. Relatively strong hydrogen bonding is observed between the first-shell OH HB donor and second-shell OH acceptor groups.

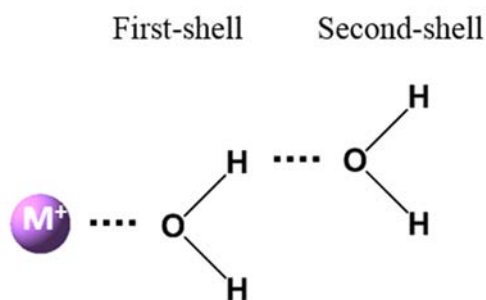


Figure 5-9 : Metal cation solvated with two water molecules. The first water molecule is bound to the metal cation ( $M^+$ ) being part of the first coordination shell. The second water molecule is bound to the first water molecule forming the second-shell.

This synergic effect is illustrated by the hydrogen bond involving the O(4)H group, which is bound to  $Li^+$  and also acts as a HB donor towards the hydroxymethyl O(6)H group. The O(4)H-O(6) hydrogen bond pattern is observed for some of the low energy  ${}^4C_1$  structures of free  $\alpha$ -glucose, and the typical bond distance is  $\sim 2$  Å. In the  $\alpha$ -Glc-C-34 structure where the O(4)H group is bound to  $Li^+$ , the O(4)H-O(6)H distance is significantly shorter (1.81 Å). This is a signature of the expected synergic effect. It should be noticed that the synergic effect is less pronounced if the O(3)H group is considered. The O(3)H-O(2) is 2.39 Å in the  $\alpha$ -Glc-C-34, which is also the order of magnitude of this bond distance in the  ${}^4C_1$  conformation of the free  $\alpha$ -glucose. This differences in the  $Li^+$  effect on the hydrogen bonding is probably due to the fact that the O(3)H-O(2) bond between two equatorial groups is relatively weak, while the O(4)H-O(6)H is much more favorable. In the latter case, the flexibility of the hydroxymethyl chain allows for the formation of a strong O(4)H-O(6)H hydrogen bond within a favorable six membered ring motif.

This latter point might be at the origin of the preference for the coordination through the O(4) and O(3) hydroxyl group starting from the  $\alpha$ -glucose in its  ${}^4C_1$  conformation. Other bidentate structures have been envisaged starting from a  ${}^4C_1$  conformation, but they were found higher in energy. In particular, the  $\alpha$ -Glc-C-56 structure, corresponding to the coordination of  $Li^+$  to the O(5) and hydroxymethyl O(6) oxygen atoms, is significantly higher in energy ( $+37.3$  kJ mol $^{-1}$ ) than the  $\alpha$ -Glc-C-34 one.

Tri-coordinated  $\text{Li}(\alpha\text{-Me-Glc})^+$  structures could be formed when  $\alpha$ -glucose was considered in a  ${}^1\text{C}_4$  or boat conformation. Both structure types are relatively low in energy. The lowest-energy structure with  $\alpha$ -glucose in a boat conformation is a tridentate structure ( $\alpha\text{-Glc-B-124}$ ). It is only  $8.6 \text{ kJ mol}^{-1}$  higher in energy than the  $\alpha\text{-Glc-C-34}$  where the  ${}^4\text{C}_1$  acts as a bidentate ligand. This relatively low energy difference could be anticipated since the boat structure is intrinsically relatively low in energy for  $\alpha$ -glucose: it is only  $35.9 \text{ kJ/mol}$  higher in energy than the lowest energy  ${}^4\text{C}_1$  structure. Second, three oxygen atoms (O(1), O(2) and O(4)) can simultaneously and efficiently bind the  $\text{Li}^+$  cation (Li-O bond lengths are  $1.91, 1.92, \text{ and } 1.94 \text{ \AA}$ , respectively), leading to a tri-coordinated complex. At the same time, one hydrogen bond can be maintained on the other face of the sugar cycle between the O(3)H and the hydroxymethyl O(6)H HB acceptor group.

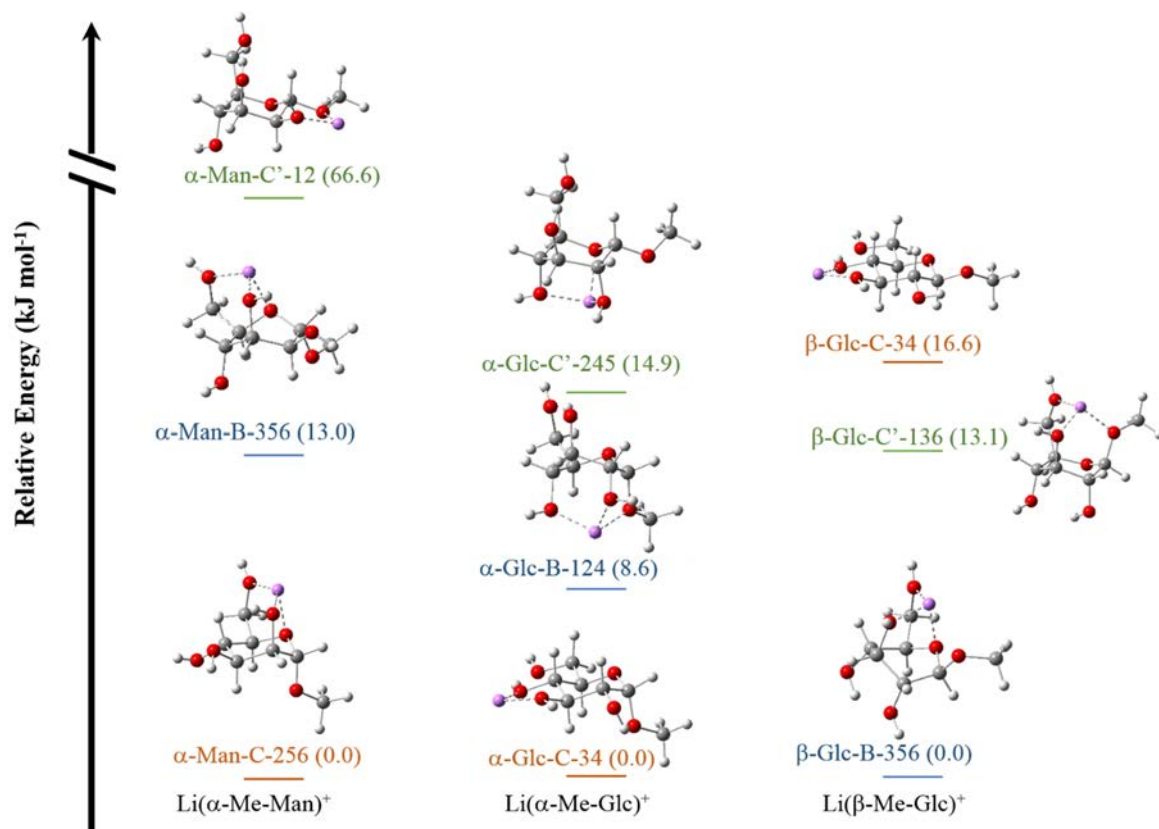


Figure 5-10 : Relative free Gibbs energies of the most stable of the  $\text{Li}(\text{Sac})^+$  complexes. Three types of structures are considered, depending on the conformation of the sugar moiety:  ${}^4\text{C}_1$ ,  ${}^1\text{C}_4$  and boat conformers are denoted as C, C' and B, respectively. Only the most stable representative structure is shown here. Structures were characterized at the B3LYP/6-31G\*\* level of theory. 298K Gibbs free energies in  $\text{kJ mol}^{-1}$  were determined at the same level.

The structures derived from the  $\alpha$ -glucose in a  ${}^1C_4$  conformation are only slightly higher in energy than those derived from the boats. The lowest energy structure of this category is the  $\alpha$ -Glc-C'-245 whose relative energy is 14.9 kJ/mol. The lithium cation is efficiently coordinated through the O(2), O(4), and O(5) atoms of  $\alpha$ -glucose in its  ${}^1C_4$  chair conformation, the Li-O bond distances being 2.02, 1.90, and 1.97 Å, respectively.

As in the case of the  $\text{Li}(\alpha\text{-Me-Glc})^+$  system, the  $\beta$ -glucose in its low energy  ${}^4C_1$  chair conformation can only bind to the  $\text{Li}^+$  cation as a bidentate ligand. The resulting  $\beta$ -Glc-C-34 structure has a structural motif very similar with the  $\alpha$ -Glc-C-34. In particular, the two O(3)H and O(4)H hydroxyl groups which are bound to the  $\text{Li}^+$  cation also acts as efficient HB donor. In contrast to the  $\alpha$ -glucose system, however, this di-coordinated  $\beta$ -Glc-C-34 structure is not the lowest energy structure of the  $\text{Li}(\beta\text{-Me-Glc})^+$  system.

The most energetically favored structure is the tri-coordinated  $\beta$ -Glc-B-356 derived from a boat conformer of the  $\beta$ -glucose unit. This energy ordering could be anticipated since the boat conformers are lower in energy with respect to the  ${}^4C_1$  chair for the  $\beta$ -glucose than for  $\alpha$ -glucose (18.3 kJ mol<sup>-1</sup>). A close inspection of the  $\text{Li}^+$ -O distances reveals that this  $\beta$ -Glc-B-356 also has a relatively short  $\text{Li}^+$ -O(1) distance (2.5 Å), and it could thus be considered as a tetra-dentate structure. In addition, an intramolecular hydrogen bonding O(4)H-O(2) (2.04 Å) interaction can be preserved on the face of the sugar opposite to the  $\text{Li}^+$  cation.

One structure ( $\beta$ -Glc-C'-136) derived from the sugar in its relatively low-energy  ${}^1C_4$  conformation is predicted to be only 13.1 kJ mol<sup>-1</sup> higher in energy than the  $\beta$ -Glc-B-356 structure. This tri-dentate structure probably also owes its relatively low energy to the hydrogen bond which is maintained between the O(2)H donor and the O(4) acceptor groups.

Overall, an interesting common aspect of the two glucose anomers is that structures with the three types of sugar conformers ( ${}^4C_1$ ,  ${}^1C_4$ , and boat) are found to lie within only ~15 kJ/mol. On the other

hand, in the case of  $\alpha$ -mannose, while structures derived from boat conformers are also relatively low in energy, the binding of  $\text{Li}^+$  to  ${}^1\text{C}_4$  conformers is disfavored ( $66.1 \text{ kJ mol}^{-1}$ ).

The preference for di-coordinated structure for glucose anomers in a chair conformation is consistent with previous results of Armentrout and coworkers [9]. As for  $\text{Li}(\alpha\text{-Me-Glc})^+$  in the present case, the lowest energy structure of the  $\text{Na}(\alpha\text{-Glc})^+$  was found to be a di-coordinated structure with the  ${}^4\text{C}_1$  chair conformer acting as a bidentate ligand. In the case of the  $\beta$ -glucose, as found here with the  $\text{Li}^+$  glucose, the lowest energy structure of the  $\text{Na}(\beta\text{-Glc})^+$  system has the  $\beta$ -glucose in a boat conformation and acting as a tridentate ligand. The lowest energy structures calculated by Armentrout and coworkers were consistent with the previous results obtained by Kentäma and coworkers for the arabinose and xylose systems [4], with Barrows *et al.* [3] for the glucose systems, and Rahal-Sekkal *et al.* [13] for galactose saccharide .

These results contrast with earlier results from Wesdemiotis and coworkers [8] on sodiated monosaccharide and disaccharide complexes. Conformers of  $\text{Na}[\text{Sac}]^+$  with the saccharide in a  ${}^4\text{C}_1$ ,  ${}^1\text{C}_4$  and boat configuration were explored producing more than 30 different conformers. The most favored structures predicted for  $\text{Na}[\text{Sac}]^+$  (Sac=  $\alpha$ -glucose and  $\beta$ -Glucose) were the tetradentate boat conformers while the calculated lowest energy structure for  $\text{Na}(\alpha\text{-Mannose})^+$  was the tridentate  ${}^4\text{C}_1$  chair.

The effect of the nature (size) of the metal cation on the sugar conformation has also been studied [14]. In the case of  $\beta$ -D-xylanopyranoside, for example, which has a  ${}^4\text{C}_1$  ground state conformer, it was shown that complexation with divalent metals induce a  ${}^4\text{C}_1$  to  ${}^1\text{C}_4$  conformational interconversion. It was suggested that the stabilization of the  ${}^1\text{C}_4$  chair depends on the ionic radii of the metal cation [14].

### 5.3.2 Structure and energetics of $\text{Li}(\text{Sac})(\text{H}_2\text{O})^+$ adducts.

The relative energies of the three types of monohydrated  $\text{Li}(\text{Sac})^+$  adducts for each sugar considered here are given in Figure 5-11. As for the bare  $\text{Li}(\text{Sac})^+$  complexes, only the lowest energy structure characteristic of a  ${}^4\text{C}_1$ ,  ${}^1\text{C}_4$  chair or boat conformation of the saccharide (Sac) moiety is

displayed. Other structures have been optimized, and the relative energies of the lowest energy ones are given in the Annexes.

As can be seen in Figure 5-11, the saccharide moiety has a  ${}^4C_1$  conformation in the lowest energy structure of  $\text{Li}(\text{Sac})(\text{H}_2\text{O})^+$  for the three saccharides. The most important change in relative energy upon addition of a water molecule on  $\text{Li}(\text{Sac})^+$  occurs for  $\text{Sac}=\beta$ -glucose. To understand this effect, one has to consider the evolution of the binding energy of water to an alkali cation as a function of its coordination number [15]. The general observed trend is a decrease of the  $\text{H}_2\text{O}-\text{M}^+(\text{H}_2\text{O})_{n-1}$  as a function of the coordination number  $n$ . This is illustrated in table 5-2 in the cases of the binding of water molecule to  $\text{Li}^+$  [16] and  $\text{Na}^+$ [17]. As can be seen in this Table the binding energy of the fourth water molecule to  $\text{Li}^+$  (71 kJ/mol) is much weaker than for the third water molecule (94 kJ/mol).

N	1	2	3	4
$\text{M}^+=\text{Li}^+$	137±14	114±10	94±4	71±5
$\text{M}^+=\text{Na}^+$	94.5±7.5	81.9±5.9	70.2±5.9	54.8±5.9

Table 5-2 : Experimental binding energy values ( $\text{kJ mol}^{-1}$ ) of  $\text{H}_2\text{O}-\text{M}^+(\text{H}_2\text{O})_{n-1}$  complexes ( $\text{M}^+=\text{Li}^+, \text{Na}^+$ ), ( $n \leq 4$ ) reported from previous studies of Armentrout and coworkers [16,17].

Binding energies of the methylated monosaccharide to  $\text{Li}^+$  in  $\text{Li}(\text{Sac})^+$  structures as well as those of water to  $\text{Li}(\text{Sac})^+$  in  $\text{Li}(\text{Sac})(\text{H}_2\text{O})^+$  complexes are given in Table 5-3. In the case of methylated  $\alpha$ -mannose and  $\alpha$ -glucose systems, the binding energies are given with respect to the lowest energy asymptote. In the case of methylated  $\beta$ -glucose complexes, however, both adiabatic and non-adiabatic binding energies are given. The non-adiabatic binding energy values for the  $\text{Li}(\text{Me}-\beta\text{-Glc})^+$  and  $\text{Li}(\text{Me}-\beta\text{-Glc})(\text{H}_2\text{O})^+$  structures listed in Table 5-3 correspond to a dissociation process where the saccharide conformation remains the same. In the lowest energy structure of the  $\text{Li}(\text{Me}-\beta\text{-Glc})^+$  complex ( $\beta\text{-Glc-B-356}$ ), the methylated  $\beta$ -glucose has a boat conformation. The non-adiabatic binding energy value given in Table 5-3 for this complex correspond to the dissociation into  $\text{Li}^+$  plus the free saccharide in the energy minimum with the “same conformation”. This is to account for the fact that the adiabatic

dissociation process is associated to a conformational change of the methylated  $\beta$ -glucose moiety from a boat in the complex to a  ${}^4C_1$  chair in the dissociated system.

Complex type	Structure name	Li <sup>+</sup> CN	Saccharide-Li <sup>+</sup> BDE		H <sub>2</sub> O-Li(Sac) <sup>+</sup> BDE	
			Adiab	Non-Adiab	Adiab	Non-Adiab
Li(Me- $\alpha$ -Man) <sup>+</sup>	$\alpha$ -Man-C-256	3	338			
Li(Me- $\alpha$ -Glc) <sup>+</sup>	$\alpha$ -Glc-C-34	2	311			
Li(Me- $\beta$ -Glc) <sup>+</sup>	$\beta$ -Glc-C-34	2	326	309		
	$\beta$ -Glc-B-356	3	320	343		
Li(Me- $\alpha$ -Man)(H <sub>2</sub> O) <sup>+</sup>	w- $\alpha$ -Man-C-256	3			63	
Li(Me- $\alpha$ -Glc)(H <sub>2</sub> O) <sup>+</sup>	w- $\alpha$ -Glc-C-34	2			81	
Li(Me- $\beta$ -Glc)(H <sub>2</sub> O) <sup>+</sup>	w- $\beta$ -Glc-C-34	2			64	81
	w- $\beta$ -Glc-B-356	3			64	59

Table 5-3 : Binding energies (in kJ mol<sup>-1</sup>) associated with the Li(Sac)<sup>+</sup> and Li(Sac)(H<sub>2</sub>O)<sup>+</sup> complexes. Non-adiabatic binding energy values are calculated with respect to a dissociation asymptote where the saccharide has the same conformation as in the complex (see text).

For a tri-coordinated Li(Sac)<sup>+</sup> complex such as  $\alpha$ -Man-C-256, the binding energy is 338 kJ mol<sup>-1</sup>. A very similar dissociation energy value (343 kJ mol<sup>-1</sup>) is obtained for the tri-coordinated  $\beta$ -Glc-B-356 structure of the Li(Me- $\beta$ -Glc)<sup>+</sup> complex assuming a non-adiabatic dissociation process. It is interesting that these values for the Li<sup>+</sup> bound to three oxygen of a saccharide in a  ${}^4C_1$  or in a boat complex are very similar to sum of the binding energies (94 kJ mol<sup>-1</sup>) of the three water molecules to Li<sup>+</sup>. If di-coordinated complexes are considered, however, the Sugar-Li<sup>+</sup> binding energies are larger than expected if the water solvated systems are considered. Indeed, the binding energy of Li(Me- $\alpha$ -Glc)<sup>+</sup> with the  ${}^4C_1$  chair conformation bound to Li<sup>+</sup> in a bidentate fashion is 311 kJ mol<sup>-1</sup> and a very similar value (309 kJ mol<sup>-1</sup>) is obtained if the non-adiabatic process is considered for the corresponding structure of the Li(Me- $\beta$ -Glc)<sup>+</sup> complex. This value is larger than sum of the two H<sub>2</sub>O-Li<sup>+</sup> binding energies (251 kJ mol<sup>-1</sup>) in Li(H<sub>2</sub>O)<sub>2</sub><sup>+</sup>. This difference might be in part related to the cooperative effect between the bonding of the O(4)H to Li<sup>+</sup> and the O(4)H-O(6) hydrogen bonding, *i.e.* to the partial ionic character of

the O(4)H-O(6) hydrogen bond. Water binding energies to a tri-coordinated  $\text{Li}(\text{Sac})^+$  complex is on the order of  $60\text{-}65 \text{ kJ mol}^{-1}$ , *i.e.* slightly weaker than the  $\text{H}_2\text{O-Li}(\text{H}_2\text{O})_3^+$  value ( $71\pm 5 \text{ kJ mol}^{-1}$ ). As expected, it is much more favorable to bind the water molecule to a di- ( $\sim 80 \text{ kJ mol}^{-1}$ ) than to a tri-dentate structure.

The difference between the binding energies of the third and fourth water molecules to  $\text{Li}^+$  (23 kJ/mol) is very close to the relative stabilization energy of bi- and tri-dentate  $\text{Li}(\text{Sac})^+$  structures upon addition of one water molecule ( $\sim 15\text{-}20 \text{ kJ/mol}$ ). Overall, the relative energies of the tri-dentate complexes, disregarding the conformation ( ${}^4\text{C}_1$ ,  ${}^1\text{C}_4$  or boat), does not significantly change upon addition of one water molecule. Conversely, the bi-dentate structures derived either from a  ${}^1\text{C}_4$  or a  ${}^4\text{C}_1$  saccharide conformations are significantly stabilized.

The most important change is observed in the case of methylated  $\beta$ -glucose. The lowest energy structure of the lithiated complex has the sugar in a boat conformation acting as a tri-dentate ligand. Upon addition of a water molecule, however, the energy ordering of the three types ( ${}^4\text{C}_1$ ,  ${}^1\text{C}_4$  or boat) of structure changes and the lowest energy structure of  $\text{Li}(\beta\text{-Me-Glc})(\text{H}_2\text{O})^+$  complex has the  $\beta$ -glucose acting as a bidentate ligand.

In the case of  $\text{Li}(\alpha\text{-Me-Man})(\text{H}_2\text{O})^+$ , the relative energy of the lowest bi-dentate structure ( $w\text{-}\alpha\text{-Man-C}'\text{-}12$ ) is  $45.7 \text{ kJ/mol}$ , which corresponds to a stabilization of  $\sim 21 \text{ kJ/mol}$  of the bi-dentate structure with respect to the tri-dentate structure. As discussed in the previous section, when  $\alpha$ -mannose has a  ${}^4\text{C}_1$  and boat conformation, tri-dentate structures can be formed. Upon addition of water, no significant changes of the relative energies are observed. The lowest energy structure of  $\text{Li}(\alpha\text{-Me-Man})(\text{H}_2\text{O})^+$  is  $w\text{-}\alpha\text{-Man-C-}256$ , with  $\alpha$ -mannose in a  ${}^4\text{C}_1$  chair conformation. Boat structures are found to be slightly higher in energy and the relative energy of the  $w\text{-}\alpha\text{-Man-B-}356$  structure is  $12.5 \text{ kJ mol}^{-1}$ .

The bi-dentate coordination of  $\alpha$ -glucose in a  ${}^4\text{C}_1$  chair is the most favorable for  $\text{Li}(\alpha\text{-Me-Glc})^+$  complex. The addition of water further increases the energy preference for bi- versus tri-dentate sugar complexes. The lowest energy structure of  $\text{Li}(\alpha\text{-Me-Glc})(\text{H}_2\text{O})^+$  is the  $w\text{-}\alpha\text{-Glc-C-}34$  one, and one can estimate that the addition of water increases the energy preference for the bi-dentate structure by  $\sim 15 \text{ kJ}$

mol<sup>-1</sup>. On the other hand, the relative energies of the tri-dentate complexes either from the boat (w- $\alpha$ -Glc-B-124) and the <sup>1</sup>C<sub>4</sub>  $\alpha$ -glucose conformer (w- $\alpha$ -Glc-C'-245) remains almost constant.

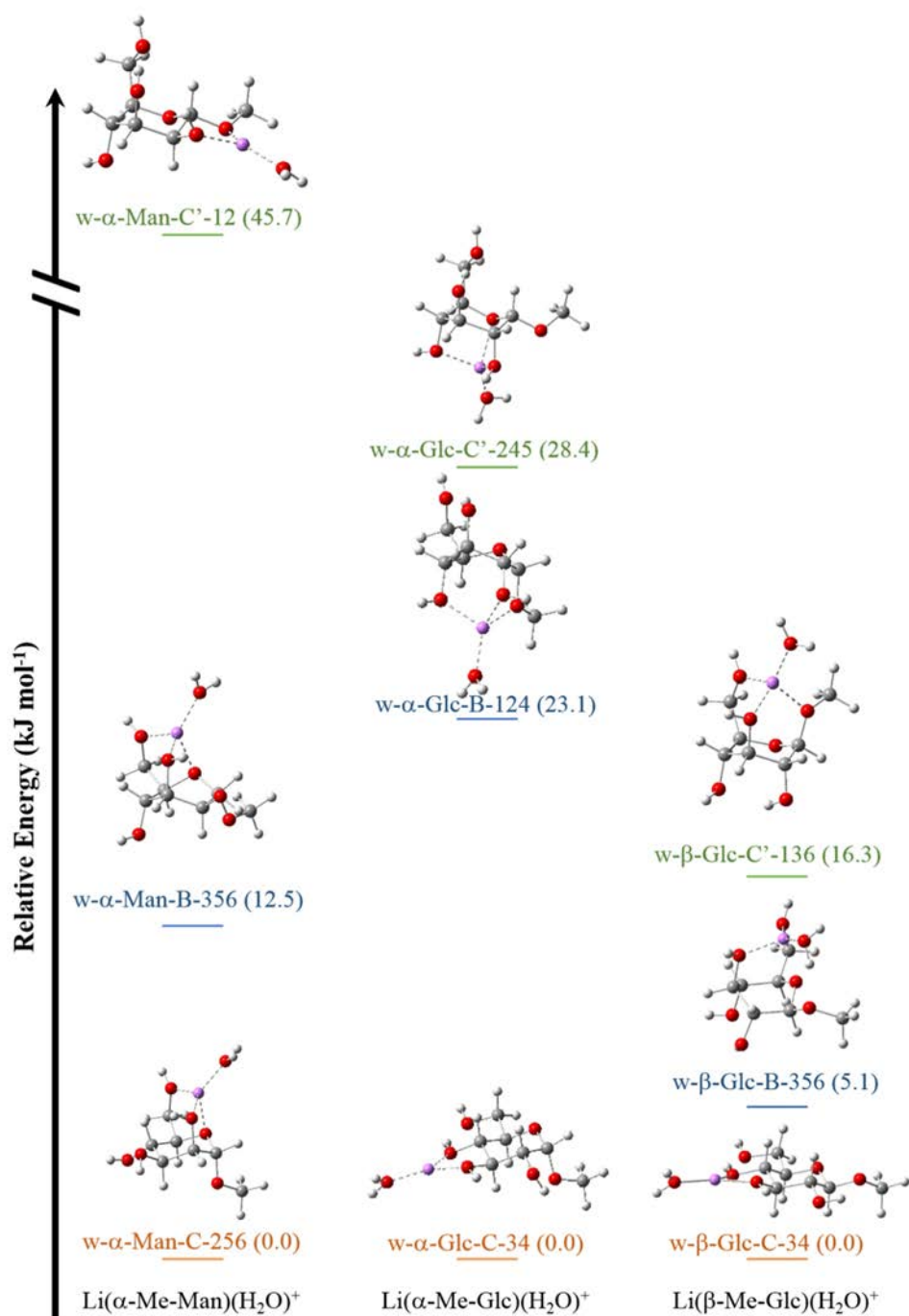


Figure 5-11 : Relative Gibbs free energies of the most stable <sup>4</sup>C<sub>1</sub>, <sup>1</sup>C<sub>4</sub> and boat conformers of the Li(Sac)(H<sub>2</sub>O)<sup>+</sup> complexes. Gibbs free energies are provided in parentheses in kJ mol<sup>-1</sup>. Li(Sac)<sup>+</sup> structures were characterized at the B3LYP/6-31G\*\* level of theory.

The stabilization effect of the bi-dentate saccharide complexes upon addition of a water molecule has a significant effect on the relative energies in the case of the  $\beta$ -glucose complexes. There is a reversing of the energy order of the bi-dentate  ${}^4C_1$  conformers and the tri-dentate boat structures. The former was 16.6 kJ mol<sup>-1</sup> higher in energy than the latter in the bare complexes, but it becomes more favorable by 5.1 kJ mol<sup>-1</sup> after addition of a water molecule. This relative stabilization energy (~20 kJ mol<sup>-1</sup>) is consistent with those observed for the two other saccharide systems.

The most stable structure of Li( $\beta$ -Me-Glc)(H<sub>2</sub>O)<sup>+</sup> is the bi-dentate w- $\beta$ -Glc-C-34 structure. The w- $\beta$ -Glc-B-356 structure, which is calculated 5.1 kJ mol<sup>-1</sup> higher in energy, is the most stable structure derived from a boat  $\beta$ -glucose conformer. As in the two previous cases, the energy difference between tridentate complexes remains similar to that of the Li( $\beta$ -Me-Glc)<sup>+</sup>. For example, the relative energy of the lowest tridentate  ${}^1C_4$  (w- $\beta$ -Glc-C'-136) and boat (w- $\beta$ -Glc-B-356) conformers is ~11 kJ mol<sup>-1</sup>, *i.e.* very similar to that of the bare complex (~13 kJ mol<sup>-1</sup>).

Overall, on the basis of the theoretical results, the lowest energy structure for the three Li(Sac)(H<sub>2</sub>O)<sup>+</sup> systems derives from the  ${}^4C_1$  chair conformation of the saccharide. In the case of the two glucose anomers, the saccharide acts as a bidentate ligand, while the  $\alpha$ -mannose in its  ${}^4C_1$  chair conformation acts as a tridentate ligand. This difference is essentially related to the stereochemistry of the C(2) carbon atom. In the case of  $\alpha$ -mannose, the O(2)H is in the axial position while it is in an equatorial position in the glucose anomers in their  ${}^4C_1$  chair conformation. As a result, when the hydroxymethyl O(6)H group is in the axial position, three oxygen atoms (O(2), O(5) and O(6)) of  $\alpha$ -mannose are available for an efficient tri-coordination of the Li<sup>+</sup> cation. In the case of the glucose anomers, however, no such tri-coordination is possible from the  ${}^4C_1$  conformation. Conversely, the flexibility of the hydroxymethyl group may favor the bi-dentate coordination through the formation of the Li<sup>+</sup>-O(4)H-O(6) bonding motif.

The most interesting case is the  $\beta$ -glucose one. First, the energy ordering of the di- and tri-coordinated complexes changes upon water addition. Second, the energy gap between these two coordination types is relatively low in the mono-hydrated complex. It is predicted to be only 5.1 kJ mol<sup>-1</sup>

at the B3LYP/6-31G\*\* level of theory, and a very similar result (+5.8 kJ mol<sup>-1</sup>) in favor of the di-coordinated Li( $\beta$ -Me-Glc)(H<sub>2</sub>O)<sup>+</sup> complex has been found at the MP2/6-311+G\*\* level of theory. Nevertheless, this energy difference is so small, that it is likely to change with the nature of the metal cation.

IR spectroscopy of the bare Li(Sac)<sup>+</sup> and the monohydrated Li(Sac)(H<sub>2</sub>O)<sup>+</sup> complexes is thus of particular interest to probe the nature of the coordination of the saccharide to the Li<sup>+</sup> cation. In this perspective, infrared absorption spectra of the lowest energy structures have been calculated within the harmonic approximation. These predicted spectra will be compared in the following to the experimental spectra. As shown in the previous chapter, an IR band near  $\sim 3400$  cm<sup>-1</sup> seems to be the signature of bidentate coordination of the saccharide. A particular attention will be paid to the corresponding spectral range.

## 5.4 IR spectroscopy of monosaccharide complexes.

### 5.4.1 Experimental infrared Spectra of Li(Sac)<sup>+</sup> and Li(Sac)(H<sub>2</sub>O)<sup>+</sup> adducts.

The infrared spectra of the Li(Sac)<sup>+</sup> adducts in the 3000-3800 cm<sup>-1</sup> energy range are given in Figure 5-12. These complexes are relatively strongly bound, and the auxiliary CO<sub>2</sub> laser had to be used for enhancing their fragmentation. Since the laser power drops when going from high to low frequency, the signal-to-noise is lower in the lower energy part of the spectra. Nevertheless, a band could be clearly observed in the case of Li( $\alpha$ -Me-Glc)<sup>+</sup> near 3350 cm<sup>-1</sup>, while no band was observed below 3500 cm<sup>-1</sup> in the two other cases.

The IR bands in the 3000-3800 cm<sup>-1</sup> region are characteristic of the four OH stretching modes of the saccharide moiety. As already briefly discussed in the previous chapter, when OH groups are involved as hydrogen bond donors, the corresponding IR band is red-shifted and this red-shifted is accompanied by a broadening [12]. This would be consistent with the observed features in the case of Li( $\alpha$ -Me-Glc)<sup>+</sup>. The band near 3350 cm<sup>-1</sup> is broader than those in the higher frequency range, which corresponds to either weakly HB or free OH groups. Interestingly, the upper parts of the three experimental spectra are different, which is likely to be a signature of different types of structures.

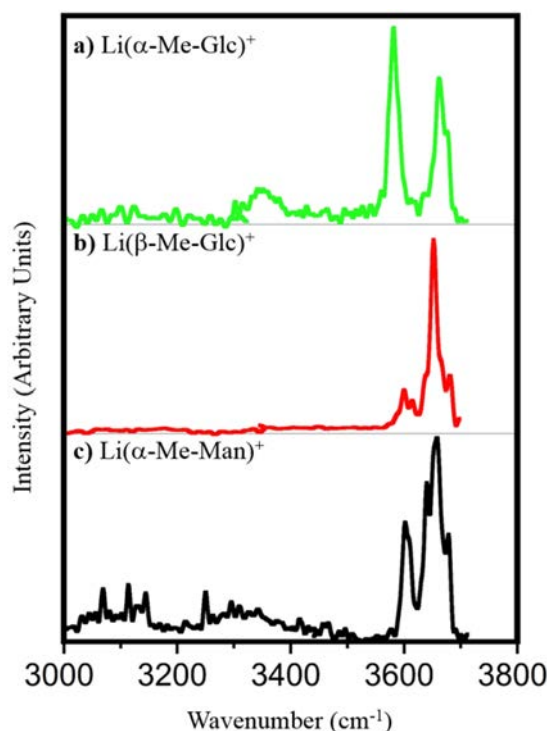


Figure 5-12 : Experimental IRMPD spectra of a)  $\text{Li}(\alpha\text{-Me-Glc})^+$  (green color), b)  $\text{Li}(\beta\text{-Me-Glc})^+$  (red), and c)  $\text{Li}(\alpha\text{-Me-Man})^+$  (black) in the  $3800\text{-}3000\text{ cm}^{-1}$  spectral range. The  $\text{Li}(\text{Sac})^+$  were irradiated during 1 second combining the tabletop OPO/OPA laser and 5 ms of cw  $\text{CO}_2$  laser.

The infrared spectra of the  $\text{Li}(\text{Sac})(\text{H}_2\text{O})^+$  complexes have been recorded in a larger spectral range ( $2800\text{-}3800\text{ cm}^{-1}$ ) than the bare complexes. As can be seen in Figure 5-13, bands were observed in the  $2800\text{-}3000\text{ cm}^{-1}$  range in the case of  $\text{Sac}=\text{Me-}\alpha\text{-Man}$ . Although the signal was weaker in the two other cases, reproducible bands were also observed for the corresponding complexes for the two glucose anomers. These infrared bands correspond to the CH stretching modes which are weakly IR active. This observation is a clear evidence of the sensitivity of the IR spectroscopy in the case of the  $\text{Li}(\text{Sac})(\text{H}_2\text{O})^+$  complexes. Since the CH stretching modes are predicted to be weakly IR active and that the laser power is low in this low frequency region, it is likely that bands associated with red-shifted OH stretches should be clearly observed for these systems. The higher sensitivity of the technique for monohydrated than for the bare system is simply due to the smaller fragmentation threshold in the former than in the latter case. Indeed the release of the water molecule from monohydrated complexes requires much less energy than the fragmentation of the bare ions.

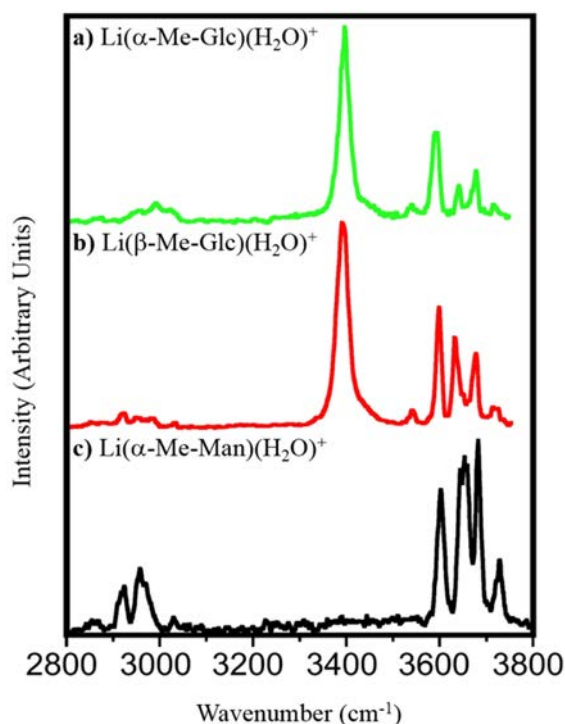


Figure 5-13 : Experimental IRMPD spectra of a)  $\text{Li}(\alpha\text{-Me-Glc})(\text{H}_2\text{O})^+$  (green), b)  $\text{Li}(\beta\text{-Me-Glc})(\text{H}_2\text{O})^+$  (red), and c)  $\text{Li}(\alpha\text{-Me-Man})(\text{H}_2\text{O})^+$  (black) in the  $2800\text{-}3800\text{ cm}^{-1}$  spectral range. The  $\text{Li}(\text{Sac})(\text{H}_2\text{O})^+$  ions were irradiated for 1 second, and each OPO/OPA pulse at 25 Hz was followed by a  $500\text{ }\mu\text{s}$  pulse of the auxiliary  $\text{CO}_2$  laser.

The IR spectra of the two glucose anomers share a common feature: an intense band near  $3400\text{ cm}^{-1}$ . This band has already been discussed in the previous chapter, and is probably the signature of a common hydrogen bonding motif for the two corresponding  $\text{Li}(\alpha\text{-Me-Glc})(\text{H}_2\text{O})^+$  and  $\text{Li}(\beta\text{-Me-Glc})(\text{H}_2\text{O})^+$  systems. It is important to notice that a feature near  $3400\text{ cm}^{-1}$  was observed for the bare  $\text{Li}(\alpha\text{-Me-Glc})^+$  complex, but not for the  $\text{Li}(\beta\text{-Me-Glc})^+$  one.

#### 5.4.2 IR Spectra of $\text{M}(\beta\text{-Me-Glc})(\text{L})^+$ : effect of $\text{M}=(\text{Li}, \text{Na})$ and $\text{L}=(\text{H}_2\text{O}, \text{CH}_3\text{CN})$

From the theoretical study on the bare and monohydrated  $\text{Li}(\text{Sac})^+$  complexes, it was concluded that the  $\beta\text{-Me-Glc}$  containing systems present two competing types of structures, lying within 5-10 kJ/mol. The saccharide could adopt a  ${}^4\text{C}_1$  conformation and bind the  $\text{Li}^+$  cation in a bi-dentate fashion. Alternatively, low-energy tri-dentate complexes could also be formed when  $\beta\text{-Me-Glc}$  adopts a boat conformation. It was thus interesting to probe the effect of the nature of the metal and of the tag molecule ( $\text{H}_2\text{O}$ ,  $\text{CH}_3\text{CN}$ ) on the IR spectrum.

The infrared spectra of the  $\text{Li}(\beta\text{-Me-Glc})(\text{CH}_3\text{CN})^+$  and  $\text{Na}(\beta\text{-Me-Glc})(\text{CH}_3\text{CN})^+$  complexes are given in Figure 5-14, along with those of the  $\text{Li}(\beta\text{-Me-Glc})^+$  and  $\text{Li}(\beta\text{-Me-Glc})(\text{H}_2\text{O})^+$  complexes. As can be seen in this Figure, a band is observed near  $3400\text{ cm}^{-1}$  for the water and acetonitrile complexes. Moreover, the position of the bands of these three complexes in the  $3550\text{-}3700\text{ cm}^{-1}$  are very similar.

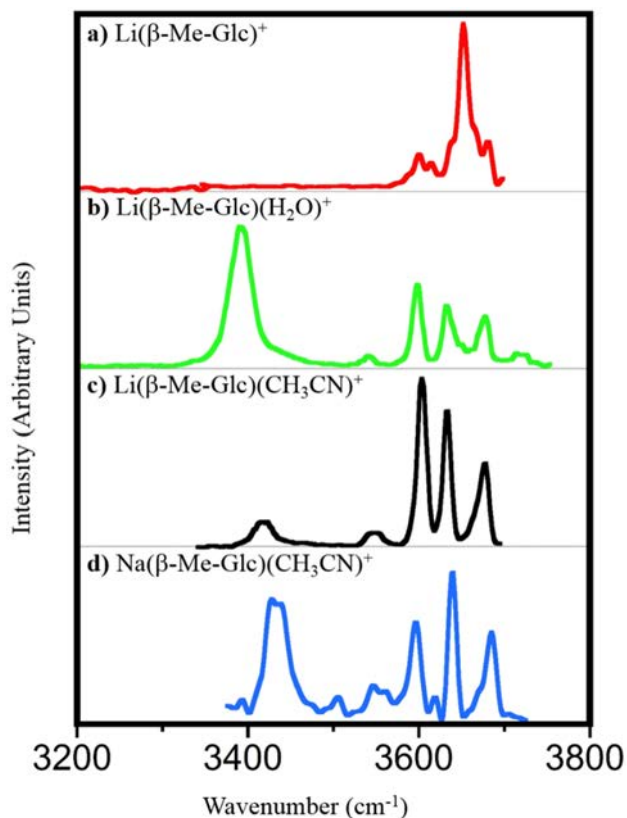


Figure 5-14 : Experimental IRMPD spectra of a)  $\text{Li}(\beta\text{-Me-Glc})^+$  (red), b)  $\text{Li}(\beta\text{-Me-Glc})(\text{H}_2\text{O})^+$  (green), c)  $\text{Li}(\beta\text{-Me-Glc})(\text{CH}_3\text{CN})^+$  (black), and d)  $\text{Na}(\beta\text{-Me-Glc})(\text{CH}_3\text{CN})^+$  (blue) in the  $3200\text{-}3800\text{ cm}^{-1}$  spectral range. The irradiation time was  $1\text{ s}$ , and each OPO/OPA pulse was followed by a pulse of the auxiliary  $\text{CO}_2$  laser. The  $\text{CO}_2$  pulse duration was longer ( $5\text{ ms}$ ) for the untagged  $\text{Li}(\beta\text{-Me-Glc})^+$  system, than for the tagged complexes ( $500\text{ }\mu\text{s}$ ).

A detailed analysis of these IR spectra is out of the scope of this section. The main idea was to probe whether a change of structure upon substitution of  $\text{Li}^+$  by  $\text{Na}^+$  and/or  $\text{H}_2\text{O}$  by  $\text{CH}_3\text{CN}$  in  $\text{Li}(\beta\text{-Me-Glc})(\text{H}_2\text{O})^+$  could be evidenced by IR spectroscopy. The most important result is that the band near  $3400\text{ cm}^{-1}$  is observed in all cases. The position of this band slightly varies from one complex to another: it is observed at  $\sim 3400$ ,  $\sim 3420$ , and  $\sim 3430\text{ cm}^{-1}$  for the  $\text{Li}(\beta\text{-Me-Glc})(\text{H}_2\text{O})^+$ ,  $\text{Li}(\beta\text{-Me-Glc})(\text{CH}_3\text{CN})^+$ , and  $\text{Na}(\beta\text{-Me-Glc})(\text{CH}_3\text{CN})^+$  complexes. A possible interpretation of this trend will be given in the section dedicated to the analysis of the  $\text{Li}(\beta\text{-Me-Glc})(\text{H}_2\text{O})^+$  IR spectrum.

## 5.5 IR spectra of monosaccharide complexes: Spectral and structural assignment

### 5.5.1 Li( $\alpha$ -Me-Glc)<sup>+</sup> complexes.

IR spectra of the Li( $\alpha$ -Me-Glc)<sup>+</sup> in the 3200-3700 cm<sup>-1</sup> energy range are shown in Figure 5-16. The experimental infrared spectrum is given in the top panel (black). The IR absorption spectra of the lowest energy structure corresponding to the three conformations of the sugar moiety (<sup>4</sup>C<sub>1</sub>, <sup>1</sup>C<sub>4</sub> and boat) are given in the three lower panels of Figure 5-16. Two intense and asymmetric features at 3580 and 3665 cm<sup>-1</sup> and one additional weaker and broad band at 3350 cm<sup>-1</sup> can be distinguished. These IR features correspond to the four OH stretching modes of the methylated  $\alpha$ -glucose. The band observed near 3350 cm<sup>-1</sup> is the most structurally diagnostic. This band near 3350 cm<sup>-1</sup> is strongly red-shifted with respect to the position of the free OH, and it is thus the signature of strongly bound OH group involved in a hydrogen bonding motif. As found for protonated peptides and proton bound dimers, the red-shift is accompanied by a substantial broadening [18-22].

As can be seen in Figure 5-16, if the positions of the bands are considered, the predicted infrared absorption spectrum of the lowest energy structure ( $\alpha$ -Glc-C-34) nicely matches with the experimental one. In particular, this structure is predicted to have an IR band near 3350 cm<sup>-1</sup>. Among the other low energy conformers (Annex), no other structure has a predicted absorption band close to 3350 cm<sup>-1</sup>. In particular, the predicted infrared spectra corresponding to the  $\alpha$ -Glc-B-124 and  $\alpha$ -Glc-C'-245 structure (with the sugar in a boat and <sup>1</sup>C<sub>4</sub> conformation, respectively) shown in Figure 5-16 do not present any IR band below 3460 cm<sup>-1</sup>. Furthermore, the predicted IR spectra of these two complexes in the higher energy part do not match with the observed spectrum. In particular, no IR absorption is predicted near 3580 cm<sup>-1</sup>. An inspection of the predicted IR spectra of higher energy structures (Annexes) reveals that no other structure than  $\alpha$ -Glc-C-34 has predicted IR features near 3350, 3580 and 3665 cm<sup>-1</sup>. It can thus be concluded that only the lowest energy  $\alpha$ -Glc-C-34 structure is formed under our experimental conditions. Nonetheless, it cannot be excluded that other conformers slightly different from the lowest-

energy  $\alpha$ -Glc-C-34 structure found are also populated, which could in particular explain the shoulder on the blue side of the band centered at  $3665\text{ cm}^{-1}$ .

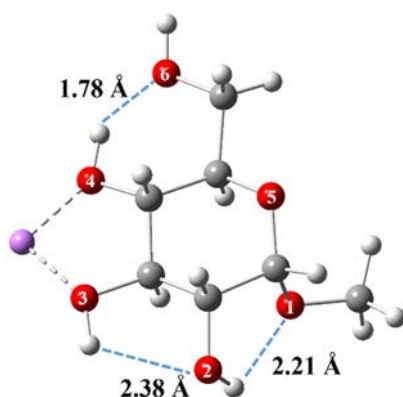


Figure 5-15 : Lowest energy structure of  $\text{Li}(\alpha\text{-Glc})^+$  system. Intra-sugar hydrogen bond interactions are represented in blue dotted lines. The hydrogen bond distances are given in Å.

A band assignment is proposed in Table 5-4 assuming that only the  $\alpha$ -Glc-C-34 structure is populated. The band centered at  $3665\text{ cm}^{-1}$  can be assigned to the OH stretching mode of the hydroxymethyl O(6)H group predicted at  $3665\text{ cm}^{-1}$ , using a scaling factor of 0.955. Search for other conformers with a slightly different O(6)H stretching frequency was performed, but no such structure could be located on the potential energy surface. The slightly red-shifted band centered at  $3580\text{ cm}^{-1}$  can be assigned to the O(3)H and O(2)H stretching modes. The corresponding predicted wavenumbers are  $3585$  and  $3575\text{ cm}^{-1}$ , respectively. As can be seen in Figure 5-15, these two hydroxyl groups are involved in hydrogen bonding. The O(2)H is a donor-acceptor group, but the two associated HB distances are relatively long (O(3)H-O(2)= $2.38\text{ Å}$ , and O(2)H-O(1)= $2.21\text{ Å}$ ). The O(4)H-O(6) hydrogen bond distance, however, is much shorter ( $1.78\text{ Å}$ ), and the corresponding O(4)-H predicted wavenumber is  $3340\text{ cm}^{-1}$ . The band observed at  $\sim 3350\text{ cm}^{-1}$  is thus the signature of the O(4)H group which is simultaneously bonded to the  $\text{Li}^+$  cation and involved as a HB donor.

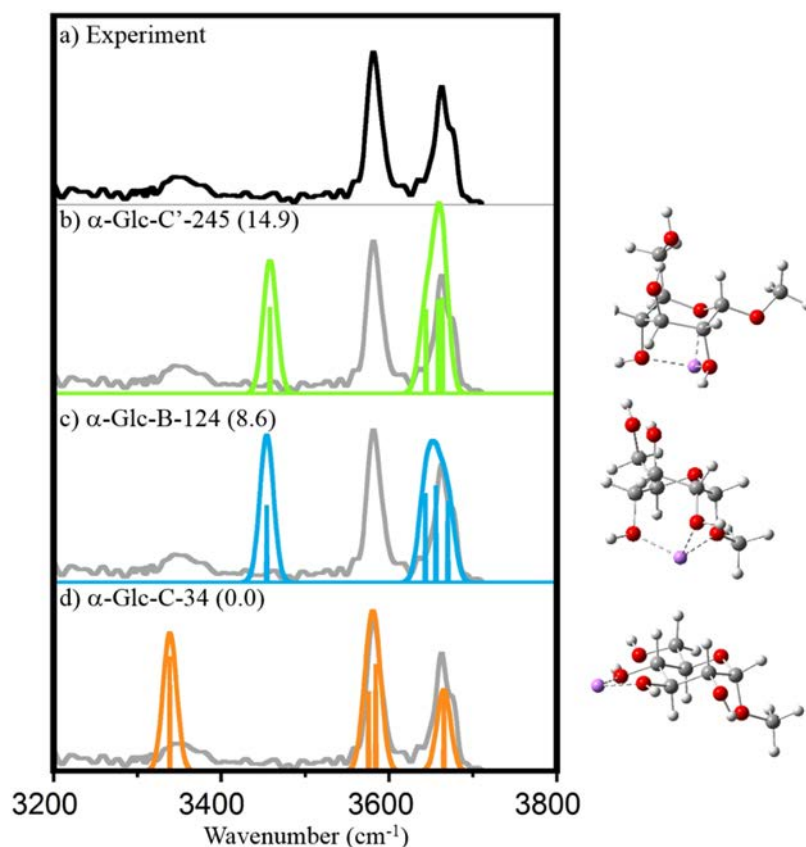


Figure 5-16 : IRMPD spectrum of the  $\text{Li}(\alpha\text{-Me-Glc})^+$  complex (upper panel). In the lower panels the experimental IRMPD spectrum (grey) is compared to the most energetically favorable structures with the sugar having a  ${}^1C_4$  chair (green), boat (blue), and  ${}^4C_1$  chair (orange) conformation. The corresponding theoretical structures as well as the relative Gibbs free energies (in  $\text{kJ mol}^{-1}$ ) are also provided. Theoretical infrared absorption spectra were calculated at the B3LYP/6-31G\*\* level of theory, and each band was convoluted using a Gaussian profile with a fwhm of  $20 \text{ cm}^{-1}$ . Harmonic frequencies were scaled with a factor of 0.955.

To conclude, the OH stretching frequencies are very sensitive to their environment and constitute an excellent structural probe in the present case. Hydroxyl groups involved as HB donors have the most red-shifted bands. The OH stretching mode of the O(6)H group, which is a HB acceptor, is predicted at  $3665 \text{ cm}^{-1}$ , which is very close to the characteristic frequency of the “free” OH stretching modes. On the other hand, OH group involved as HB donor are characterized by red-shifted bands, and there is a clear correlation between the red-shift and the corresponding HB distance. In the case of the O(3)H and O(2)H groups, the corresponding bond lengths are 2.38 and 2.21 Å, respectively, and the red-shift is  $\sim 80 \text{ cm}^{-1}$ . In the case of the O(4)H group, however, the HB distance is much shorter (1.78 Å), and the red-shift is  $\sim 300 \text{ cm}^{-1}$ .

Vibrational Mode	Theory (cm <sup>-1</sup> )	Li( $\alpha$ -Me-Glucose) (cm <sup>-1</sup> )	HB D distance (Å)
HB A O(6)H st	3665	3665	
HB A/D O(3)H st	3585	3580	2.38
HB A/D O(2)H st	3575		2.21
HB A/D O(4)H st	3340	3350	1.78

Table 5-4 : Infrared band assignment of the Li( $\alpha$ -Me-Glc)<sup>+</sup> complex. Vibrational mode description is provided in the first column. Predicted scaled (by 0.955) harmonic frequencies and the experimental infrared bands are given in column 2, and 3, respectively. The hydrogen bond distance (in Å) is given in the 4<sup>th</sup> column.

### 5.5.2 Li( $\alpha$ -Me-Glc)(H<sub>2</sub>O)<sup>+</sup> complexes.

The IR spectra of the Li( $\alpha$ -Me-Glc)(H<sub>2</sub>O)<sup>+</sup> complex in the 2800-3700 cm<sup>-1</sup> energy range are shown in Figure 5-17. The experimental spectrum is given in the top panel (black). Weak features observed between 2900 and 3100 cm<sup>-1</sup> correspond to the C-H stretching mode. Then, five IR features can be distinguished at 3395, 3590, 3640, 3675, and 3720 cm<sup>-1</sup>. They are due to the absorption bands associated with the OH stretching modes of the saccharide and/or to the symmetric and asymmetric OH stretching modes of the water molecule. IR absorption spectra of the three types of structures are given in the three lower panels of Figure 5-17.

The predicted IR spectrum of the lowest-energy structure (w- $\alpha$ -Glc-C-34) is in a good agreement with the experimental one. As for the corresponding bare Li( $\alpha$ -Me-Glc)<sup>+</sup> complex, only the lowest-energy structure has IR absorption features predicted close to the positions of all the observed bands. In particular, the w- $\alpha$ -Glc-C-34 structure has predicted bands matching the observed bands at 3395 and 3590 cm<sup>-1</sup>, which is not the case for any of the other structures which have been characterized. In particular, if the lowest energy structure associated with the methylated  $\alpha$ -glucose in a boat (w- $\alpha$ -Glc-B-124) or in a <sup>1</sup>C<sub>4</sub> chair (w- $\alpha$ -Glc-C'-245) conformation is considered, one can see that the corresponding theoretical spectra do not match the experimental one (Figure 5-17).

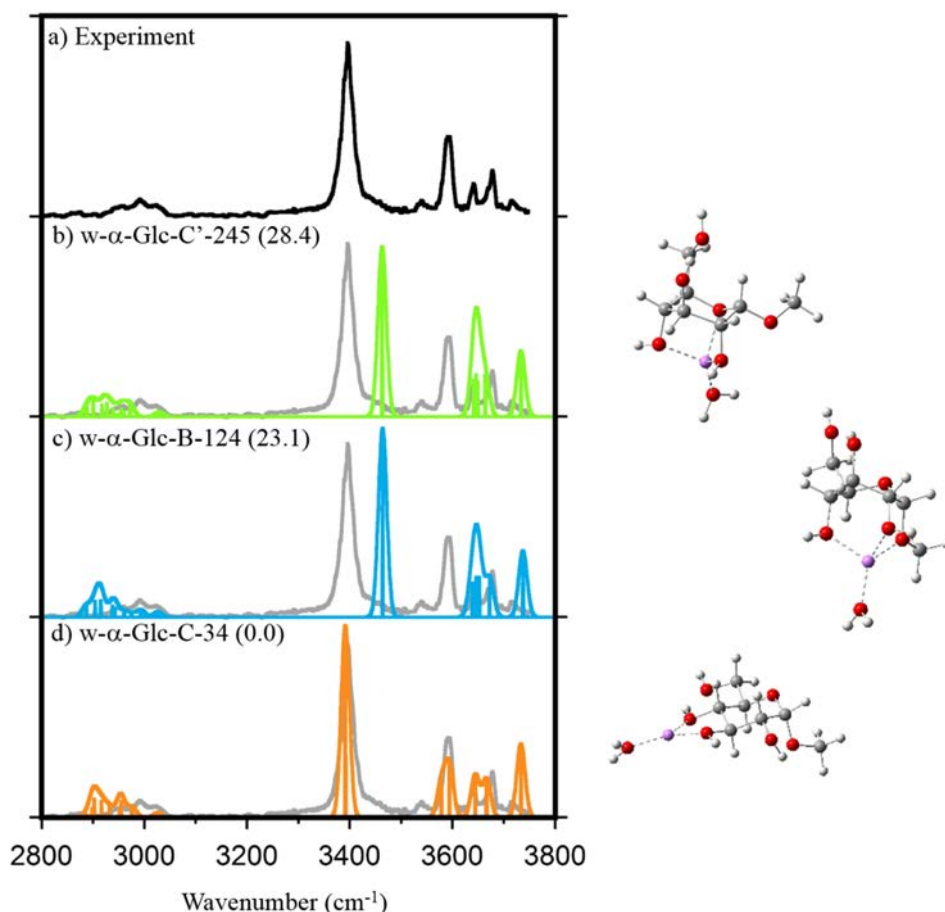


Figure 5-17 : IRMPD spectrum of the  $\text{Li}(\alpha\text{-Me-Glc})(\text{H}_2\text{O})^+$  complex (upper panel). In the lower panels, the experimental spectrum (grey) is compared to the most energetically favored structures derived from the sugar in a  ${}^1C_4$  chair (green), boat (blue), and  ${}^4C_1$  chair (orange) conformation. The corresponding theoretical structures as well as the relative Gibbs free energies (in  $\text{kJ mol}^{-1}$ ) are also provided. Theoretical infrared absorption spectra were calculated at the B3LYP/6-31G\*\* level of theory, and each band was convoluted using a Gaussian profile with a fwhm of  $20 \text{ cm}^{-1}$ . Harmonic frequencies were scaled with a factor of 0.955.

A band assignment is proposed in Table 5-5. The bands centered at  $3640$  and  $3720 \text{ cm}^{-1}$  can be assigned to the symmetric and asymmetric OH stretching modes of the water molecule, which are predicted at  $3642$  and  $3730 \text{ cm}^{-1}$ , respectively. It can be noticed that the experimental band at  $3720 \text{ cm}^{-1}$  is very weak in comparison with the predicted intensity of the asymmetric OH stretching mode. Similar observations have been made for a large variety of hydrated systems [23,24]. And it has been proposed that the weak intensity of the photodissociation signal on resonance with the water asymmetric OH is due to a weak anharmonic coupling of this mode with the other vibrational modes of the molecular ions [25] thus preventing for an efficient fragmentation.

The most structurally diagnostic band is the one observed near  $\sim 3395\text{ cm}^{-1}$ , which can be assigned to the O(4)H stretching mode. This hydroxyl group is involved in the very same hydrogen bonding motif as in the lowest energy structure of the bare  $\text{Li}(\alpha\text{-Me-Glc})^+$  complex. One can notice that this band was more red-shifted in the bare complex ( $3350\text{ cm}^{-1}$ ) than in the monohydrated complex ( $3395\text{ cm}^{-1}$ ). This blue shift effect upon addition of the water molecule can be interpreted as follows. Upon addition of water on the  $\text{Li}^+$  cation, there is an increase of the Li--O(4)H bond distance (1.91 versus  $1.86\text{ \AA}$ ). This weakening of the interaction between  $\text{Li}^+$  and the sugar unit is due to the addition of water to  $\text{Li}^+$ . This is consistent with what has been found for hydrated  $\text{Li}(\text{H}_2\text{O})_n^+$  systems: there is a substantial increase of the Li-O bond distance from  $n=2$  to  $n=3$ . As a result, the synergic effect between the electron transfer from the O(4) atom center to the  $\text{Li}^+$  cation and the O(4)H-O(6) hydrogen bond is less pronounced in the monohydrated than in the base  $\text{Li}(\alpha\text{-Me-Glc})^+$  complex. On the other hand, it is important to stress that the position of the other OH stretching modes of the  $\alpha\text{-Me-Glc}$  structure are not significantly modified upon water addition. This is consistent with the fact that no structural change associated with the  $\text{Li}^+$ -sugar interaction is observed upon addition of water.

Vibrational Mode	Theory ( $\text{cm}^{-1}$ )	$\text{Li}(\alpha\text{-Me-Glucose})(\text{H}_2\text{O})^+$ ( $\text{cm}^{-1}$ )	HB D distance ( $\text{\AA}$ )
$\text{H}_2\text{O}$ as st	3730	3715	
HB A O(6)H st	3665	3675	
$\text{H}_2\text{O}$ s st	3642	3640	
HB A/D O(3)H st	3592	3590	2.40
HB A/D O(2)H st	3575		2.21
HB A/D O(4)H st	3387	3395	1.81

Table 5-5 : Infrared band assignment of the  $\text{Li}(\alpha\text{-Me-Glc})(\text{H}_2\text{O})^+$  complex. Vibrational mode description is provided in the first column. Predicted scaled (by 0.955) harmonic frequencies and the experimental infrared bands are given in column 2, and 3, respectively. The hydrogen bond distance (in  $\text{\AA}$ ) is given in the 4<sup>th</sup> column.

Finally, it should be mentioned that a small band is observed near  $3540\text{ cm}^{-1}$ . Two interpretations can be proposed. First, one could consider that the band observed at  $3590\text{ cm}^{-1}$  is only due to the O(3)H stretching mode which is predicted at  $3592\text{ cm}^{-1}$ ; and that the weaker feature observed at  $3540\text{ cm}^{-1}$  could be assigned to the O(2)H stretching mode predicted at  $3575\text{ cm}^{-1}$ . The difference between the observed and predicted band positions would only be on the order of 1% ( $35\text{ cm}^{-1}$ ). This is a possible

interpretation considering that the absolute average difference between experiment and theory at our level of theory should be on the order of  $25\text{ cm}^{-1}$  [26]. The second interpretation would be that this  $\sim 3540\text{ cm}^{-1}$  band is a combination band. Considering the large intensity of the  $\sim 3395\text{ cm}^{-1}$  band, combination bands of this mode with low frequency modes could be observed, as found for other systems [27-31]. Inspection of the low frequency modes of the w- $\alpha$ -Glc-C-34 structure reveals that it has a vibrational mode predicted at  $157\text{ cm}^{-1}$  which could be a good candidate. As can be seen in Figure 5-18, this vibrational mode could be anharmonically coupled with the O(4)H stretch since it involves a motion of the  $\text{Li}^+$  cation, which is bound to the O(4) atom.

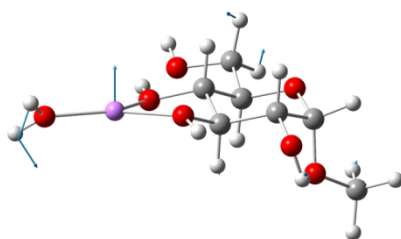


Figure 5-18 : Displacement vectors of the normal mode predicted at  $157\text{ cm}^{-1}$ . This vibrational mode could be coupled to the O(4)H stretching mode giving rise to the combination band observed at  $3540\text{ cm}^{-1}$ .

### 5.5.3 $\text{Li}(\alpha\text{-Me-Man})^+$ complexes.

The experimental infrared spectra of the  $\text{Li}(\alpha\text{-Me-Man})^+$  complex recorded between  $3200$  and  $3800\text{ cm}^{-1}$  is shown in the top panel of the Figure 5-19. Since we were to probe whether this system has strongly red-shifted OH bands, the low energy region was scanned carefully using a large pulse of  $\text{CO}_2$  laser following each OPO/OPA pulse. As for the other bare  $\text{Li}(\text{Sac})^+$  complexes, the signal-to-noise in the low energy part of the spectrum is very low, and it can be concluded that there is no significant band below  $3500\text{ cm}^{-1}$ . Only two broad and asymmetric features can be distinguished, and they are centered at  $3605$  and  $3655\text{ cm}^{-1}$ . The IR absorption spectra of the three type of structures of  $\text{Li}(\alpha\text{-Me-Man})^+$ , each one characteristic of a conformation ( ${}^4\text{C}_1$ ,  ${}^1\text{C}_4$  or boat) of the sugar unit, are given in the three lower panels.

It follows from inspection of Figure 5-19 that, in contrast to the previously discussed cases, none of the three predicted IR spectra perfectly matches the experimental one. IR spectra of other structures derived from the sugar unit in a  ${}^4C_1$ ,  ${}^1C_4$  or boat conformation have been determined (Annex). Nevertheless, in contrast to the previously discussed cases, none of these predicted spectra provides a good visual match with the experimental spectrum. Considering that no strong feature could be observed below  $3500\text{ cm}^{-1}$ , it can be safely concluded that no bidentate structure such as  $\alpha\text{-Man-C}^{\prime}\text{-12}$  is strongly populated (Figure 5-19).

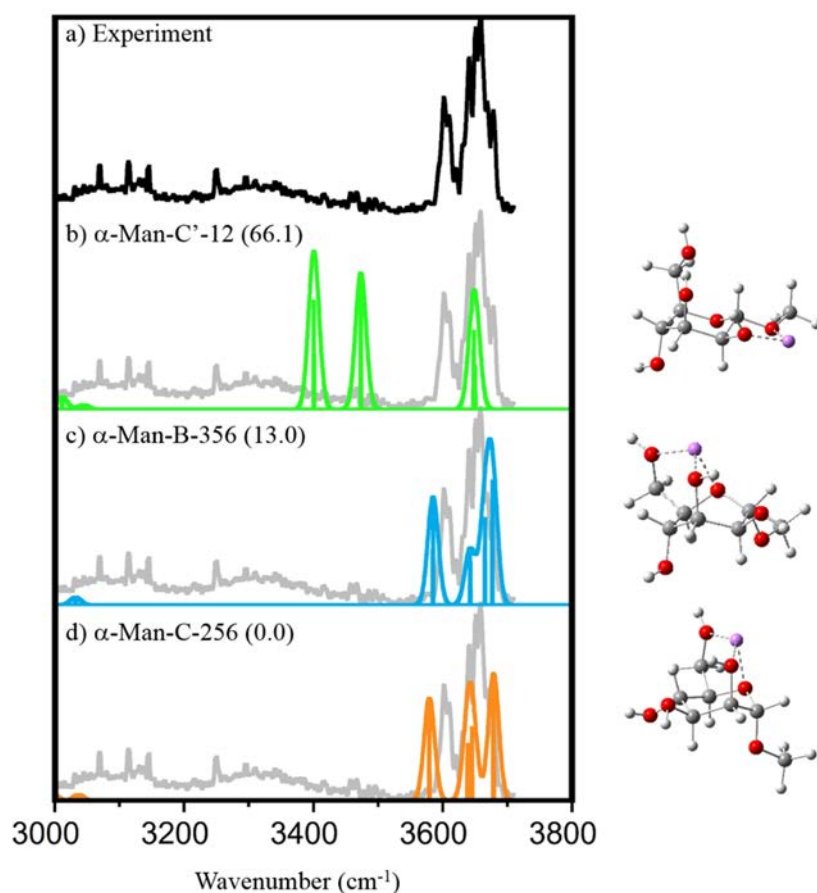


Figure 5-19 : IRMPD spectrum of the  $\text{Li}(\alpha\text{-Me-Man})^+$  complex (upper panel). In the lower panels, the experimental IRMPD spectrum (grey) is compared to the most energetically favored structures with the sugar unit in a  ${}^1C_4$  chair (green), boat (blue), and  ${}^4C_1$  chair (orange) conformation. The corresponding theoretical structures as well as the relative Gibbs free energies (in  $\text{kJ mol}^{-1}$ ) are also provided. Theoretical infrared absorption spectra were calculated at the B3LYP/6-31G\*\* level of theory, and each band was convoluted using a Gaussian profile with a fwhm of  $20\text{ cm}^{-1}$ . Harmonic frequencies were scaled with a factor of 0.955.

A tentative assignment of the IRMPD spectrum can be proposed assuming that only the lowest energy structure ( $\alpha\text{-Man-C-256}$ ) is formed. One can notice, however, that population of relatively low energy structures such as  $\alpha\text{-Man-B-356}$  (Figure 5-19) or  $\alpha\text{-Man-B-1456}$  (Annex) could not be excluded

on the basis of IR spectroscopy. The predicted relative energies of these structures (13.0 and 16.2 kJ mol<sup>-1</sup>), however, are high, and the corresponding population should be very small (less than 1%) assuming a room temperature Boltzmann population.

Assuming the exclusive formation of the <sup>4</sup>C<sub>1</sub> chair conformer ( $\alpha$ -Man-C-256), a band assignment is provided in Table 5-6. The band centered at 3655 cm<sup>-1</sup> can be assigned to the O(3)H stretching mode predicted at 3645 cm<sup>-1</sup>. The asymmetric shape of the band centered at 3655 cm<sup>-1</sup> could be due to the contribution of the absorption bands of the OH stretching modes of the O(6)H and the O(4)H groups predicted at 3678 and 3639 cm<sup>-1</sup>, respectively. Finally the IR feature observed at 3605 cm<sup>-1</sup> could be assigned to the O(2)H stretching mode predicted at 3580 cm<sup>-1</sup>. The  $\alpha$ -Man-C-256 structure is characterized by only one hydrogen bond. The O(2)H hydroxyl group acts as a proton-donor group, but the corresponding HB distance is relatively large (2.32 Å). This is consistent with the fact that the O(2)H stretching mode is only red-shifted by ~60 cm<sup>-1</sup>, and that no IR feature is predicted below 3500 cm<sup>-1</sup>.

Vibrational Mode	Theory (cm <sup>-1</sup> )	Li( $\alpha$ -Me-Mannose) (cm <sup>-1</sup> )	HB D distance (Å)
HB A O(6)H st	3678		
HB A/A O(3)H st	3645	3655	
HB D O(4)H st	3639		2.70
HB A/D O(2)H st	3580	3605	2.32

Table 5-6 : Infrared band assignment of the Li( $\alpha$ -Me-Man)<sup>+</sup> complex. Vibrational mode description is provided in the first column. Predicted scaled (by 0.955) harmonic frequencies and the experimental infrared bands are given in column 2, and 3, respectively. The hydrogen bond distance (in Å) is given in the 4<sup>th</sup> column.

#### 5.5.4 Li( $\alpha$ -Me-Man)(H<sub>2</sub>O)<sup>+</sup> complexes.

The infrared spectrum of the Li( $\alpha$ -Me-Man)(H<sub>2</sub>O)<sup>+</sup> complex recorded in the 2800-3800 cm<sup>-1</sup> spectral range is shown in the top panel of Figure 5-20. In this IR spectrum, the features corresponding to the CH stretching modes of the monohydrated complex are well resolved, and two bands centered at 2920 and 2960 cm<sup>-1</sup> are observed. No strongly red-shifted OH band is observed, and four well-structured features centered at 3600, 3650, 3680, and 3730 cm<sup>-1</sup> are observed. Note that the band centered at 3650

$\text{cm}^{-1}$  is somewhat broader than the three others. The IR absorption spectra of the three different types of structures of the  $\text{Li}(\alpha\text{-Me-Man})(\text{H}_2\text{O})^+$  complex are given in the lower panels of Figure 5-20.

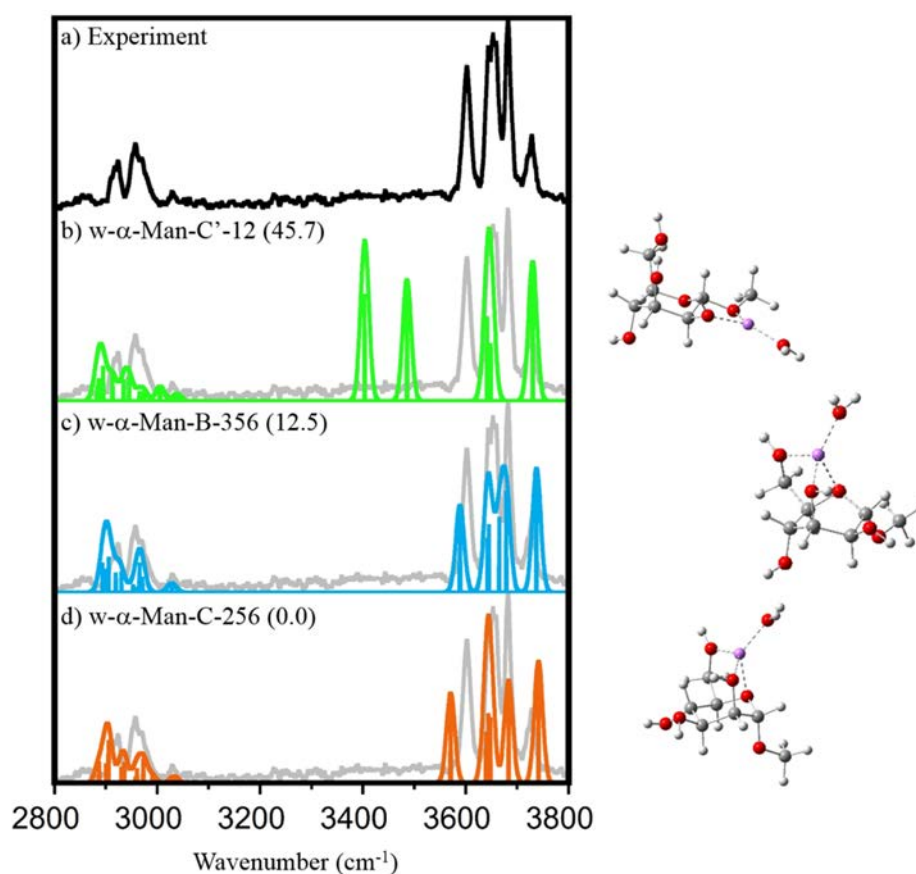


Figure 5-20 : IRMPD spectrum of the  $\text{Li}(\alpha\text{-Me-Man})(\text{H}_2\text{O})^+$  complex (upper panel). In panels b-d the experimental IRMPD spectrum (grey) is compared to the most energetically favored structures of the  ${}^1\text{C}_4$  chair (green), boat (blue), and  ${}^4\text{C}_1$  chair (orange) conformers. The corresponding theoretical structures as well as the relative Gibbs free energies (in  $\text{kJ mol}^{-1}$ ) are also provided. Theoretical infrared absorption spectra were calculated at the B3LYP/6-31G\*\* level of theory, and each band was convoluted using a Gaussian profile with a fwhm of  $20 \text{ cm}^{-1}$ . Harmonic frequencies were scaled with a factor of 0.955.

A bidentate structure was found to be the lowest energy structure ( $w\text{-}\alpha\text{-Man-C}'\text{-12}$ ) when the methylated  $\alpha$ -mannose is in its  ${}^1\text{C}_4$  chair conformation. The relative energy of this structure is  $66.6 \text{ kJ mol}^{-1}$ , and it is thus unlikely to be formed under our experimental condition. As expected, the corresponding IR absorption spectrum (panel b in Figure 5-20) shows bands corresponding to strongly red-shifted OH stretching modes which are not consistent with the experimental observation.

As for the corresponding  $\text{Li}(\alpha\text{-Me-Man})^+$  bare complex, the lowest energy structures correspond to tri-coordinated  $\text{Li}^+$  by the sugar unit in its  ${}^4\text{C}_1$  conformation through the O(2), O(5) and

hydroxymethyl O(6) oxygen atoms. Overall, the lowest energy structure found on the potential energy surface is w- $\alpha$ -Man-C-256 (panel d in Figure 5-20). Next in energy are tri-coordinated structures derived from a boat conformer of the methylated  $\alpha$ -mannose. The lowest representative structure is the w- $\alpha$ -Man-B-356 structure (panel c in Figure 5-20). It is relatively high in energy (13.0 and 18.6 kJ mol<sup>-1</sup> at the B3LYP/6-31G\*\* and MP2/6-311+G\*\*), and it is unlikely to be populated under our experimental conditions. Nevertheless, as for the corresponding structure of the bare complex, the population of the w- $\alpha$ -Man-B-356 structure could not be excluded on the sole basis of the IR spectroscopy data.

Assuming that only the <sup>4</sup>C<sub>1</sub> chair conformer is formed, the band assignment is provided in Table 5-7. The band frequencies of the Li( $\alpha$ -Me-Man)<sup>+</sup> moiety are not modified upon water addition. There are only two additional features. The two features observed at 3730 and 3655 cm<sup>-1</sup> can be assigned to the OH asymmetric and symmetric stretching modes of the water molecule predicted at 3741 and 3648 cm<sup>-1</sup> respectively.

Vibrational Mode	Theory (cm <sup>-1</sup> )	Li( $\alpha$ -Me-Mannose)(H <sub>2</sub> O) <sup>+</sup> (cm <sup>-1</sup> )	HB D distance (Å)
H <sub>2</sub> O as st	3741	3730	
HB A O(6)H st	3683	3680	
H <sub>2</sub> O s st	3648	3655	
HB A/A O(3)H st	3644		
HB D O(4)H st	3639	3645	2.68
HB A/D O(2)H st	3570	3600	2.27

Table 5-7 : Infrared band assignment of the Li( $\alpha$ -Me-Man)(H<sub>2</sub>O)<sup>+</sup> complex. Vibrational mode description is provided in the first column. Predicted scaled (by 0.955) harmonic frequencies and the experimental infrared bands are given in column 2, and 3, respectively. The hydrogen bond distance (in Å) is given in the 4<sup>th</sup> column.

### 5.5.5 Li( $\beta$ -Me-Glc)<sup>+</sup> complexes.

The infrared spectra of Li( $\beta$ -Me-Glc)<sup>+</sup> in the 3200-3800 cm<sup>-1</sup> spectral range are shown in Figure 5-21. Two broad and asymmetric features can be observed at 3600 and 3660 cm<sup>-1</sup> (panel a Figure 5-21). The broad band with a maximum at 3660 cm<sup>-1</sup> has a shoulder on its blue side with a maximum at 3680 cm<sup>-1</sup>, and also a less pronounced shoulder on its red side near 3640 cm<sup>-1</sup>. IR absorption spectra have been calculated for multiple types of coordination modes and hydrogen bonding. Some representative

structures and their corresponding IR absorption spectra are shown in the Annex. In Figure 5-21, only the results for the lowest energy representative structure of each type ( ${}^4C_1$ ,  ${}^1C_4$ , boat) of the sugar coordination are given.

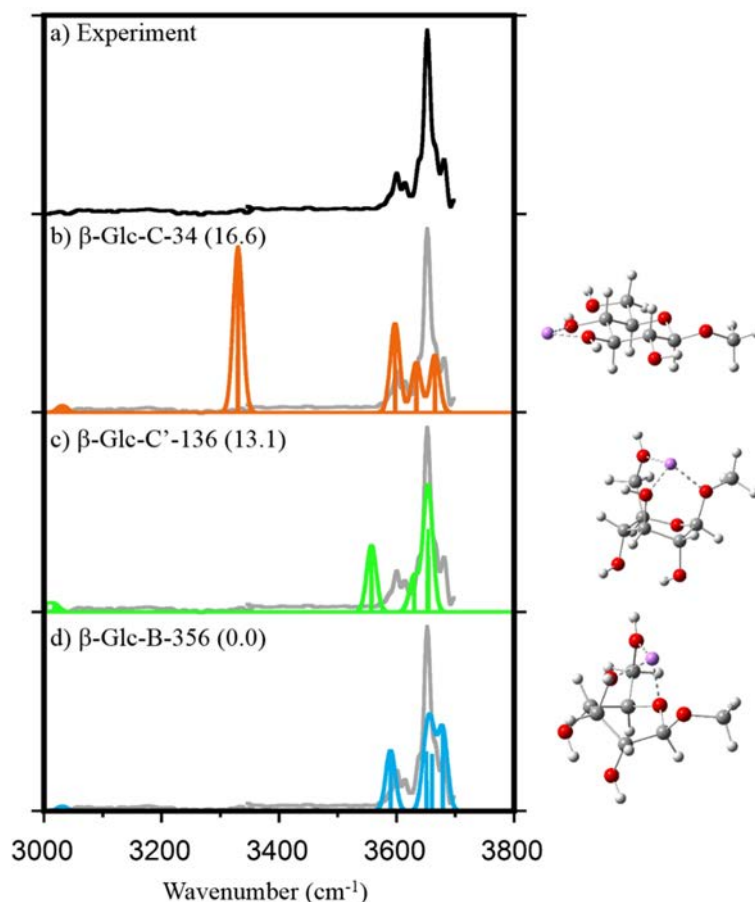


Figure 5-21 : IRMPD spectrum of the  $\text{Li}(\beta\text{-Me-Glc})^+$  complex (upper panel). In the lower b-d panels the experimental IRMPD spectrum (grey) is compared to the most energetically favored structures with the  $\beta$ -glucose in a  ${}^4C_1$  chair (orange),  ${}^1C_4$  chair (green), and boat (blue) conformation. The corresponding theoretical structures as well as the relative Gibbs free energies (in  $\text{kJ mol}^{-1}$ ) are also provided. Theoretical infrared absorption spectra were calculated at the B3LYP/6-31G\*\* level of theory, and each band was convoluted using a Gaussian profile with a fwhm of  $20 \text{ cm}^{-1}$ . Harmonic frequencies were scaled with a factor of 0.955.

Within all the structures that have been characterized, the best match with the experimental IRMPD spectrum is found if the lowest energy structure ( $\beta\text{-Glc-B-356}$ ) is considered. In this structure, the methylated  $\beta$ -glucose acts as a tridentate ligand and the three O(3), O(5), and O(6) oxygen atoms are bound to  $\text{Li}^+$ . Since no band characteristic of strongly red-shifted OH were observed, one can safely

conclude that structure such as  $\beta$ -Glc-C-34 (panel b in Figure 5-21) are not formed under our experimental conditions.

A band assignment is proposed in Table 5-8 assuming that only the  $\beta$ -Glc-B-356 isomer is populated under our experimental conditions. The broad character of the band with a maximum at 3660  $\text{cm}^{-1}$  is probably due to the fact that three IR absorption bands are predicted in this region for the  $\beta$ -Glc-B-356 isomer (Table 5-8). Besides the band associated with the O(2)H stretching mode, which is predicted at 3660  $\text{cm}^{-1}$ , the OH stretching modes of the O(3)H and O(6)H groups are predicted at 3652 and 3678  $\text{cm}^{-1}$ , respectively. The former nicely matches with the position of the shoulder on the blue-side ( $\sim 3680 \text{ cm}^{-1}$ ), while the latter would be consistent with the asymmetric shape on the red-side. The last feature observed at  $\sim 3600 \text{ cm}^{-1}$  can be assigned to the OH stretching mode of the O(4)H group which is predicted at 3589  $\text{cm}^{-1}$ . This band is slightly more red-shifted because it is involved as a donor in a hydrogen bond with the acceptor O(4)H group, and the corresponding intra-sugar hydrogen bond distance is 2.04 Å.

Vibrational Mode	Theory ( $\text{cm}^{-1}$ )	Li( $\beta$ -Me-Glucose) <sup>+</sup> ( $\text{cm}^{-1}$ )	HB D distance (Å)
HB A O(6)H st	3678		
HB A O(2)H st	3660	3660	
HB A O(3)H st	3652		
HB D O(4)H st	3589	3600	2.04

Table 5-8 Infrared band assignment of the Li( $\beta$ -Me-Glc)<sup>+</sup> complex. Vibrational mode description is provided in the first column. Predicted scaled (by 0.955) harmonic frequencies and the experimental infrared bands are given in column 2, and 3, respectively. The hydrogen bond distance (in Å) is given in the 4<sup>th</sup> column.

### 5.5.6 Li( $\beta$ -Me-Glc)(H<sub>2</sub>O)<sup>+</sup> complexes.

The determination of the structure the Li( $\beta$ -Me-Glc)(H<sub>2</sub>O)<sup>+</sup> complex is more challenging since the energy order of di- and tri-coordinated structures is predicted to change upon addition of a water molecule on the Li( $\beta$ -Me-Glc)<sup>+</sup> complex. When the boat structure of the sugar unit is considered, tri-coordinated complexes can be formed through the O(3), O(5) and O(6) oxygen atoms. This is the structure which is predicted to be the lowest in energy for the bare Li( $\beta$ -Me-Glc)<sup>+</sup> complexes at the two level of theory. For the Li( $\beta$ -Me-Glc)(H<sub>2</sub>O)<sup>+</sup> complex, however, a di-coordinated structure ( $w$ - $\beta$ -Glc-C-

34) is predicted to be the lowest energy structure, but structures such as w- $\beta$ -Glc-B-356 derived from a boat are predicted to be only slightly higher in energy.

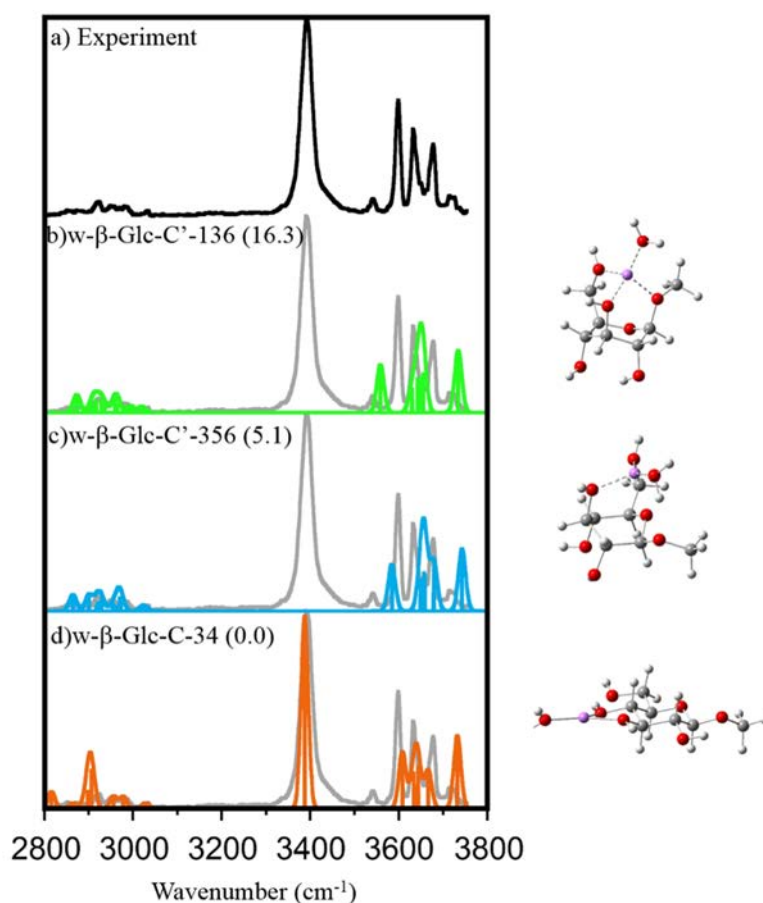


Figure 5-22 : IRMPD spectrum of the  $\text{Li}(\beta\text{-Me-Glc})(\text{H}_2\text{O})^+$  complex (upper panel). In the lower b-d panels the experimental IRMPD spectrum (grey) is compared to the most energetically favored structures with the sugar unit in its  ${}^1C_4$  chair (green), boat (blue), and  ${}^4C_1$  chair (orange) conformation. The corresponding theoretical structures as well as the relative Gibbs free energies (in  $\text{kJ mol}^{-1}$ ) are also provided. Theoretical infrared absorption spectra were calculated at the B3LYP/6-31G\*\* level of theory, and each band was convoluted using a Gaussian profile with a fwhm of  $20 \text{ cm}^{-1}$ . Harmonic frequencies were scaled with a factor of 0.955.

IR spectra of the  $\text{Li}(\beta\text{-Me-Glc})(\text{H}_2\text{O})^+$  complex in the  $2800\text{-}3800 \text{ cm}^{-1}$  energy range are shown in Figure 5-22. The experimental IRMPD spectrum is given in the top panel. A relatively weak signal is observed in the CH stretching region. Five IR features centered at  $3390$ ,  $3600$ ,  $3635$ ,  $3675$ , and  $3720 \text{ cm}^{-1}$  can be observed. The  $3390 \text{ cm}^{-1}$  band is a clear signature of the structural change occurring upon water addition on the  $\text{Li}(\beta\text{-Me-Glc})^+$  complex, since no strongly red-shifted OH stretch was observed in the corresponding IRMPD spectrum.

IR absorption spectra have been calculated for multiple bonding motifs, and the results are summarized in the annex. Overall, the best match with the experimental IRMPD spectrum is found if the lowest energy structure (w- $\beta$ -Glc-C-34) is considered (panel d, Figure 5-22). Considering the relative energy of the w- $\beta$ -Glc-B-356 structure, which is only 5.1 kJ/mol (5.8 kJ/mol) higher in energy at the B3LYP/6-31G\*\* (MP2/6-311+G\*\*) level of theory, one could also consider that a mixture of isomers is formed under our experimental conditions. Nevertheless, considering the narrowness of the band observed at 3600  $\text{cm}^{-1}$ , a significant population of other isomers than the lowest energy one is very unlikely.

A band assignment of the spectrum of the  $\text{Li}(\beta\text{-Me-Glc})(\text{H}_2\text{O})^+$  complex is provided in Table 5-9 assuming that only the w- $\beta$ -Glc-C-34 structure is formed. The experimental feature at 3720  $\text{cm}^{-1}$  can be assigned to the water asymmetric OH stretching mode predicted at 3731  $\text{cm}^{-1}$ . The band observed at 3675  $\text{cm}^{-1}$  corresponds to the stretching mode of the nearly free O(6)H group which is predicted at 3665  $\text{cm}^{-1}$ . The asymmetric character of the band with a maximum at 3635  $\text{cm}^{-1}$  can be interpreted considering that the water symmetric OH stretching mode and the O(2)H stretching mode are predicted very close to each other (3642 and 3633  $\text{cm}^{-1}$ , respectively). Finally, the two observed bands at 3600 and 3390  $\text{cm}^{-1}$  can be assigned to the OH stretching mode of the O(3)H and the O(4)H groups which are bonded to the  $\text{Li}^+$  cation. These bands are predicted at 3605 and 3390  $\text{cm}^{-1}$ , respectively. As for the  $\alpha$ -Glucose analogue, the O(4)H-O(6) hydrogen bond distance is short (1.80 Å), which is consistent with the strong red-shift of the corresponding stretching mode of the hydrogen bond donor O(4)H group. As for the other systems studied here, there is a good correlation between the red-shift of the stretching modes of the hydrogen bond donor groups and the corresponding HB distance (Table 5-9).

As for the  $\alpha$ -Glucose analogue, a weak band near  $\sim 3540 \text{ cm}^{-1}$  is observed and cannot be interpreted as a fundamental transition on the basis of the harmonic frequencies calculated for the w- $\alpha$ -Glc-C-34 structure. One possible interpretation for the observation of this band is that it results from a combination of the O(4)H-O(6) stretching, associated with an intense band at 3390  $\text{cm}^{-1}$ , with a low frequency mode. Inspection of the low frequency modes of the w- $\beta$ -Glc-C-34 structure reveals that it

has a vibrational mode predicted at 157 cm<sup>-1</sup> and involving a motion of the Li<sup>+</sup> cation could be a good candidate.

Vibrational Mode	Theory (cm <sup>-1</sup> )	Li(β-Me-Glucose)(H <sub>2</sub> O) <sup>+</sup> (cm <sup>-1</sup> )	HB D distance (Å)
H <sub>2</sub> O as st	3731	3720	
HB A O(6)H st	3665	3675	
H <sub>2</sub> O s st	3642		
HB A/D O(2)H st	3633	3635	2.56
HB A/D O(3)H st	3605	3600	2.37
HB A/D O(4)H st	3385	3390	1.80

Table 5-9 Infrared band assignment of the Li(β-Me-Glc)(H<sub>2</sub>O)<sup>+</sup> complex. Vibrational mode description is provided in the first column. Predicted scaled (by 0.955) harmonic frequencies and the experimental infrared bands are given in column 2, and 3, respectively. The hydrogen bond distance (in Å) is given in the 4<sup>th</sup> column.

Overall, the analysis of the experimental and theoretical results provide a consistent picture for the Li(β-Me-Glc)<sup>+</sup> and Li(β-Me-Glc)(H<sub>2</sub>O)<sup>+</sup> complexes. Upon addition of a water molecule on Li(β-Me-Glc)<sup>+</sup>, a strong conformational change is induced. The methylated β-glucose initially in a boat conformation and acting as a tridentate ligand, is converted into its <sup>4</sup>C<sub>1</sub> chair conformation in the Li(β-Me-Glc)(H<sub>2</sub>O)<sup>+</sup> complex, and it acts as a bidentate ligand.

Nonetheless, it is important to stress that di- and tri-coordinated structures are predicted to be very close in energy for the Li(β-Me-Glc)(H<sub>2</sub>O)<sup>+</sup> complex. We thus thought that the energy ordering could be easily reversed either by changing the nature of the metal cation and/or by changing the nature of the tag molecule (L=H<sub>2</sub>O). In the cases of the Li(β-Me-Glc)(CH<sub>3</sub>CN)<sup>+</sup> and the Na(β-Me-Glc)(CH<sub>3</sub>CN)<sup>+</sup> systems, it seems that the structure and coordination mode of the sugar moiety do not change since a band near ~3400 cm<sup>-1</sup> is observed. Only a slight frequency shift of the band was observed. The position of this band slightly varies from one complex to the other: it is observed at ~3400, ~3420, and ~3430 cm<sup>-1</sup> for the Li(β-Me-Glc)(H<sub>2</sub>O)<sup>+</sup>, Li(β-Me-Glc)(CH<sub>3</sub>CN)<sup>+</sup>, and Na(β-Me-Glc)(CH<sub>3</sub>CN)<sup>+</sup> complexes.

In the case of the α-glucose complexes, this structurally diagnostic band was observed to be blue-shifted from the bare Li(α-Me-Glc)<sup>+</sup> complex (near ~3350 cm<sup>-1</sup>) to the monohydrated Li(α-Me-

Glc)(H<sub>2</sub>O)<sup>+</sup> (near ~3395 cm<sup>-1</sup>). This blue shift effect upon addition of the water molecule could be interpreted considering the electron donation of water to the Li<sup>+</sup> cation. Upon addition of the third (water) ligand, the electron donation from the sugar is reduced and the net result is an increase of the Li--O(4)H bond distance (1.91 versus 1.86 Å).

In the case of the β-glucose complexes, a similar interpretation can be proposed. The blue shift observed from Li(β-Me-Glc)(H<sub>2</sub>O)<sup>+</sup> to Li(β-Me-Glc)(CH<sub>3</sub>CN)<sup>+</sup> can be interpreted considering the gas basicity of the neutral molecules. The gas basicity of the CH<sub>3</sub>CN is higher (~370 kcal mol<sup>-1</sup>) than that of the H<sub>2</sub>O molecule (~30 kcal mol<sup>-1</sup>). As a result, the charge transfer to the Li<sup>+</sup> cation from the CH<sub>3</sub>CN molecule is greater than that from the water molecule, which could explain the weakening of the Li--O(4)H bond, and consequently a blue-shift of the O(4)H frequency band from ~3400 to 3420 cm<sup>-1</sup>.

## 5.6 Conclusions

Combination of DFT calculations and IRMPD spectroscopy has been shown to be a very suitable and powerful tool for the structural characterization of monosaccharides complexes in the gas phase. Compelling evidences have been provided that Li(Sac)<sup>+</sup> and Li(Sac)(H<sub>2</sub>O)<sup>+</sup> formed in a Fourier Transform Mass Spectrometer have different structures depending on the stereochemistry of the monosaccharide structure.

The interaction between an alkali cation and the sugar moiety is the result of a trade-off between the intrinsic stabilization of the sugar units such as intra-sugar hydrogen bonding and maximization of the coordination of the alkali cation. B3LYP calculations are consistent with experimental spectroscopic results. When the most stable <sup>4</sup>C<sub>1</sub> chair conformation of the sugar moiety can act as an efficient tridentate ligand, tri- and tetra-coordinated Li<sup>+</sup> complexes are formed for the Li(Sac)<sup>+</sup> and Li(Sac)(H<sub>2</sub>O)<sup>+</sup> complexes, as in the case of methyl-α-mannose. In the cases of the two glucose anomers, however, the <sup>4</sup>C<sub>1</sub> chair conformation cannot act as a tridentate ligand. Bidentate coordination of the glucose anomers to the Li<sup>+</sup> cation can be favorable, and in the cases of the monohydrated complexes of the glucose anomers, this leads to the lowest energy structure.

The flexibility of the hydroxymethyl plays an essential role for the stabilization of bi- or tri-coordinated structures. If the free methylated monosaccharides are considered in their  ${}^4C_1$  chair conformation, the hydroxymethyl O(6)H group is involved in the same hydrogen bonding network in the three cases. It acts as a hydrogen bond acceptor with the O(4)H donor group. In the case of  $\alpha$ -mannose, when breaking this O(4)H-O(6) hydrogen bond, it is possible to find an orientation of the hydroxymethyl group allowing for a tri-coordination of the  $Li^+$  cation. In the cases of the glucose anomers, however, this is not the case, and the  ${}^4C_1$  chair conformation can only act as a bidentate ligand. Such bidentate structures are predicted to be the most favorable for the monohydrated complexes of the glucose anomers using our two levels of theory.

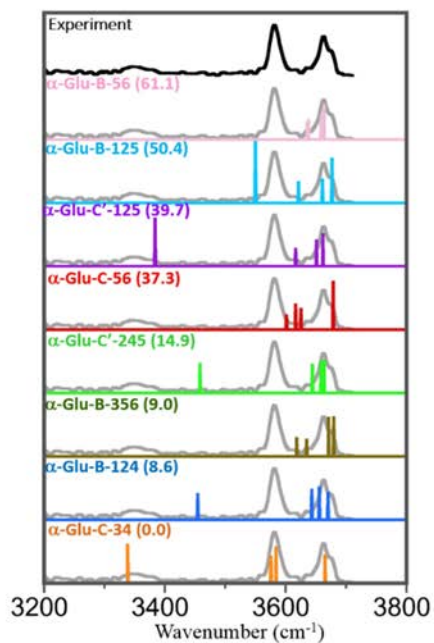
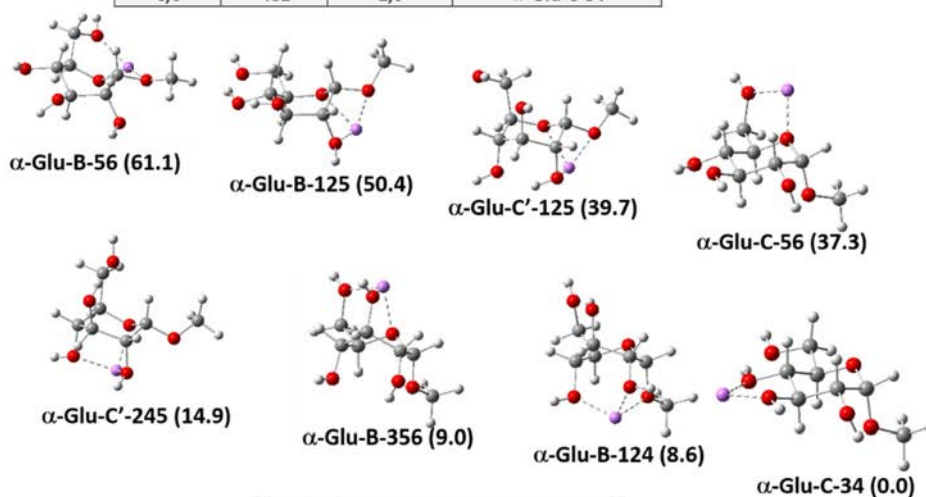
The hydroxymethyl group seems to be strongly involved in the stabilization of the bidentate structures. Indeed, the analysis of the IR spectra of these complexes reveals that these bidentate structures are characterized by a band near  $3400\text{ cm}^{-1}$  which can be assigned to the O(4)H-O(6) hydrogen bond. This hydrogen bond is intrinsically strong in the free sugar since a six-membered ring hydrogen bond is formed. Upon coordination of the sugar to  $Li^+$  through the O(3) and O(4) hydroxyl groups, the O(4)H-O(6) hydrogen bond is strongly reinforced as shown by the decrease of the HB distance (near  $-0.2\text{ \AA}$ ), consistent with the significant red-shift of the O(4)H stretching frequency.

This  $3400\text{ cm}^{-1}$  band could be used to monitor the change of coordination mode of methyl- $\beta$ -glucose when adding a water molecule to  $Li(\beta\text{-Me-Glc})^+$ . This observation is consistent with the relative energies of the bi- and tridentate structures calculated for the  $Li(\beta\text{-Me-Glc})^+$  and  $Li(\beta\text{-Me-Glc})(H_2O)^+$ . Nonetheless, it is important to stress that these two types of coordination structures are very close in energy in the case of the methyl- $\beta$ -glucose, and it is likely that this energy ordering is sensitive to the nature of the metal cation. If it was the case, this could provide an interpretation for some changes in the DIMS chromatograms.

## 5.7 Annexes

### $\text{Li}(\alpha\text{-Me-Glc})^+$

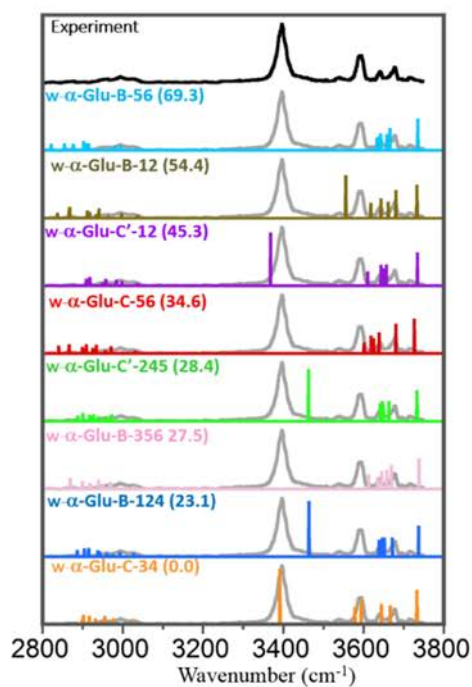
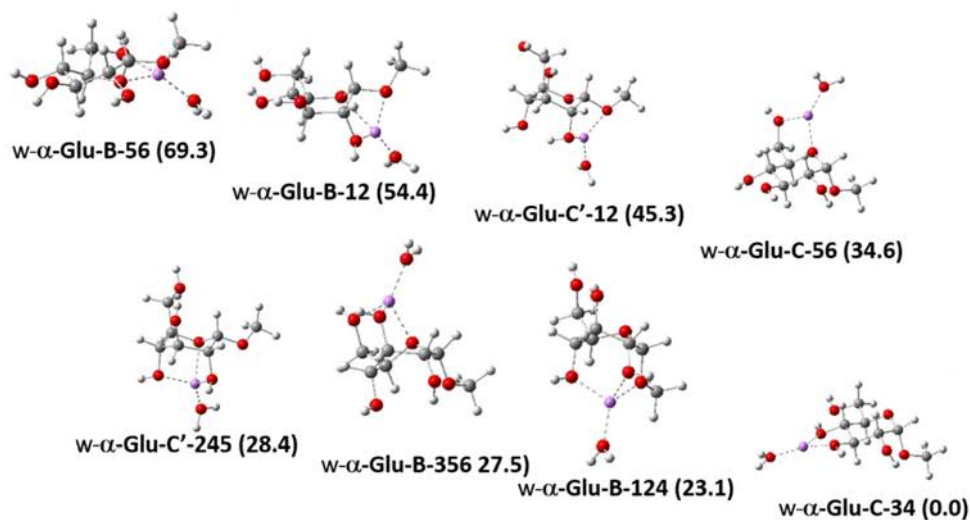
Rel G298K	ISOMER	Coordination	New Name
61,1	Boat	2,0	$\alpha\text{-Glu-B-56}$
50,4	Boat	3,0	$\alpha\text{-Glu-B-125}$
39,7	1C4	3,0	$\alpha\text{-Glu-C}'\text{-125}$
37,3	4C1	2,0	$\alpha\text{-Glu-C-56}$
14,9	1C4	3,0	$\alpha\text{-Glu-C}'\text{-245}$
9,0	Boat	3,0	$\alpha\text{-Glu-B-356}$
8,6	Boat	3,0	$\alpha\text{-Glu-B-124}$
0,0	4C1	2,0	$\alpha\text{-Glu-C-34}$



Annex 5-1 : Structure and energetics of the lowest energy structure of the  $\text{Li}(\alpha\text{-Me-Glc})^+$  system. The free Gibbs energy is given in parenthesis in  $\text{kJ mol}^{-1}$ . The stationary points were computed at B3LYP/6-31G\*\* level of theory. The harmonic absorption spectrum of each individual conformer is compared with the experimental IR spectrum in the bottom of the Figure. A scaling factor of 0.955 was applied to the predicted harmonic frequencies.

## w-Li( $\alpha$ -Me-Glc)<sup>+</sup>

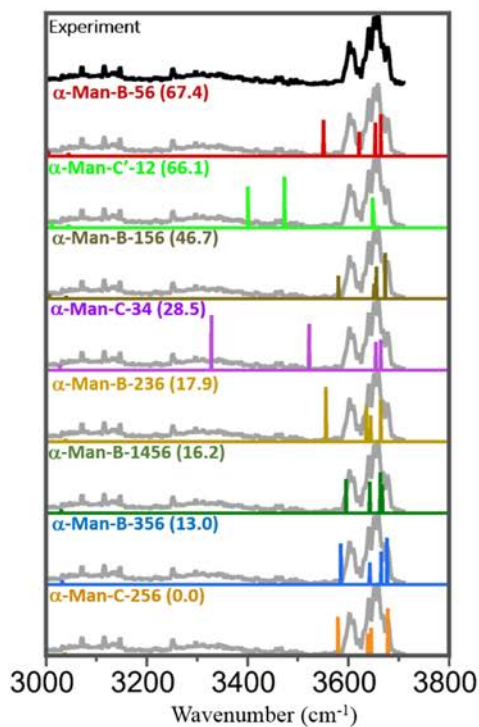
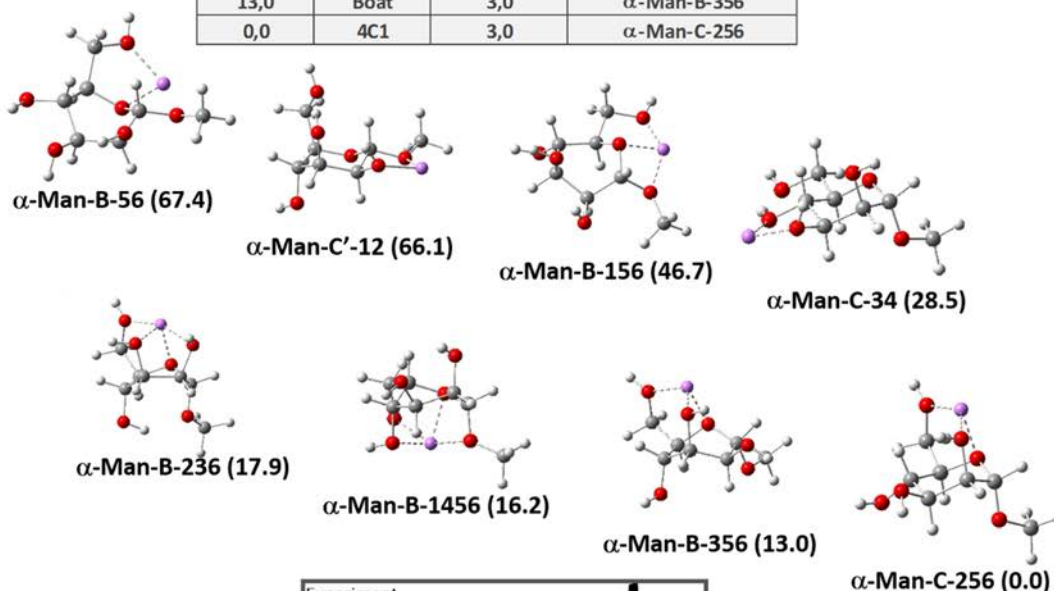
Rel G298K	ISOMER	Coordination	New Name
69,3	Boat	2,0	w- $\alpha$ -Glu-B-56
54,4	Boat	2,0	w- $\alpha$ -Glu-B-12
45,3	1C4	2,0	w- $\alpha$ -Glu-C'-12
34,6	4C1	2,0	w- $\alpha$ -Glu-C-56
28,4	1C4	3,0	w- $\alpha$ -Glu-C'-245
27,5	Boat	3,0	w- $\alpha$ -Glu-B-356
23,1	Boat	3,0	w- $\alpha$ -Glu-B-124
0,0	4C1	2,0	w- $\alpha$ -Glu-C-34



Annex 5-2 :Structure and energetics of the lowest energy structure of the Li( $\alpha$ -Me-Glc)(H<sub>2</sub>O)<sup>+</sup> system. The free Gibbs energy is given in parenthesis in kJ mol<sup>-1</sup>.The stationary points were computed at B3LYP/6-31G\*\* level of theory. The harmonic absorption spectrum of each individual conformer is compared with the experimental IR spectrum in the bottom of the Figure. A scaling factor of 0.955 was applied to the predicted harmonic frequencies

## Li( $\alpha$ -Me-Man)<sup>+</sup>

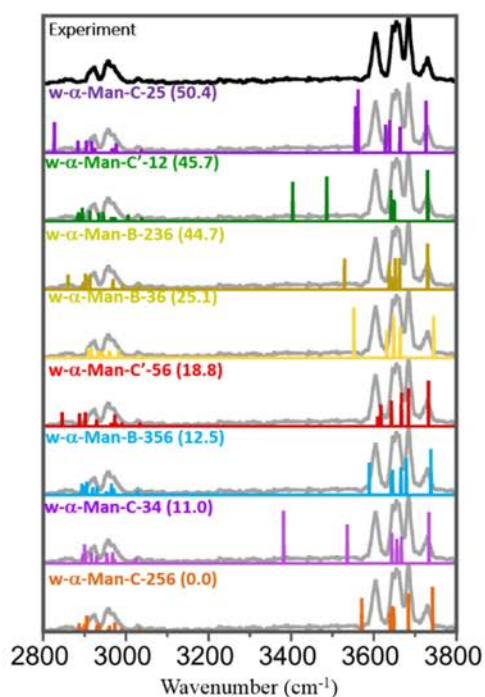
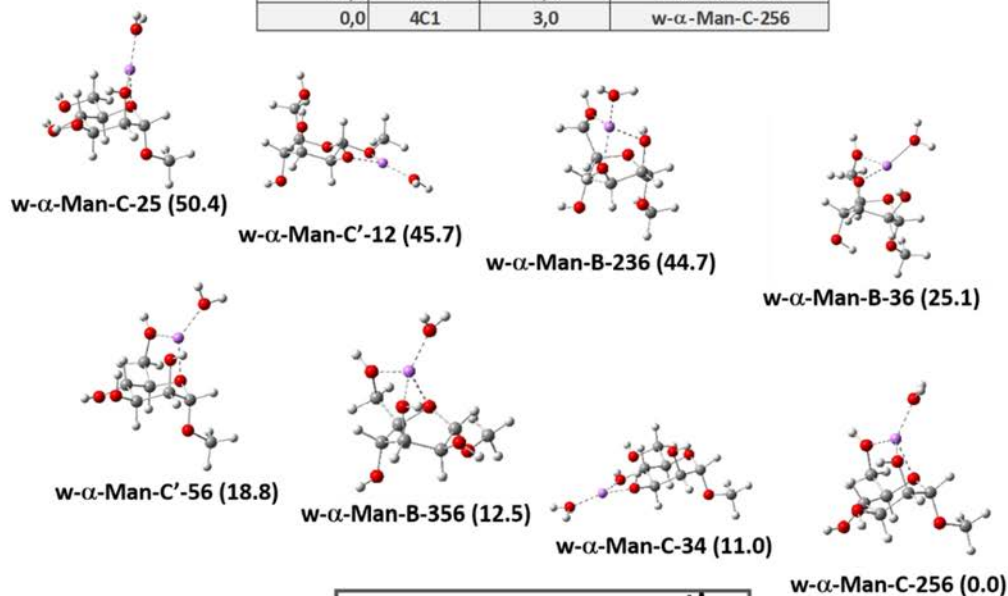
Rel G298K	ISOMER	Coordination	New Name
67,4	Boat	2,0	$\alpha$ -Man-B-56
66,1	1C4	2,0	$\alpha$ -Man-C'-12
46,7	Boat	3,0	$\alpha$ -Man-B-156
28,5	4C1	2,0	$\alpha$ -Man-C-34
17,9	Boat	3,0	$\alpha$ -Man-B-236
16,2	Boat	4,0	$\alpha$ -Man-B-1456
13,0	Boat	3,0	$\alpha$ -Man-B-356
0,0	4C1	3,0	$\alpha$ -Man-C-256



Annex 5-3 : Structure and energetics of the lowest energy structure of the Li( $\alpha$ -Me-Man)<sup>+</sup> system. The free Gibbs energy is given in parenthesis in kJ mol<sup>-1</sup>. The stationary points were computed at B3LYP/6-31G\*\* level of theory. The harmonic absorption spectrum of each individual conformer is compared with the experimental IR spectrum in the bottom of the Figure. A scaling factor of 0.955 was applied to the predicted harmonic frequencies.

## w-Li( $\alpha$ -Me-Man)<sup>+</sup>

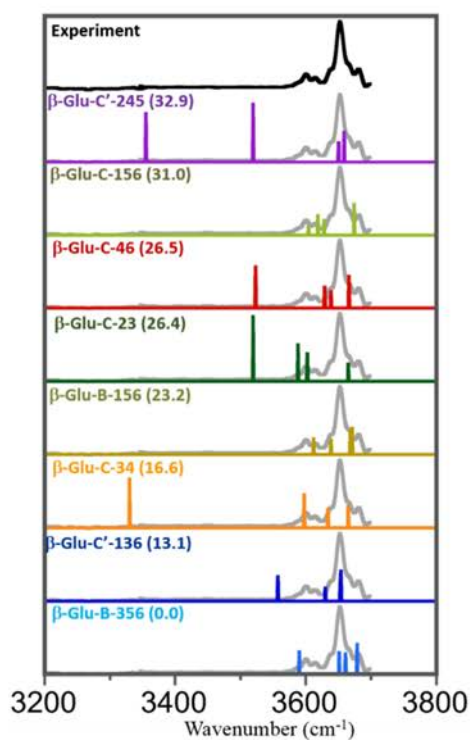
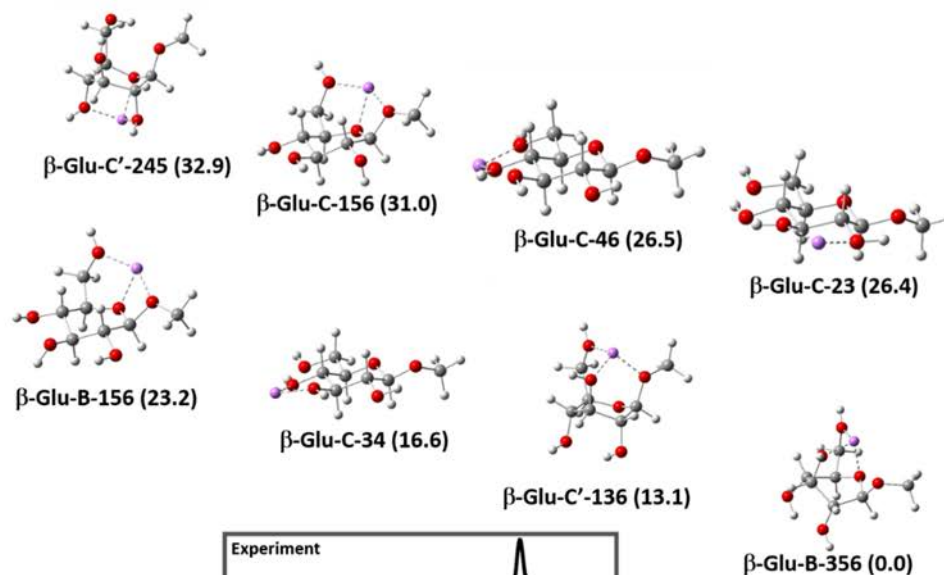
Rel G298K	ISOMER	Coordination	New Name
50,4	4C1	2,0	w- $\alpha$ -Man-C-25
45,7	1C4	2,0	w- $\alpha$ -Man-C'-12
44,7	Boat	3,0	w- $\alpha$ -Man-B-236
25,1	Boat	2,0	w- $\alpha$ -Man-B-36
18,8	4C1	2,0	w- $\alpha$ -Man-C-56
12,5	Boat	3,0	w- $\alpha$ -Man-B-356
11,0	4C1	2,0	w- $\alpha$ -Man-C-34
0,0	4C1	3,0	w- $\alpha$ -Man-C-256



Annex 5-4 : Structure and energetics of the lowest energy structure of the Li( $\alpha$ -Me-Man)(H<sub>2</sub>O)<sup>+</sup> system. The free Gibbs energy is given in parenthesis in kJ mol<sup>-1</sup>. The stationary points were computed at B3LYP/6-31G\*\* level of theory. The harmonic absorption spectrum of each individual conformer is compared with the experimental IR spectrum in the bottom of the Figure. A scaling factor of 0.955 was applied to the predicted harmonic frequencies.

## Li( $\beta$ -Me-Glc)<sup>+</sup>

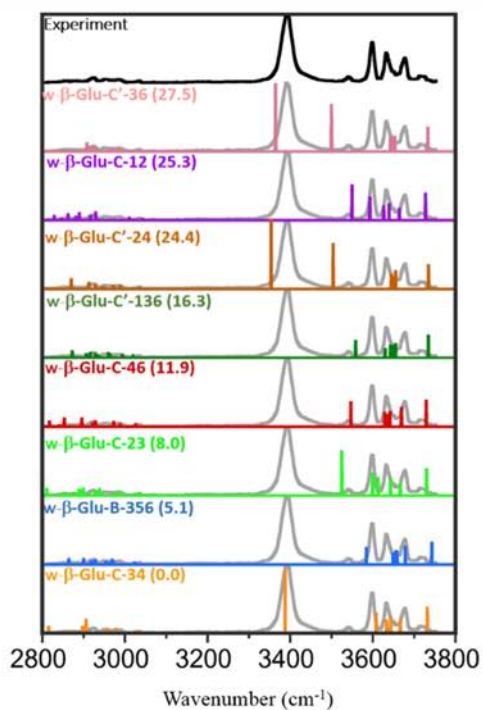
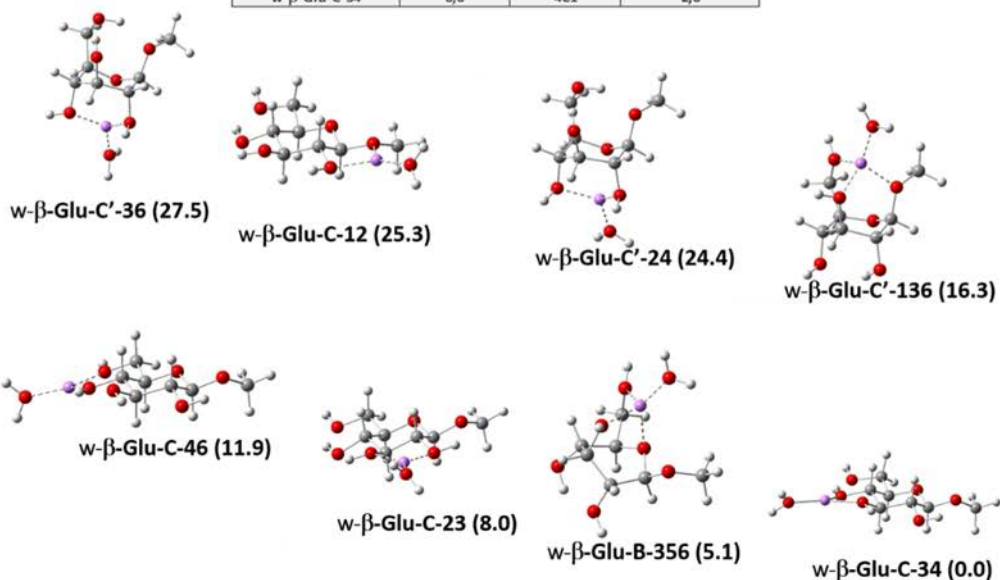
Structure Name	Rel G 298K	ISOMER	Coordination
$\beta$ -Glu-C'-245	32,9	1C4	3,0
$\beta$ -Glu-C-156	31,0	4C1	3,0
$\beta$ -Glu-C-46	26,5	4C1	2,0
$\beta$ -Glu-C-23	26,4	4C1	2,0
$\beta$ -Glu-B-156	23,2	Boat	3,0
$\beta$ -Glu-C-34	16,6	4C1	2,0
$\beta$ -Glu-C'-136	13,1	1C4	3,0
$\beta$ -Glu-B-356	0,0	Boat	3,0



Annex 5-5 : Structure and energetics of the lowest energy structure of the Li( $\beta$ -Me-Glc)<sup>+</sup> system. The free Gibbs energy is given in parenthesis in kJ mol<sup>-1</sup>. The stationary points were computed at B3LYP/6-31G\*\* level of theory. The harmonic absorption spectrum of each individual conformer is compared with the experimental IR spectrum in the bottom of the Figure. A scaling factor of 0.955 was applied to the predicted harmonic frequencies.

## w-Li( $\beta$ -Me-Glc)<sup>+</sup>

Structure Name	Rel G298K	ISOMER	Coordination
w- $\beta$ -Glu-C'-36	27,5	1C4	2,0
w- $\beta$ -Glu-C-12	25,3	4C1	2,0
w- $\beta$ -Glu-C'-24	24,4	1C4	2,0
w- $\beta$ -Glu-C'-136	16,3	1C4	3,0
w- $\beta$ -Glu-C-46	11,9	4C1	2,0
w- $\beta$ -Glu-C-23	8,0	4C1	2,0
w- $\beta$ -Glu-B-356	5,1	Boat	3,0
w- $\beta$ -Glu-C-34	0,0	4C1	2,0



Annex 5-6 : Structure and energetics of the lowest energy structure of the  $\text{Li}(\beta\text{-Me-Glc})(\text{H}_2\text{O})^+$  system. The free Gibbs energy is given in parenthesis in  $\text{kJ mol}^{-1}$ . The stationary points were computed at B3LYP/6-31G\*\* level of theory. The harmonic absorption spectrum of each individual conformer is compared with the experimental IR spectrum in the bottom of the Figure. A scaling factor of 0.955 was applied to the predicted harmonic frequencies.

## 5.8 Bibliography

- (1) Brown, J. W.; Wladkowski, B. D. *J. Am. Chem. Soc.* **1996**, *118*, 1190.
- (2) Jebber, K. A.; Zhang, K.; Cassady, C. J.; ChungPhillips, A. *J. Am. Chem. Soc.* **1996**, *118*, 10515.
- (3) Barrows, S. E.; Storer, J. W.; Cramer, C. J.; French, A. D.; Truhlar, D. G. *J. Comput. Chem.* **1998**, *19*, 1111.
- (4) Guler, L. P.; Yu, Y. Q.; Kenttamaa, H. I. *J. Phys. Chem. A* **2002**, *106*, 6754.
- (5) Alonso, J. L.; Lozoya, M. A.; Pena, I.; Lopez, J. C.; Cabezas, C.; Mata, S.; Blanco, S. *Chem. Sci.* **2014**, *5*, 515.
- (6) Bakker, J. M.; Sinha, R. K.; Besson, T.; Brugnara, M.; Tosi, P.; Salpin, J. Y.; Maitre, P. *J. Phys. Chem. A* **2008**, *112*, 12393.
- (7) Bythell, B. J.; Hernandez, O.; Steinmetz, V.; Paizs, B.; Maitre, P. *Int. J. Mass spectrom.* **2012**, *316*, 227.
- (8) Cerda, B. A.; Wesdemiotis, C. *Int. J. Mass spectrom.* **1999**, *189*, 189.
- (9) Heaton, A. L.; Armentrout, P. B. *J. Phys. Chem. A* **2008**, *112*, 10156.
- (10) Carcabal, P.; Jockusch, R. A.; Hunig, I.; Snoek, L. C.; Kroemer, R. T.; Davis, B. G.; Gamblin, D. P.; Compagnon, I.; Oomens, J.; Simons, J. P. *J. Am. Chem. Soc.* **2005**, *127*, 11414.
- (11) Kovacs, A.; Ivanov, A. Y. *J. Phys. Chem. B* **2009**, *113*, 2151.
- (12) Walters, R. S.; Pillai, E. D.; Duncan, M. A. *J. Am. Chem. Soc.* **2005**, *127*, 16599.
- (13) Rahal-Sekkal, M.; Sekkal, N.; Kleb, D. C.; Bleckmann, P. *J. Comput. Chem.* **2003**, *24*, 806.
- (14) Fabian, W. M. F. *Theor. Chem. Acc.* **2007**, *117*, 223.
- (15) Rao, J. S.; Dinadayalane, T. C.; Leszczynski, J.; Sastry, G. N. *J. Phys. Chem. A* **2008**, *112*, 12944.
- (16) Rodgers, M. T.; Armentrout, P. B. *J. Phys. Chem. A* **1997**, *101*, 1238.
- (17) Dalleska, N. F.; Tjelta, B. L.; Armentrout, P. B. *J. Phys. Chem.* **1994**, *98*, 4191.
- (18) Nagornova, N. S.; Guglielmi, M.; Doemer, M.; Tavernelli, I.; Rothlisberger, U.; Rizzo, T. R.; Boyarkin, O. V. *Angewandte Chemie-International Edition* **2011**, *50*, 5383.
- (19) Wassermann, T. N.; Boyarkin, O. V.; Paizs, B.; Rizzo, T. R. *J. Am. Soc. Mass. Spectrom.* **2012**, *23*, 1029.
- (20) Kamrath, M. Z.; Garand, E.; Jordan, P. A.; Leavitt, C. M.; Wolk, A. B.; Van Stipdonk, M. J.; Miller, S. J.; Johnson, M. A. *J. Am. Chem. Soc.* **2011**, *133*, 6440.
- (21) Leavitt, C. M.; Wolk, A. B.; Kamrath, M. Z.; Garand, E.; Van Stipdonk, M. J.; Johnson, M. A. *J. Am. Soc. Mass. Spectrom.* **2011**, *22*, 1941.
- (22) Roscioli, J. R.; McCunn, L. R.; Johnson, M. A. *Science* **2007**, *316*, 249.
- (23) Carnegie, P. D.; Bandyopadhyay, B.; Duncan, M. A. *J. Chem. Phys.* **2011**, *134*, 9.
- (24) Carnegie, P. D.; Bandyopadhyay, B.; Duncan, M. A. *J. Phys. Chem. A* **2008**, *112*, 6237.
- (25) Pankewitz, T.; Lagutschenkov, A.; Niedner-Schatteburg, G.; Xantheas, S. S.; Lee, Y.-T. *J. Chem. Phys.* **2007**, *126*.
- (26) Halls, M. D.; Velkovski, J.; Schlegel, H. B. *Theor. Chem. Acc.* **2001**, *105*, 413.
- (27) Kunttu, H. M.; Seetula, J. A. *Chem. Phys.* **1994**, *189*, 273.
- (28) Rasanen, M.; Seetula, J.; Kunttu, H. *J. Chem. Phys.* **1993**, *98*, 3914.
- (29) Pivonka, N. L.; Kaposta, C.; von Helden, G.; Meijer, G.; Woste, L.; Neumark, D. M.; Asmis, K. R. *J. Chem. Phys.* **2002**, *117*, 6493.
- (30) Pivonka, N. L.; Kaposta, C.; Brummer, M.; von Helden, G.; Meijer, G.; Woste, L.; Neumark, D. M.; Asmis, K. R. *J. Chem. Phys.* **2003**, *118*, 5275.
- (31) Fridgen, T. D.; McMahon, T. B.; MacAleese, L.; Lemaire, J.; Maitre, P. *J. Phys. Chem. A* **2004**, *108*, 9008.







## CONCLUSION

Au cours de cette thèse, deux spectromètres de masse tandem ont été utilisés pour effectuer la spectroscopie infrarouge d'ions, et j'ai donc été particulièrement attentif à la reproductibilité des expériences d'un appareil à l'autre. Ce travail a contribué, je l'espère, à montrer que les spectres obtenus avec ces deux appareils commerciaux sont parfaitement si les conditions expérimentales sont bien définies.

Cette thèse a contribué à montrer que des signatures spectrales intéressantes peuvent apparaître dans la gamme spectrale correspondant aux vibrations d'élongation des groupes NH et OH des fragments de peptides. Dans le cas des ions an, ce travail a permis de définitivement conclure qu'il peut y avoir une permutation de séquence associée à leur formation dans des conditions de CID. Cette isomérisation est relativement lente mais peut se produire lors de l'étape CID. Nous avons pu caractériser par spectroscopie la dynamique d'isomérisation. Ce travail met en lumière le fait que les conditions expérimentales, en particulier associées aux étapes de CID et de thermalisation des ions, devraient être plus précisément définies pour les études spectroscopiques.

La caractérisation des ions fragments de taille moyenne, notamment les ions  $b_n$  ( $n=6-9$ ) étudiés au chapitre 3, devra être poursuivie, tant pour les parties expérimentales que théoriques. D'un point de vue théorique, il semble que dans le cas de l'ion  $b_6$  d'une oligoalanine nous ayons mis en évidence le fait qu'une structure de type Zundel peut être formée. La modélisation du spectre infrarouge associé à ce type de structure est complexe, compte tenu de la forte anharmonicité de certains modes de vibration, et devra être complétée. A ce jour, seules de petits systèmes tels que  $H+(H_2O)_2$  ont pu être modélisés avec succès. D'un point de vue expérimental, la voie que nous avons envisagée, à savoir combiner spectroscopie infrarouge et réaction ion-molécule, s'est avérée être intéressante. Nous avons pu montrer que la formation spécifique d'adduits entre  $NH_3$  et des ions fragments  $b_n$  de taille moyenne est bien spécifique de la structure macrocyclique des fragments. Une perspective intéressante, que nous n'avons pas pu mettre en œuvre, serait la sélection par mobilité ionique d'ions fragments qui seraient sondés ultérieurement par spectroscopie infrarouge.

Un prototype de mobilité ionique a pu être implémenté dans le cadre de cette thèse, grâce à la collaboration avec le groupe de G. L. Glish (Caroline du Nord). Le dispositif basé sur la Differential Ion Mobility Spectrometry (DIMS) est opérationnel, et nous avons pu obtenir pour la première fois des spectres infrarouges d'ions sélectionnés par DIMS.

D'un point de vue fondamental, l'intégration simultanée de la séparation par mobilité ionique et de la spectroscopie infrarouge à un spectromètre de masse permet de sonder la structure d'un isomère unique, voire la dynamique d'interconversion vers un autre isomère. Notre montage actuel ne peut être utilisé pour séparer et sonder des conformères, c'est pourquoi nous nous sommes focalisés sur la séparation d'isomères. Comme l'ont montré D. Clemmer en combinant deux tubes IMS, et plus récemment T. Rizzo en combinant la séparation par FAIMS avec la spectroscopie de photo-fragmentation UV-Visible, les isomères sélectionnés par mobilité ionique sont activés par collisions à la sortie de la zone de haute pression. Dans le cas de notre montage, nous avons mis en évidence cette isomérisation dans le cas de la triglycine protonée, dont deux conformères ont été caractérisés par spectroscopie IRMPD. Même si l'on pouvait maîtriser cette phase d'activation, il faut garder à l'esprit que l'isomérisation peut également se produire au sein du piège de Paul.

D'un point de vue analytique, l'intégration de la séparation par DIMS et de la caractérisation par activation infrarouge pourrait être intéressante pour une recherche ciblée au sein d'un mélange complexe, à condition que les molécules cibles soient caractérisées par un groupe fonctionnel ayant une signature vibrationnelle particulière. Comme illustré en fin de chapitre 4, on pourrait dans ce cas utiliser le laser à fréquence fixe pour fragmenter sélectivement les ions cibles, au sein d'une fraction d'un mélange complexe sélectionnée par DIMS. C'est une perspective qui est actuellement explorée dans le groupe dans le champ de la protéomique.

